IMPACT OF FREEZE-THAW AND DE-ICER ON THE STRUCTURAL AND FUNCTIONAL PERFORMANCE OF CANADIAN AIRPORT ASPHALT MATERIALS

by

Yang (Frank) Liu

A thesis

presented to the University of Waterloo

in fulfillment of the

thesis requirement for the degree of

Doctor of Philosophy

in

Civil Engineering

Waterloo, Ontario, Canada, 2021

Examining Committee Membership

The following served on the Examining Committee for this thesis. The decision of the Examining Committee is by majority vote.

External Examiner **Dr. Ernest Heymsfield**

Civil Engineering, University of Arkansas

Supervisor **Dr. Susan Tighe**

Civil and Environmental Engineering, University of Waterloo

Co-Supervisor **Dr. Rebecca Saari**

Civil and Environmental Engineering, University of Waterloo

Internal Member **Dr. Hassan Baaj**

Civil and Environmental Engineering, University of Waterloo

Internal Member **Dr. Hamid Jahed**

Mechanical and Mechatronics Engineering, University of Waterloo

Internal-external Member **Dr. Sina Varamini**

McAsphalt Industries Limited, Scarborough, Ontario

Author's Declaration

This thesis consists of material all of which I authored or co-authored: see Statement of Contributions included in the thesis. This is a true copy of the thesis, including any required final revisions, as accepted by my examiners.

I understand that my thesis may be made electronically available to the public.

ABSTRACT

Asphalt pavement is widely used on roadways and airside pavement across Canada. Despite various benefits including smooth driving experience, rapid construction, as well as the high recyclability of asphalt pavement, common failures such as permanent deformation on the heavy traffic-dominated road and shear-related, distresses on airport pavement have drawn the attention of researchers and pavement engineers. During hot summer, slow-moving heavy trucks during rush hours can generate permanent deformation and shorten the pavement service life. During the long harsh winter, big diurnal temperature variations make asphalt material experience numerous freeze-thaw cycles. Various anti-icing and de-icing agent are often applied on roads and airport pavements to improve safety during these hazardous weather conditions. However, these ice control chemicals can also potentially impact the asphalt pavement in the long term.

Compared with roadway pavement, the loading conditions on airport pavement are often less frequent but much higher in terms of loading. Under various aircraft ground maneuverings such as taxi, landing, and takeoff operation, airside pavement bears not only enormous vertical loading but also a significant horizontal force generated between gear tires and pavement surface when turning the aircraft.

Three typical Ontario road-used asphalt mixtures were tested with the Hamburg Wheel Tracking Test to investigate the effect of different mix design parameters on the permanent deformation resistance. Industrial X-Ray CT and digital image process technology were employed to explore the morphological properties of processed two-dimensional images and their relations with the permanent deformation of the corresponding mixtures. Typical Road asphalt mixture along with airport asphalt mixture was exposed with Freeze-thaw cycle and de-icing agent, namely potassium acetate to investigate the effect of those factors would have on extreme weather conditions. The de-icing chemicals were also evaluated to examine permanent deformation and shear resistance performance through Hamburg Wheel Tracking Test

and Simplified Uniaxial Shear Test. It was found that the asphalt binder PG level has a significant impact on the permanent deformation performance of roadways mixtures, the passing rate of the 4.75 mm sieve plays an important role in rutting resistance. The rutting depth and morphological indexes are not well-correlated, the possible explanations include whether the rut test can represent the actual stiffness of the corresponding asphalt mixture, the binary process might misrecognize the small particles and voids. 50% Potassium acetate liquid seems to have the softening effect on asphalt mixture's overall stiffness for both airport and roadway mixes. De-icing treatment and freeze-thaw cycles have the potentials to induce stripping. Simplified Uniaxial Shear Tester (UST) is capable of evaluating the shear resistance of asphalt mixture. Mix type and treatments to the specimen have a significant impact on the shear performance of the asphalt mixture.

A three-dimensional Finite Element model was built based on the pavement structure of taxiways in Toronto Pearson International Airport using ABAQUS, both vertical and horizontal loads were applied where nose gear and main gear contact with the pavement surface. Linear viscoelasticity was considered for engineering properties of asphalt layers. Various ground maneuverings such as landing, taxi, takeoff, zero fuel, and operating empty were simulated in the model to analyze their respective impact on shear stress and displacement distributions within the pavement structure. The results show that Shear Stress S12 generated by main gear loads is 5 times greater than that generated by nose gear on asphalt surface; Shear stress S13 generated by main gear loads is equal to that by nose gear but with an opposite direction; Shear stress S23 generated by main gear loads is almost 16 times greater than that by nose gear loads on asphalt surface layer. For shear stress S12, taxi creates the greatest level while the operating empty the lowest. For shear stresses S13 and S23 however, takeoff generates the highest stress level while empty operating generates the lowest.

Keywords: Asphalt Pavement, HWTT, Rutting, Shear Distress, X-Ray CT, ANOVA, ABAQUS, Aircraft Maneuvers

TABLE OF CONTENTS

ACKNOWLEDGEMENT

I would like to express my sincere gratitude to my supervisor Prof. Susan Tighe for her patient guidance, and priceless encouragement and support throughout my Ph.D. study. What I have learned and gained from her in the past four years is not only professional advice for my research and career, but also illuminative attitude and positivity towards various challenges; heartwarming generosity and kindness to every one of us in her research team; as well as life-changing confidence and courage approaching my life in the future.

I would like to acknowledge my Ph.D. committee members Prof. Ernest Heymsfield, Prof. Hassan Baaj, Prof. Rebecca Saari, Prof. Hamid Jahed, and Dr. Sina Varamini for their review of my Ph.D. thesis and for participating in my Ph.D. defense.

I would like to express my sincere thanks to Greater Toronto Airports Authority and Golder Associates for funding this research project and providing testing materials. I appreciate China Scholarship Council for sponsoring my Ph.D. study. Special thanks to PAVE-AL, McAsphalt, MTO, Region of Waterloo International Airport for providing airport mixes, asphalt binder, SMA loose mix, and airport de-icing agent. I would also like to express my thanks to Dr. Josef Zak from the Czech technical university in Prague for providing the Uniaxial Shear Tester apparatus and suggestions regarding test performance. Many thanks to Dr. Wei Yu for his dedicated time and effort for image processing and analysis in Chapter 5. I appreciate Prof. Adil Al-Mayah and Mustafa Alhusain for their assistance with X-Ray CT scanning. My heartiest appreciation to PSI technologies for letting me conduct experimental tests to finish my Ph.D. research during the pandemic, big thanks to Dr. Vimy Henderson, Dr. Danial Pickel, Mathias Cawthra, Madeleine Myles, and Anthony Luu for their help and support.

I would also like to thank all the staff from the Department of Civil and Environmental Engineering, Peter Volcic, Richard Morrison, and Doug Hirst for their technical assistance throughout my whole Ph.D. study.

I would extend my appreciation to all my colleagues in CPATT for their kind support, Xinyue (Crystal) Ni, Taher Moghaddam, Pezhouhan Tavassoti, Guangyuan (Luke) Zhao, Edward Abreu, Rob Aurilio, Saeid Salehiashani, Abimbola Grace Oyeyi, Frank Mi-Way Ni, Jessica Achebe, Hawraa Kadhim, Hanaa Al-Bayati, Taha Younes, Shenglin Wang, Hui Liao, Dandi Zhao, and Ju Huyan. Thank you for your help, company, and friendship.

I would also like to express gratitude to my two Canadian families, Mr. Marcus Diemand and his family; Mr. Steven Hanov, and his family for their consistent trust, support, and company in the past four and a half years.

Finally, I would like to thank my parents and my siblings for their love and support, although we are far away from each other, our hearts are always together.

LIST OF FIGURES

LIST OF TABLES

LIST OF ABBREVIATIONS

AASHTO…..The American Association of State Highway and Transportation Officials

AIMS ……Aggregate Image Measurement System

ANOVA……Analysis of Variance

APA……..…Asphalt Pavement Analyzer

ASTM……..American Society for Testing and Materials

BRD……...Bulk Relative Density

CPATT……. Centre for Pavement and Transportation Technology

CT……...Computed Tomography

DEM……Discrete Element Method

DOT ……..Department of Transportation

EEP……... Element Energy Projection

FEM ……Finite Element Method

FLM…… Finite Layer Method

FLRT ……...French Laboratory Rutting Tester

FN ……Flow Number

FOD…….. Foreign Object Debris

HL……...Hot Laid

HMA……. Hot Mix Asphalt

HS……High stability

HWTT……. Hamburg Wheel Tracking Test

JMF…… Job Mix Formula

MEPDG…….……Mechanistic Empirical Pavement Design Guide

MRD……..Theoretical Maximum Relative Density

MTO……..Ministry of Transportation of Ontario

OAPC……Ontario Asphalt Pavement Council

OHMPA…….Ontario Hot Mix Producers Association

OPSS……. Ontario Provincial Standard Specification

PG……Performance Grade

SGC……Superpave Gyratory Compactor

SMA ……...Stone Mastic Asphalt

SP.……Superpave

SST…….……Superpave Shear Test

UST……...Uniaxial Shear Test

UTM……..……Universal Testing Machine

Chapter 1
INTRODUCTION

1.1 Overview

This Chapter delivers the motivation behind this research, the research objectives, major assumptions, and hypotheses that were made to this research were illustrated. An organization of the thesis was provided in the end, which introduced the basic content of each Chapter.

1.2 Problem Statement

Asphalt pavement is widely used on roadways and airport pavement all over the world. In Europe, over 90 percent of the road network has an asphalt surface (European Asphalt Pavement Association, 2018). In China, the semi-rigid asphalt pavement comprises about 90 percent of total pavement structures (Sultan & Guo, 2017). In North America, asphalt pavement is the most predominant material for highways and airport pavement. The United States has more than 4.3 million kilometers of paved roads and highways, and 94 percent of those are paved with asphalt (Buncher, 2020). In Ontario, there are approximately 150,000 centerline kilometers of paved roads and 95 percent of them are paved with asphalt (Ontario Asphalt Pavement Council, 2017). Lower initial cost, faster construction, easier maintenance, and materials that are almost 100 percent recyclable make asphalt mixture a popular choice for road construction.

According to the methods of load transfer through the materials, asphalt pavement is categorized as flexible pavement as the traffic load is supported by the aggregates-asphalt binder system, from where the loading is uniformly distributed along with aggregate to aggregate or aggregate to asphalt binder to aggregate. Contrary to the concrete pavement in which aggregates, sands, and cement result in a rigid structure, asphalt pavement is flexible and exhibits viscoelastic characteristics, which means asphalt pavement performs differently from the rigid pavement. In asphalt pavement, each size of aggregates proportionally existed in a form of designated gradation with mineral fillers, sometimes fibers, and specified asphalt binder that has been selected

based on the climate condition of the applied locations. A typical asphalt mixture, which contains aggregates and mineral fillers compose approximately 95 % of total mass while asphalt binder composes only 5 % of the mix. For Hot Mix Asphalt, all these materials were heated to approximately 165 °C and compacted before traffic can run over the surface. In the asphalt mixture, all aggregates are bonded by asphalt binder and therefore the strength of the asphalt mixture lies on either the strength of aggregates or the bond strength between aggregates and asphalt binder. Different geological source or manufacturing protocols can affect the physical properties of aggregate, the performance of asphalt binder and adhesion of asphalt to aggregates can be influenced by various factors, the asphalt performance grade is the most significant indicator that distinguishes different binders, ambient temperature, moisture, freeze-thaw cycles, oxidation, and loading speed and frequency play an important role in the asphalt binder's behavior and adhesion of binder to aggregates.

All the factors that impact the performance of asphalt pavement can be categorized as external and internal sources. External factors include temperature, moisture, freeze-thaw cycles, loading frequency. Internal factors include material properties, compaction degree, pavement layer combination, the thickness of each layer, and construction quality control. Flexible pavement distress is usually a combined effect of multiple variables. For example, rutting can be a result of high ambient temperature, a section where slowly moving heavy trucks frequently appear, a poor gradation design and unsuitable asphalt binder selection, and inefficient compaction effort or any of these above elements combination. Thermal cracking is low temperature-induced pavement distress, which can usually be attributed to an extremely low temperature, inappropriate selection of asphalt binder, or poor compaction during construction. Alligator cracking is considered as fatigue cracking and caused by a myriad of reasons; it could be low-frequency over-loading traffic; insufficient structural design; subbase failure reflecting the asphalt surface; poor drainage. Raveling is a material characteristic and moisture-related pavement distress. Due to aggregate segregation during the paving process,

coarse aggregates and fine aggregates were ununiformly distributed in different pavement areas. When water gets trapped in such an area under repetitive traffic loading, asphalt binder was dislodged from the coarse aggregate. Other severe pavement distresses are usually a combined effect of poor drainage design, disqualified materials selection, or dissatisfied construction. Particularly, extreme high temperature and low temperature as well as moisture are the most common causes for premature pavement distresses.

Permanent deformation is one of the most common and challenging pavement distress for flexible pavement. It is an irreversible deformation that normally occurs in the wheel or gear pathways on roadways, parking lots, or airport pavement under hot weather conditions. Several types of permanent deformation commonly appear on asphalt pavement, rutting is the most typical and frequently developed pavement failure on road surfaces as shown in Figure 1a.

Pavement rutting adversely affects the driving experience and can be a safety hazard especially when water gets trapped into the lower area of the rut, the thin water film elevates the tires and reduces the friction between the tires and pavement, this situation leads to the need for a longer distance before a vehicle proceeds to a full stop. In Canada, asphalt pavement rutting is more difficult to overcome due to the wide range of maximum and minimum temperatures. Given the complexity of asphalt viscoelasticity, modification on asphalt binder to improve rutting resistance can sometimes result in poorer low-temperature performance as increasing the stiffness of asphalt binder will cause the material to brittle at low temperature. Asphalt pavement experiences multiple freeze-thaw cycles in winter to spring season at most regions in Canada, de-icing protocols such as road salt, urea, and potassium acetate are being used in highway, airside pavement to ensure the safety of driving vehicles and aircraft taxiing. Freeze-thaw cycles and de-icing treatments can affect the performance of asphalt pavement in many ways, the resistance of permanent deformation is of great significance to be learned.

In Canada, resurfacing to restore pavement to an acceptable service level is the most common way to address rutting distress. The maintenance cost for asphalt pavement is 10,000 dollars per lane kilometre, the rehabilitation cost is 80,000 dollars per kilometre (Collier, 2011). Frequent road maintenance construction causes lane closure and brings down the traffic capacity and efficiency.

Shear-related distress is another type of permanent deformations that usually appears on airside pavement, especially on taxiways where aircraft often move slowly or perform various ground maneuverings. Shear-related pavement distresses have a few different forms: transverse deformation, longitudinal deformation, transverse slippage (delamination) (White et al., 2016), and rippling as shown in Figure 1-1.

a. Pavement Rutting
(Johnston et al., 2017)

b. Rippling (Pavement Wave)
(Engineerign Forum, 2020)

c. Transverse Deformation
(Rizvi et al., 2015)

d. Layers delamination
(Advisory Circular, 2016)

e. Grooved Transverse Deformation (White, 2016)

Figure 1-1 Permanent Deformation on Roadways and Airport Pavements

Shear-related airport pavement distress harms aircraft safety. Asphalt materials withstand a tremendous amount of horizontal force generated by aircraft gear loads and airside pavement under various ground maneuverings such as takeoff, taxi, and landing. This horizontal force strains the asphalt materials in the direction of aircraft travel during each dynamic interaction between the pavement and aircraft gear tires. This can result in shear failure. The accumulated horizontal impact generated by various shear stresses in different directions within the asphalt pavement causes various airside pavement damage. Transverse deformation or horizontal deformation is the most common distresses observed on airport taxiways. This distress often occurs after numerous aircraft taxi to the runway, which results in pushing the asphalt materials forward and causing asphalt creep. Another type of airport pavement shear failure is layer slippage or delamination. It occurs when the tack coat materials fail. A tack coat is often used to bind two asphalt layers together. The intent is to develop sufficient bond strength. If the horizontal force or shear stress exceeds the bond bearing strength, delamination happens as a result of failure between the two asphalt layers. Both horizontal deformation and delamination can reduce aircraft safety, deteriorated deformation and delamination can strip aggregate and asphalt binders. Dislodged aggregates on the airport runway are extremely dangerous as they are regarded as

foreign object debris (FOD), which is a major safety concern for aircraft engine operation. These FOD can be picked up by a rotating engine fan and cause catastrophic damage to the aircraft engine. If severe, it can even cause a plane to fail and crash. Thus airports carefully monitor FOD and try to avoid them on all airport surfaces.

This horizontal force between the airside pavement and aircraft gear tires has not been considered during the airport mix design procedure due to the difficulty of testing such force in the laboratory and the field.

1.3 Research Objectives

The main objectives of this research are as follows:

- To evaluate the permanent deformation resistance of various Canadian asphalt mixtures that are commonly used in Ontario, and to identify the effect of different mix design variables on the rutting resistance of these roadway mixtures.
- To determine if the rutting resistance is related to morphological properties of 2D images through investigating various images and whether computing tomography can be used as a reliable resource for characterizing the mechanical performance of asphalt mixture.
- To correlate rutting resistance performance of road-used asphalt mixture with the morphological indexes of two components inside of asphalt specimen, namely voids and particles.
- To evaluate rutting resistance and shear resistance of asphalt mixtures applied in airports and highways treated with potassium acetate under freeze-thaw cycles.
- To identify the critical shear stress, strain, and displacement of airport taxiway under the horizontal impact and vertical load from aircraft ground maneuverings by a three-dimensional finite element model through ABAQUS.

1.4 Research Hypotheses

The research hypotheses of this study are listed as follows:

- Asphalt binder PG affects the permanent deformation and shear resistance of asphalt pavement.

- The air voids and morphological indexes from processed images relate to asphalt pavement rutting resistance.
- The freeze-thaw cycle can deteriorate asphalt pavement performance while the de-icing agent can mitigate this effect.
- The shear distresses of asphalt pavement are caused by the corresponding shear stresses.

1.5 Research Assumptions

This study is based on the following assumptions:

- For road-used asphalt mixtures, Hot Laid 3 (HL3), HL3 HS, HL1 HS, the original mix design for each mixture has one asphalt binder attached, and they were all produced from the central plant. For research purposes, another asphalt binder using a different Performance Grade was assigned to each type of mixture and fabricate the mixtures in the laboratory. This study uses asphalt materials that were produced in the laboratory and obtained from the central plant. The materials from both sources were assumed to be consistent and homogeneous as they were all designed using Ontario Provincial Standard Specification.
- For the Maximum Theoretical Relative Density test (MRD), this study assumes that two 1.5 kg quarterly split loose material samples are capable of representing the total materials.
- For Superpave gyratory compaction, the same amount of materials were used to obtain the Bulk Relative Density (BRD) and to meet the targeted air voids ratio. Segregation can occur during compaction, however, great care was taken during material preparation and materials transferring. The study thus assumes that the laboratory prepared materials were the same and no segregation was observed.
- For the asphalt mixture freeze-thaw and de-icing treatments, it is assumed that a 50 percent concentration of potassium acetate has the same effect on different asphalt binders regardless of manufacturer and performance grade. It is also

assumed that the potassium acetate that is absorbed by the specimen and attached to the surface does not diffuse into the water bath and affects the thawing period.

- During the Simplified Uniaxial Shear Test, as the testing time is less than 20 seconds, it is assumed that the temperature loss during this time is negligible. Also soaking the specimens into the de-icing agent for 12 hours has the same effect of saturating them with the de-icing agent through a vacuum device.
- For the FEM model, the study assumes that asphalt surface course and lower binder course follow linear viscoelastic material behavior. The remaining materials including Portland concrete cement layer, cement stabilized base layer, granular subbase layer, and subgrade soil were all assumed to follow linear elastic behavior.
- The weight allocation between the aircraft nose gear and the main gear is usually between 5-15 percent and 85-95 percent. The research assumes that the nose gear takes 10 percent of the total weight of the Boeing 777-300ER. The tire and pavement contact area was assumed into squares.
- The boundary conditions of the left and right sides, front and back sides of the airport taxiway FEM model were assumed to be the same.

1.6 Organization of the Thesis

This thesis is organized into nine chapters with the following contents:

Chapter 1: Introduction – This chapter covers the motivation, objectives, hypotheses, and assumptions that are related to this research.

Chapter 2: Literature Review – A systematic review of previous studies on the current state of knowledge on asphalt pavement permanent deformation, using X-Ray CT to investigate the internal structure and phases distribution, the impact of the freeze-thaw cycle, and the de-icing agents on pavement performance, as well as using finite element method to study pavement mechanical response under various loading scenarios.

Chapter 3: Research Methodology – A brief explanation of the basic methodology used in this research from materials collection, testing specimen fabrication, and

treatment to permanent deformation resistance laboratory test, machine learning technology, statistical tool, as well as finite element method.

Chapter 4: Rutting Resistance Evaluation of Canadian Asphalt Mixtures Applied on Roadways Via Laboratory Experiment – Using Hamburg Wheel Tracking Test to evaluate rutting resistance of three typical roadway asphalt mixtures in Ontario with different asphalt binders.

Chapter 5: Rutting Resistance Evaluation of Canadian Roadway Asphalt Mixtures by Industrial X-Ray CT - Industrial X-ray CT was used to collect the two-dimensional images of road-used asphalt mixture. These images were processed through machine learning technology to obtain several morphological indexes of particles and voids. This chapter is intended to bridge the permanent deformation resistance to 2-D image properties of asphalt mixture.

Chapter 6: Evaluating Rutting Resistance of Canadian Asphalt Mixtures Applied on Roadway and Airport Pavement Under Freeze-Thaw Cycles and De-Icing Agent – Two airport pavement mixtures and three road mixtures were treated with de-icing chemicals and freeze-thaw cycle in various ways to investigate the impact of extreme climate conditions and winter road-applied chemicals to the permanent deformation performance of asphalt mixture.

Chapter 7: Evaluating Shear Resistance of Canadian Asphalt Mixtures Applied on Road and Airport Pavement Under Freeze-Thaw Cycle and De-Icing Agent

A simplified Uniaxial Shear Test (UST) apparatus was established to evaluate the shear resistance performance of asphalt mixture, same asphalt mixture used in Chapter 6 was treated with 25°C, 50°C, de-icing agent, freeze-thaw cycle, and de-icing plus freeze-thaw cycle before conducting UST test.

Chapter 8: Analysis of Mechanical Response of Canadian Airside Pavement Under Various Ground Maneuverings by Using Finite Element Method – A three-dimensional FEM model was established by considering realistic airport taxiway

structures and linear viscoelastic characteristics of asphalt material to study the mechanical response of pavement structure under various aircraft ground maneuverings.

Chapter 9: Conclusions and Recommendations – This chapter provides the main contributions of this research and suggestions for further study use.

Chapter 2
LITERATURE REVIEW

2.1 Overview

This Chapter covers the previous studies' reviews on the main topics of this study, namely the laboratory tests for permanent deformation and shear resistance of asphalt mixture applied in airport pavement and roadways, the X-Ray CT used for obtaining the microscopic properties of asphalt specimen, and Finite Element Methods for simulating the airport ground maneuverings and mechanical response of airport pavement. The research gaps were provided based on literature reviews.

2.2 Previous Studies

2.2.1 Laboratory Tests for Pavement Rutting

Permanent deformation or rutting in pavements is a result of accumulated heavy traffic loads under high temperatures and is one of the major distresses for Canadian asphalt pavements (Uzarowski et al., 2004). Permanent deformation can lead to unsatisfactory ride quality and is a safety hazard during rain because of increased pooling on the surface which can result in hydroplaning and increased braking distance. Typically, asphalt resurfacing is an easy way to address permanent deformation and the cost of frequent resurfacing has become the major maintenance budget burden in Canada (Mills et al., 2009).

The internal factors relevant to permanent deformation can be summarized as material properties (volumetric parameters) and construction quality (compaction ratio), while external factors are traffic loads and environmental impact (temperature and moisture). Material properties are the most essential consideration among all the factors as they define the mechanical performance of asphalt mixture.

The Hamburg Wheel Tracking Test (HWTT) has been used to evaluate permanent deformation for decades and has been proven to be capable of realistically reflecting pavement performance under specific moisture and temperature conditions (Schram et al., 2014). Extensive research has been conducted using HWTT to evaluate the permanent deformation of asphalt mixtures. HWTT has been used for evaluating

temperature and moisture susceptibility in the USA since 1990. Colorado Department of Transportation studied the effects of different testing variables on the test results of HWTT, testing temperature, asphalt stiffness, air voids, short-term aging, and the presence of lime, and also provided a corresponding recommendation for different variables (Aschenbrener & Currier, 1993). Based on an analysis of 20 pavements, HWTT proved to have the potential to distinguish stripping performance and different levels of severity of moisture damage and had an excellent correlation with known pavement performance. The study also showed that HWTT is sensitive to (a) the quality of aggregates, (b) asphalt binder stiffness, (c) length of short-term aging, (d) refining or crude oil source, (e) anti-stripping agents, and (f) compaction temperature (Aschenbrener, 1995). It was found that the results are less sensitive to air void distribution (Kassem et al., 2011), but the specimen sitting time has a significant impact on the results (Walubita et al., 2016). Williams and Prowell suggested that the selection of an appropriate compaction temperature and more realistic compaction method in the laboratory is extremely important for permanent deformation performance evaluation (Williams & Prowell, 1997). Chaturabong compared the results of HWTT in dry conditions with the results of confined and unconfined Flow Number (FN) tests and found that the dry HWTT results have a good correlation on creep slope with both confined and unconfined FN tests (Chaturabong & Bahia, 2017). Kanitpong quantified the effect of polymer modifier and anti-stripping agent on the adhesion and cohesion of the asphalt binders and related it to the performance of asphalt mixtures measured using HWTT before and after conditioning in water (Kanitpong & Bahia, 2005). AASHTO T-324 does not standardized the analysis and reporting of the HWTT results and different agencies have their tests reporting requirements (Izzo and Tahmoressi 1999). Schram (Schram et al., 2014) statistically analyzed the test results of more than 135 runs using gyratory-compacted specimens, and he found that measurement location is a source of significant variation for rut depth. Yin (Yin et al., 2014) proposed a novel method to analyze the HWTT results by introducing three parameters: stripping

numbers (LC_{SN}), stripping life (LC_{ST}), and the visco-plastic strain increment ($\nabla\varepsilon^{VP}$). Significant advantages were demonstrated in characterizing the moisture susceptibility and rutting resistance of asphalt mixtures using these proposed new parameters. A study conducted at the University of California, Berkeley, however, questioned the accuracy of HWTT. Laboratory-fabricated specimens and field-cored samples were used to correlate field performance with laboratory test results, and it was found that HWTT tends to overestimate the performance of mixtures containing conventional asphalt binders and underestimate the performance of mixtures containing polymer-modified asphalt binders. The correlation between laboratory test results and field performance was not satisfactory. However, the study did not further investigated the reason behind it. The conclusions drawn from this study were questioned and discussed by researchers from the Department of Transportation, in the U.S. Most DOTs are satisfied with the consistency and accuracy of HWTT and provided extensive evidence from both laboratory and field test experience (Lu & Harvey, 2006).

There are also studies using various methods to evaluate the rutting resistance of asphalt pavement in Canada. Uzarowski (Uzarowski, Paradis, and Lum 2004) conducted accelerated performance tests on field-prepared specimens using three common rut testers in Canada: Asphalt Pavement Analyzer (APA); Hamburg Wheel Tracking Tester; and the French Laboratory Rutting Tester. The procedures and performances are different for each of these testers. It was suggested that a reliable accelerated performance test to evaluate rutting resistance is necessary. However, the conclusions were not provided as the study wasn't completed yet. 17 sites in Canada were analyzed using AASHTO software's Mechanistic Empirical Pavement Design Guide and the climate indicators of deterioration showed that in the next 50 years low temperature cracking will no longer be a problem. Pavement structures will freeze later and thaw earlier with a shortened freezing season. In contrast, increases in in-service pavement temperature will raise the potential for rutting distress (Mills et al., 2009). However, the selected sections are mainly located in southern Canada, additional sites and a greater

number of climate change scenarios could have been incorporated. Ten different types of HMA mix were tested on a laboratory dynamic and resilient modulus testing program, and the results were correlated with rutting resistance data from HWTT and French Laboratory Rutting Tester (FLRT). A strong relationship between dynamic modulus and rutting depth was observed at a testing temperature of 46.1°C and 54.4°C with a frequency of 0.1-1.0 Hz (Safiuddin et al., 2014b). Site observations and cored samples from two Canadian airports were analyzed to determine the cause of rutting and provide corrective measures. The areas extensively affected were found to be in slower traffic areas including taxiways, holding areas, touch-down areas, and run-up pads (Wensel et al., 2002). The study lacks analysis on how are these distressed areas related to the material properties.

Flow number test is another testing method that can be used to evaluate permanent deformation resistance of asphalt materials (Dongré et al., n.d.). In this study, The Francken model, a combination of a power-law function and an exponential function used in Flow Number test output regression, was used to fit the rutting depth data collected from HWTT. The Francken model can be expressed as follows:

$$\varepsilon_P(N) = AN^B + C(e^{DN} - 1) \qquad \text{Equ. } \mathbf{2\text{-}1}$$

Where:

$\varepsilon_P =$ permanent deformation or permanent strain from the HWTT test.

N = number of loading pass, and

A, B, C, D = regression constants

2.2.2 X-Ray Computed Tomography Technique

Asphalt mixture is a nonhomogeneous material as it consists of aggregates, asphalt mastics, and air voids. Understanding the distribution of different phases inside of asphalt mixture is key to predict pavement performance. Using X-Ray Computed Tomography (CT) to detect the internal structure of asphalt material has been proven to be one of the most efficient tools in pavement engineering in the past two decades (Shashidhar, 1999).

Extensive research had been conducted regarding using X-Ray CT to investigate the air voids distribution within the asphalt mixture. Wang (Wang et al., 2001) statistically analyzed the WestTrack mixture's premature failure by evaluating the spatial and size distribution of void systems using X-Ray CT images and stereology methods. It was found that coarse-graded mix is more severely damaged and gave consistent performance ranking of all three mixes with field observations. However, the information of aggregates was not included in the study. Masad (Masad et al., 2002) used X-Ray CT along with image analysis technology to capture air void distribution in asphalt mixture. Specimens were prepared in different compaction factors --- compaction effort, compaction method, aggregate size distribution. It was shown that air voids distribution of Superpave gyratory compacted specimen exhibited a "bathtub" shape, and different aggregate sizes had noticeably different air voids size. Abdul (Abdul et al., 2014) introduced air voids and crack properties as damage indicators for characterizing two modes of failures under uniaxial monotonic compression and indirect tensile fatigue by using two-dimensional image analysis. By comparing the X-Ray CT images before and after applying loads, these researchers established a set of procedures for extracting and verifying the damaged area. The proposed damaged parameters were shown to be useful for interpreting the damage behavior. Osmari (Osmari et al., 2020) evaluated volumetric and rheological characteristics of Fine Aggregate Matrix specimens with distinct air void content by performing micro CT scanning. Wu (Wu, Li, Zhang, & Li, 2018) analyzed CT images by setting up different segment thresholds for different areas of the same image and then combined these parts into one image. The results of the Rotary Load Wheel Tester were compared before and after the test for the drilling specimen and Marshall specimen. The scanning images show significant differences in the internal structures, namely the air voids and aggregates distribution between the two types of specimens. Hu (Hu et al., 2020) evaluated the homogeneity of the asphalt mixture by quantifying the vertical air voids distributions from X-Ray computed tomography images and aggregate gradations. The

results show that air void content in the middle part of the specimen was lower than on both ends and homogeneity was better under higher compaction effort. The above studies all focused on air voids distribution within asphalt specimen using X-Ray CT, the morphological information, and distribution of the aggregates, as another essential component of the mixture however, were not incorporated into performance characterization and analysis.

There are studies involved with using X-Ray CT with Finite Element Modeling (FEM) to investigate the mechanical response of asphalt mixture. You (You et al., 2009) predicted the dynamic modulus of asphalt mixture using both 2-dimensional and 3-dimensional Discrete Element Method (DEM) generated from X-Ray CT images. It was revealed that the 3D discrete element models can accurately predict the asphalt mixture dynamic modulus over a range of temperature and loading frequencies while the 2D models under predicated the asphalt mixture dynamic modulus. Erdem (Coleri et al., 2012) develops 2D and 3D micromechanical finite element models to predict the shear modulus of asphalt mixture by using X-Ray computed tomography (CT) imaging. It shows that 2D numerical models always under-predicted the shear modulus values at all testing temperatures and frequencies due to its reduced numerical prediction accuracy while 3D models serve as a valuable tool to understand certain problems in asphalt pavement design. Dai (Dai, 2011) established 2D and 3D micromechanical finite element models to predict the viscoelastic properties of asphalt mixture. She used the horizontal surface scanned images from X-Ray computed tomography techniques and created 2D and 3D digital samples. The results indicate that the developed micromechanical FE model is capable of accurately predicting the global viscoelastic properties of the stone-based materials. Hao (Ying et al., 2014) developed a three-dimensional, heterogeneous model to describe asphalt mixture response in dynamic modules through an X-Ray computed tomography image. Hot-mix asphalt and warm-mix asphalt were used to validate and calibrate the FEM model in this study. It was found that most deformation during dynamic modules test are derived from mastic and

it had more influence than the aggregates on the results of the dynamic modules. However, none of the studies attempts to correlate the permanent deformation laboratory test result with the morphological properties of aggregates from a compacted asphalt specimen through X-Ray CT.

Studies that focused on developing algorithms or making use of other commercial software to improve X-Ray image quality were also conducted by researchers. Zelelew (Zelelew & Papagiannakis, 2011) established a grey-level threshold to identify air voids, mastic, and aggregates by using volumetric properties as the main criterion. The algorithm was implemented in MATLAB and was shown to produce realistic rendering for the microstructure of asphalt concrete. Wang (Wang, Huang, Li, You, & Chen, 2014) developed a 3D reconstruction algorithm for X-Ray computed tomography by obtaining the voxel positions and the relationship between the pixel element and node. Another investigated the effect of sample size, aggregate lithology, and compaction pattern on the image scanning quality through X-Ray CT (Wang et al., 2015). Wu (Wu et al., 2018) studied the gravel aggregate of quartzite by using the industrial CT instrument. MATLAB was used to capture the aggregate slice properties and MIMICS for the establishment of a 3D model.

Researchers have also been trying to connect the microstructure of different phases inside asphalt mixture to road performance. Hassan (Hassan et al., 2012) investigated the effect of different compaction methods on the structure of the aggregate inside of asphalt mixture. Three laboratory compaction options, namely gyratory, vibratory, and slab roller compaction were used in this study. All the specimens were scanned through the X-Ray computed tomography (CT) and analyzed using the image analysis technique. He found that aggregate near the edge of a specimen tend to form circumferential alignment while those near the center are randomly oriented. Khan (Khan & Collop, 2010) quantified the damage induced during constant strain rate and fatigue test on asphalt mixture using X-Ray computed tomography. He used image analysis techniques to grade aggregates and found that the particles that are larger than 5 mm can be seen

in comparison to the mix design curve of the asphalt mixture. From the constant strain rate test, the air voids were found to increase with increasing strain as damage accumulates in the specimen. Coleri (Coleri, 2013) analyzed the microstructure changes of asphalt concrete caused by full-scale accelerated pavement testing with a heavy vehicle simulator through X-Ray computed tomography. A viscoelastic-micromechanical finite element model was also employed to investigate the effects of asphalt mastic and aggregates skeleton properties on shear resistance. He found that dense gradation and larger aggregates sizes appear to be capable of dissipating more shear stress and therefore gain more shear resistance.

Shaheen (Shaheen et al., 2013) evaluated the rutting resistance of six typical Superpave mixes used in Ontario for the surface course using laboratory and digital imaging techniques. The Research found that aggregate orientation and contact were important factors in HMA rutting resistance. 2D image analysis under the wheel pass can provide a good estimate of these two parameters. Lv (Lv et al., 2018) confirmed and further supplemented the failure mechanisms of the HWTT by image analysis and air voids analysis based on computed tomography scanned asphalt samples. He found that optimum binder content can reflect both rutting resistance and moisture susceptibility of HMA. Xing (Xing et al., 2018) used fuzzy network, multilevel threshold, and morphological methods to reduce the noise, enhance the contrast, and segment images. The 3D gradation is transferred by stereological methods from 2D aggregate gradation obtained from the digital image segmentation procedure. The results show that all three processing procedures proposed in this study can be used to obtain the gradation information of Asphalt Concrete, Stone Mastic Asphalt, and Open Graded Friction Course accurately and effectively.

Gong (Gong et al., 2018) scanned four kinds of asphalt mixtures before and after freeze-thaw cycles using CT, the distribution characteristics, morphology, and the number of air voids were studied and analyzed based on image processing technology. The results provide the basis for understanding the performance attenuation mechanism of asphalt

mixture and for establishing the attenuation models for freeze-thaw cycles. Wang (Wang et al., 2020) used the Aggregate Imaging Measurement System (AIMS) and X-Ray Computed Tomography (CT) to evaluate the shape of particles. It was found that changes in the morphological characteristics of particles are the main causes for degradation in the skid resistance of asphalt pavement. Liu (Liu et al., 2014) established a segregation evaluation standard based on fractal dimensions by using X-Ray computed tomography, the improved OTSU image method, and fractal theory. By testing the physical indexes such as density, air voids, strain, fatigue life, and stiffness modulus of the specimens. It was concluded that 3D segregation of asphalt pavement can be well defined by fractal dimension.

Based on previous studies review, no standardized method was proposed in processing digital images obtained from X-Ray CT, and most of the study did not quantitatively correlate the performance of asphalt concrete to the properties of particles and voids from processed images. The accuracy of processed images is not consistent due to various image process protocols adopted in different studies.

2.2.3 De-icing Treatment for Airport Pavement

Runway ice control is of paramount importance for airport infrastructure safety management in cold region countries like Canada. Snow and ice that are accumulated on airside pavement can drastically reduce the friction force between tires and pavement, which is the major cause for aircraft skidding. Using ice control chemicals is an essential measure in maintaining safe winter operations (Runway Ice Control Chemicals, 2013). Typically, two modes of applying ice control chemicals are being used in airside pavement, anti-icing, and de-icing methods, the main difference between these two operational modes is the applying time of ice control chemicals (Airport Winter Maintenance and Planning, 2018). Anti-icing aims at preventing the formation of ice or reduces the bond between ice and pavement surface; De-icing operations are focusing on removing ice or snow after they have been formed (Hassan et al., 2002). Urea was widely used and the only available ice control chemicals for airside pavement

in the past. In the 1990s, organic salt-based ice control chemicals such as potassium acetate, potassium formate, and sodium formate were introduced in airside application. These chemicals have a lower biological oxygen demand thus comply better with environmental regulations and are also more effective in low temperatures than Urea (Runway Ice Control Chemicals, 2013). With several advantages regarding environmental compatibility and ice-control efficiency, however, study shows that road agencies and individuals still tend to choose traditional ice removal chemicals, it also reported that negative impacts of acetates and formates are greater than perceived by survey respondents in the study (Fay et al., 2008).

Previous studies showed that traditional chemicals like chloride product harm asphalt pavement (Wright, 2013)(Leahy et al., 2014), it was reported that magnesium chloride has a most significant effect on mechanical strength reduction than other chloride-based de-icers (Xie et al., 2015)(Sumsion et al., 2013). Researchers found that the low-temperature performance and fatigue life can also be severely affected by de-icing salt (Feng et al., 2010) (Yu et al., 2013). Among all the traditional ice control chemicals, liquids de-icers are proved to be more effective than solid chemicals, a combination of liquids and solids should be of interest for preventive operations (Schweigert, 2016).

With the introduction of acetate-based and formate-based chemicals as new ice control chemicals, the negative impact of which is being used on asphalt pavement has drawn attention for researchers. Back in 1999, several Nordic airport pavements were recorded as experiencing a durability reduction issue relating to the use of acetate-based and formate-based ice control chemicals, showing that the formate-based product has more severe impact than acetate-based ones (Edwards et al., 1999)(Safiuddin et al., 2014a)(Julio-Betancourt, 2009). It was found that using newer de-icing agents can adversely affect the asphalt pavement's performance in different levels compared to traditional de-icing control chemicals, the mechanism of de-icing agents to asphalt pavement seems to be a combination of emulsification, chemical reaction, and distillations (Shi, Akin, et al., 2009)(Shi, Fay, et al., 2009). The use of de-icing

chemicals often synchronizes with harsh weather conditions such as extremely low temperature, freeze-thaw cycles. A Canadian study shows that the fatigue life of asphalt pavement is affected by freeze-thaw cycles (Badeli, 2018), the concentration of acetate-based, formate-based, and urea between 1 to 2 % can significantly decrease the indirect tensile strength, and modulus of elasticity when subjected to freeze-thaw cycles (Y. Hassan et al., 2002). A follow-up study found that the sodium acetate treated samples show the greatest overall strength and elasticity reduction after wet-dry cycles (Farha & Hassan, 2002). It seems that freeze-thaw cycles tend to soften the asphalt binders, while wet-dry cycles and de-icers have the opposite effect (Shi, 2008).

There are also studies showing that potassium formate may promote stripping to a certain extent which depends on types of aggregates and asphalt binders (Santagata et al., 2013). Another study used a higher concentration of acetate de-icers to confirm the existence of acetate-induced pavement distress and proposed a physiochemical mechanism of the asphalt concrete deterioration process (Pan et al., 2008). Anti-icing measures were also studied by some researchers via blending ice-melting fillers into asphalt mixture during the mix design process (Zheng et al., n.d.).

Based on the literature review, the impact of the above-mentioned de-icing control chemicals on the rutting resistance and shear resistance of asphalt mixture was not investigated so far.

2.2.4 Asphalt Shear Resistance Test

Shear-related pavement failures are difficult to measure using a common asphalt specimen testing system as shear stresses induced by horizontal force, which is parallel to the analyzed plane. Various testing programs are commonly used for the mechanical performance of asphalt mixture. HWTT, dynamic modulus, flow number, TSRST, and four-point bending beam test are widely used in universities and research institutions all over the world. All the above tests measure the mechanical response of asphalt specimens under vertical loads, however are unable to simulate horizontal force. So far, Superpave Shear Test (SST) is the only test that can evaluate the shear resistance of

asphalt. Due to the high cost and technical difficulty of the testing system, the application of SST is limited to only a few universities in the United States.

Studies have been conducted by pavement researchers using various approaches regarding shear-related asphalt distress. White developed a framework for diagnosing shear distresses and concluded that shear-related failures can be divided into two categories: delamination happening between asphalt layers and shear creep within the asphalt layer (White et al., 2016). The research showed that groove closure in slow-moving areas and shearing in aircraft heavy brake zones are frequently reported and reliable performance-indictive testing methods are expected to develop in the future (White, 2018). The Octahedral Shear Stress (OSS) was used as an indicator of shear stress and calculated peak surface force through mePADS/GAMES software. It was found that peak shear stress did not significantly increase with increased braking effort, the presence of shear-related distress in braking areas is indicative of shear creep rather than layer slippage (White, 2016). Vacin evaluated the bond strength of different types of tack coats using a simple shear test by applying three points loading on asphalt briquettes (Vacin et al., 2005). However, research on testing the shear strength of asphalt mixture in a laboratory using a more accessible device is limited to only a few studies. The shear stress under aircraft gears is difficult to measure to verify the modeling results.

2.2.5 Finite Element Method

Shear-related pavement distresses, as a typical form of permanent deformation frequently observed in airside pavement (Figure 1a), have not been widely studied by pavement researchers. Other than layer slippage or delamination, most of the shear distresses are exhibited as horizontal deformation, it is difficult to visually inspect such distress except for those in grooved or color-marked areas. Compared with rutting damage which is considered as vertical load mainly induced pavement failure, shear-related distress is more complicated to test and evaluate in the laboratory and field. Finite element modeling has been proved to be an effective tool by many researchers in the flexible pavement field both in roadway and airport applications.

Extensive research has been conducted using the Finite Element Method (FEM) to analyze the mechanical performance of asphalt pavement applied in the airport. Shafabakhsh (Shafabakhsh et al., 2018) analyzed pavement response under loading of different aircraft by using Abaqus. Dynamic analysis of runway pavement was performed in the study and it shows that a speed of 5-8 km/h leads to the highest stresses and deflections. Buonsanti and Leonardi (Buonsanti & Leonardi, 2012) studied the contact stresses in a flexible pavement under landing aircraft loads during the landing phase using finite element methods. The study considered two tires on the structural pavement with the real loads applied on the two wheels of the gear system. Leonardi (Leonardi, 2016) also simulated the behavior of flexible pavement during the landing phase by implementing a finite element code to investigate the impact of repeated cycles of loads on permanent deformation. The results demonstrated the capability of the model in predicting the permanent deformation in the asphalt layer. However, the model did not incorporate other aircraft ground maneuvers, and as a common airport pavement distress, shear damage was not discussed in these two studies.

Liu (Liu et al., 2015) developed a specific computational program based on the semi-analytical finite element method. He added infinite elements into the program to reduce the computational time. It shows that finite-infinite element coupling analysis has higher reliability and efficiency. In another study, it involved developing a specific computation code EasyFEM based on the finite layer method (FLM) for analyzing pavement response under static load. It implemented a newly developed Element Energy Projection (EEP) method to improve the accuracy of solutions. The results showed that the predicted responses from EasyFEM and ABAQUS are in good agreement with each other (Liu et al., 2017). Hu (Hu et al., 2017) investigated and quantified the effects of tire inclination and dynamic loading on the stress-strain responses of a pavement structure under various loading and environmental conditions. The results indicated that inclined tires and deceleration vehicles induced the most severe shear stresses and vertical strains on the pavement in terms of magnitude. Khanal

(Khanal et al., 2016) used finite element modeling to determine the pavement layer stress and strains when subjected to super heavy moves in spring and winter conditions. The stresses and strains determined were then used to calculate and predict the key types of pavement damage. Wollny (Wollny et al., 2016) modeled tire-pavement interaction at static as well as rolling contact conditions through a program interface, which connects tire and contact simulation in a commercial finite element (FE) code to pavement simulation in an in-house FE code. The potential of this program interface was demonstrated by two examples. A similar study was conducted to predict tire-pavement contact stress distributions by Hernandez (Hernandez et al., 2015) using three-dimensional finite element modeling. Different vehicle loading and speed, tire inflation pressure, vehicle maneuvering (braking, acceleration, and steady-state), and rolling conditions are studied. The results demonstrate the existence of non-uniformity vertical contact stresses and localized tangential contact stresses at the tire-pavement interface. However, the horizontal force, which induced by aircraft gear tires, was not investigated in these studies.

Viscoelasticity has been considered by many pavement researchers while using finite element modeling as an effective tool to analyze pavement mechanical response. Wang (Wang et al., 2013) treated asphalt material as linear viscoelastic material and used the nonuniformed distribution of aircraft tire loading in five different ribs, it shows that traditional loading assumption underestimated the impact of critical tensile and shear strains in the asphalt layer. To represent the asphalt pavement response under various temperature and loading rates, Huang (Huang et al., 2011) developed a nonlinear viscoelastic-viscoplastic constitutive model with ABAQUS user material subroutine UMAT, the results demonstrated the capability of the model in simulating the influence of temperature on permanent deformation and in predicting viscoelastic strain distributions in the asphalt layer. Kim (Kim & Tutumluer, 2011) developed a three-dimensional nonlinear finite element model using measured responses of airfield flexible pavement tests trafficked under two types of aircraft gear configurations. It was

found that gear arrangements have a significant influence on critical pavement responses. The asphalt surface displacements were more affected than other layers. Uzarowski (Uzarowski, 2006) used a nonlinear viscoplastic model in the finite element method to predict the rutting resistance of asphalt mixture. The laboratory testing results are in good relationship with the analytically predicted performance of asphalt mixtures. Each finite element model of asphalt mixtures has its advantages and limitations. The above research did not provide a detailed explanation on the reason why such a model was adopted and the adaptation of this model under various mechanical response range. Additionally, none of the above research addresses airport asphalt pavement shear related-distress from a perspective of a stress tensor.

2.3 Research Gaps

The following research gaps can be concluded based on the literature review:

- The relationship between permanent deformation of asphalt pavement in Canada and materials properties such as asphalt binder PG, asphalt binder content, and gradation has not been investigated by previous research.
- Microscopic indexes, such as volumetric indicators and aggregate particle morphological properties have not been successfully correlated to pavement performance.
- Less attention has been devoted to the impact of freeze-thaw cycles and de-icing chemicals on the permanent deformation and shear resistance of asphalt pavement in Canadian airport pavement and roadways.
- The influence of aircraft ground maneuverings on the mechanical response of airport pavement in Canada needs more attention from pavement engineers.

Chapter 3
RESEARCH METHODOLOGY

3.1 Overview

In this Chapter, a research flowchart that shows how this research was conducted, how each section connects, and how each section contributes to the main goal of this research was provided. The testing materials, specimen fabrication, and specimen treatments were introduced. Laboratory tests, namely Hamburg Wheel Tracking Test and the simplified Uniaxial Shear Test, as well as the Finite Element Method were briefly explained. Machine Learning Technology was also introduced as the main research tool for this research.

3.2 Research Flowchart

The flow chart of this research is shown in Figure 3-1.

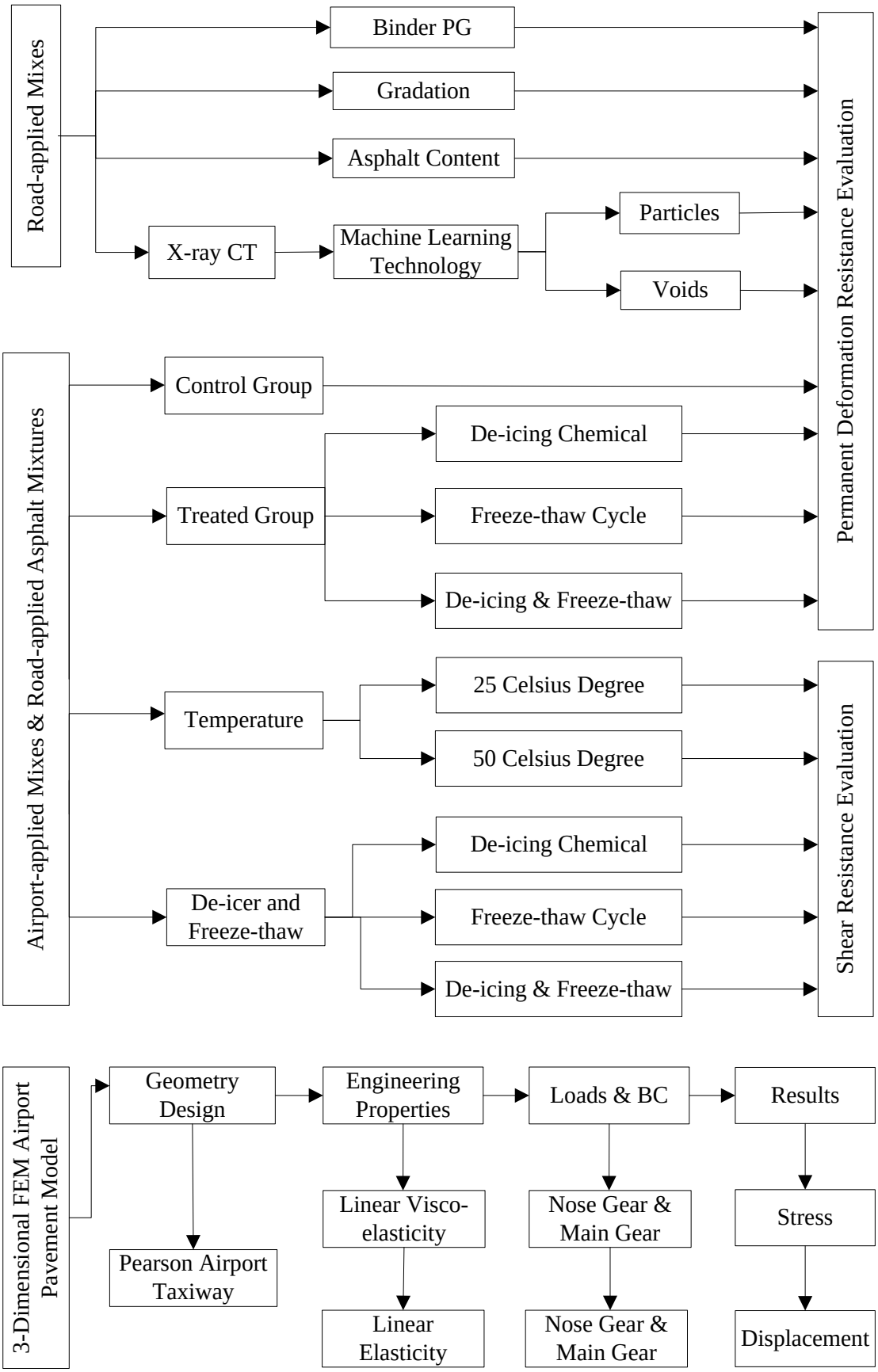

Figure 3-1 Research Flow Chart

3.3 Materials

3.3.1 Material Collection

The road-used material HL3 58-28, HL3 HS 64-28, and HL1 HS 70-28 were collected from the central plant of COCO Paving and Gazzola Paving. HL3 64-28, HL3 HS 70-28, and HL1 HS 64-28 were fabricated from Golder Associates Cambridge laboratory. The airport-used material Air-surface, and Air-base materials were collected from PAVE-AL central plant (Figure 3-2), which provides asphalt materials for Toronto Pearson International Airport. The de-icing chemical potassium acetate was provided by the Region of Waterloo International Airport (Figure 3-3).

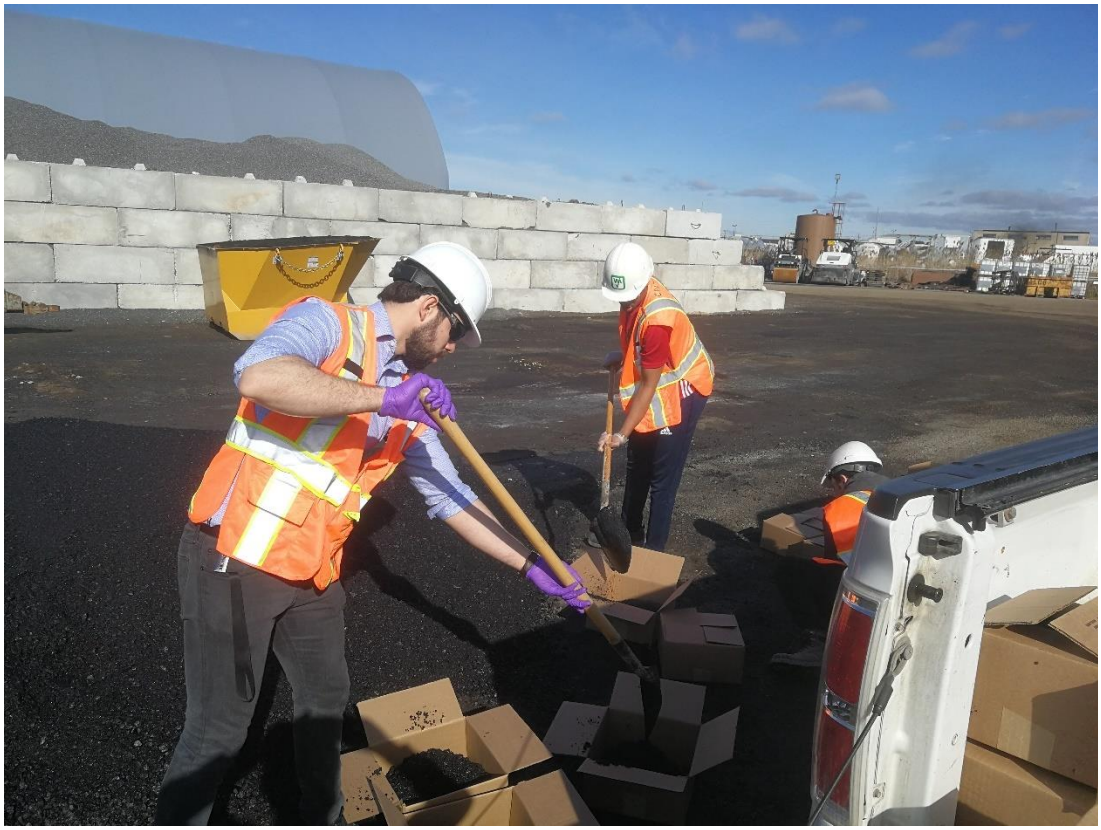

Figure 3-2 Airport Asphalt Materials Collection from PAVE-Al Central Plant

Figure 3-3 Collection of Potassium Acetate from Region of Waterloo International Airport

3.3.2 Specimen Fabrication

According to AASHTO 324 (AASHTO, 2016), the air voids of the tested asphalt specimen should be controlled within the range of 7 ± 0.5 % for all-purpose mechanical property tests. For loose asphalt mixtures, regardless of whether they were fabricated from the laboratory or central plant, using the vacuuming method to test the maximum theoretical relative density is the first step of controlling air voids percentage of a test specimen (Figure 3-4). In Ontario, the minimum weight requirement of test material varies from different types of asphalt mixes as specified in Table 3-1.

Table 3-1 Size of Test Sample (MTO, 2012)

Mix Type	Designated Large Sieve Size (mm)	Minimum Mass of Sample (kg)
HL 2	2.36	0.5
SMA 9.5, Superpave 9.5	4.75	1.0
HL1, HL3, HL3A, DFC, SMA 12.5, Superpave 12.5, 2.5 FC 1, 12.5 FC 2	9.50	1.5
HL4 (Binder and Surface)	13.20	1.5
Superpave 19.0, SMA 19.0	12.50	2.0
HL 8, MDBC, HDBC	16.00	2.0
Superpave 25	19.00	3.0
Superpave 37.5	25.00	4.0

Where:

SMA: Stone Mastic Asphalt

HL: Hot Laid Asphalt

DFC: Dense Friction Course

FC: Friction Course

MDBC: Medium Duty Binder Course

HDBC: Heavy Duty Binder Course

a. Hand Separated Loose Materials b. MRD Testing Apparatus

Figure 3-4 Maximum Theoretical Density Test

Based on MRD testing results and targeted air voids ratio, the minimum weight of material for a designated specimen (Marshall Method compacted cylindrical specimen, Gyratory compacted cylindrical specimen, vibratory compacted slab, shear compacted slab, etc.) can be back-calculated from the following equation:

$$m_r = s * h * MRD * (100 - 7)\% \quad \textbf{Equ.3-1}$$

Where: m_r= Required weight of asphalt mixture in mass, g.

s = Transverse section area of specimen, cm^2.

h = Specimen height, cm.

MRD = Maximum theoretical relative density, g/cm^3.

a. Superpave Gyratory Compactor b. BRD Measurement Apparatus

Figure 3-5 Gyratory Compaction and BRD Measurement

Cold loose materials need to be split before heating, the boxed materials were warmed in the microwave until they are easy to separate, warmed loose asphalt material were divided equally into four quarters, they were transferred from these quarters to squared pans for compaction heating based on calculated required weight of loose material. Laboratory fabricated materials need to be heated at 135 ± 5 °C for about 4 hours before

proceeding with compaction, the plant-produced materials can directly be compacted once the material reaches the required compaction temperature.

Superpave gyratory compactor (Figure 3-5a) was set to height control mode to ensure a targeted height of specimens, the compactor will terminate once the specimen reaches the height. The compacted cylindrical specimens were cooled to room temperature before conducting a Bulk Relative Density measurement (Figure 3-5b). The air voids can be calculated from the following equation:

$$Air\ Voids\ Ratio = \left(\frac{MRD-BRD}{BRD}\right) * 100\% \qquad \textbf{Equ.3-2}$$

3.3.3 Specimen Treatments

Road-used asphalt mixture was compacted into two groups, one group used for X-Ray CT scanning as discussed in Chapter 5. The specimens were treated into 100 mm in diameter and 63 mm in height by a drilling machine as indicated in Figure 3-6; the other group was tested through HWTT as detailed in chapter 4. In chapter 6, specimens were treated with freeze-thaw cycles and de-icing chemicals before proceeding to the test. Two airport mixes, air-surface, and air-binder course, and three road mixes, HL3, HL3 HS, and HL1 HS, were treated into four groups. Group 1 was the control group without any special treatment, Group 2 was treated with potassium acetate de-icing liquid, Group 3 was treated with one freeze-thaw cycle, and Group 4 was treated with de-icing liquid and freeze-thaw cycle as specified in Chapter 6. In Chapter 7, the same roadway mixes and airport pavement mixes were tested under different temperatures, potassium acetate de-icing agent, and freeze-thaw cycle using the simplified Uniaxial Shear Test.

Figure 3-6 Coring a Cylindrical Asphalt Specimen (Al-Bayati, 2019)

3.4 Laboratory Tests and Numerical Simulation

3.4.1 Hamburg Wheel Tracking Test

For the HWTT, AASHTO T324 does not specify the requirement for testing temperature, it only mentions that the temperature control system should be capable of controlling the temperature within ± 1°C over a range of 25 to 70 °C (AASHTO 2016). MTO specifications indicate that HWTT should be conducted at 60 °C (Ministry of Transportation of Ontario, 2011). The preconditioning time (when the specimens are submerged in a water bath) is 30 min after the temperature reaches 60 °C. Figure 3-7 shows the HWTT at the Centre for Pavement and Transportation Technology (CPATT) at the University of Waterloo.

Figure 3-7 Hamburg Wheel Tracking Tester in CPATT

3.4.2 Simplified Uniaxial Shear Test

Uniaxial Shear Test was developed as a substitute for Superpave Shear Tester with a lower cost and easier operation procedures. It involved a cylindrical asphalt specimen with 50 mm height and has a 50 mm diameter hollow at the center. In the original design, as shown in Figure 3.8, an oscillated load is applied around the inner circle of the hollow to obtain a shear zone. A reasonable simplification was made on the loading method to explore the shear strength of the test material. Detailed introduction and simplification are illustrated in Chapter 7.

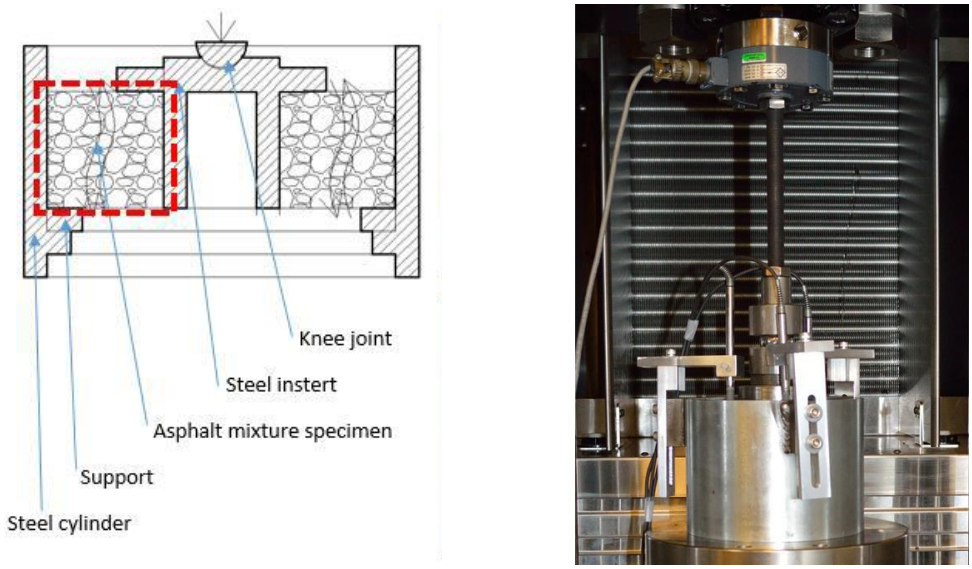

a. Uniaxial Shear Tester (Original Design) b. UST in UTM

Figure 3-8 Uniaxial Shear Tester (Zak et al., 2017a)

3.4.3 Finite Element Method

Finite Element Method was used in this research to study the impact of various aircraft ground maneuverings on the airside pavement mechanical response. A three-dimensional airport taxiway model was established in ABAQUS and linear viscoelasticity was considered in the engineering properties of the asphalt surface layer. Stress and displacement underneath the nose gear and main gear loads were quantitatively analyzed under each ground maneuver. Detailed analysis approaches were illustrated in Chapter 8.

3.5 Machine Learning

In Chapter 5, three road-used asphalt mixes were scanned through X-Ray CT. Two-dimensional images were obtained in three different views: top, front, and right. The top view images were further processed with Machine Learning to identify the different components of asphalt mixtures. Voids and particles were extracted from the original images and analyzed with morphological indexes. A detailed methodology was deliberated in Chapter 5.

3.6 Analysis of Variance

Analysis of Variance (ANOVA) is the most commonly used statistical tool to investigate whether the dependent variable was significantly affected by independent variables. In

Chapter 4, ANOVA was used to analyze the significance of mix design parameters to rut depths. In Chapter 6 and Chapter 7, ANOVA was served to investigate the influence of different mix types and treatment methods on the rutting resistance and shear resistance of asphalt mixture applied in roadway and airport pavement.

Chapter 4
RUTTING RESISTANCE EVALUATION OF CANADIAN ASPHALT MIXTURES APPLIED ON ROADWAYS VIA LABORATORY EXPERIMENT

4.1 Materials

In Ontario, Hot Laid 1 (HL 1) is a dense-graded surface course mix with a premium quality coarse aggregate that is used on high volume roads and has a maximum aggregate size of 16 mm. Hot Laid 3 (HL 3) is a dense-graded surface course mix for intermediate volume roads that also has a maximum coarse aggregate size of 16 mm (*Material Specification for Hot Mix Asphalt*, 2008). In this study, three types of loose asphalt material were provided by Golder Associates: HL 3, HL 3 HS (High Stability), and HL 1 HS. Samples of each type of material were prepared in both plant and laboratory settings with the same aggregate gradations but different asphalt binder Performance Grades (PG). HL 3 samples were plant prepared with PG 58-28 and laboratory prepared with PG 64-28; HL 3 HS samples were plant prepared with PG 68-28 and laboratory prepared with PG 70-28, and HL 1 HS samples were plant prepared with PG 70-28 and laboratory prepared with PG 64-28. The Job Mix Formula (JMF) and sieve passing rate of each sieve size of HL 3, HL HS, and HL1 HS are shown in Table 4-1 and Figure 4-1a and 4-1b. HL3 and HL3 HS have the same upper and lower limits for the passing rate of all sieve sizes according to the requirement in Ontario Provincial Standard Specification (OPSS) 1150 (*Material Specification for Hot Mix Asphalt*, 2008).

Table 4-1 Passing Rate of HL3, HL3 HS, and HL1 HS

Mix Type	Sieve Size	Coarse Aggr %	16	13.2	9.5	4.75	2.36	1.18	0.6	0.3	0.15	0.075	Pan
HL3	Cumulated	N/A	100	100	84.1	58.4	42.4	31.4	21.5	10.2	5.4	3.8	0
	Retained	41.6	0	0	15.9	25.7	16	11	9.9	11.3	4.8	1.6	3.8
HL3 HS	Cumulated	N/A	100	98.9	85.1	58.2	45.8	28	18.8	10.1	6.9	4.7	0
	Retained	41.8	0	1.1	13.8	26.9	12.4	17.8	9.2	8.7	3.2	2.2	4.7
HL1 HS	Cumulated	N/A	100	100	81.9	61	55.9	34.2	18.4	10	5.9	4.1	0
	Retained	39	0	0	18.1	20.9	5.1	21.7	15.8	8.4	4.1	1.8	4.1

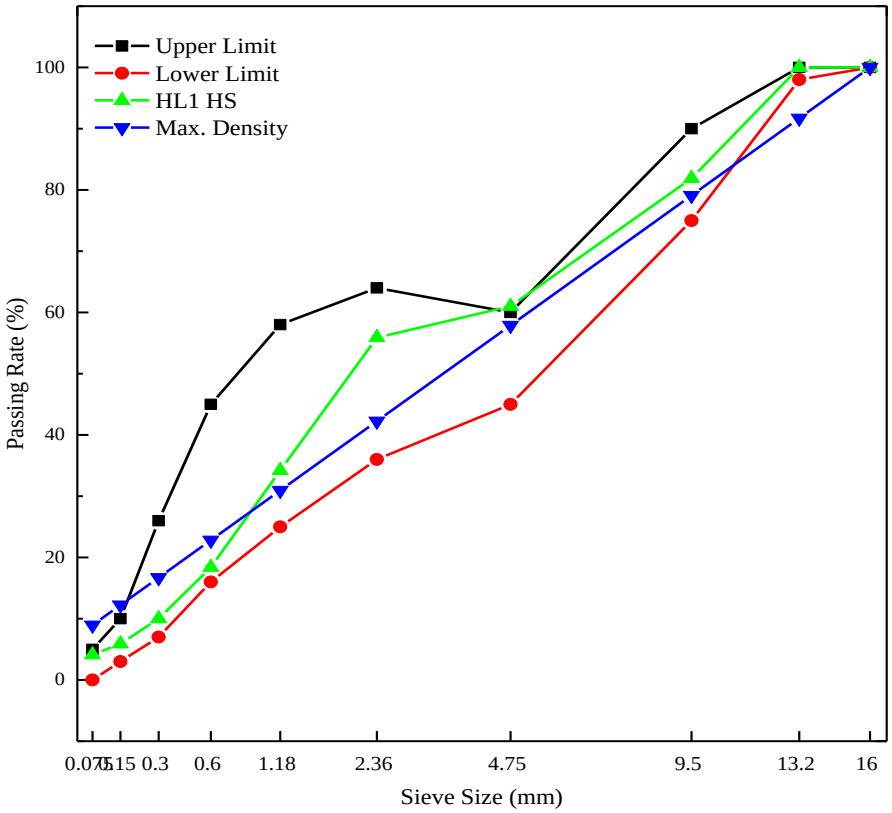

a. HL1 HS

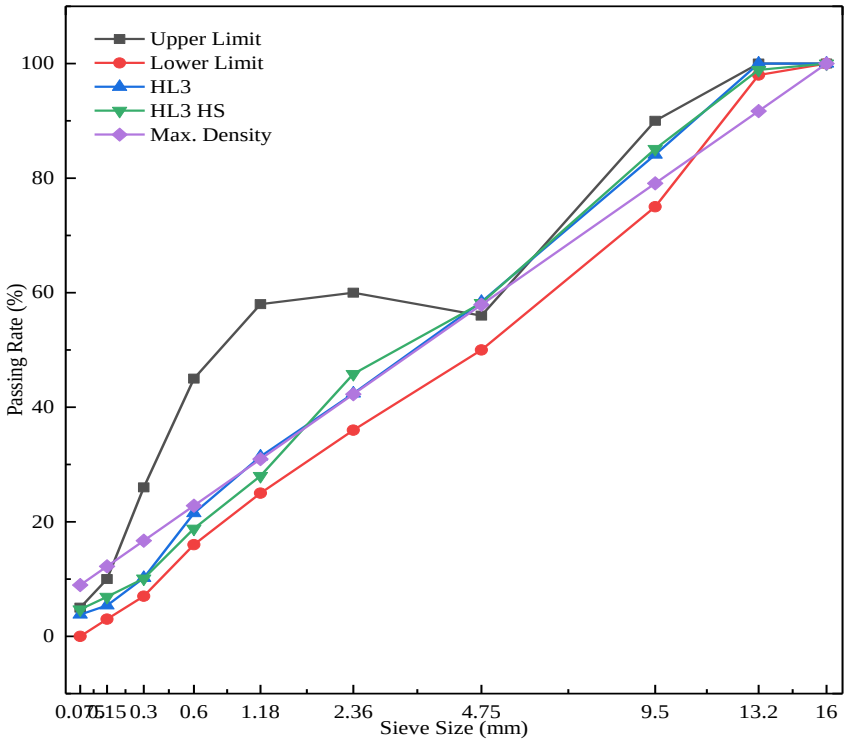

b. HL3 & HL3 HS

Figure 4-1 Gradation for HL 3, HL 3 HS, and HL1 HS

4.2 Experimental Program

The Marshall Mix Design Method was adopted in all three mix design procedures in this study. According to AASHTO 324, the procedure for HWTT includes specimen preparation and testing. For specimen preparation, each specimen was compacted to achieve air voids of 7 % ± 0.5 % using a Superpave Gyratory Compactor. Specimen sizes were controlled at 150 mm diameter and 63 mm thickness, which is within the requirement that specimen thickness should be within 38 mm-100 mm in AASHTO 324 (AASHTO 2016). The specimen requirements from the Ministry of Transportation of Ontario (MTO) are following AASHTO, but the air voids ratio has a wider range from 6% to 8% (Ministry of Transportation of Ontario, 2011). Four cylindrical specimens were prepared from each mixture. For plant-produced material, compaction was conducted immediately after the material's temperature reached the compaction temperature; for laboratory-produced material, four hours of short aging conditioning was undertaken before compaction. Theoretical Maximum Relative Density (MRD) of laboratory prepared loose mixture, Bulk Relative Density (BRD), and Air Voids ratio of each gyratory compacted specimen was tested and calculated following specifications of Ministry of Transportation, Ontario (MTO)(MTO, 2012)(MTO, 1999)(MTO, 1996)(ASTM, 2017). The BRD, MRD, and Air Voids calculation results are shown in Table 4-2, where HL3 64-28 and HL1 HS 64-28 slightly exceed the air voids requirements of MTO. The author decided to proceed with the test using these two off-limit specimens due to a shortage of materials. The HWTT experiment flowchart is shown in Figure 4-2.

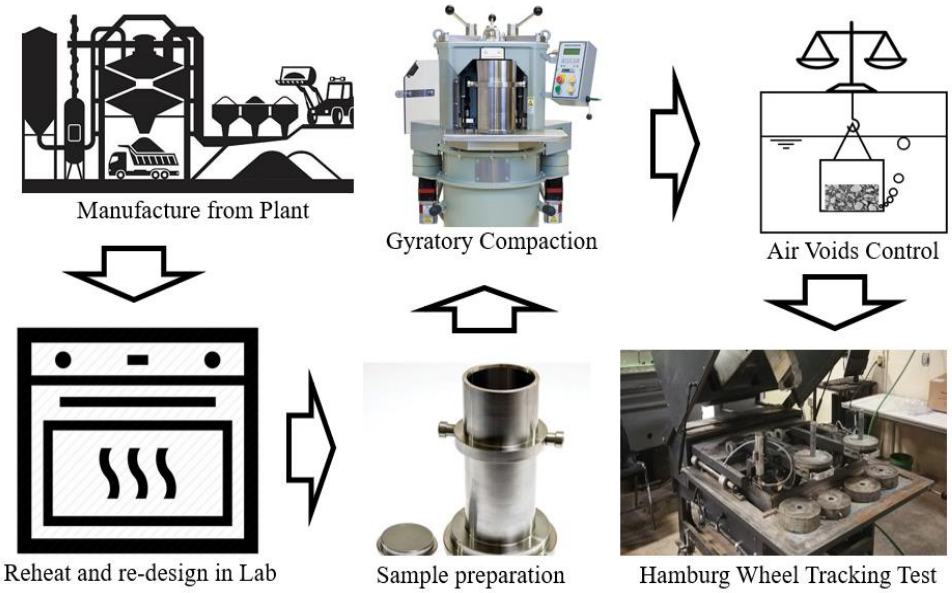

Figure 4-2 Experimental Program

Table 4-2 BRD, MRD, and Air Voids Ratio of HL3, HL3 HS, and HL1 HS

	Specimen #	HL3 64-28	HL3 58-28	HL3 HS 70-28	HL3 HS 64-28	HL1 HS 70-28	HL1 HS 64-28
BRD (g/cm3)	1	2.311	2.320	2.335	2.344	2.424	2.380
	2	2.250	2.315	2.338	2.345	2.423	2.379
	3	2.266	2.314	2.327	2.343	2.431	2.378
	4	2.255	2.309	2.325	2.352	2.417	2.381
	Average	2.271	2.315	2.331	2.346	2.424	2.379
MRD (g/cm3)		2.479	2.483	2.517	2.548	2.601	2.607
Air Voids (%)	1	0.068	0.066	0.073	0.080	0.068	0.081
	2	0.092	0.068	0.072	0.080	0.068	0.081
	3	0.085	0.068	0.076	0.081	0.066	0.082
	4	0.090	0.070	0.077	0.077	0.071	0.080
	Average	0.084	0.068	0.074	0.079	0.068	0.081

4.3 Results and Discussion

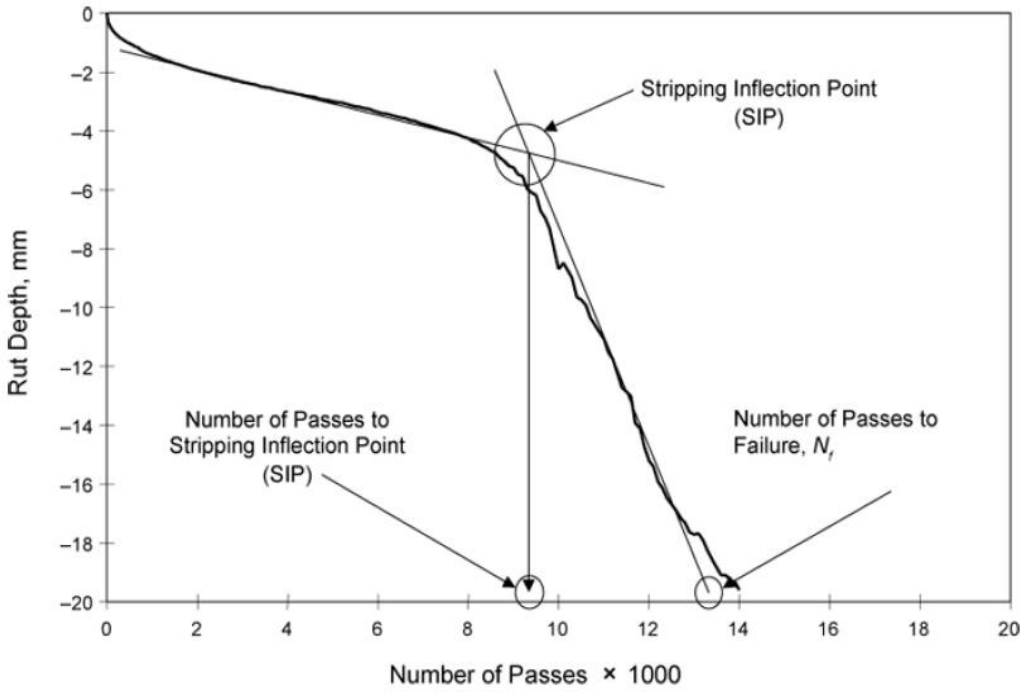

Figure 4-3 Calculation of Stripping Inflection Point (AASHTO 2016)

According to AASHTO T324, the calculation of Stripping Inflection Point (SIP) can be expressed as follows:

$$Stripping\ Inflection\ Point\ (SIP) = \frac{intercept\ (second\ portion) - intercept\ (first\ portion)}{slope\ (first\ portion) - slope\ (second\ portion)}$$

Equation 4-1

Figure 4-3 is a typical plot of output produced by HWTT, and it shows two distinct portions of the curve with consistent slopes. However, most HWTT results do not show a significant difference between the first and second portions. Therefore, it is challenging and unreliable to calculate stripping inflection points through visual inspection.

4.3.1 Rut Depth

All the test results were fitted with the least squared method using the Francken model. The tested and fitted results of six different types of mixes are shown in Figure 4. Fitted model constants are presented in Table 4-3.

Table 4-3 Regression Model Fitting Constants

Constants	HL3 58-28	HL3 64-28	HL3 HS 64-28	HL3 HS 70-28	HL1 HS 64-28	HL1 HS 70-28
A	3.601E-01	2.658E-01	3.642E-01	5.504E-02	9.575E-02	1.001E-01
B	2.312E-01	1.632E-01	1.692E-01	2.150E-01	1.903E-01	2.008E-01
C	8.999E-01	3.969E-03	4.105E-03	4.092E-03	0.000E+00	4.271E-01
D	0.000E+00	6.592E-07	0.000E+00	2.821E-04	0.000E+00	0.000E+00

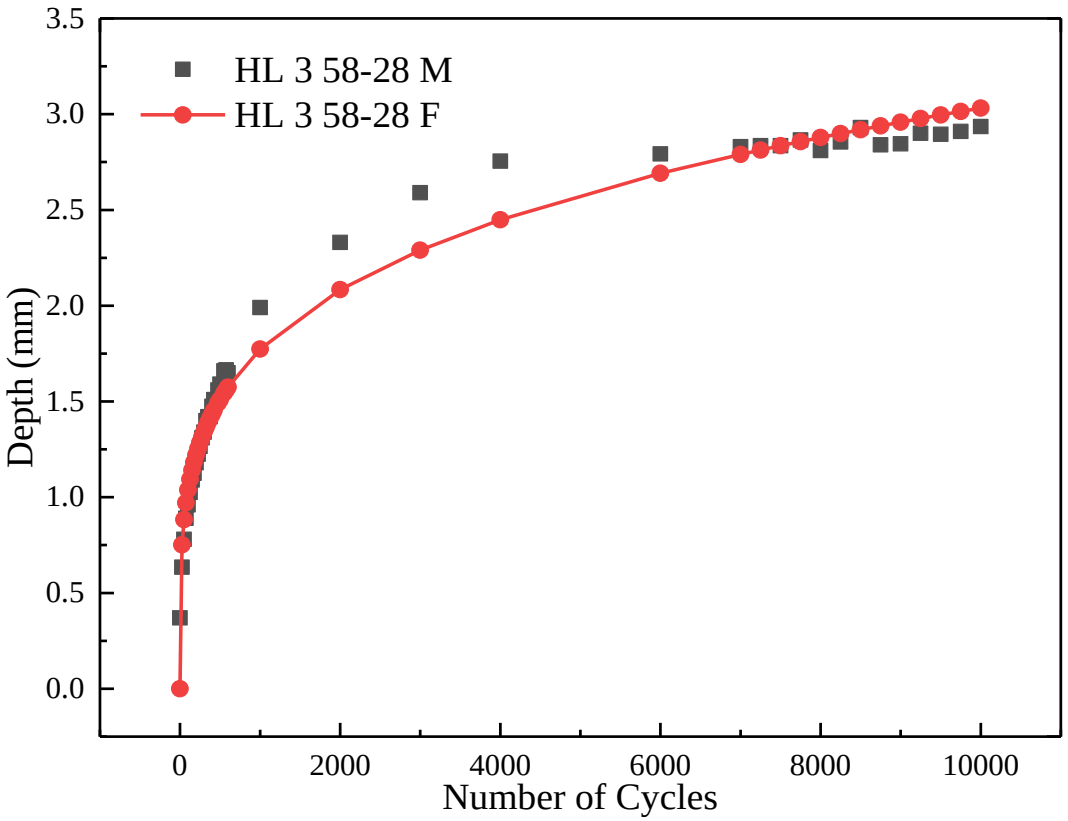

(a) HL3 58-28

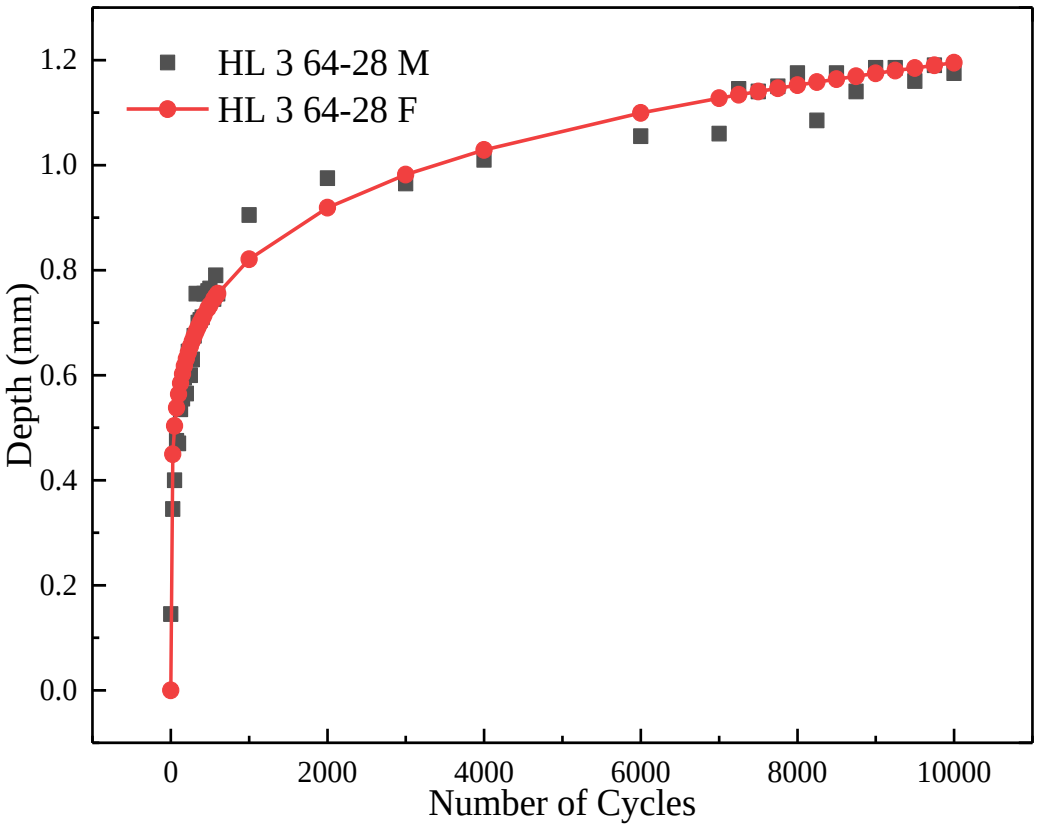

(b) HL3 64-28

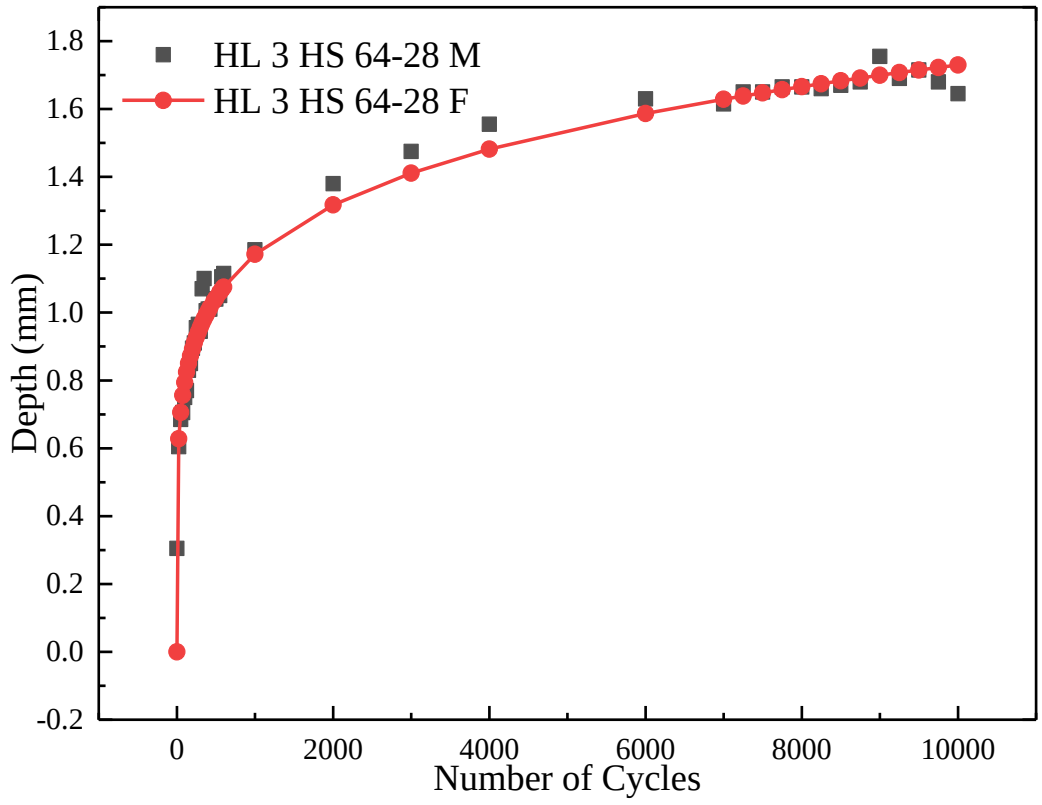

(c) HL3 HS 64-28

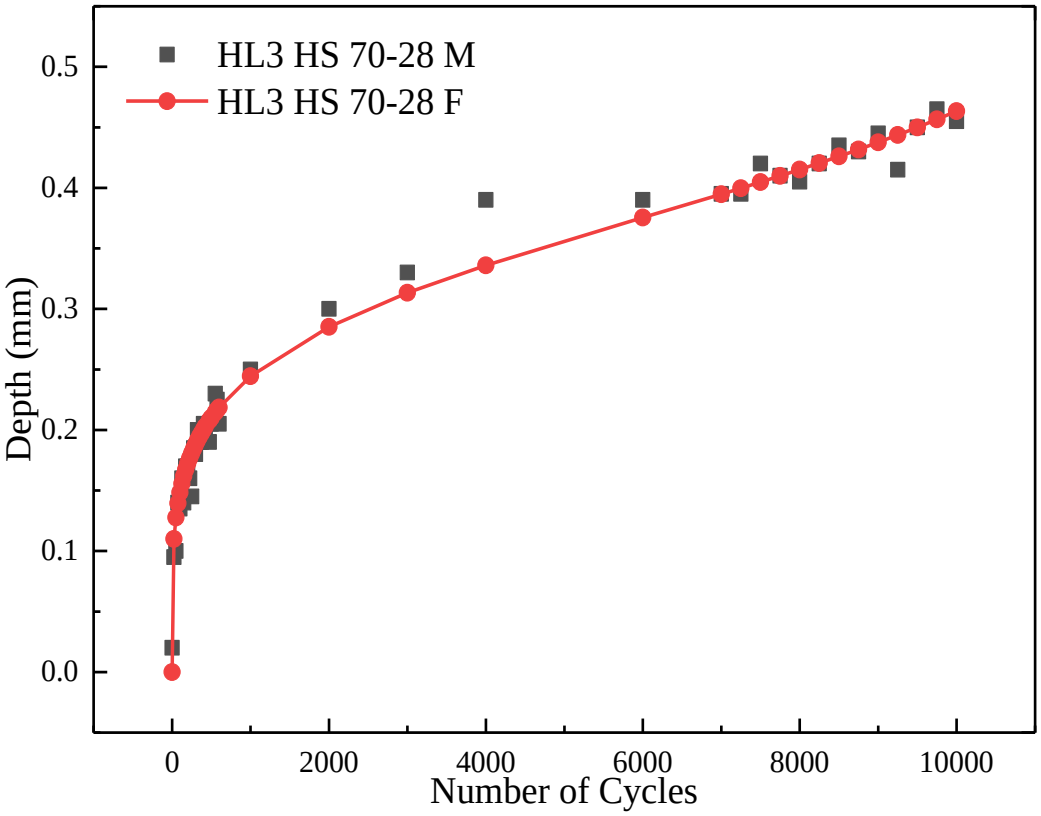

(d) HL3 HS 70-28

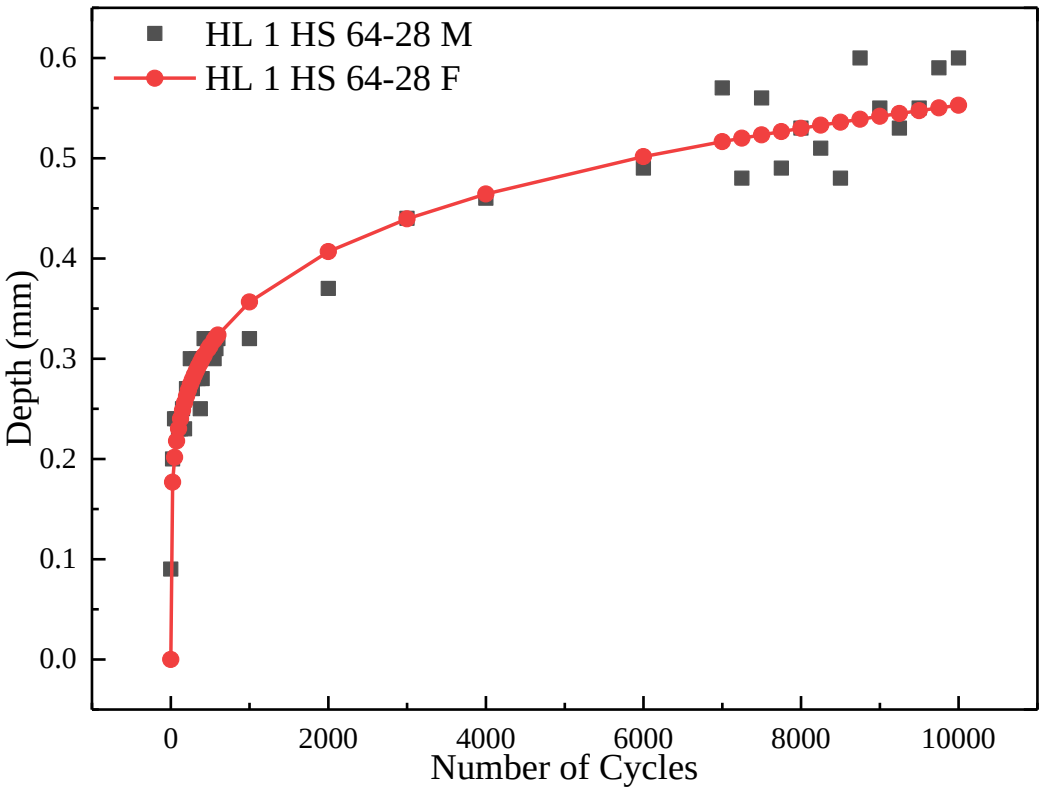

(e) HL1 HS 64-28

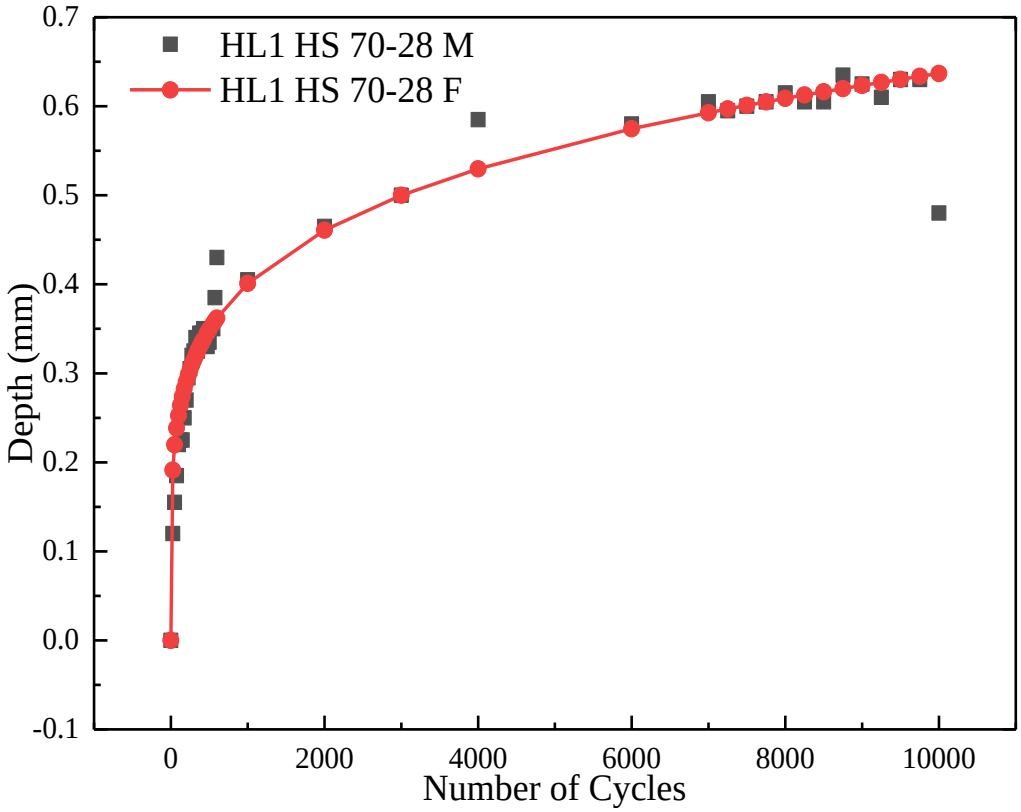

(f) HL1 HS 70-28

Figure 4-4 HWTT Results and Fitted Curves

The testing results in Figures 4-4 were calculated using the mean value of the rutting depths for the two wheels. Some of the test runs showed false-negative rut depth at the very beginning of the test due to the uneven sample surface.

From Figure 4-4, it is shown that all of the six mixes rutting depths do not show an obvious stripping stage as shown in Figure 4-3. Among all the test results, only HL 3 70-28 and HL 1 64-28 show unstable rut depth at the tail of the rut curve. This could be due to several reasons. Firstly, data collecting frequency isn't consistent, for the first 500 cycles, the data was recorded every 25 cycles; from 500 cycles to 1,000 cycles, the data collection frequency increases from every 50 cycles to every 400 cycles; from 1,000 cycles to 7,000 cycles, the data was collected only every 1000 cycles; and from 7,000 cycles to 10,000 cycles, the collection drops to every 250 cycles. Secondly, the test automatically ends at 10,000 cycles, which means the HWTT assumes that most asphalt mixtures start stripping before 10,000 cycles. More testing cycles might be

necessary for stripping to become obvious. For example, the French Laboratory Rutting Tester (FLRT) is capable of 30,000 cycles (Uzarowski et al., 2004).

Figures 4-4 (a) and (b), (c) and (d), and (e) and (f), show that overall rutting depth is significantly influenced by the stiffness of the asphalt binder. The rutting depth of mixtures with polymer modified asphalt (PMA) PG 64-28 is approximately 2 mm less than that of PG 58-28; HL3 HS with PMA PG 70-28 has 1 mm less rut depth than that of PMA PG 64-28. However, HL1 HS with PMA PG 70-28 does not display a significant difference with that of PMA PG 64-28.

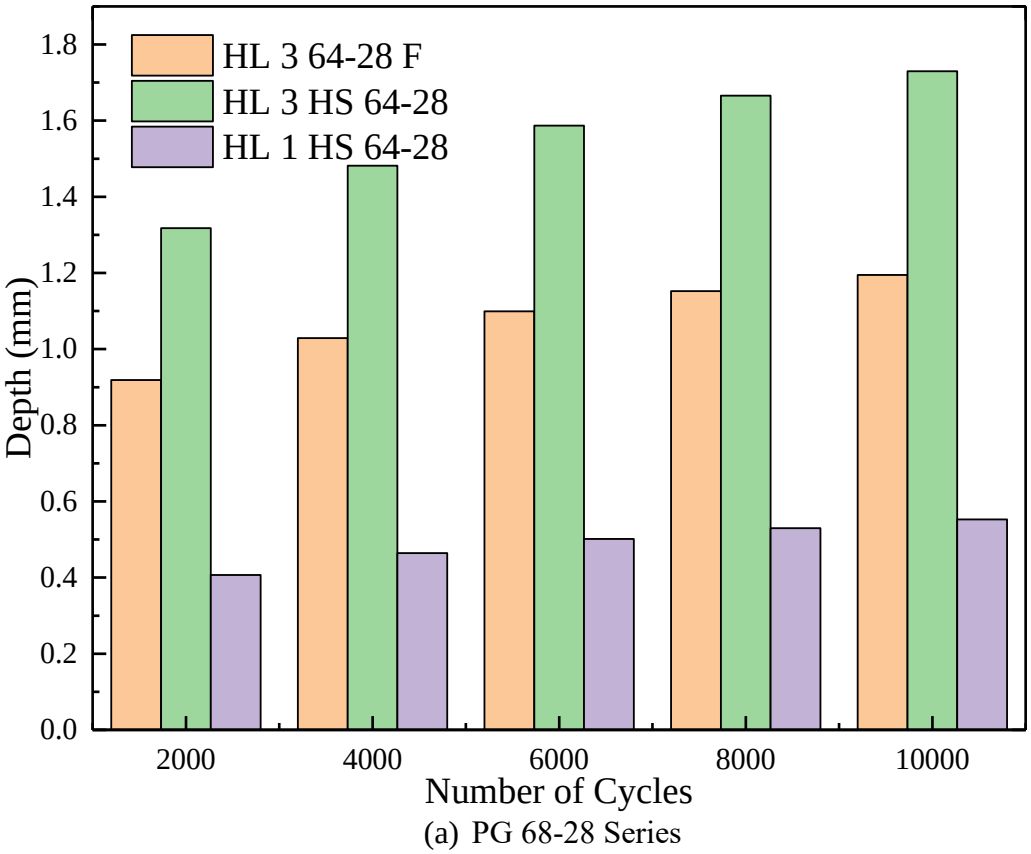

(a) PG 68-28 Series

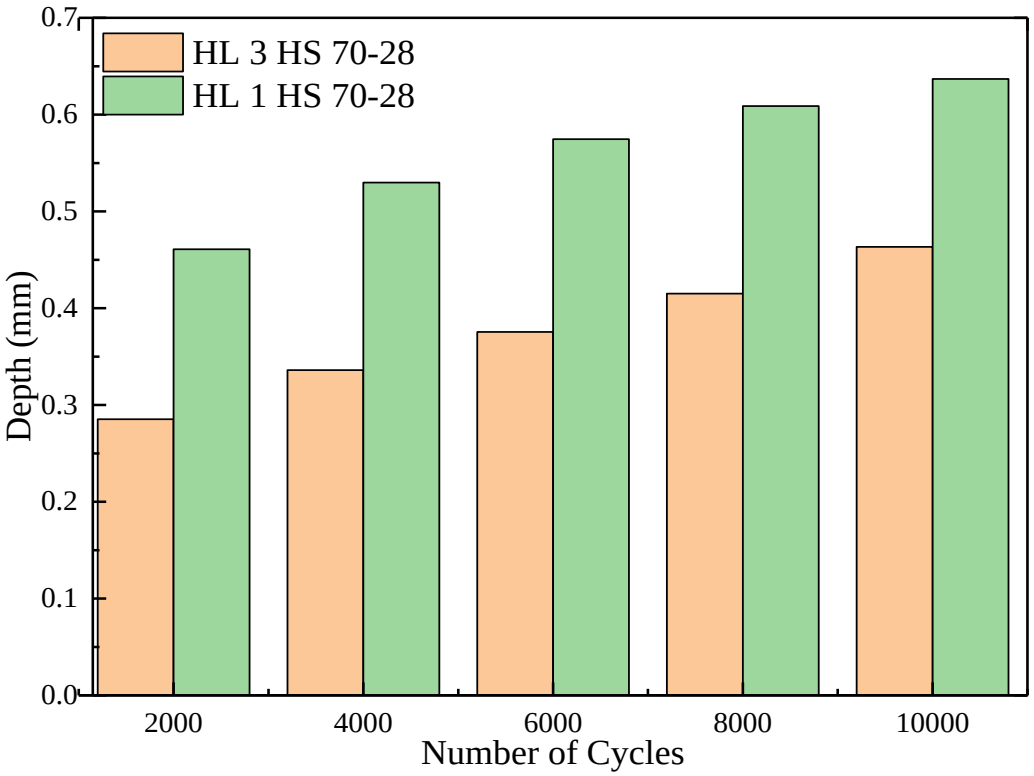

(b) PG 70-28 Series

Figure 4-5 Rut Depth of Different Mixes with Same Asphalt Binder PG Level

Figure 4-5 presents the rut depths of three different mix types with the same asphalt binder PG level at five loading cycles. It can be concluded that more than 75 % of rut growth occurred in the first 2,000 cycles and that the rut depth increase rate is approximately linear from 2,000 cycles to 10,000 cycles. Moreover, gradation plays an important role in rutting resistance. PMA 64-28, HL1 HS is shown to be the best in terms of rutting resistance performance for a given PG level by having less than 0.5 mm total rut depth, while HL3 and HL3 HS have 1.1 mm and 1.7 mm of rut depth, respectively. According to OPSS 1150, aggregate passing sieve size 4.75 mm is the key to controlling permanent deformation resistance. The lower the speed limit of the designed pavement, the higher the passing rate of 4.75 mm should be (*Material Specification for Hot Mix Asphalt*, 2008). Therefore, a higher passing rate of 4.75 mm sieve can provide better rutting resistance as low-speed vehicles tend to cause more rutting distress. As shown in Table 1 and Figure 4-5(a) HL1 HS has the highest passing rate of 61 % for a 4.75 mm sieve among the three mixes and presents the best rutting

resistance. HL3 and HL3 HS have 58.4 % and 58.2 % passing the 4.75 mm sieve, respectively, and show decreasing resistance to rutting. However, this conclusion conflicts with the results of HL1 HS 70-28 and HL3 HS 70-28 (Figure 4-5(b)). HL3 HS shows a better rutting resistance than HL1 HS despite having the same binder type. One possible explanation is that the HL1 HS mix has a higher asphalt content of 5.5 % than HL3 HS, which is 5 %.

4.3.2 ANOVA of Mix Parameters to Rut Depth

Six different factors related to the materials identity have been considered for their impact on rutting resistance of asphalt mixture in this study as shown in Table 4-4, including asphalt binder performance grade, the passing rate of 4.75 sieves, asphalt content, coarse aggregate content, source of material, and air voids. In statistics, homogeneity of variance is the premise for one-way analysis of variance (ANOVA), ANOVA should not proceed if the factors' variances are not the same. The homogeneity test of all six factors is displayed in Table 4-5.

Table 4-4 Factors and Levels for One-way ANOVA

Factors (Levels)	A (3)	B (3)	C (3)	D (2)	E (2)	F (6)	DpdtVrb
Mix Type	AsphPG	4.75 PsRt	AsphCont	CrsAggrCont	PrdcFrm	AV	RutDept
Unit	--	%	%	%	--	%	mm
HL3	58-28	58.4	5.1	40	0	0.068	2.897
HL3	64-28	58.4	5.1	40	1	0.084	1.179
HL3 HS	64-28	58.2	5.0	50	0	0.079	1.697
HL3 HS	70-28	58.2	5.0	50	1	0.074	0.446
HL1 HS	70-28	61.0	5.5	40	0	0.068	0.440
HL1 HS	64-28	61.0	5.5	40	1	0.081	0.564

Where:

AsphPG = Asphalt Binder Performance Grade

4.75 PsRt = Passing rate of 4.75 mm sieve size

AsphCont = Asphalt Content

CrsAggrCont = Coarse Aggregate Content

PrdcFrm = Produce From, 0 is for plant-made, and 1 is for laboratory-made

AV = air voids

DpdtVrb = Dependent Variable

RutDept = Rut Depth

Table 4-5 Test of Homogeneity of Variance

Factor (3)	Levene Statistic	Degree of Freedom 1	Degree of Freedom 2	Significance
A	2.804	1	3	0.193
B	-	-	-	-
C	-	-	-	-
D	0.158	1	4	0.712
E	1.632	1	4	0.270
F	-	-	-	-

As shown in Table 4-5, the significance level of factors A, D, and E are greater than 0.05, which can not reject the hypothesis that all the variances are equal. Therefore, asphalt binder PG, asphalt binder content, coarse aggregate content can proceed with ANOVA. While the other three factors failed to pass the test and can not be analyzed further with One-way ANOVA.

Table 4-6 One-way ANOVA for Factor A, D, and E

Factor	Source	Sum of Squares	df.	Mean Square	F-Value	Sig.
A	Between Groups	4.034	2	2.017	9.405	0.051
	Within Groups	0.643	3	0.214		
	Total	4.678	5			
D	Between Groups	0.053	1	0.053	0.046	0.842
	Within Groups	4.625	4	1.156		
	Total	4.678	5			
E	Between Groups	1.349	1	1.349	1.621	0.272
	Within Groups	3.329	4	0.832		
	Total	4.678	5			

As shown in Table 4-6, all three factors' significance levels are greater than 0.05, which means the original hypothesis can not be rejected as these three factors do not have a significant impact on rut depth.

4.3.3 Rutting Growth Rate

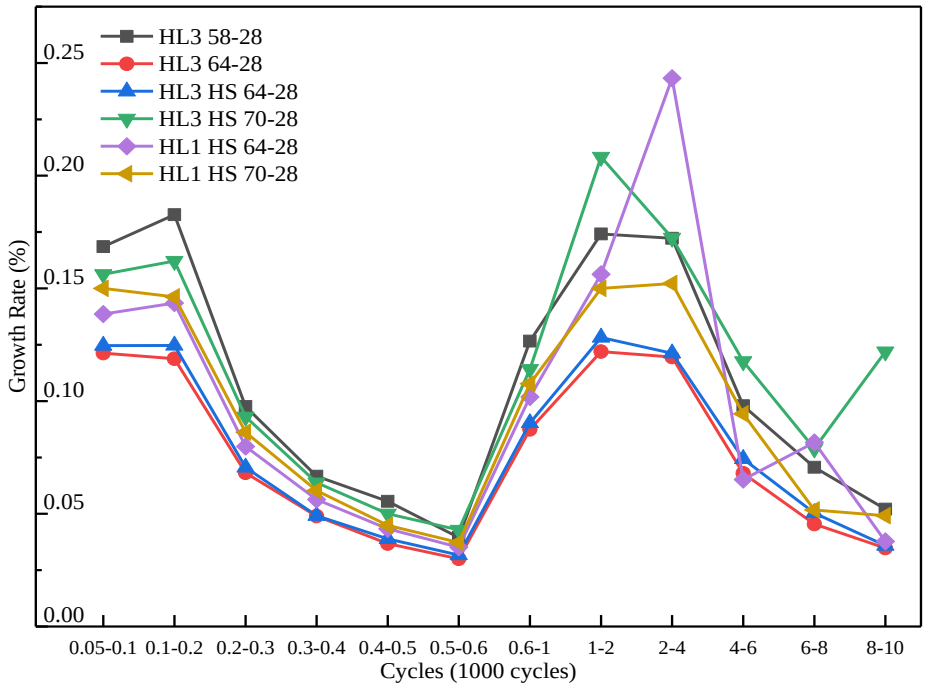

Figure 4-6 Rutting Growth Rates at Different Loading Cycle

Figure 4-6 presents the rutting growth rate of all six mixes under different loading cycles. All the mixes show the highest rut growth rate between 100 cycles and 200 cycles except HL1 HS 64-28 and HL3 HS, which exhibit the highest rate between 2000 cycles and 4000 cycles. Rut growth rates of all mixes decrease until 500-600 cycles where each shows the lowest level but drastically increases to approximately 15 % between 500-600 cycles and 1000-2000 cycles. At 2000-4000 cycles where the second peak rate is reached, another decreasing trend appears and drops below 5 percent till the end of the test.

4.4 Summary

Throughout all the HWTT results for HL3, HL3 HS, and HL1 HS with two different PG asphalt binders for each mix, the following conclusions can be drawn:

1. Asphalt binder PG level has a significant impact on the permanent deformation performance of HL3 and HL3 HS. Higher PG can provide asphalt mixtures with stronger rutting resistance of those two mixes. However, the impact of a higher PG level on HL1 HS is negligible.

2. Mix gradation affects permanent deformation resistance. The rate of aggregate passing the 4.75 mm sieve plays an important role in rutting resistance: a higher passing rate can result in a better rutting performance. However, HL3 HS and HL1HS with PG 70-28 do not follow this trend.
3. At testing temperature of 60 °C and standard loading weight for HWTT, the mixtures tested performed as follows, from best to worst:
    - HL3 HS with PG 70-28, HL1 HS with PG 64-28, and PG 70-28 (< 0.7 mm)
    - HL3 with PG 64-28 (1.2 mm)
    - HL3 HS with PG 64-28 (1.7 mm)
    - HL3 with PG 58-28 (3 mm)
4. Due to a limited number of experimental samples and each set of HWTT samples requiring approximately 7 hours to operate, all the mix design parameters are not statistically significant for rut depth. More repeated indoor experiments are recommended to compensate at this point.
5. Rutting growth rates of all six mixes show similar trends: a short increase within the first 200 cycles, then a drop until 500-600 cycles, then another increase to a peak at 1000-2000 cycles, and another decrease until the end of the test.

As rutting deformation continues to become a greater concern for Canadian pavement designers, these findings should be considered in pavement material design. High rut resistance can be achieved with both HL1 and HL3 materials when the proper binder performance grade is selected.

During the test sample preparation and testing, some difficulties were encountered. It is of significant value and interest to record and make suggestions in this study for the reference of future research activities. The following suggestions are made based on the author's laboratory experience for this study:

- For all the laboratory-produced loose mixes (HL3 64-28, HL3 HS 70-28, and HL1 HS 70-28), it's very difficult to obtain a 63 mm height of cylindrical specimen from Superpave Gyratory compactor at a required air voids level of 7 ± 0.5 percent. The

author tried to minimize all the causes of aggregate segregation during the preparation of specimens. Increasing gyrations can help some specimens to reach 63 mm, but over compaction may cause crushing of coarse aggregates and affect overall gradation. Some specimens ended up at 64 mm height for the compaction workability and testing specimen size requirements.

- All the HWTT results did not present an obvious stripping stage at a testing temperature of 60 °C and 10000 loading cycles. It is recommended that the overall loading cycles of HWTT should be extended. For example, the French Laboratory Rutting Tester (FLRT) is capable of 30,000 cycles for asphalt mixture to display rutting failure.
- A single LVDT rutting data collector on each load wheel is not enough to provide accurate rutting information. The false-negative rut depth appearing at the very beginning of some tests and extremely unstable depth records at the end of every test support this finding. Aggregate relocation and shear flow under test conditions might be possible explanations for this finding.

Chapter 5
RUTTING RESISTANCE EVALUATION OF CANADIAN ROADWAY-USED ASPHALT MIXTURES BY X-RAY CT

5.1 Materials and Methods

5.1.1 Materials

Three typical Canadian asphalt mixtures used in Ontario were tested in this study, Hot Laid 3 (HL3), Hot Laid 3 High Stability (HL3HS), and Hot Laid 1 High Stability (HL1HS). Each mix was evaluated with two different PG asphalt binders as described herein. Among the six mixes, three of them were produced from an asphalt plant and the other three were prepared in a commercial laboratory. HL3 was prepared with PG 58-28 and PG 64-28, with the former prepared from an asphalt plant and the latter from a consultant laboratory. HL3 HS was assigned with PG 64-28 and PG 70-28. Mixes with PG 64-28 were produced in the plant and the one with PG 70-28 was prepared in a laboratory. HL1 HS was also mixed with PG 64-28 and PG 70-28 while the former was prepared in the laboratory and the latter from the asphalt plant. The gradation curve of the Job Mix Formula, upper and lower limit for HL3, HL3 HS, and HL1 HS are presented in Figure 5-1 (*Material Specification for Hot Mix Asphalt*, 2008).

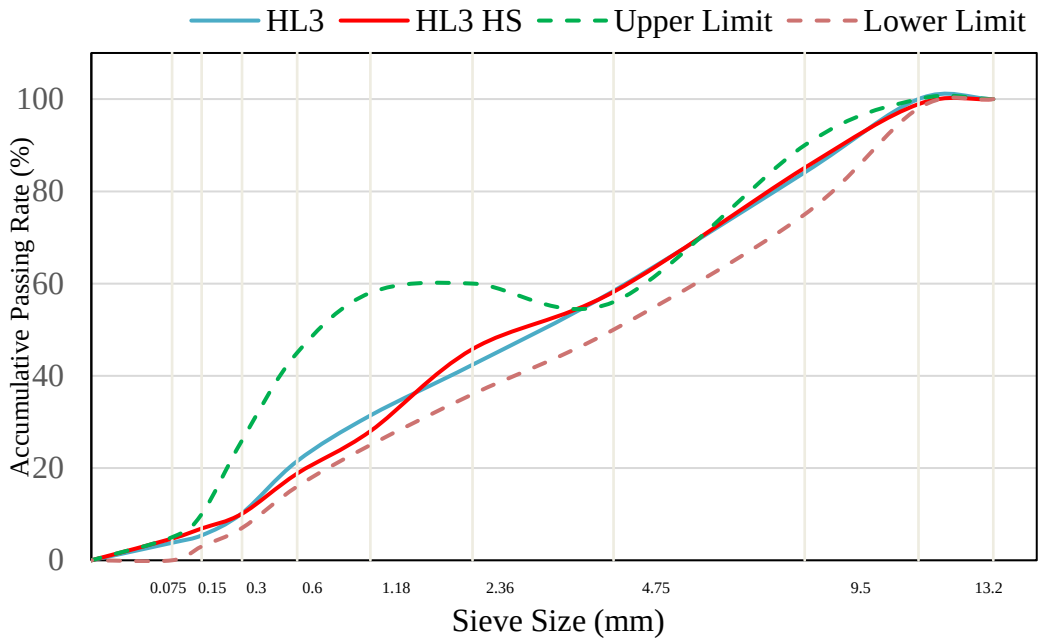

a. Gradation curve of HL3 and HL3 HS

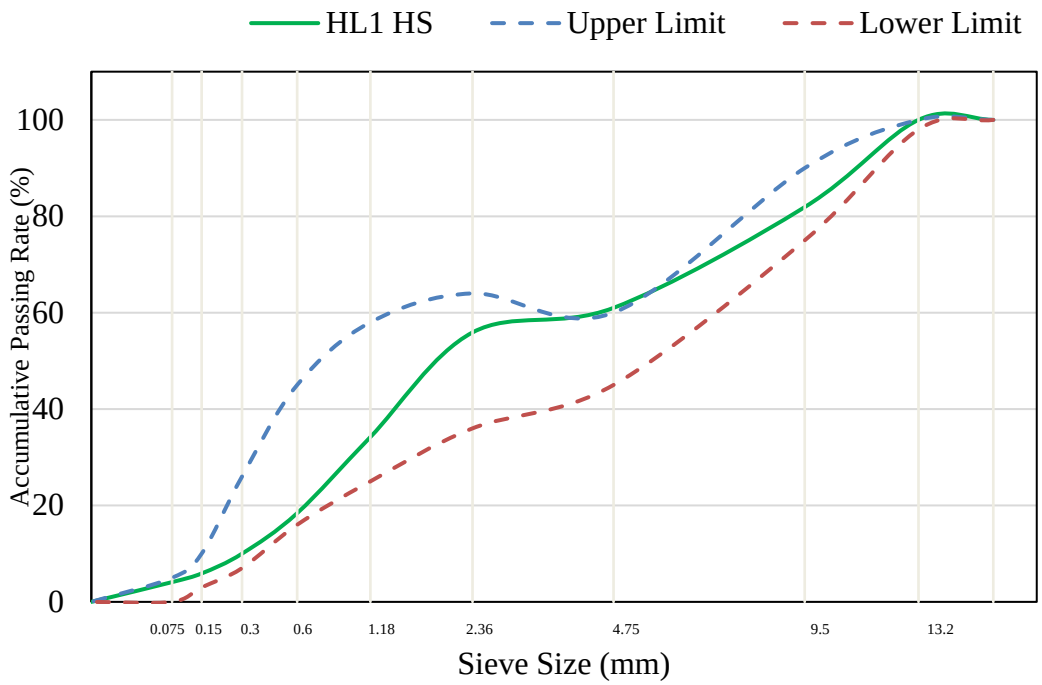

b. Gradation curve of HL1 HS

Figure 5-1 Gradation Curve for Tested Material and Gradation Limits

All the mixes used in this study were prepared in the Marshall mix design method. Six mixes were divided into two groups; one was tested using the HWTT, the other was processed for X-Ray CT scanning as shown in Figure 5-2. The specimens used for HWTT were compacted in Superpave Gyratory Compacter (SGC) with a height of 63 mm and 150 mm diameter cylinder as required in AASHTO T324 (AASHTO, 2016). The samples used for the CT scanning were also prepared in a gyratory compacter with the same height and diameter. According to the scanning scope limitation of the X-Ray CT at the University of Waterloo, the samples were further cored into 100 mm diameter. The air voids of all the specimens were controlled at 7 ± 0.5 percent as specified in AASHTO T324. Notably, laboratory-prepared loose mixes were conditioned in an oven at 135 ± 3°C for 4 hours ± 5 minutes to simulate the short-term aging process before compaction (AASHTO, 2013c). While the plant-produced materials were directly compacted once they reached the required compaction temperature.

a. HWTT Samples b. X-Ray CT Samples

Figure 5-2 Asphalt Specimens for Testing and Scanning

5.1.2 Hamburg Wheel Tracking Test

Many studies show that the HWTT has the capacity of accurately characterizing rutting resistance of asphalt pavement (Aschenbrener & Currier, 1993)(Aschenbrener, 1995)(Schram et al., 2014). The device moves a 203.2-mm (8-in.) diameter, 47-mm (1.85-in.) wide steel wheel over an asphalt specimen with an extra 705 ± 4.5 N on top as shown in Figure 3. The wheel runs 52 ± 2 per minute passes across the specimen (AASHTO, 2016). The temperature of the water bath was set up at 60 Celsius degree and the conditioning time was 30 minutes before the testing (Ministry of Transportation of Ontario, 2011). The test was set to terminate once 10,000 cycles were completed.

a. Industrial X-Ray CT Laboratory at University of Waterloo

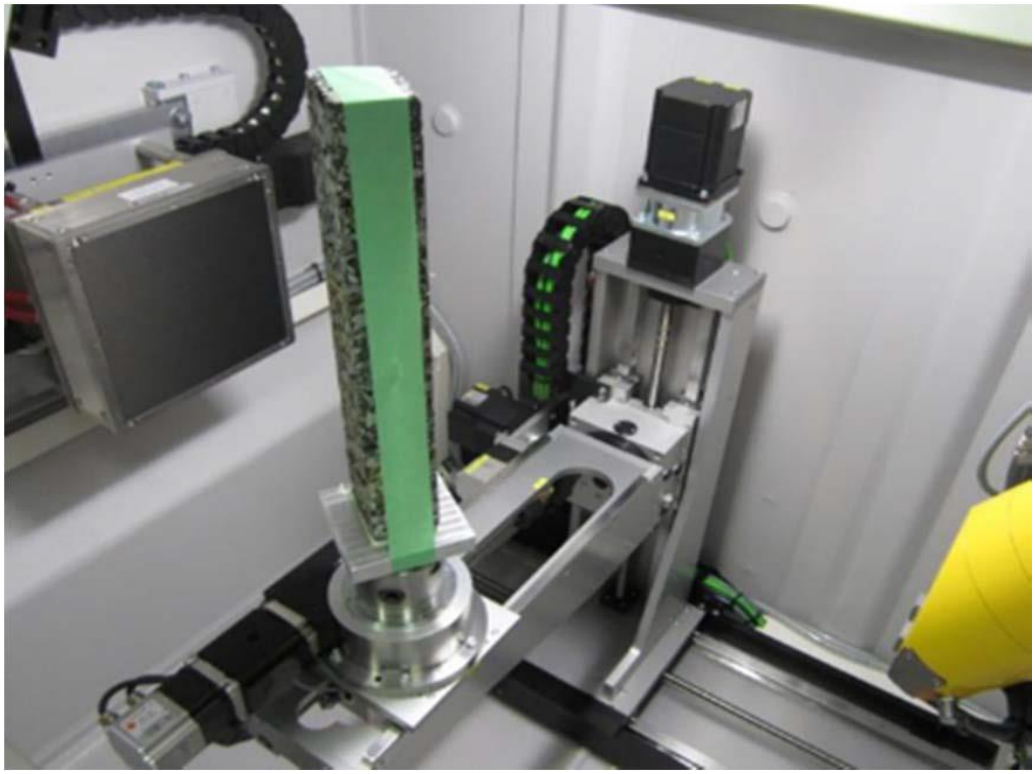

b. The Interior Scanning Room (Shaheen, 2015)

Figure 5-3 Industrial X-Ray CT

5.1.3 Industrial X-Ray Computed Tomography (CT)

X-Ray computed tomography has been used for pavement research since 1998 (Mora, Kwan1, 1998). Industrial computed tomography, which originates from medical tomography, is becoming a more common measurement technique in engineering applications. By applying higher energies and higher intensity of X-Ray radiation, it is possible to inspect complex machine parts made of materials with X-Ray attenuation coefficients higher than human tissues. Tomography for engineering applications enables measurements, which are unattainable by other metrological devices, for objects made of different materials such as asphalt concrete, metals, and ceramics.

In this study, based on the X-Ray CT device as shown in Figure 5-3, the top view, front view, and right view images were obtained. Moreover, the distance between slices is 0.2mm. Finally, 300 tomograms to the top view, and 500 tomograms separately to the front and right view were obtained. Then, the obtained 2D stack was segmented using the binary thresholding technique to convert the greyscale stack to binary stack.

Machine learning technologies (MLTs) were used to segment the particles, asphalt mortar, and voids during this procedure. MLTs can be classified into supervised learning techniques, unsupervised learning techniques, semi-supervised learning techniques, and reinforced learning techniques (Alpaydin, 2009)(Ivanović & Radovanović, 2014). Among those methods, supervised and unsupervised learning algorithms are the most widely used approaches in engineering. In this study, Fast-Random-Forest (FastRF) is used, which is an improved Random-Forest (RF) method. Figure 5-4 shows the main procedures of MLTs.

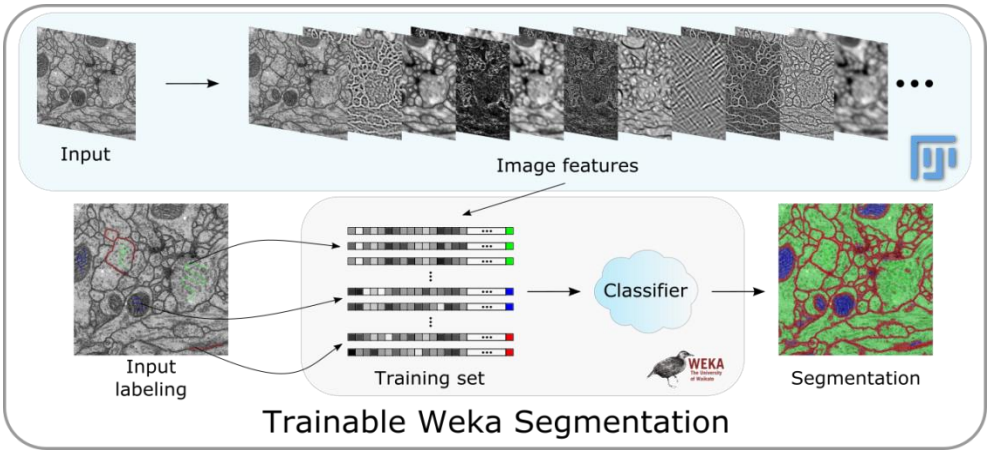

Figure 5-4 Procedure of MLTs (Arganda-Carreras I, Kaynig V, 2017)

RF is a supervised learning algorithm that is used for both classifications as well as regression. Random forest algorithm creates decision trees on data samples and then gets the prediction from each of them and finally selects the best solution employing voting. It is an ensemble method that is better than a single decision tree because it reduces the over-fitting by averaging the result. Figure 5-5 shows procedures of random forest.

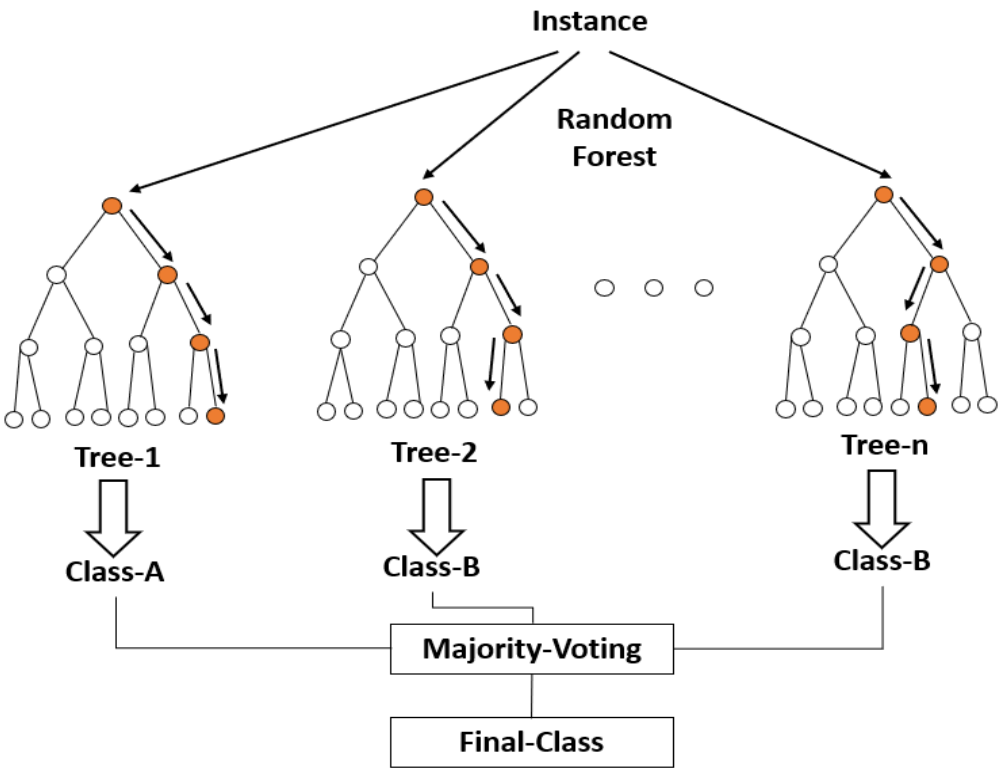

Figure 5-5 Random Forest Simplified

The training algorithm for random forests applies the general technique of bootstrap aggregating, or bagging, to tree learners. This bootstrapping procedure leads to better model performance because it decreases the variance of the model, without increasing the bias (James et al., 2013). The training and test error tends to level off after some number of trees have been fit. The above procedure describes the original bagging algorithm for trees. Random forests differ in only one way from this general scheme. They use a modified tree learning algorithm that selects, at each candidate split in the learning process, a random subset of the features. This process is called "feature bagging". In this way, the correlation of the trees in an ordinary bootstrap sample can be avoided (Ho, 2002).

Fast-Random-Forest (FastRF) is a re-implementation of the RF classifier for the Weka machine learning environment. FastRF brings speed and memory use improvements over the original Weka RF, particularly for datasets with a large number of features or instances. FastRF brings significant benefits in speed over RF if datasets have a large number of instances or attributes with missing values.

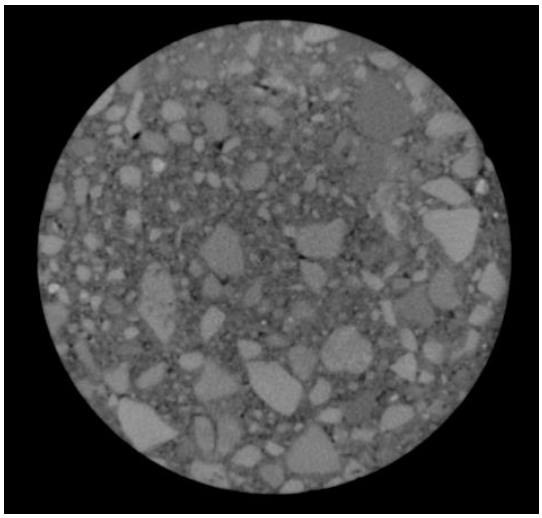

a. Original image

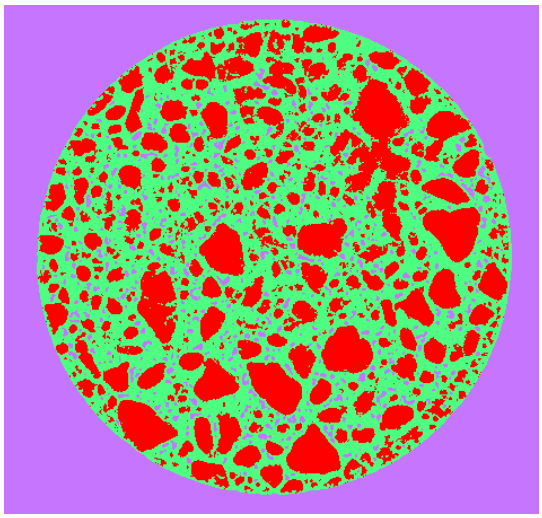

b. Segmentation result of FastRF

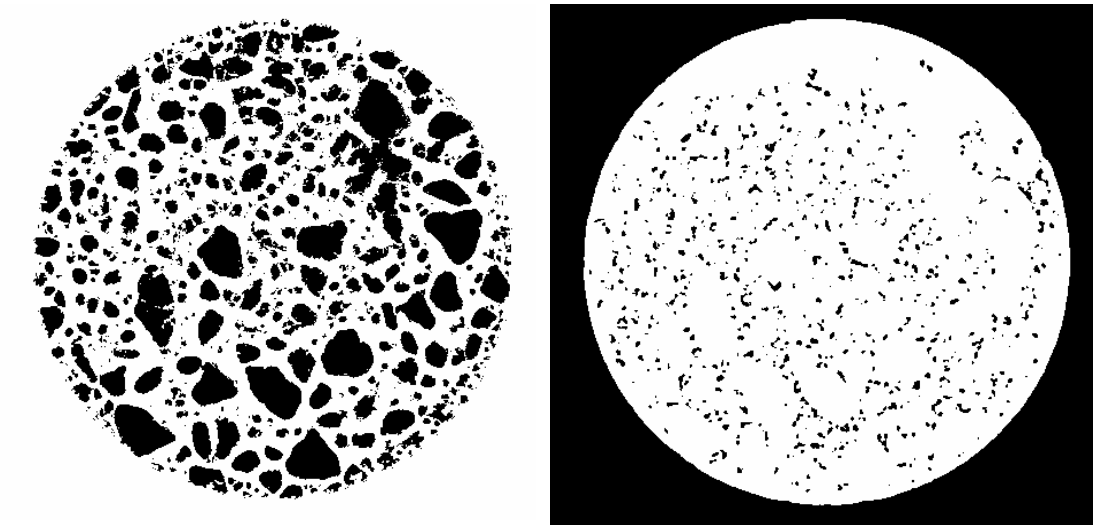

c. Binary image of Particles d. Binary image of Void

Figure 5-6 Segmentation Result of FastRF

In Figure 5-6 (b), different colors - red, purple, and green – separately represent identified particles, air voids, and asphalt. (c) and (d) show the binary image of particles and void. Based on the binary segmentation image, features of particles, void and asphalt can be obtained, which are used for further study.

5.1.4 Morphological Properties of Processed Images

Morphological properties of aggregate images such as solidity, roundness, and angularity are related to the resilient modulus, marshal stability, adhesion properties, as well as permanent deformation resistance of asphalt mixtures (Wang, 2016)(Cui, 2018)(Pan, 2005). In this study, four morphological property indexes were used to evaluate the shape of the particles obtained from the scanned images. Aspect Ratio (AR) is defined as a ratio of its sizes in different dimensions, in this study, the AR was calculated as the ratio of the major and minor axis of the equivalent ellipse as shown in Equation 5-1.

$$Aspect\ Ratio = \frac{Major\ Axis}{Minor\ Axis} \qquad \textbf{Equation 5-1}$$

The circularity (Cir.) is used to describe how close a two-dimensional shape is to a true circle. Equation 5-2 indicates the definition of circularity (Olson, 2011).

$$Circularity = 4\pi \times \frac{Area}{Perimeter^2} \quad \textbf{Equation 5-2}$$

Solidity is the measurement of the overall concavity of a particle. It is defined as the image area divided by the convex hull area as shown in Equation 5-3 (Olson, 2011).

$$Solidity = \frac{area\ of\ image}{convex\ hull\ area} \quad \textbf{Equation 5-3}$$

Roundness, similar to Circularity, is the measure of how close a shape of an object approaches a mathematically perfect circle as shown in Equation 5-4 (Olson, 2011).

$$Roundness = 4 \times \frac{area\ of\ image}{\pi \times Major\ Axis^2} \quad \textbf{Equation 5-4}$$

5.2 Results and Discussion

5.2.1 Data Process of Particles and Voids

Six samples in three gradation types were scanned through X-Ray CT. The results are presented as two-dimensional images in three directions; the top view, the front view, and the right view. These 2D images were further processed by MATLAB to extract the particle data and voids data. The morphological properties defining the particles include area, perimeters, aspect ratio, circularity, roundness, and solidity as shown in Table 5-1. The properties for voids are area and perimeter as shown in Table 5-2.

Table 5-1 Statistical Description for Morphological Properties of Scanned Particles

Statistical Indicators	Sample #	Mean	Median	Standard Deviation	Sample Variance	Kurtosis	Skewness	Confidence Level (95.0%)
Aspect Ratio	1	1.698	1.549	0.639	0.409	8.772	1.821	0.015
	2	1.642	1.464	0.760	0.577	12.723	2.198	0.018
	3	1.653	1.516	0.599	0.359	2.383	1.306	0.012
	4	1.685	1.477	0.755	0.570	3.855	1.597	0.015
	5	1.475	1.000	0.724	0.524	4.236	1.814	0.007
	6	1.710	1.553	0.633	0.401	7.217	1.851	0.017
	Average	1.644	1.426	0.685	0.473	6.531	1.765	0.014
Circularity	1	0.758	0.797	0.224	0.050	-0.454	-0.700	0.005
	2	0.814	1.000	0.238	0.057	-0.481	-0.928	0.004
	3	0.759	0.809	0.243	0.059	-0.412	-0.775	0.005
	4	0.778	0.822	0.241	0.058	-0.795	-0.680	0.005
	5	0.903	1.000	0.194	0.038	2.901	-1.986	0.002
	6	0.793	0.857	0.222	0.049	-0.285	-0.851	0.006
	Average	0.801	0.881	0.227	0.052	0.079	-0.987	0.004
Roundness	1	0.660	0.646	0.207	0.043	-0.891	0.159	0.005
	2	0.715	0.683	0.258	0.067	-1.496	-0.131	0.004
	3	0.676	0.660	0.211	0.045	-1.030	0.146	0.004
	4	0.694	0.677	0.247	0.061	-1.374	-0.026	0.005
	5	0.797	1.000	0.260	0.068	-1.199	-0.697	0.002
	6	0.653	0.644	0.204	0.042	-0.770	0.261	0.005
	Average	0.699	0.718	0.231	0.054	-1.126	-0.048	0.004
Solidity	1	0.838	0.848	0.115	0.013	-0.363	-0.350	0.003
	2	0.870	1.000	0.150	0.022	-0.854	-0.687	0.002
	3	0.833	0.841	0.129	0.017	-0.573	-0.355	0.003
	4	0.859	0.871	0.142	0.020	-0.876	-0.543	0.003
	5	0.889	1.000	0.185	0.034	0.570	-1.406	0.082
	6	0.847	0.857	0.114	0.013	-0.338	-0.372	0.003
	Average	0.856	0.903	0.139	0.020	-0.406	-0.619	0.016

In statistics, skewness is used as a measure of a dataset's symmetry or lack of symmetry. Positive skewness indicates right-skewed data, while negative skewness means left-skewed data (Wheeler, 2004). In a right-skewed dataset, the mean value is greater than the median value, and the median value is greater than the mean in a left-skewed dataset as shown in Figure 5-7. Among all the four indicators, only roundness shows the skewness value is within the range of ± 0.5, and therefore roundness is considered as symmetrically distributed. The skewness of circularity and solidity is less than 1 and can be treated as moderately skewed, and the aspect ratio is highly skewed since its skewness is greater than 1. When the dataset is skewed, the median is a better measure of the central tendency than the mean (Wheeler, 2004). Therefore, circularity, solidity, and aspect ratio used the median while roundness used the mean as data representation. Other morphological properties such as area, perimeter, major axis, and minor axis are determined by mixture gradation and therefore have no statistical significance. Morphological properties are not suitable for analyzing air voids as they have a very small area and perimeter. The total area and perimeters of particles and air voids are presented in Table 5-2 and Figure 5-8.

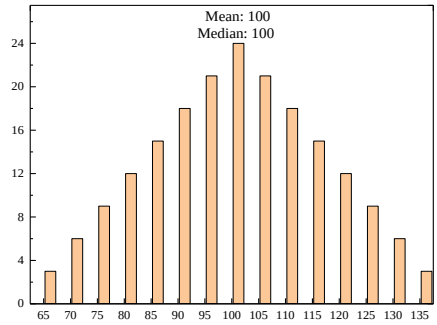

a. Symmetric Distribution

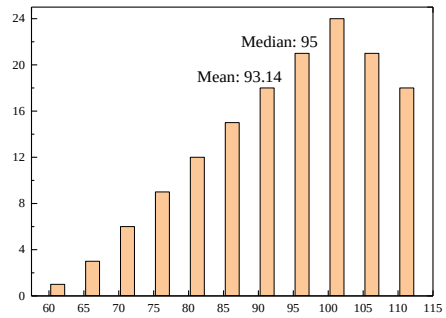

b. Left Skewed Distribution

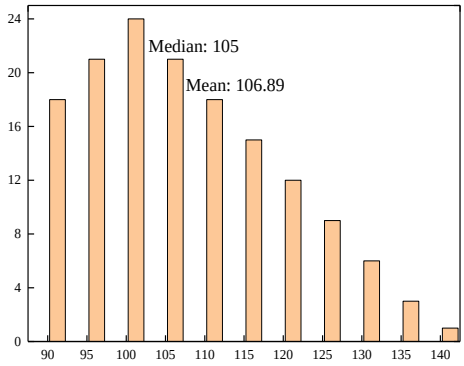

c. Right Skewed Distribution

Figure 5-7 Symmetric and Skewed Distributed Dataset

Table 5-2 Statistical Description for Scanned Particles and Voids

	Image Indexes	Sample #1	Sample #2	Sample #3	Sample #4	Sample #5	Sample #6
Particles	Total Area	69739.64	60832.99	90944.84	74658.47	68955.61	60700.18
	Total Perimeter	72662.75	78470.54	100498.88	78453.48	110688.88	53046.89
	Counts	6964	15569	9678	10030	46848	5596
Voids	Total Area	59504.26	67278.63	100705.99	77276.69	80421.98	94959.56
	Total Perimeter	29976.99	70100.16	104371.93	40379.36	61846.17	97247.43
	Counts	7909.00	13636.00	15216.00	8891.00	17340.00	19095.00

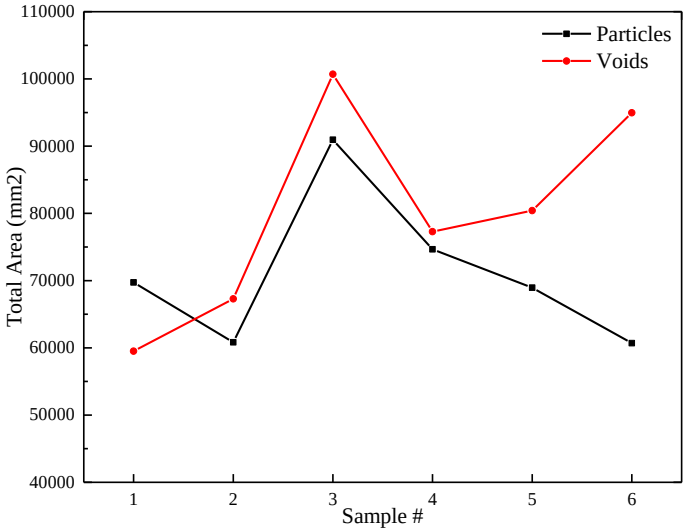

a. Total Area

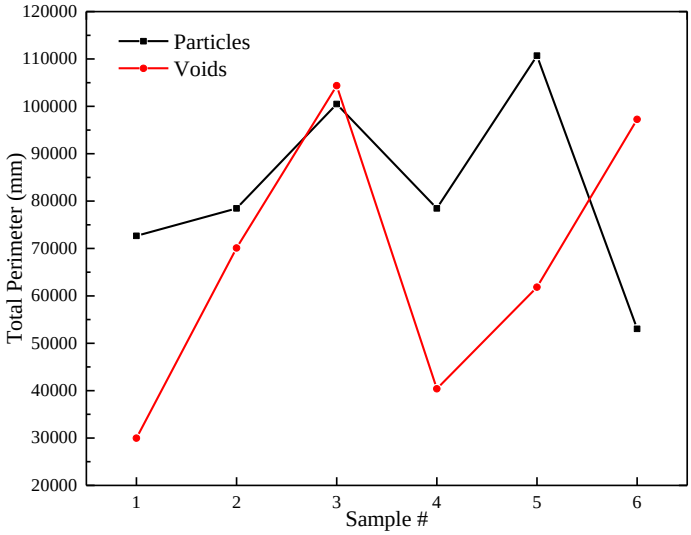

b. Total Perimeter

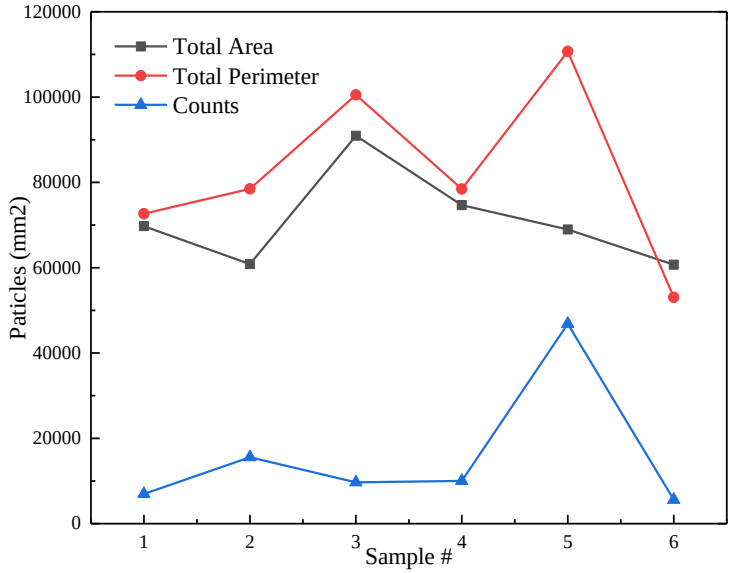

c. Particles

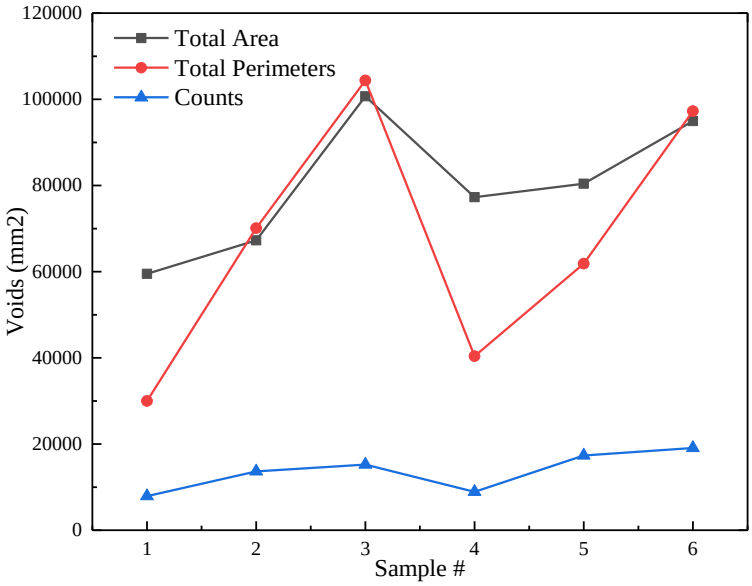

d. Voids

Figure 5-8 Total Area and Perimeter of Different Sample

From Table 2 and Figure 8, the total area of the particles and voids for each sample shows the same trend while the total perimeter does not follow the same pattern. The total area and perimeter of each sample follow the trend of the number of particles and voids.

5.2.2 Particles Image Processing

The top view images of all six samples were used in this study to analyze morphological properties of aggregates and air voids of typical Canadian asphalt mixture applied in

roadways. Through the binary process, three phases of asphalt specimen namely, aggregate, asphalt binder, and air voids were separately extracted from the CT scanning images. Particles represent the aggregates and are evaluated by two-dimensional image-related indexes. The particle distribution in a different area, perimeter, as well as roundness and solidity are shown in Table 5-3 and 5-4, and Figures 5-9, 5-10, and 5-11.

Table 5-3 Particles Distribution in Different Area Range

Area (mm^2)	Sample #1	Sample #2	Sample #3	Sample #4	Sample #5	Sample #6	Total	Percentage
(0,10)	5544	14389	8354	8587	45843	4728	87445.00	92.38%
(10,20)	575	453	548	505	249	206	2536.00	2.68%
(20,30)	246	213	191	267	139	119	1175.00	1.24%
(30,40)	141	139	130	153	115	90	768.00	0.81%
(40,50)	96	85	88	116	108	82	575.00	0.61%
(50,60)	69	59	56	68	79	67	398.00	0.42%
(60,70)	40	42	48	65	61	46	302.00	0.32%
(70,80)	40	39	35	54	42	43	253.00	0.27%
(80,90)	35	14	29	33	30	34	175.00	0.18%
(90,100)	27	21	12	28	28	32	148.00	0.16%
>100	126	115	187	154	154	149	885.00	0.93%
Total	6939	15569	9678	10030	46848	5596	94660	100%

Table 5-4 Particles Distribution in Different Perimeter Range

Perimeter(mm)	Sample	Sample #2	Sample #3	Sample #4	Sample #5	Sample #6	Total	Percentage
(0,10)	4943	13618	7575	7855	45056	4409	83456.00	88.16%
(10,20)	1080	1041	1089	1099	838	474	5621.00	5.94%
(20,30)	381	407	425	459	342	245	2259.00	2.39%
(30,40)	190	221	181	255	247	173	1267.00	1.34%
(40,50)	135	117	103	126	149	95	725.00	0.77%
(50,60)	65	58	72	82	81	68	426.00	0.45%
(60,70)	40	35	47	59	57	43	281.00	0.30%
(70,80)	32	20	21	29	28	17	147.00	0.16%
(80,90)	13	16	24	21	20	16	110.00	0.12%
(90,100)	12	7	19	20	9	10	77.00	0.08%
>100	48	29	122	25	21	46	291.00	0.31%
Total	6939	15569	9678	10030	46848	5596	94660	100%

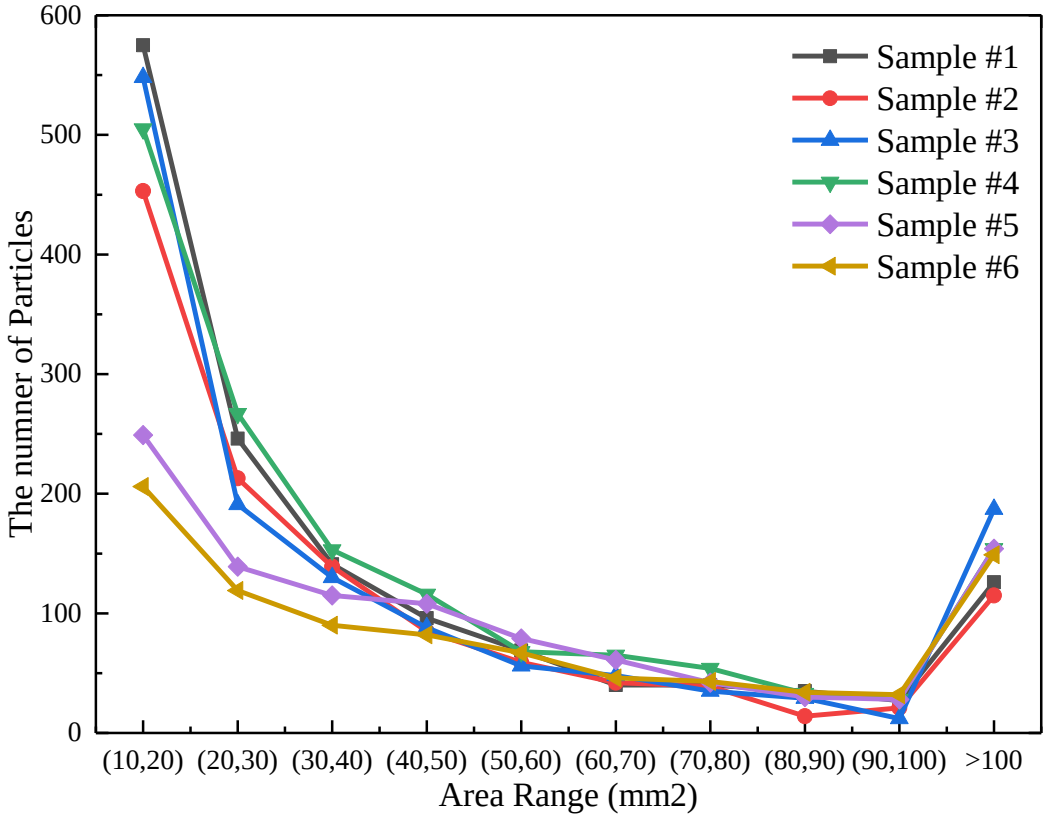

a. Area

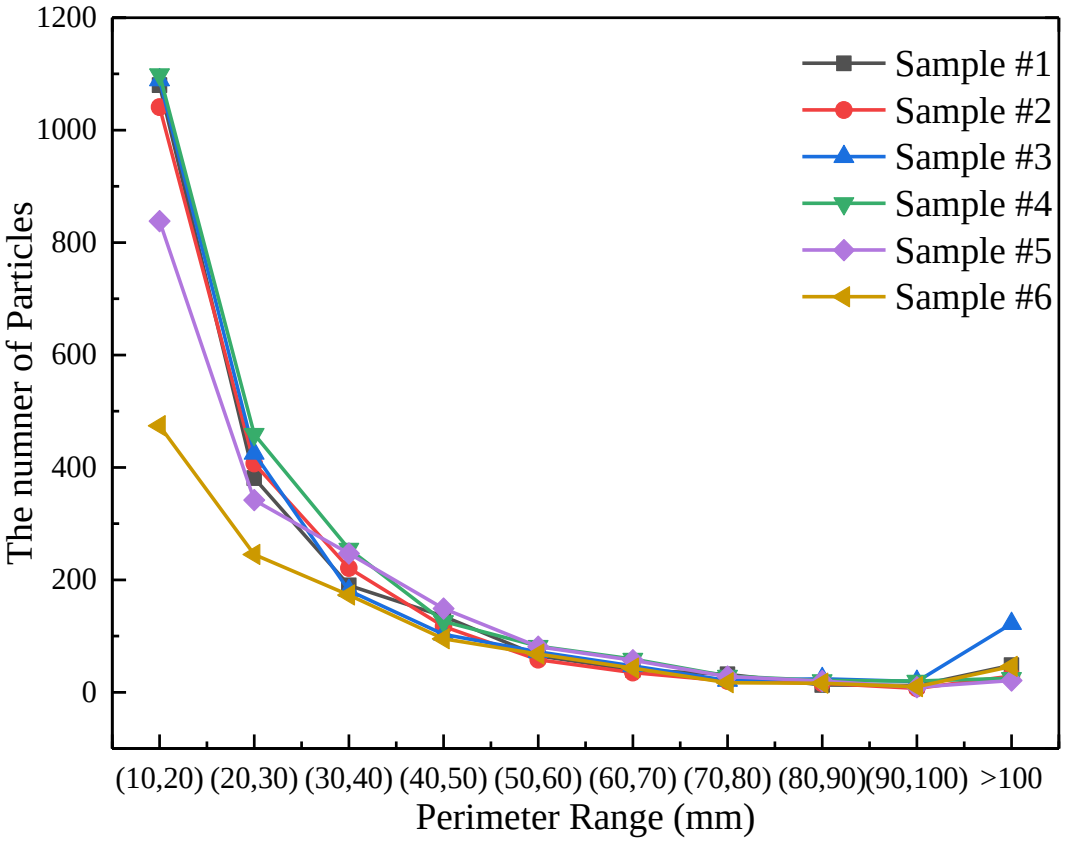

b. Perimeters

Figure 5-9 Particles Distributions in Different Area and Perimeter Range

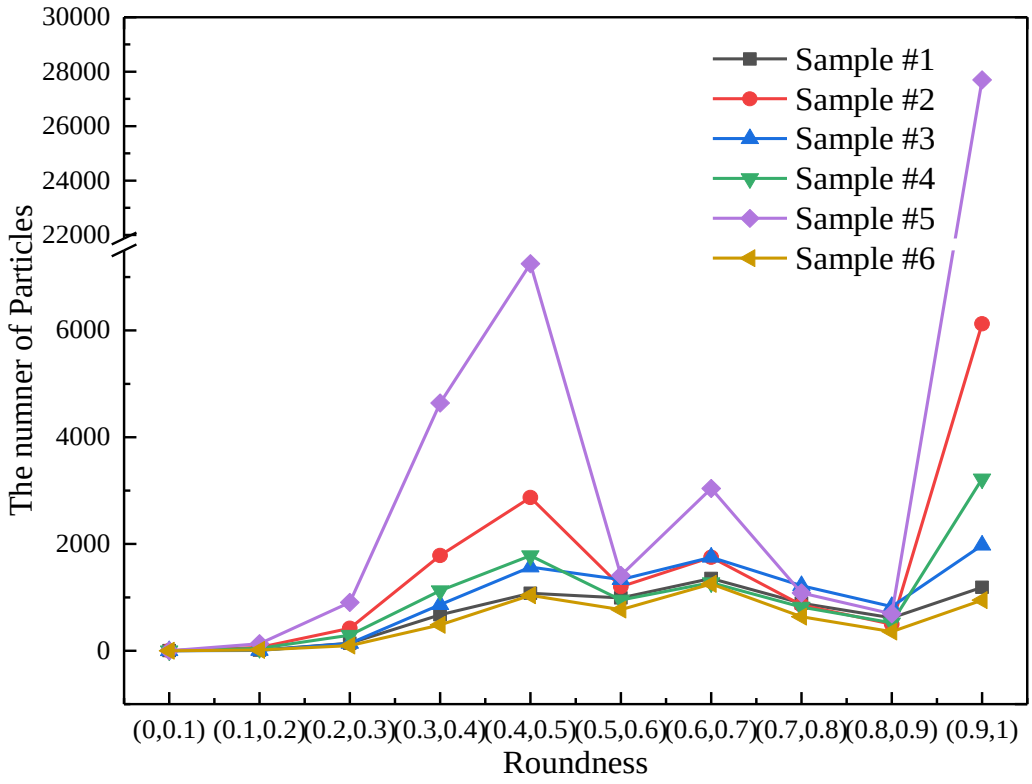

a. Roundness

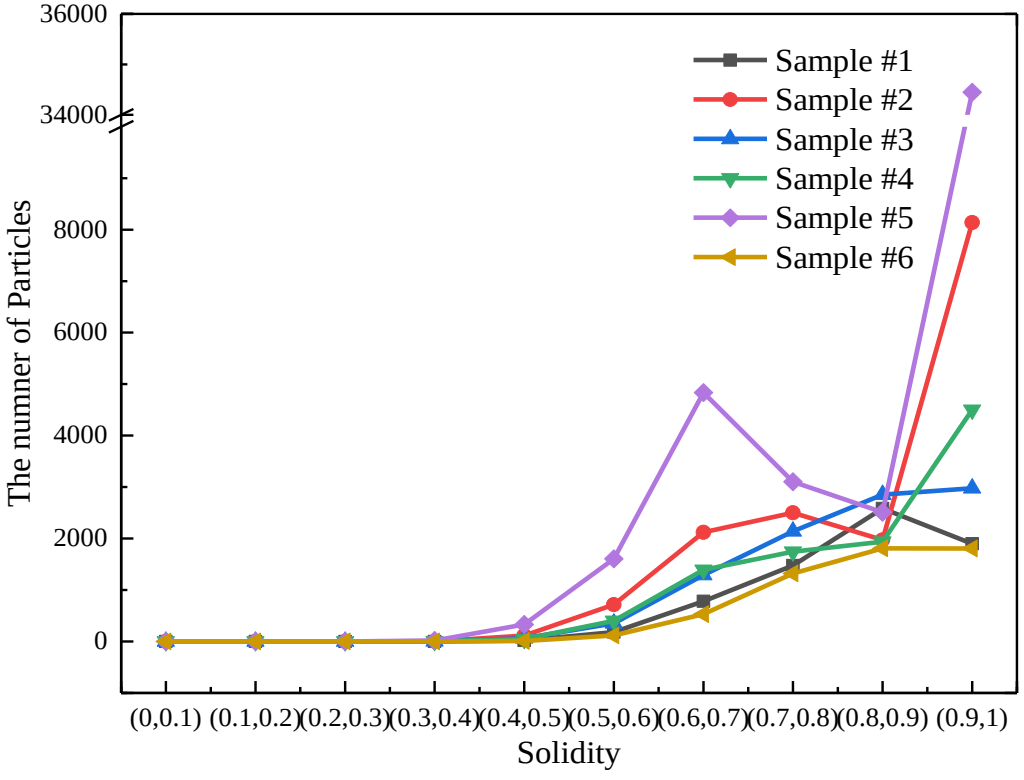

b. Solidity

Figure 5-10 Particles Distributions in Morphological Properties

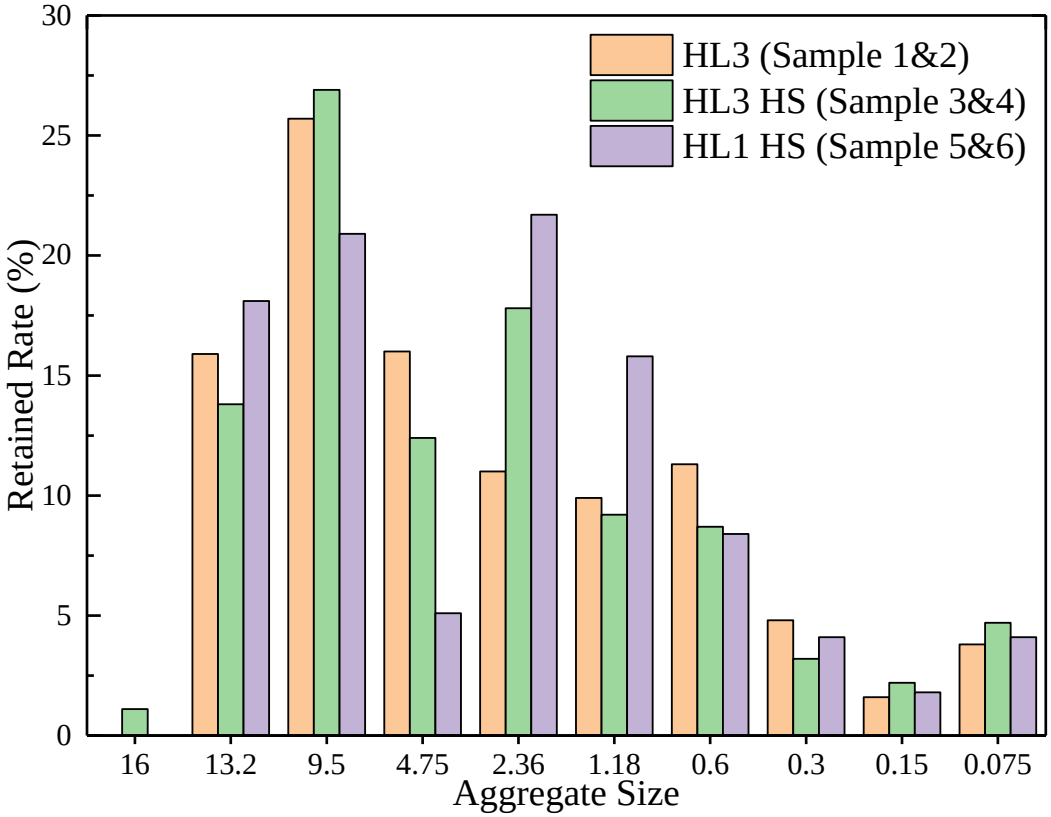

a. Retained Rate from Gradation

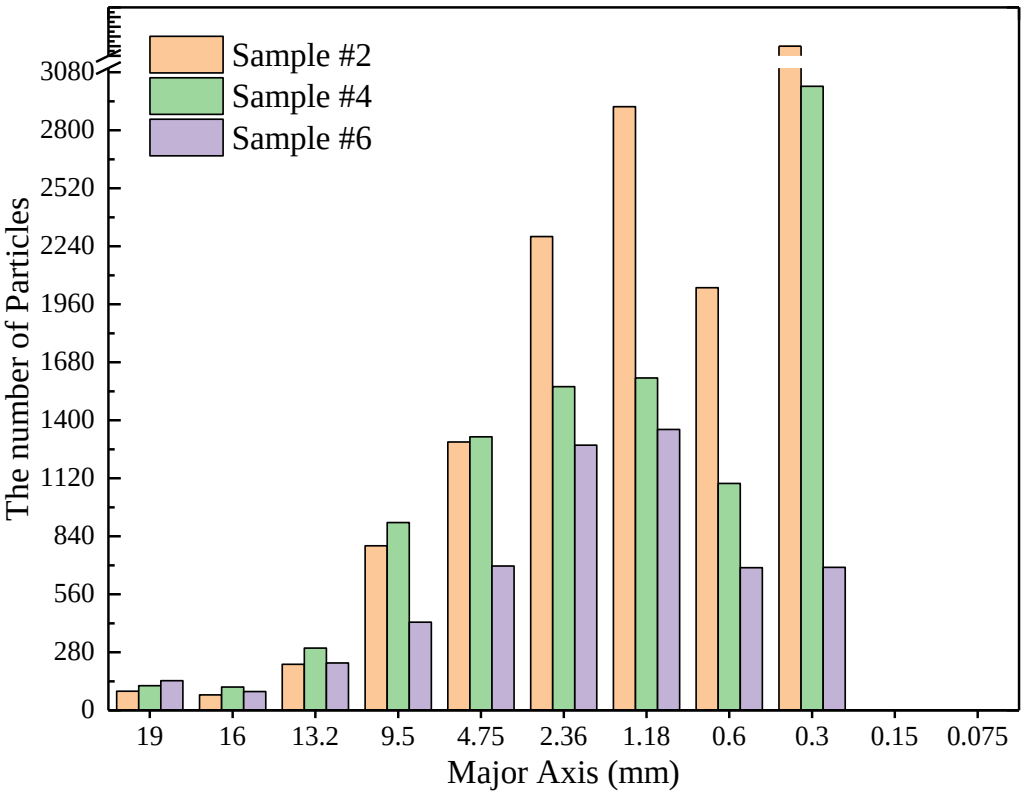

b. Particle Distribution of Lab Mix

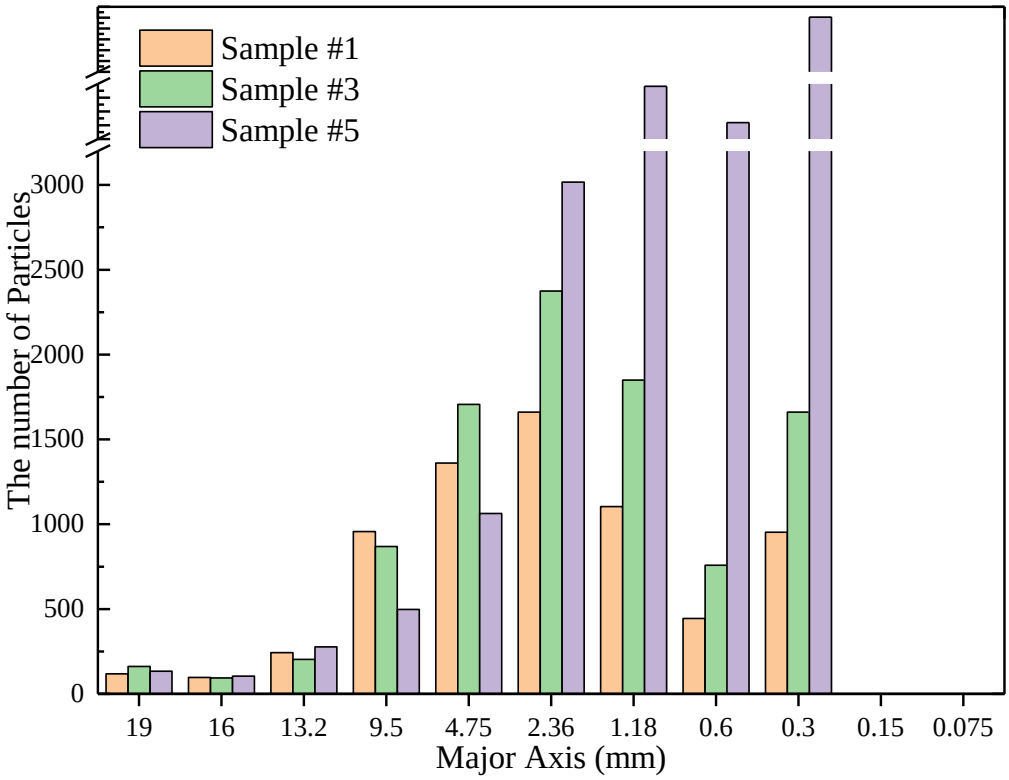

c. Particle Distribution of Plant Mix

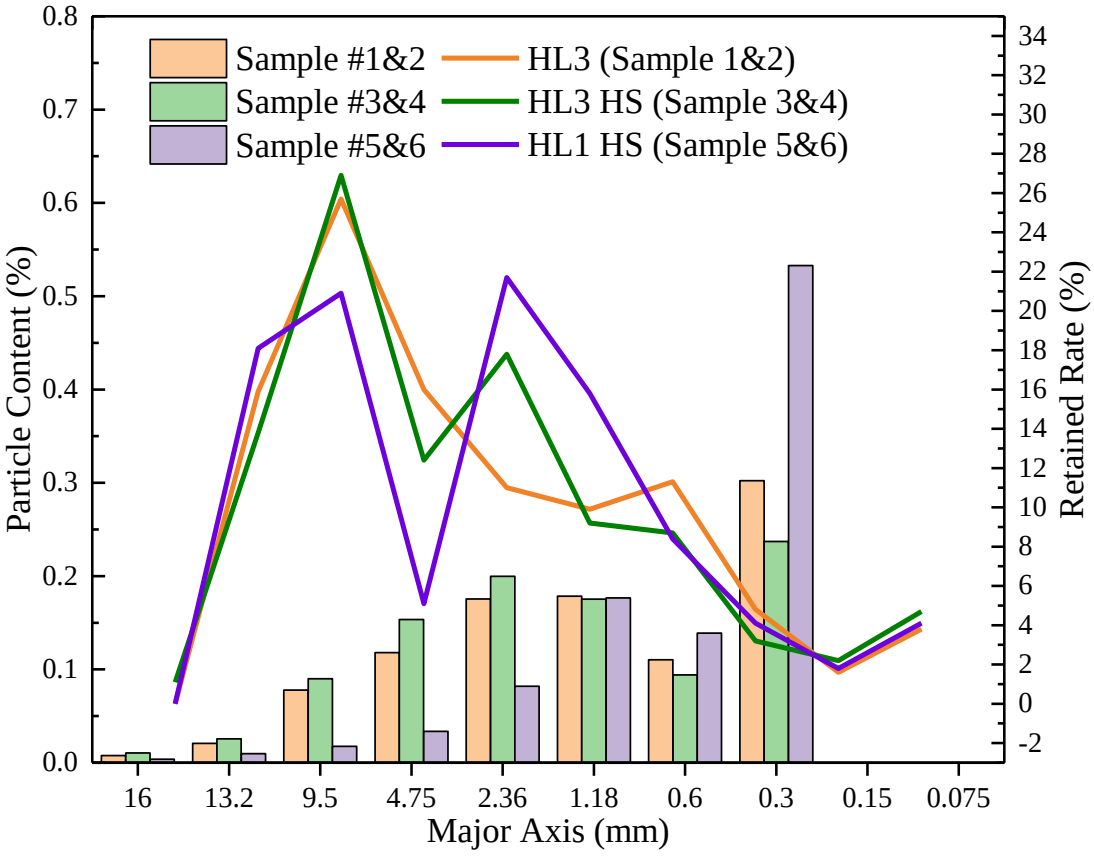

d. Particle Distribution and Gradation

Figure 5-11 Gradation and Particle Distribution

As is shown in Table 5-3 and Table 5-4, particles that have less than 10 mm in perimeter and 10 mm^2 in the area are the majority, which occupies nearly 90 percent of all the processes particles. The number of particles decreases with the increase of particle area and perimeters. The area between 90 mm^2 and 100 mm^2 only takes 0.16 percent of all the particles, and the perimeter between 90 to 100 mm takes only 0.08 percent. Sample 5 and 6 display a lower quantity of particles in terms of area and perimeter, the remaining sample does not exhibit a significant difference as shown in Figure 5-10. For morphological properties such as roundness and solidity, sample 5 presents a higher proportion of high roundness and solidity particles. Figure 5-11 presents aggregates composition from gradation curve and processed particles distribution in major axis. As can be observed from Figure 5-11b and 11 c, lab mix, and plant mix displayed similar proportions under different sieve sizes, which shows an opposite trend to the gradation distribution in Figure 5-11 a and 11 d. In gradation distribution, fine aggregates have a lower proportion than coarse aggregates; while in processed particles, fine aggregates occupy more than coarse aggregates. Particularly, gradation distribution does not have aggregates in 19 mm sieve size while processed images do. Processed images do not have aggregate in 0.15 mm and 0.075 mm while gradation distribution does. A possible explanation lies on several points: 1. The procedure in which all the particles were processed. Particles whose major axis is less than 0.15 mm may be difficult to detect and process by computer. Therefore, they were considered in larger size particles. 2. Lab mixes and plant mixes have different gradation control accuracy. For example, sample #5 is a plant mix and shows an extremely dense gradation in processed particles, which has almost ten times more particles than other samples. 3. Processed particle distribution based on the major axis is incapable of representing mix gradation. The former dataset is collected via two-dimension images from one cross-section of each aggregate. Considering that each section of aggregate keeps changing in the normal direction of the section, the accuracy of the 2D images representing realistic aggregate

distribution highly depends on the image processing threshold and the gap distance between the two nearest cross-sections.

5.2.3 Voids Image Processing

Air voids are considered crucial for pavement performance as it reflects the compaction rate. Road performances of different asphalt mixtures are comparable only when the air voids are at the same level. For mechanical performance purposes, the air voids of all test specimens are specified to be controlled at 7 ± 0.5% (AASHTO, 2013a). The distribution of air voids for all the processed images in a different area and perimeter range are presented in Tables 5-4, 5-5 and 5-6, and Figure 5-12.

Table 5-5 Voids Distribution in Different Area Range

Area Range(mm^2)	#1	#2	#3	#4	#5	#6	Total	Percentage
(0,0.25)	3863	2706	2860	2509	6930	4917	23785	29.35%
(0.25,0.5)	1642	1996	1746	1707	3182	2829	13102	16.17%
(0.5,0.75)	1052	2149	1542	1331	2339	2507	10920	13.48%
(0.75,1)	454	1369	885	651	1112	1439	5910	7.29%
(1,2)	648	3213	2779	1403	2243	3542	13828	17.06%
(2,3)	136	1213	1679	520	738	1465	5751	7.10%
(3,4)	45	475	1012	264	343	851	2990	3.69%
(4,5)	15	235	718	187	170	512	1837	2.27%
(5,10)	26	225	1441	239	216	767	2914	3.60%
Total	7881	13581	14662	8811	17273	18829	81037	100.00%

Table 5-6 Voids Distribution in Different Perimeter Range

Perimeter Range (mm)	#1	#2	#3	#4	#5	#6	Total	Percentage
(0,1)	1408	927	940	753	2974	1685	8687	10.58%
(1,2)	2942	2255	2485	2353	4826	4119	18980	23.12%
(2,3)	1730	3223	2325	2253	3980	3800	17311	21.09%
(3,4)	806	2360	1710	1195	1915	2526	10512	12.80%
(4,5)	379	1540	1387	649	1127	1683	6765	8.24%
(5,6)	235	1007	1142	441	694	1163	4682	5.70%
(6,7)	133	663	849	316	448	890	3299	4.02%
(7,8)	83	498	725	232	345	584	2467	3.01%
(8,9)	53	309	565	159	244	503	1833	2.23%
(9,10)	37	231	472	128	162	377	1407	1.71%
(>10)	104	624	2617	413	626	1766	6150	7.49%
Total	7910	13637	15217	8892	17341	19096	82093	100.00%

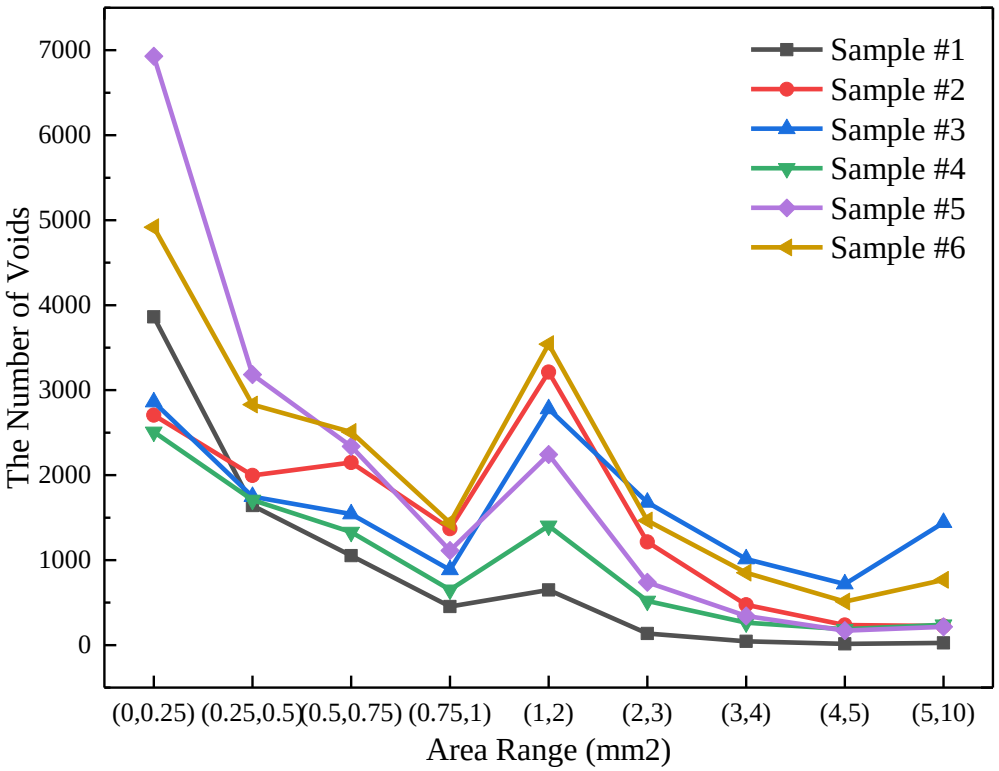

a. Area

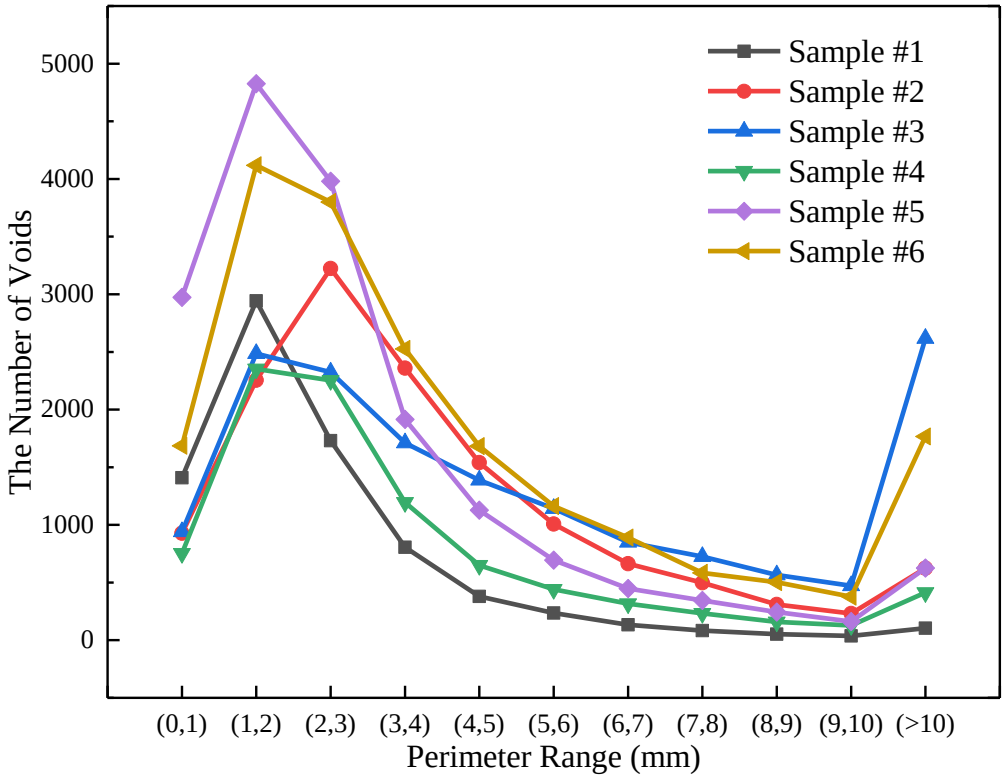

b. Perimeter

Figure 5-12 Voids Distribution in Different Area and Perimeter Range

Table 5-5 shows the voids distribution in the different area range. More than 60 percent of voids have an area less than 1 mm^2, and almost 30 percent are less than 0.25 mm^2. The perimeter distribution in Table 5-6 shows a uniform allocation of voids from 0 to 10 mm. All the six different types of mixes displayed a similar pattern in regards to perimeter and area. Figure 5-11 shows that the air voids of processed images presented a similar trend. The distribution of the voids in 9 different area ranges in Figure 5-12. a displayed that all the six mixes have similar area distributions. Sample #5 has the most particles based on area processed images and sample #1 has the least. Figure 5-12.b shows the distribution of the voids of all six mixes is consistent and voids perimeter distributions are mainly allocated between 1 mm and 3 mm. The number of voids gradually decreased with the increase of perimeter range.

5.2.4 Rutting Resistance Evaluation

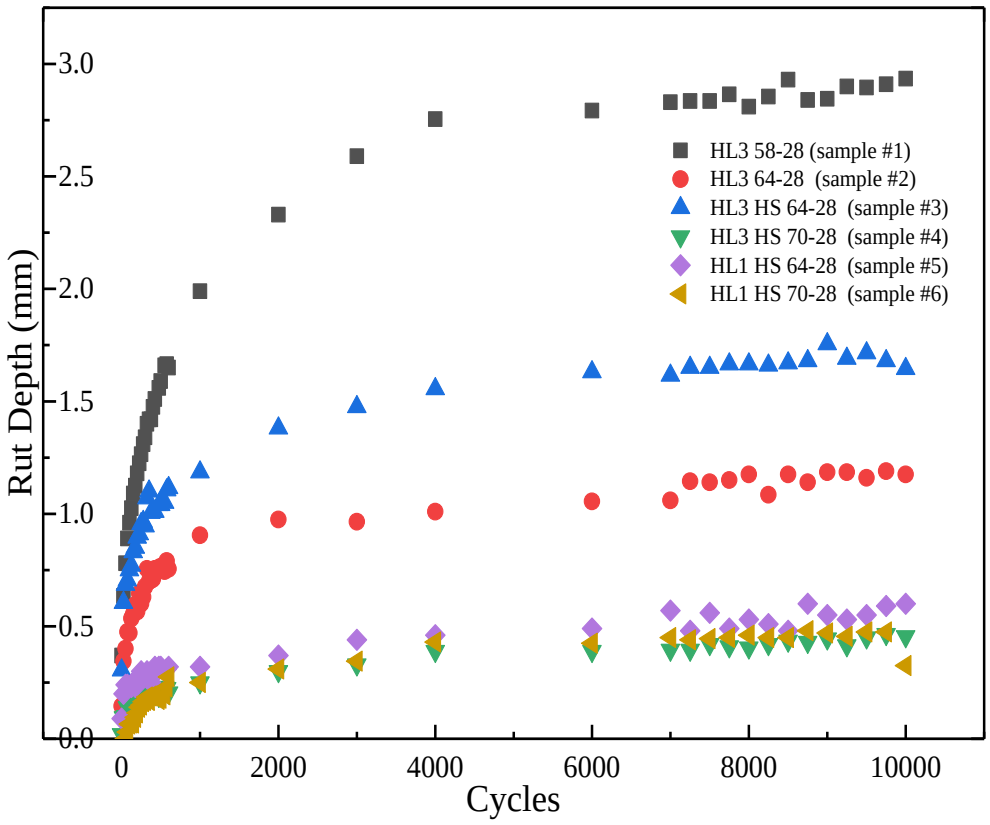

a. Rut Curve of HL Mixes

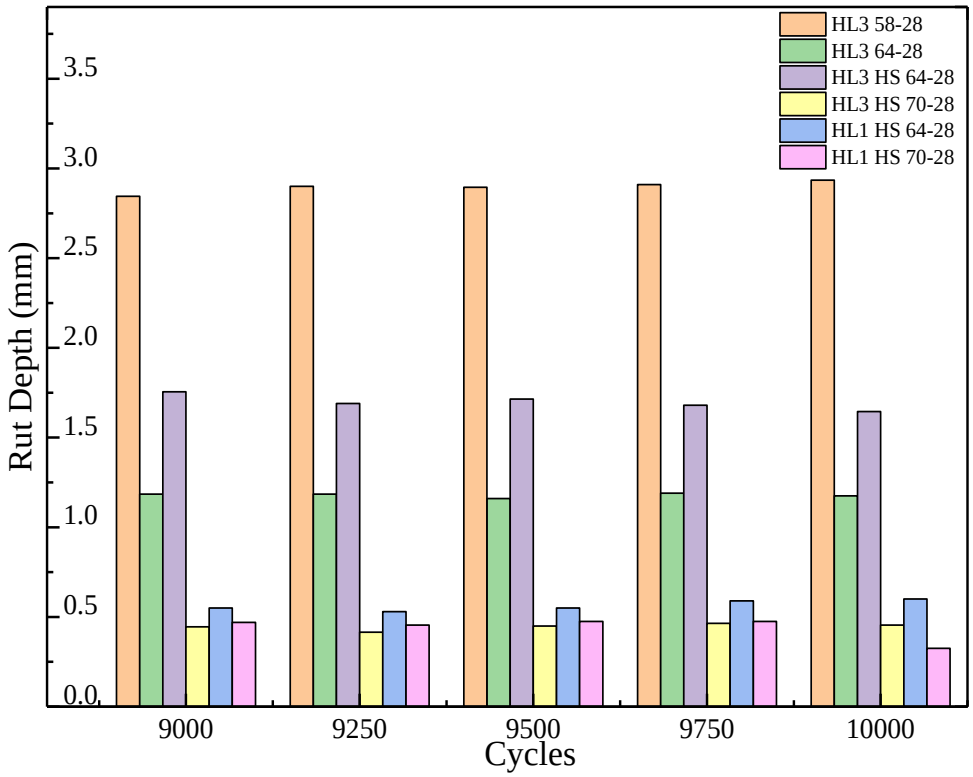

b. Rut Depth of HL Mixes

Figure 5-13 Hamburg Wheel Tracking Test Results

The results of HWTT are shown in Figure 5-13. Variables such as gradation type, asphalt binder performance grade, coarse aggregate content are all playing a role in the performance of asphalt mixture. Hot laid 3 High Stability (HL3 HS) with PG 70-28 and HL1 HS with PG 70-28 shows the most satisfactory rutting resistance and regular HL3 with PG 58-28 exhibits the least desirable rut depth.

5.2.5 Rut Performance and 2D Image Processing Indexes

Based on X-Ray CT scanning and post-processing technique, particle-related indexes such as the total area of particles, the number of particles, the average area of particles, the total perimeter of particles, the average perimeter of particles, aspect ratio, circularity, solidity, and roundness was plotted with the rut depth of six different types of asphalt mixtures in Figure 5-14. Indexes regarding air voids that were selected in the diagrams are the total area of voids, the average area of the voids, and the number of voids.

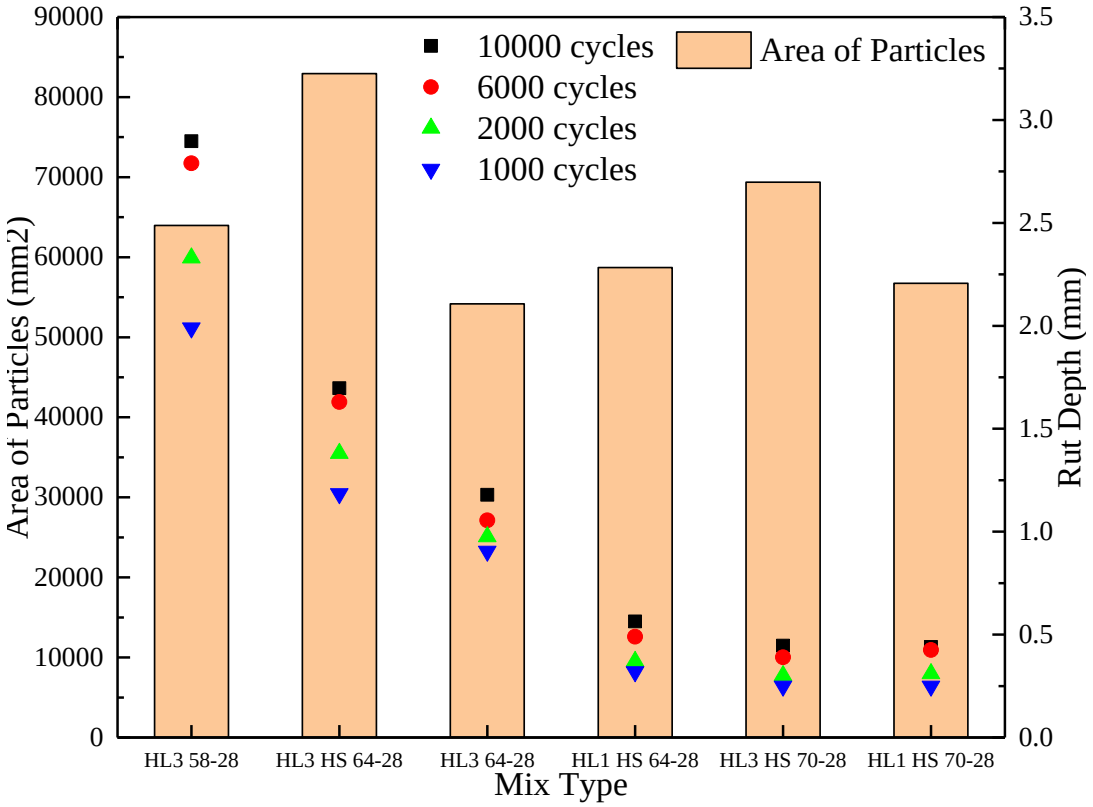

a. Rut Depth and Total Particle Area

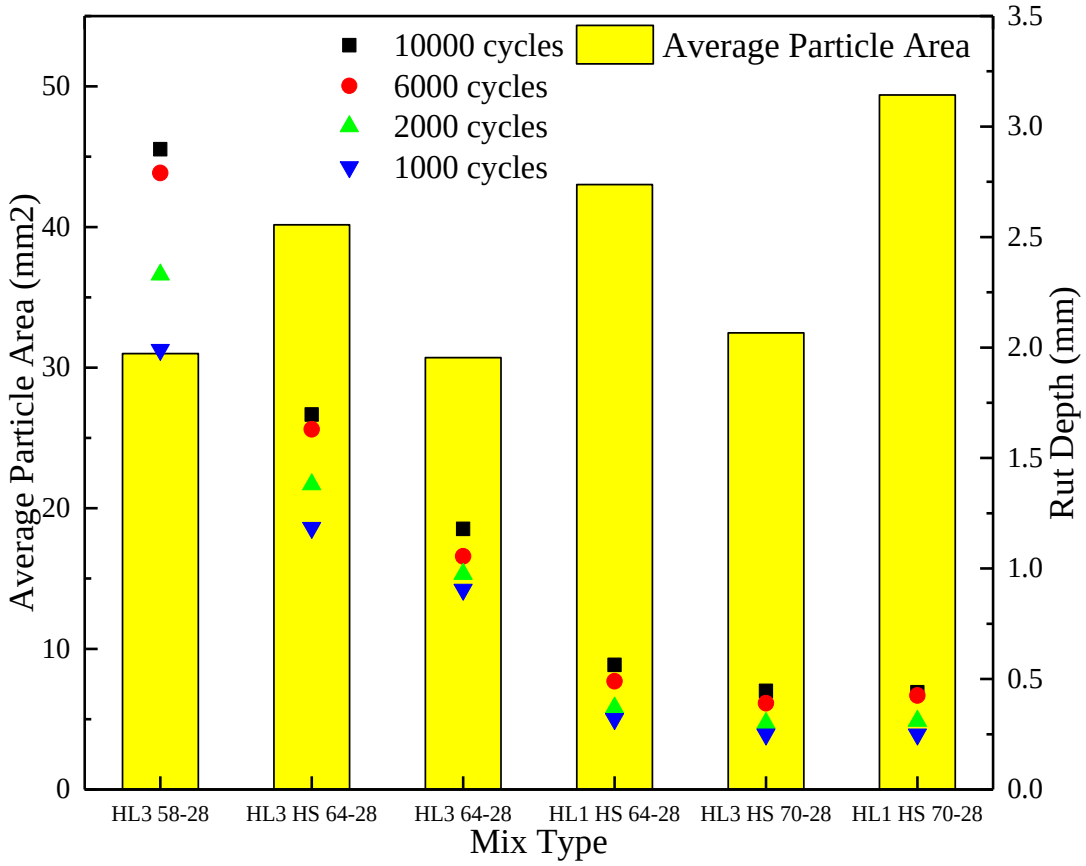

b. Rut Depth and Average Particle Area

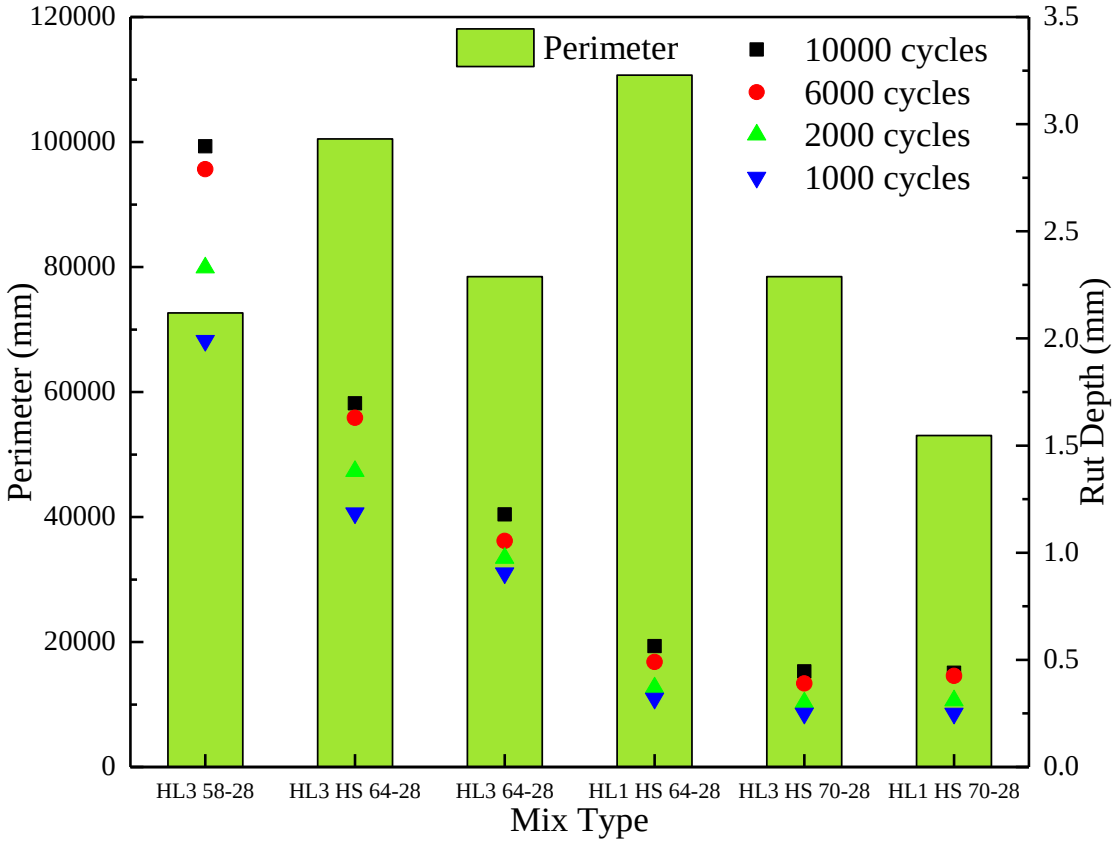

c. Rut Depth and Total Particles Perimeter

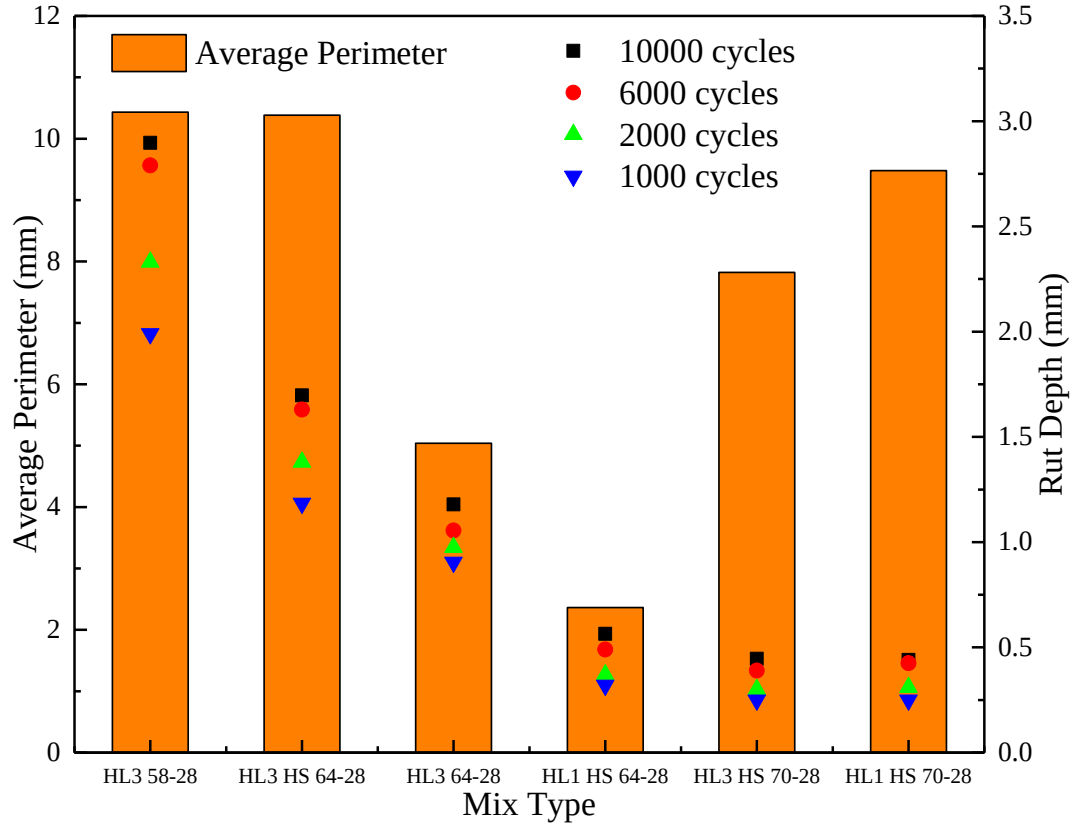

d. Rut Depth and Average Particle Perimeter

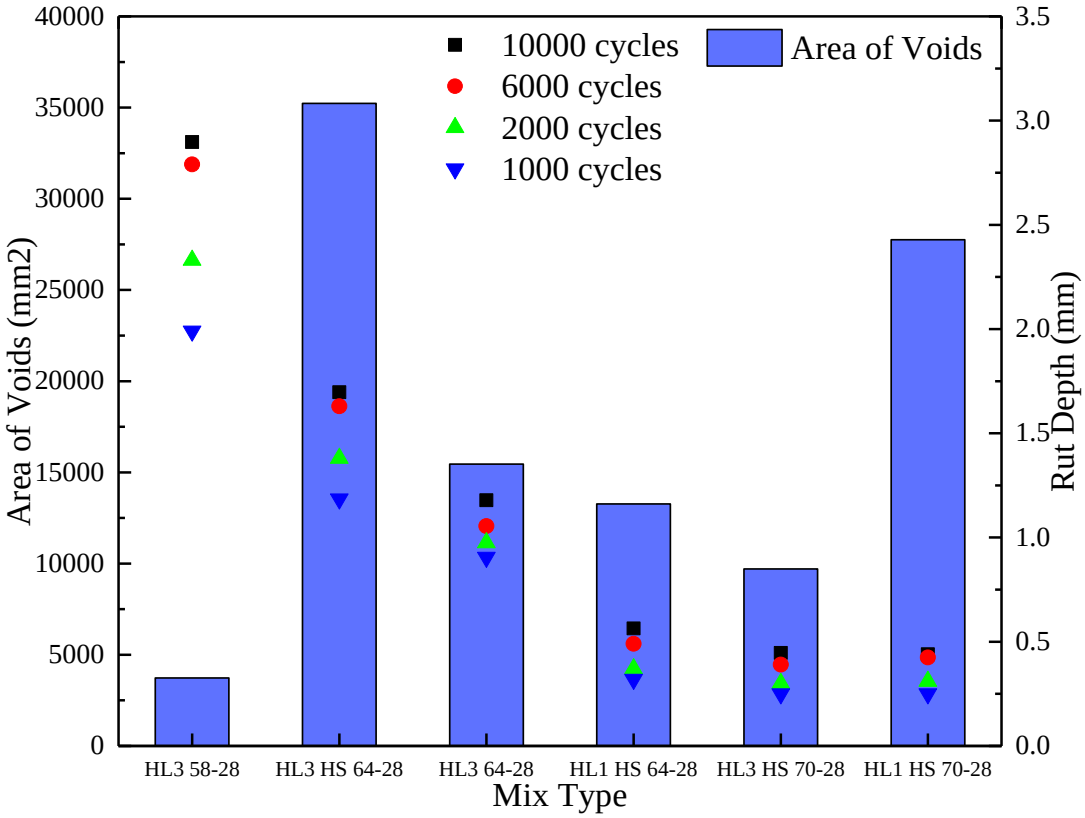

e. Rut Depth and Area of Voids

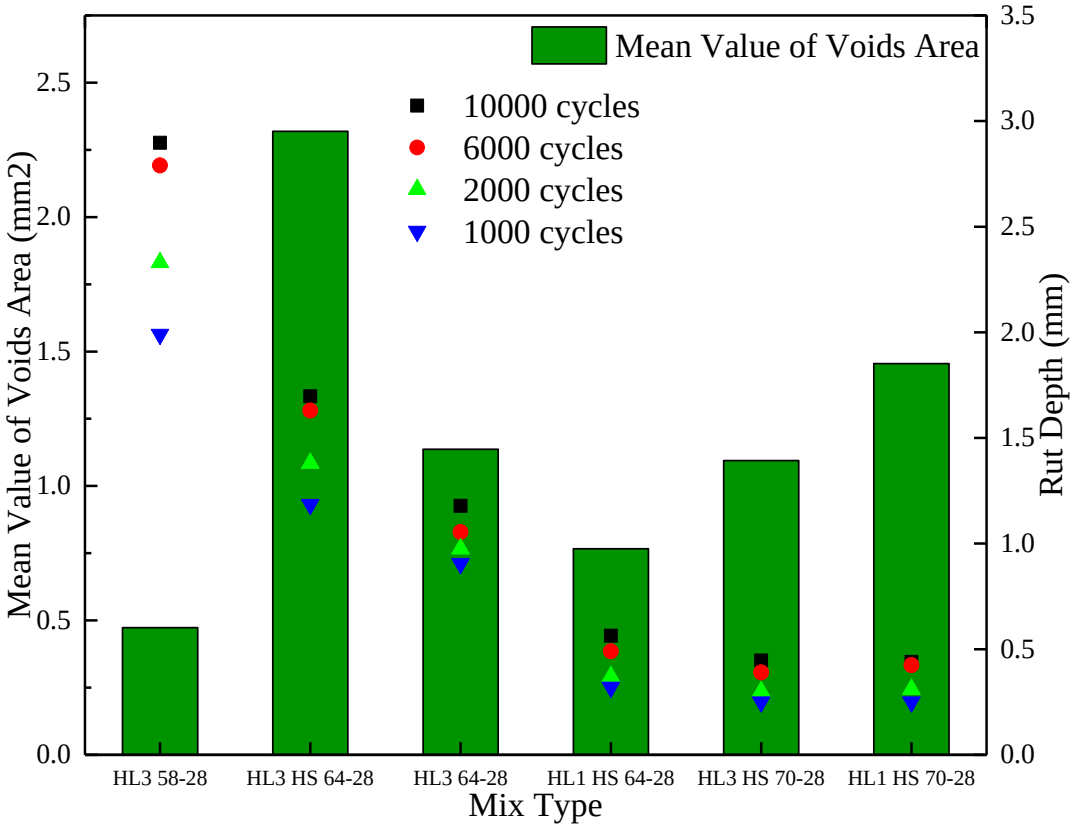

f. Rut Depth and Average Voids Area

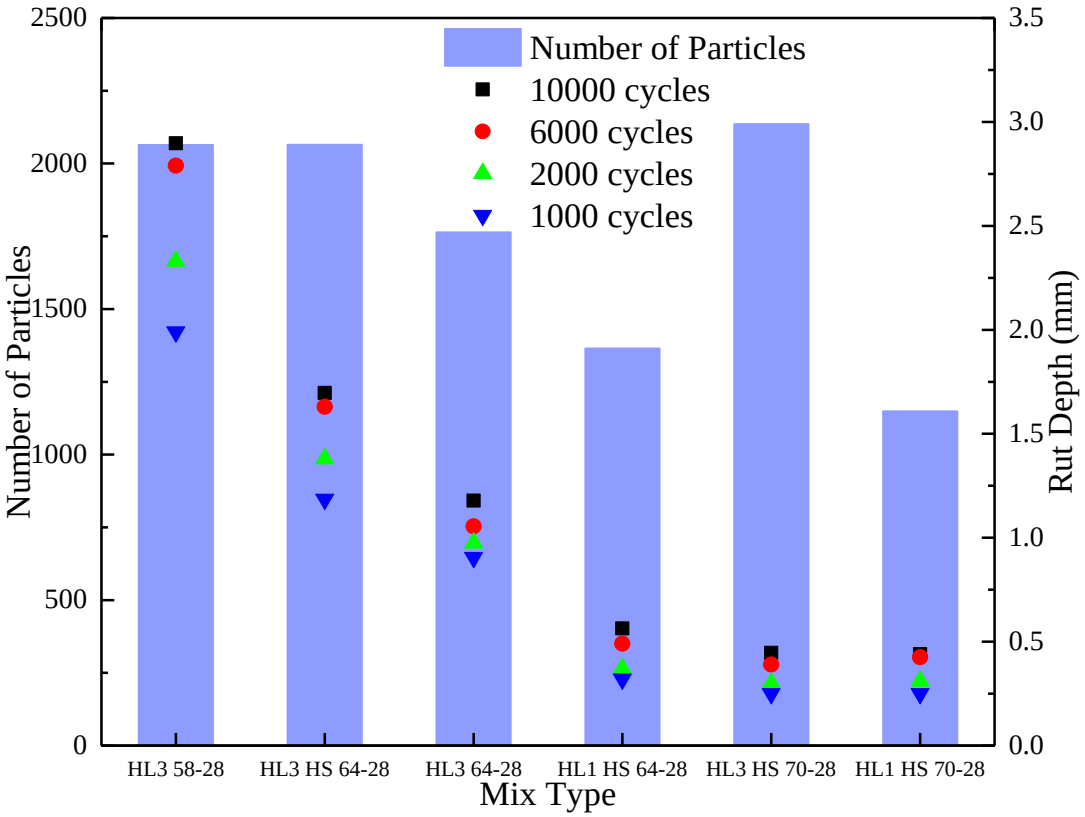

g. Rut Depth and Number of Particles

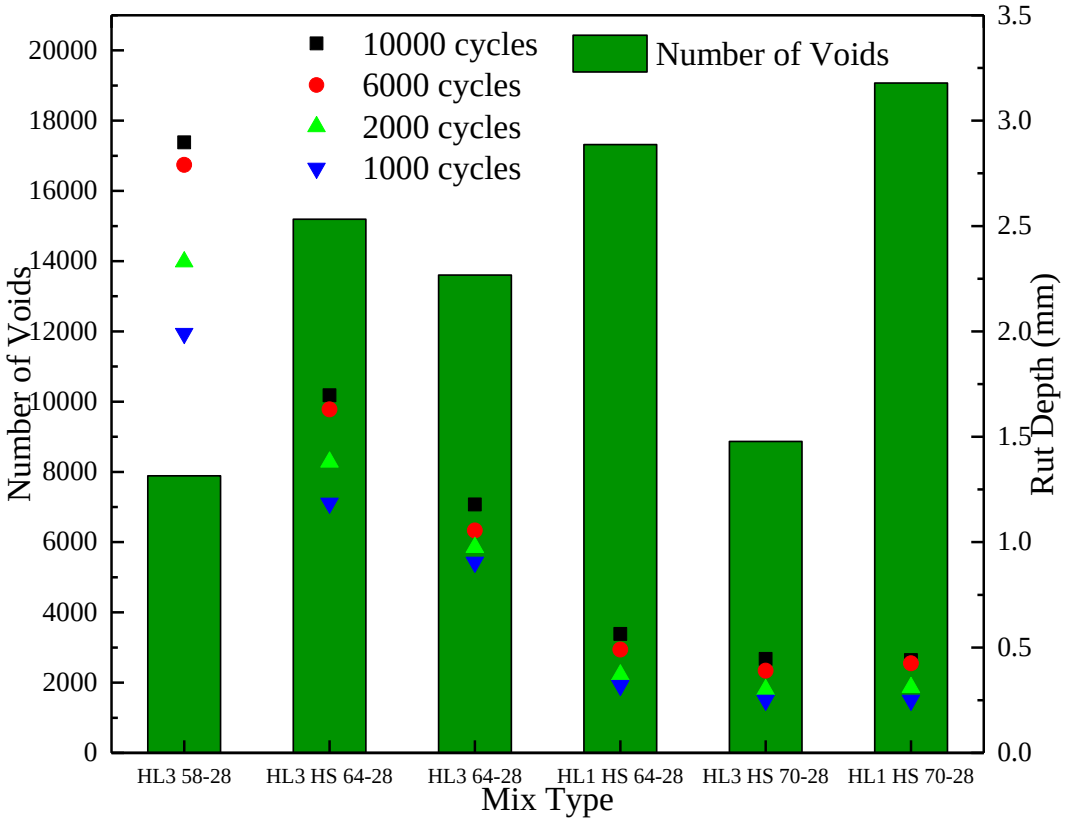

h. Rut Depth and Number of Voids

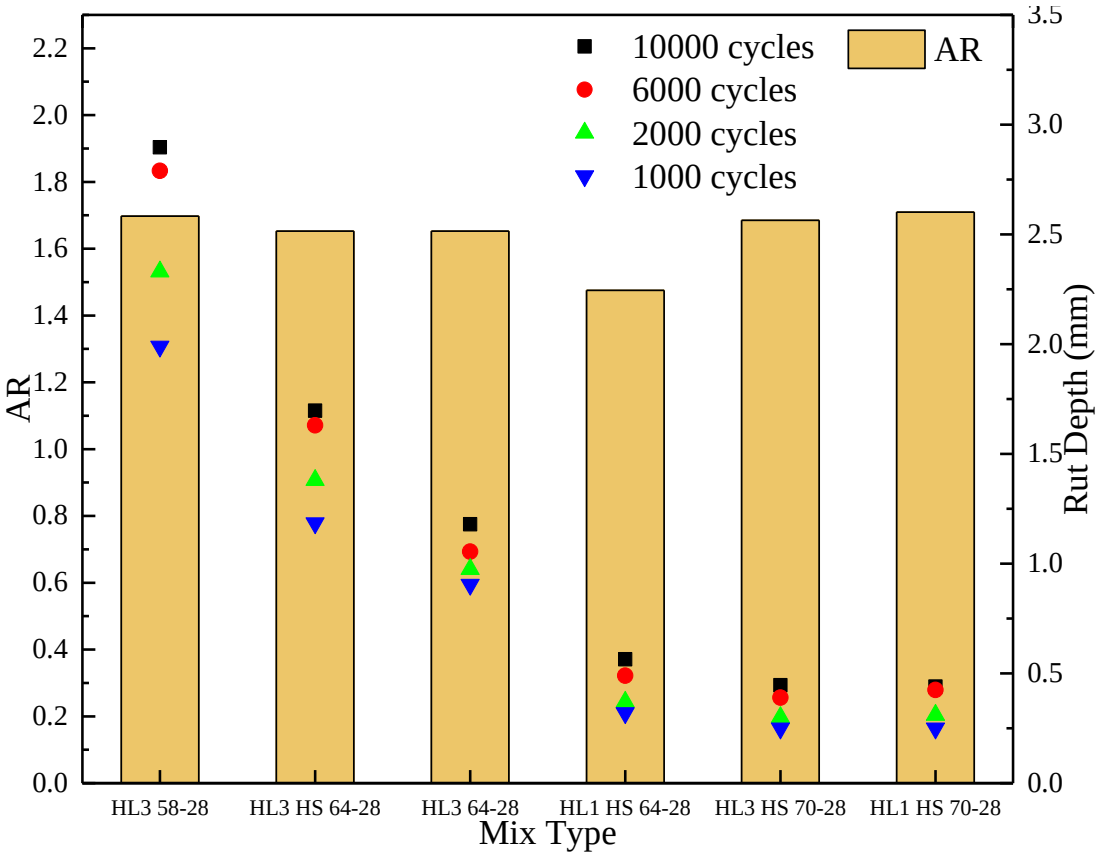

i. Rut Depth and Aspect Ratio

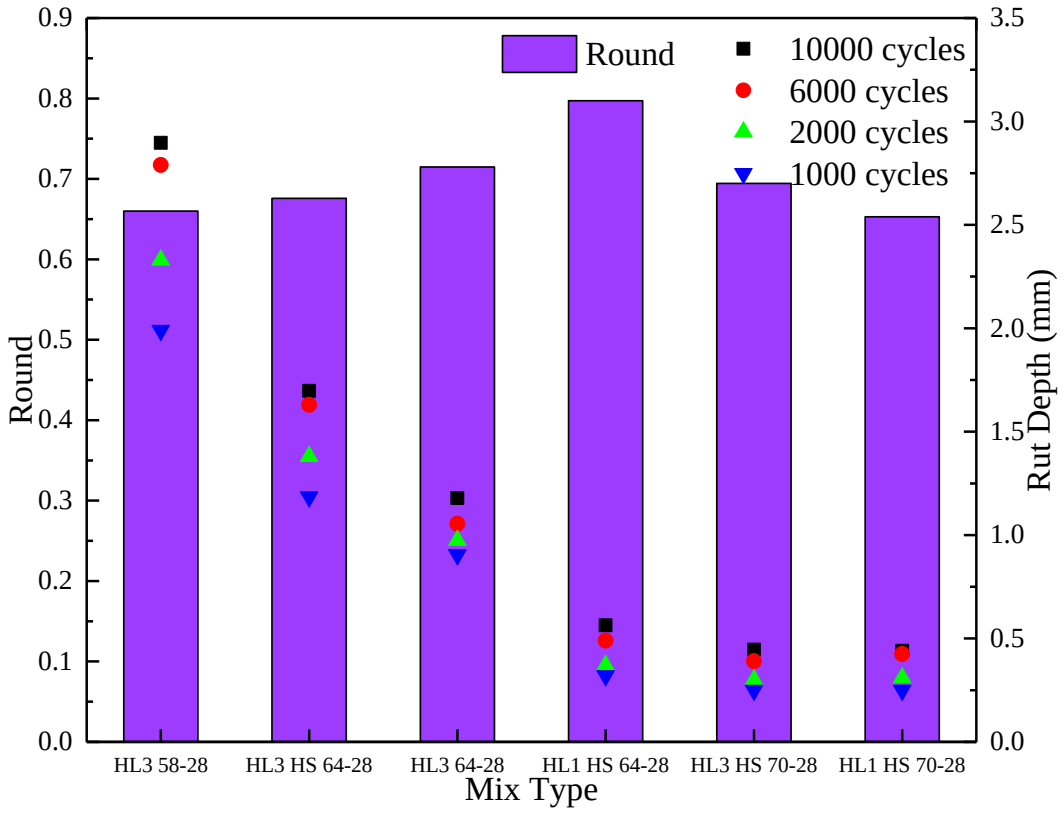

j. Rut Depth and Roundness

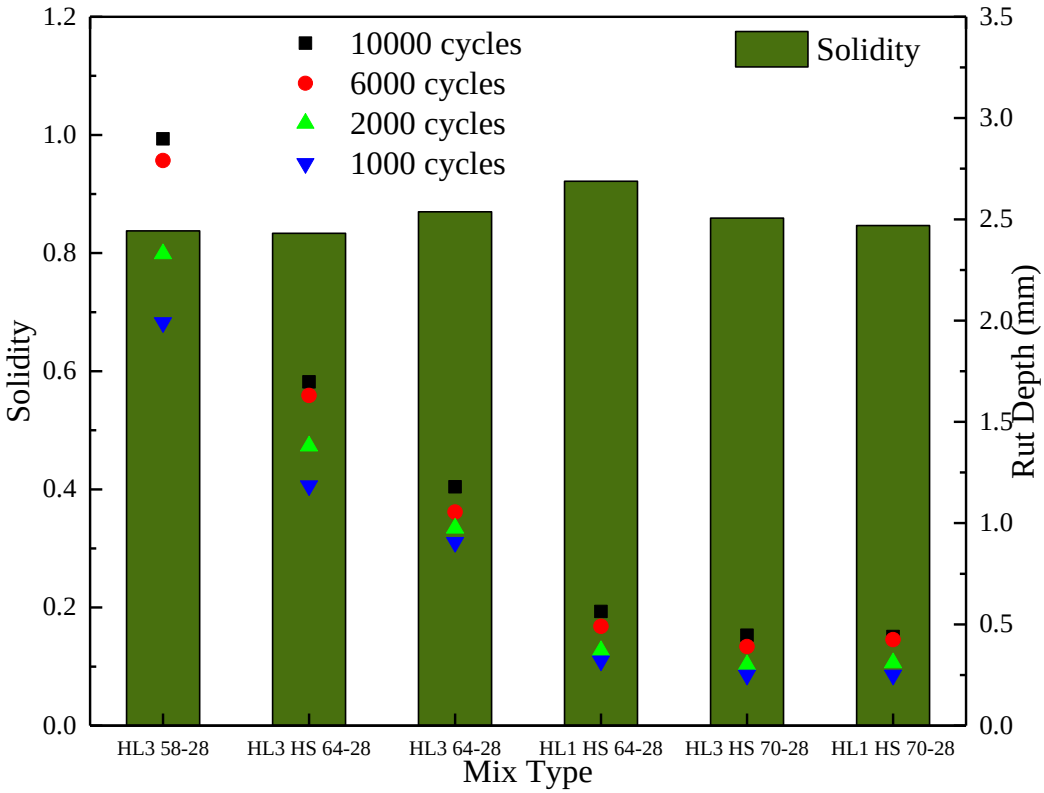

k. Rut Depth and Solidity

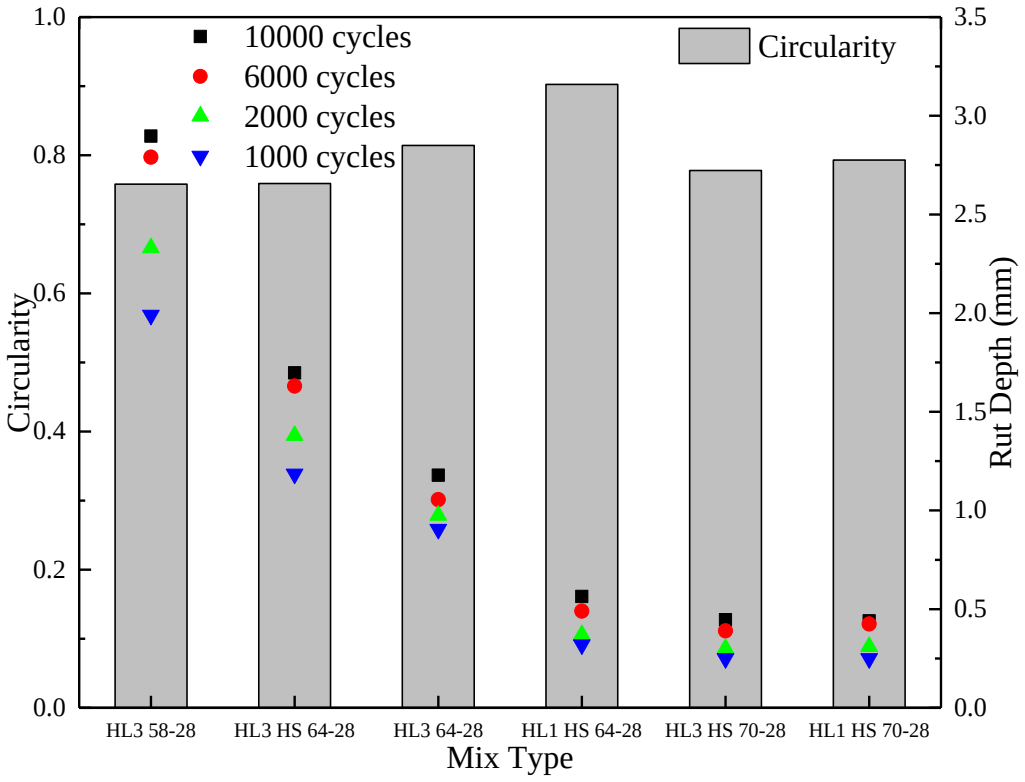

l. Rut Depth and Circularity

Figure 5-14 Rut Performance and Particle Indexes

As shown in Figure 5-14, the total area of all the analyzed particles for each type of mix is aligned with the rut depth of the corresponding mix. Rut depth increases with the increase of the total area of particles as shown in Figure 5-14.a. The average area of particles seemingly shows a negative correlation with rut depth, which decreases with the growth of the average area of particles as shown in Figure 5-14.b. The average area of particles is representing the overall size of aggregates. A larger average area means a bigger nominal aggregate size. Accordingly, Figure 5-14.b indicates that a larger nominal aggregate size can contribute to better rutting resistance. The rut depth does not correlate well with the total perimeters of all the particles and the average perimeter of each particle as in Figure 5-14.c and 5-14.d. Rut resistance is a cumulative permanent deformation of asphalt under long-term heavy loads. The compaction rate of asphalt pavement directly affects road performance. Air voids ratio is the indicator of an asphalt mixture compaction rate. Figure 5-14.e and 5-14.f illustrates that the air voids level and rut depth line up with each other except for HL1HS 70-28. The rut depth was also dependent on the number of particles and air voids except for HL1 HS 70-28. The selected four 2D shape indexes include aspect ratio, roundness, solidity, and circularity seem to not correlate well with the rut resistance of each mix. However, roundness, solidity, and circularity are highly correlated to each other.

Several elements might explain the unsatisfied correlation between rut depth level and imaged processed morphological indexes of particles and voids. Firstly, the rutting test used in this study is a single Linear Variable Differential Transformer (LVDT) captured test. Namely, the rut depth captured is purely relying on one data collection point. Under repeated wheel load applied on the testing specimen, coarse aggregates tend to dislocate due to asphalt stripping at the end of the test. The single data collection point, therefore, may not necessarily represent the actual rut depth of the corresponding asphalt mixture. Plus, as the HWTT is highly time-consuming, each test can take approximately 7 hours, thus each mix was only tested through two samples per test. Secondly, the image binary processing may misrecognize the small particles and voids. The technology used in this

study only extracts particles and voids, thus it is highly possible that a particle of which area is smaller than 1 mm^2 can be recognized as a void or the opposite situation may occur as well. These small particles and voids are difficult to accurately distinguish through the binary process and thus can significantly affect the overall morphological index distributions. Thirdly, the purpose of using 2D processed images through X-CT scanning is to correlate volumetric properties of asphalt mixture to the road performance without considering the impact from binder types. The rutting resistance performance is affected by the binder types, volumetric parameters, as well as their combined effect.

5.3 Summary

Throughout the Hamburg Wheel Tracking Testing and X-Ray CT scanning as well as MATLAB image processing, the rut resistance of typical Ontario road applied asphalt materials were evaluated. The morphological properties of 2D scanned images corresponding to these mixtures were processed and quantitively analyzed. The main findings can be concluded as follows:

1. Machine learning technology (MLT) was used to segmentize the particles and voids, among various supervised learning methods, Fast-Random-Forest (FastRF) is adapted in this study. Through the binary process, the particles, asphalt binder, and voids were obtained.
2. Four morphological indexes were introduced in analyzing the 2D shapes of particles: aspect ratio, roundness, solidity, and circularity. Among the four indexes, only roundness has a skewness value less than ± 0.5 and therefore is considered symmetrically distributed. The skewness of circularity and solidity is less than 1 and is treated as moderately skewed. The aspect ratio is highly skewed as its skewness is greater than 1.
3. From the particle processed images, the majority of particles' perimeter and the area are less than 10 mm and 10 mm^2. The number of particles drastically decreases when the perimeter is greater than 10 mm and the area is greater than 10 mm^2. All

six samples follow the same pattern. Sample #5 shows a higher roundness and solidity level. The processed images from lab-produced and plant-produced mix have a similar distribution according to the major axis of particles. While aggregate gradation distribution shows the opposite trend to major axis particle distribution, which demonstrated that the distribution of image processed particles based on the major axis does not reflect the gradation curve.

4. The voids distribution of processed images shows consistency in perimeter and area for all six mixes. More than 60 percent of the voids have less than 1 mm^2 in the area for all the processed images. However, the void distributions of all the mixes show a similar pattern in perimeter from 0 to 10 mm. The number of voids decreases with the increase of the area and perimeter ranges.
5. The relationship between rutting depth and morphological indexes is not satisfied. The possible explanations include whether the rut test can represent the actual stiffness of the corresponding asphalt mixture, the binary process might misrecognize the small particles and voids, the analysis ignored the effect of asphalt binder impact, and the combined impact of volumetric parameters and binder types.

Chapter 6
EVALUATING RUTTING RESISTANCE OF CANADIAN ASPHALT MIXTURES APPLIED ON ROADWAY AND AIRPORT UNDER FREEZE-THAW CYCLES AND DE-ICING AGENT

6.1 Materials

6.1.1 De-icing Chemicals

The de-icing chemical used in this study is liquid potassium acetate, which is being used at Region of Waterloo International Airport. The physical and chemical properties of potassium acetate in solid and 50% concentration are shown in Table 6-1, the appearance of two forms of potassium acetate is displayed in Figure 6-1.

Table 6-1 The Physical and Chemical Properties of Potassium Acetate

Solid (ScienceLab.com, 2013)		50 % Concentration (Harmoney Deicing Product, 2020)	
Physical State and Appearance:	Solid	Appearance:	clear, blue liquid
Molecular Weight:	98.14 g/mole	Biochemical Oxygen Demand (5-day):	0.25
Color:	White	Water Miscibility:	Complete
pH: (1% soln/water):	10 [Basic.]	pH:	9~11
Boiling Point:	Decomposes	Active Ingredients:	50%
Melting Point:	292c (557.6F)	Freezing Point:(F)	-72
Specific Gravity:	1.57 (Water =1)	Specific Gravity:	1.282

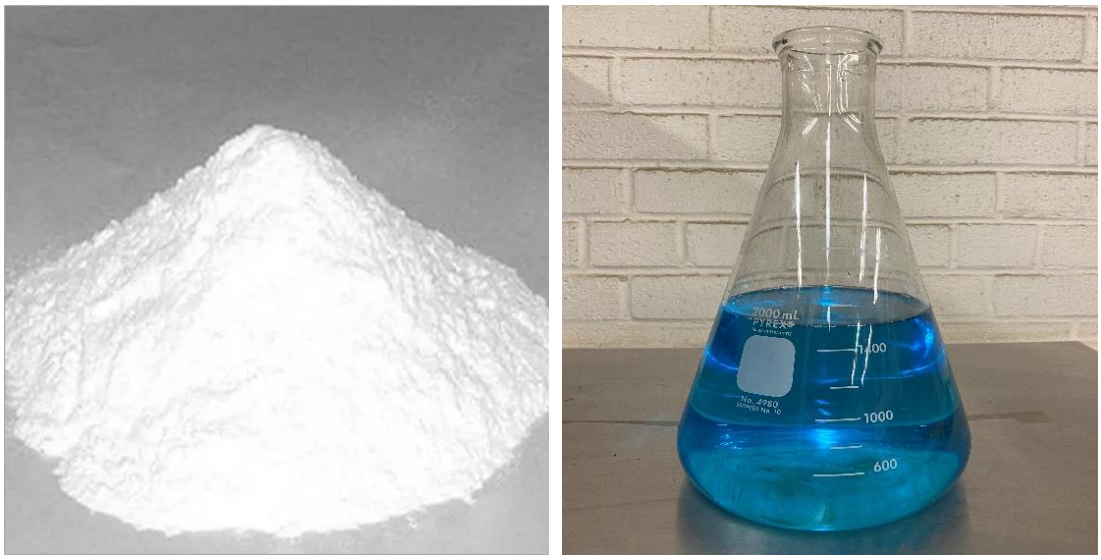

a. Solid State

(Akash Purochem Pvt. Ltd, 2020)

b. Liquid State

Figure 6-1 Potassium Acetate in Different Forms

6.1.2 Asphalt Mixtures

Two types of asphalt mixture were collected from the PAVE-AL Limited construction site for taxiways resurfacing of Lester B. Pearson International Airport, air-surface (AS), and air-base (AB). Three kinds of highway applied asphalt mixture in Ontario, Canada, were also used in this study, Hot Laid 3 (HL3), Hot Laid 3 High Stability (HL3 HS), and Hot Laid 1 High Stability (HL1 HS).

The asphalt binders assigned to these mixtures are varying. For airport mixes, Performance Grade (PG) 70-28 J was used in the surface course mix, and PG 64-28 was added in the lower course mix. For road mixes, PG 64-28 was used in HL3 and HL1 HS mixes, and PG 70-28 was for HL3 HS. Notably, all the road mixes used in this study are laboratory-produced while the airport mixes were fabricated in the plant. The Job Mix Formula (JMF) and asphalt content (AC) of the five different mixes are shown in Table 6-2 and Figure 6-2.

Table 6-2 Asphalt content and Job Mix Formula of Tested Mixture

% AC	Mix Types	26.5	19	16	13.2	9.5	4.75	2.36	1.18	0.6	0.3	0.15	0.075
5.2	AS	100	100	100	98	80.3	54.3	38.7	25.3	17.5	10.3	5.5	3
5.2	AB	100	95.6	89.4	81.9	66.9	48.2	38.1	25.5	16.2	10.1	6.6	4.7
5.1	HL3	100	100	100	100	84.1	58.4	42.4	31.4	21.5	10.2	5.4	3.8
5	HL3 HS	100	100	100	98.9	85.1	58.2	45.8	28	18.8	10.1	6.9	4.7
5.5	HL1 HS	100	100	100	100	81.9	61	55.9	34.2	18.4	10.1	5.9	4.1

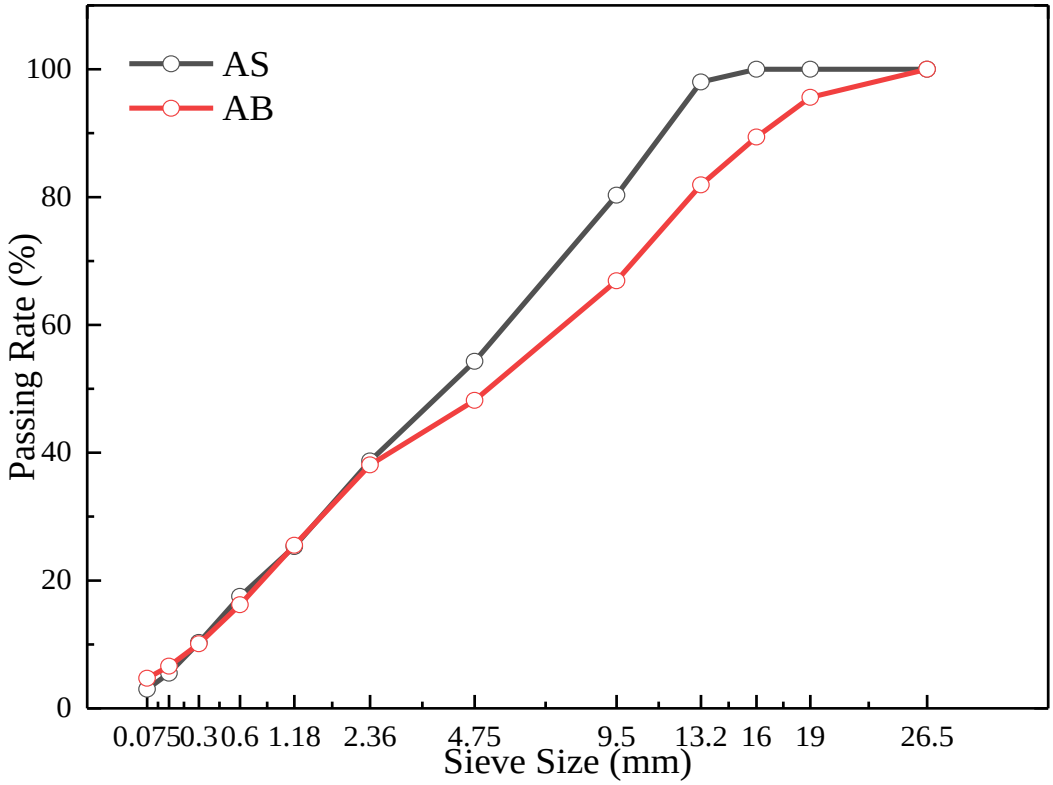

a. Airport Pavement Mixes

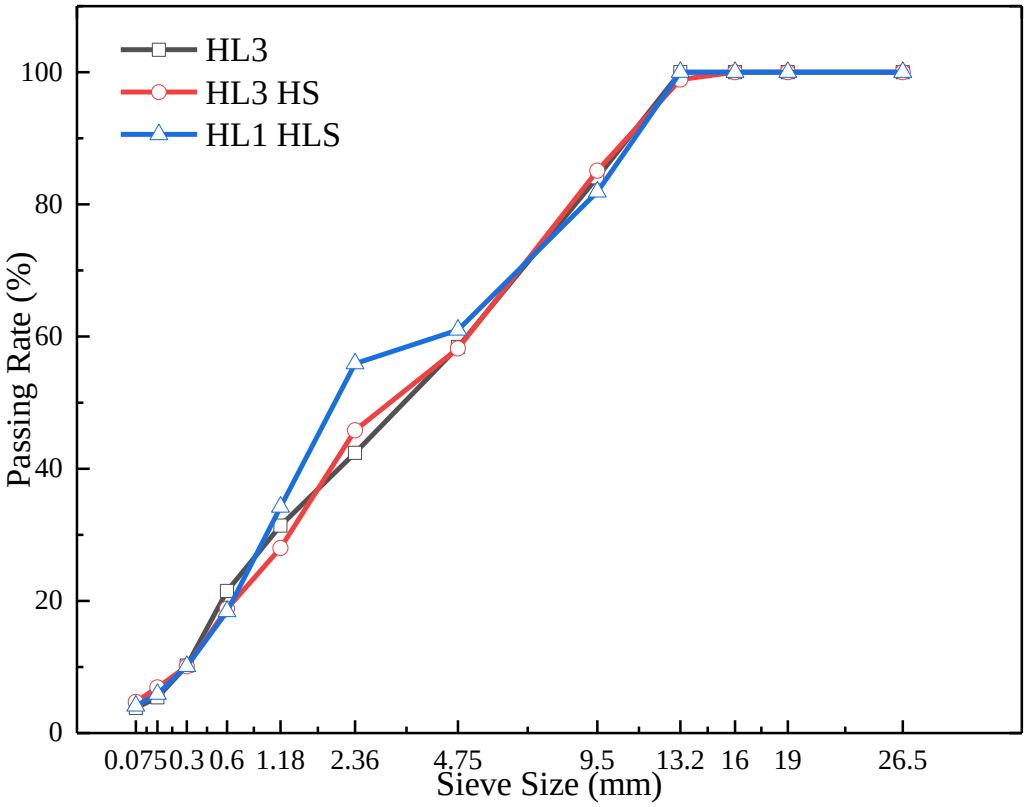

b. Highway Pavement Mixes

Figure 6-2 Aggregate Gradation for Five Tested Mixtures

6.2 Experimental Programs

6.2.1 Specimen Preparation

For the airport mixes fabricated in the plant, the compaction shall conduct once the loose mix reaches its compaction temperature, which is 147°C and 144°C for the surface course and lower course, respectively. For roadway mixes, they should be oven conditioned for 4 hours ± 5 minutes at 135 ± 3°C following the short-term conditioning procedures specified in AASHTO R30 (AASHTO, 2013c).

Cylindrical specimens with a diameter of 150 mm and 63 mm in height were compacted in a gyratory compactor by height-control mode. AASHTO T324 has a wide range of height requirements (38 mm – 100 mm) (AASHTO, 2016), however, the mold for HWTT was used by different road agencies and research institutions vary in terms of specimen's height. Air voids ratio is the dominant factor to determine if an asphalt specimen is eligible for mechanical properties tests. According to AASHTO T 324, for

laboratory-produced and plant-produced mixes, 7 ± 0.5 % of targeted air voids) were recommended for laboratory-compacted cylindrical specimens. Using height-control mode makes air voids control easier compared to gyrations-control mode as the mass of mixture needed to obtain a targeted air voids ratio can be back-calculated based on Maximum Theoretical Relative Density of loose mix. The specimen preparation procedures and air voids ratio of all the five mixes are shown in Figure 6-3 and Table 6-3.

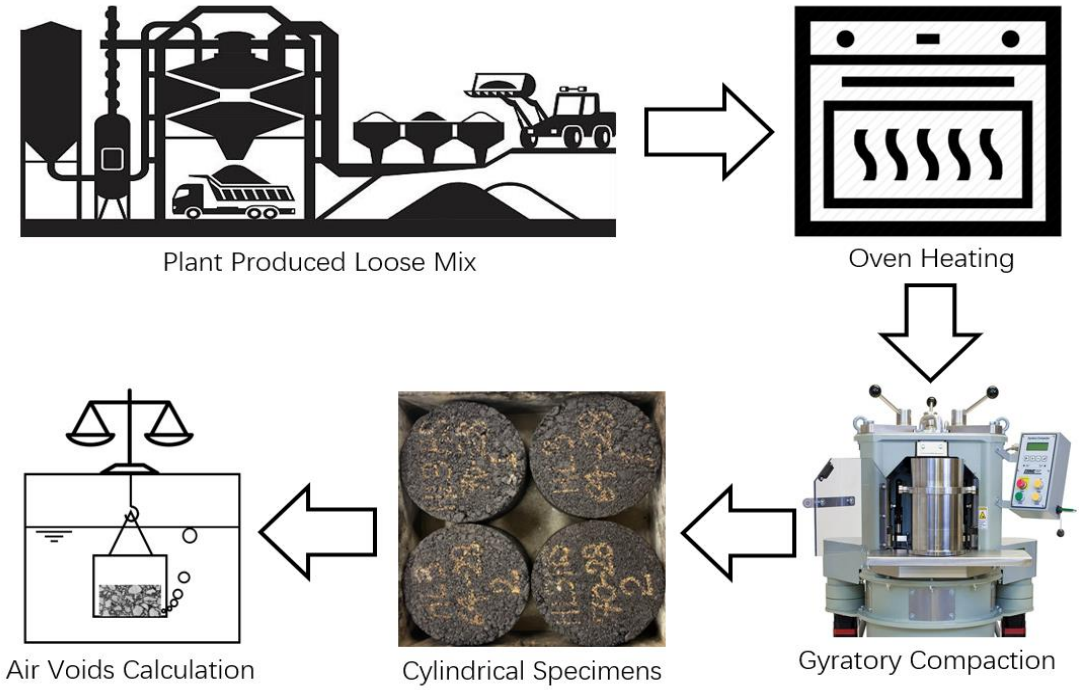

Figure 6-3 Specimen Preparation in Laboratory

Table 6-3 Target Air Voids of Tested Mixes

Mixes	A[1]	B[2]	C[3]	BRD[4]	MRD[5]	Air Void Ratio (%)[6]
AS	2651.4	2664.7	1581.8	2.448	2.638	7.18
AB	2551.1	2563.9	1487.8	2.371	2.558	7.32
HL3	2504.3	2518.4	1434.9	2.311	2.478	6.72
HL3 HS	2571.3	2591.8	1491.9	2.338	2.518	7.15
HL1 HS	2653.2	2664.2	1567.3	2.419	2.607	7.21

Note:

1. A = mass of the specimen in air, g.

2. B = the mass of the specimen in water, g.

3. C = the mass of the specimen after the saturated surface dried, g.

4. BRD = Bulk Relative Density, g/cm^3.

$$BRD = \frac{B}{A-C}$$ (AASHTO, 2013)(ASTM, 2019a)

5. MRD = Theoretical Maximum Relative Density, g/cm^3,

MRD is calculated following procedures specified in AASHTO T209 or ASTM D2041 (AASHTO, 2013e)(ASTM, 2019b)

6.2.2 Specimen Treatments

In order to understand the effect of the freeze-thaw cycle, de-icing liquid, as well as the combination of freeze-thaw and de-icing liquid to permanent deformation resistance of airport-used and road-used asphalt mixture, four experimental groups were designed based on their treatment methods. Group 1 was set as the experimental control group, all the specimens were directly tested for HWTT after checking the air voids ratio. No freeze-thaw was applied for specimens. For group 2, the specimens were submerged into potassium acetate liquid and vacuumed for 10 minutes. Therefore, all the air voids were saturated with de-icer. After the vacuuming, the specimens were soaked in potassium acetate liquid for 40 hours before HWTT. The treatment of group 3 was adapted from Resistance of Compacted Hot Mix Asphalt (HMA) Moisture-induced damage in AASHTO T 283 (AASHTO, 2013d). The specimens were saturated with water by the de-airing process as in Group 2. After the specimens were saturated with water, they were transferred to a freezer at -18 °C for 16 hours, and then into a water tub at 60 °C for 24 hours before conducting the HWTT test. Specimens in group 4 were treated in the same way as group 3 except that the de-airing process used potassium acetate, the specimens were saturated with de-icer instead of water before they went through a freeze-thaw cycle. The HWTT test followed the procedures specified in

AASHTO (AASHTO, 2016). For a high level of water or de-icer saturation, the saturation degree for groups 3 and 4 was calculated by weighing the mass before and after the vacuuming. The saturation degree for those two groups is shown in Table 6-4, and the treatment procedures of all the groups are shown in Figure 6-4.

Table 6-4 Degree of Saturation for Airport and Roadway Mixes

Groups	Mix Type	Pa[1]	E[2]	Va[3]	B'[4]	A[5]	M'[6]	J'[7]	S'[8]	Average
Group 3	HL3	6.72	1113.30	74.81	2586.80	2513.70	73.10	73.10	97.71	100.9171
					2577.00	2499.10	77.90	77.90	104.13	
	HL3 HS	7.15	1113.30	79.60	2628.30	2558.00	70.30	70.30	88.32	84.42095
					2646.90	2582.80	64.10	64.10	80.53	
	HL1 HS	7.21	1113.30	80.27	2707.70	2607.30	100.40	100.40	125.08	124.0827
					2699.40	2600.60	98.80	98.80	123.09	
	AS	7.18	1113.30	79.94	2718.10	2654.50	63.60	63.60	79.56	90.07309
					2712.90	2632.50	80.40	80.40	100.58	
	AB	7.32	1113.30	81.49	2637.30	2603.40	33.90	33.90	41.60	43.07081
					2633.70	2597.40	36.30	36.30	44.54	
Group 4	HL3	6.72	1113.30	74.81	2590.30	2476.60	113.70	88.69	118.55	112.4996
					2620.00	2517.90	102.10	79.64	106.45	
	HL3 HS	7.15	1113.30	79.60	2654.10	2555.10	99.00	77.22	103.22	95.51078
					2675.40	2585.80	89.60	69.89	87.80	
	HL1 HS	7.21	1113.30	80.27	2731.50	2604.40	127.10	99.14	124.55	127.2371
					2740.90	2607.20	133.70	104.29	129.93	
	AS	7.18	1113.30	79.94	2719.60	2624.50	95.10	74.18	92.42	91.63261
					2714.10	2621.00	93.10	72.62	90.85	
	AB	7.32	1113.30	81.49	2639.00	2569.50	69.50	54.21	67.82	77.70053
					2630.70	2539.20	91.50	71.37	87.58	

Note:

1. Pa = air voids, percent.
2. E = Volume of the specimen, cm^3.
3. Va = Volume of the air voids, cm^3.

$$V_a = \frac{P_a E}{100}$$

4. B’ = Mass of the saturated, surface-dry specimen after partial vacuum saturation, g.
5. A = Mass of the dry specimen, in air, g.
6. M’ = Mass of the liquid, g.
7. J’ = Volume of the absorbed liquid, cm^3.

$$J' = B' - A$$

8. S’ = degree of saturation, percent.

$$S' = \frac{100J'}{V_a}$$

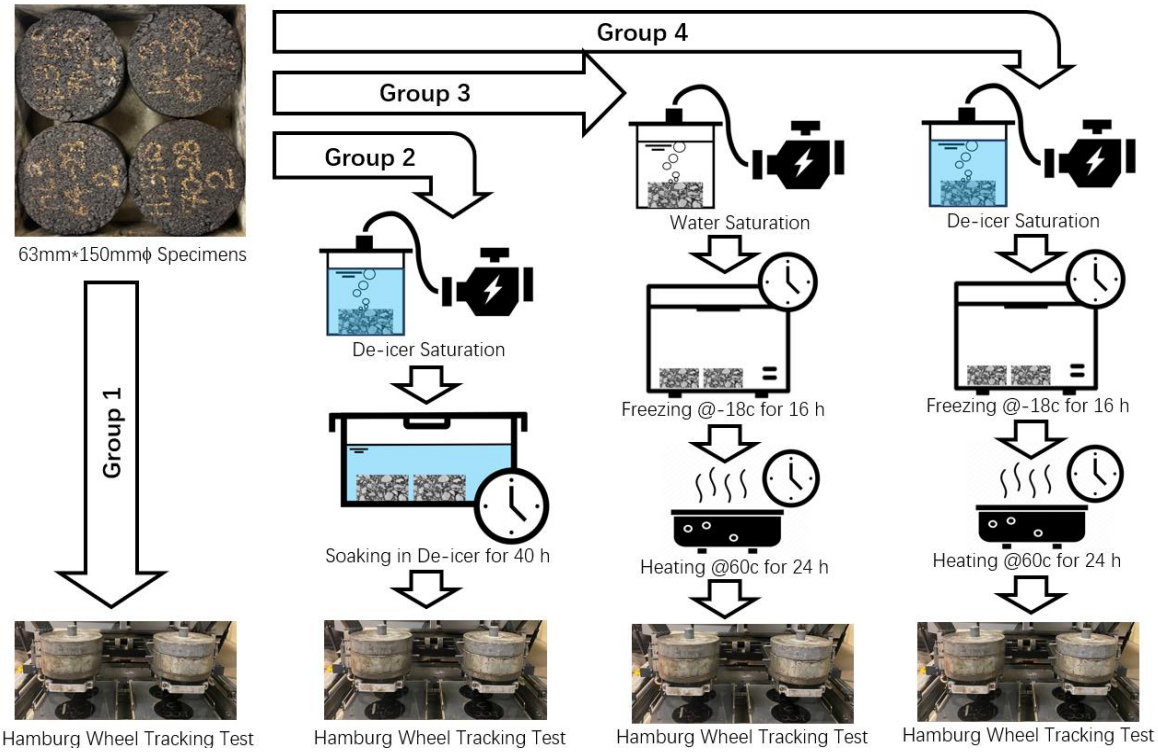

Figure 6-4 Specimens Treatment Before HWTT

6.3 Results and Discussions

6.3.1 Effects of Treatments on Rutting Performance

The HWTT results for the surface course and lower binder course mixes are shown in Figure 6-5, which shows that all the treatments had a significant impact on overall rut depth as well as rut depth propagation. For airport surface course mix, it shows from Figure 5.a that de-icer has an impact on the overall stiffness of asphalt mixture. After 1,000 cycles, the rut depth of the de-icer treated group is 1 mm deeper than the

controlled group that has 1.5 mm total rut depth. This indicates that potassium acetate liquid might have an effect of reducing the stiffness of asphalt mix. Moreover, the rutting depth of the de-icer treated group shows a more unstable trend at the end of the test, which indicates that the aggregate right underneath the rut depth probe has relocated as a result of shear stress. This proves that potassium acetate could induce stripping. Figure 6-5.b shows a similar trend whereas, for lower course mixes, the effect of de-icer shows a more severe impact for rut depth. This impact is greater than the effect of the freeze-thaw cycle while for airport surface the effect freeze-thaw has the most influence.

When the combination of freeze-thaw cycle and de-icer was applied to the specimens, the impact is between that of pure de-icer and the freeze-thaw cycle treated groups separately. It seems using potassium acetate during extreme weather conditions can mitigate the impact of moisture-induced damage.

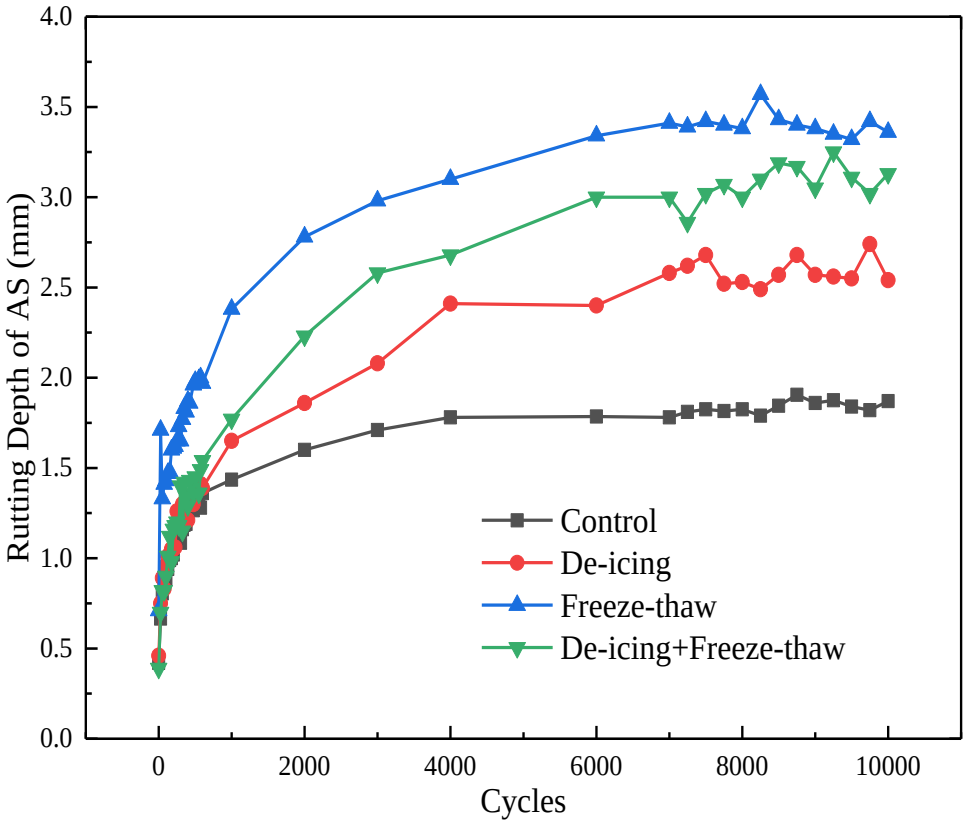

a. Rut Depth of Airport Surface Course

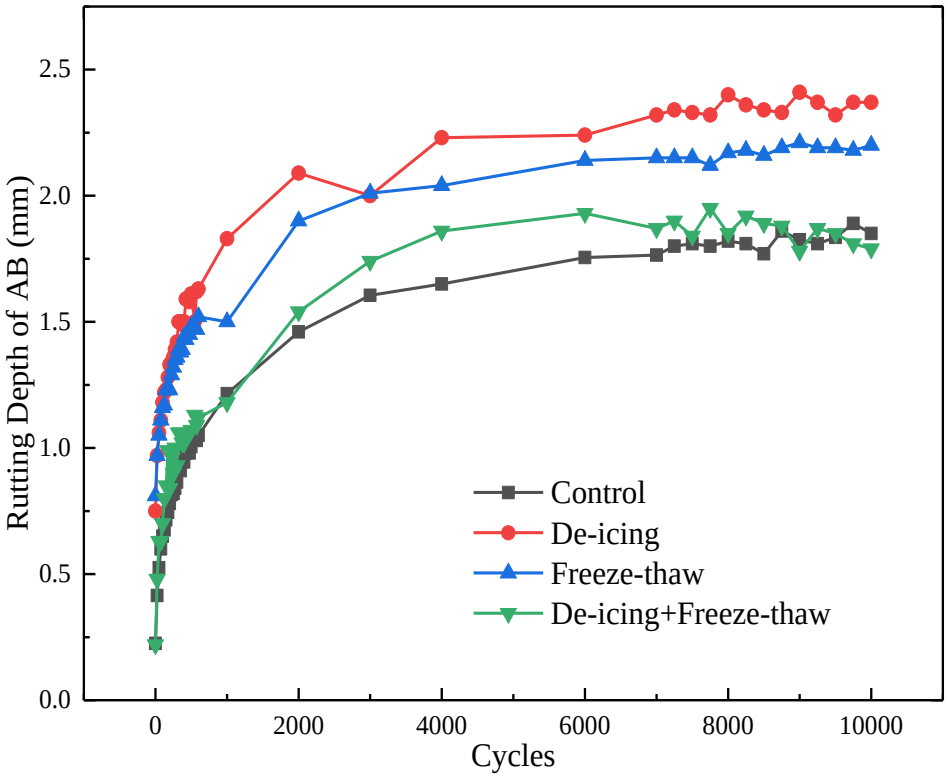

b. Rut Depth of Airport Lower Binder Course

Figure 6-5 Effects of Different Treatments to Airport Mixes' Rut Depth

For roadway mixes showed in Figure 6-6, the increased rate of rutting depth drops with the increase of wheel passes, more than 80 percent of rut occurs at first 2000 cycles. Among all the experimental groups, the control groups show the lowest rut depth for all three types of mixes. Freeze-thaw shows the most significant impact for rut resistance in HL3 HS and HL1 HS while the combination of freeze-thaw and de-icer shows the most influence. Figure 6-6.a – 6-6.d show that the rutting depth curve is significantly affected by the treatment of potassium acetate and freeze-thaw cycle, separately. Similar to airport mixes, roadway asphalt mixture also shows a high frequency of oscillation at the end of each rutting curve, which indicates that potassium acetate, freeze-thaw treatment can cause potential stripping. Figure 6-6.d shows that compared with freeze-thaw cycles, potassium acetate shows a mild impact on rutting resistance on asphalt mixture. The combined effect of potassium acetate and freeze-thaw cycles could potentially mitigate the adverse effect of de-icer and freeze-thaw cycles to asphalt mixture's stiffness, respectively, which is less than the freeze-thaw cycles group and greater than that of de-icer.

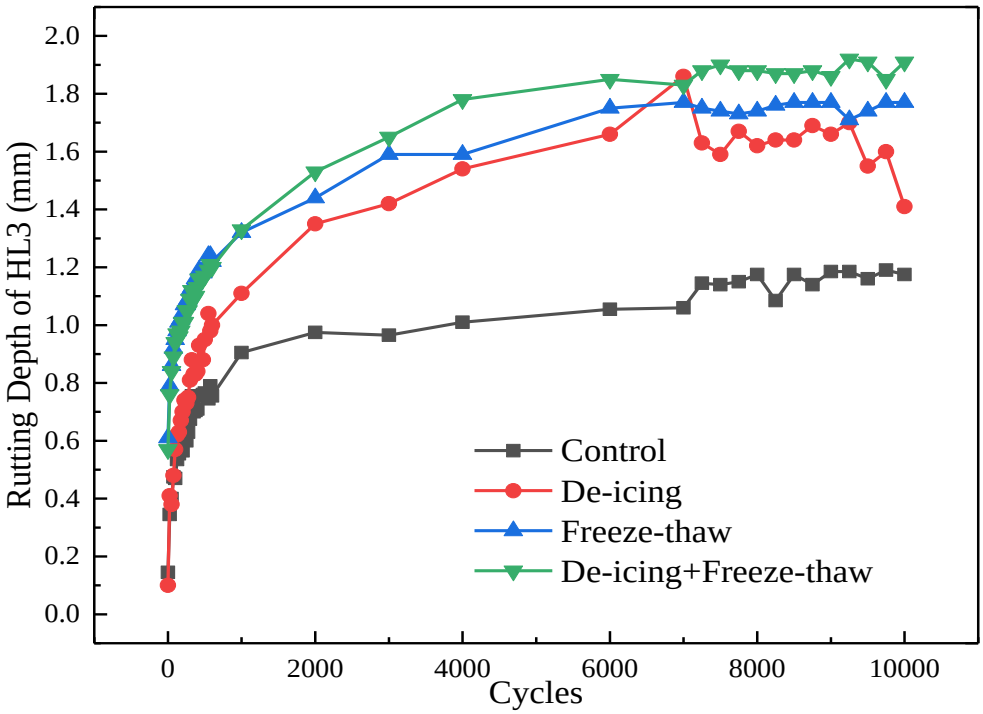

a. Rut Depth Curve of HL3 Mix

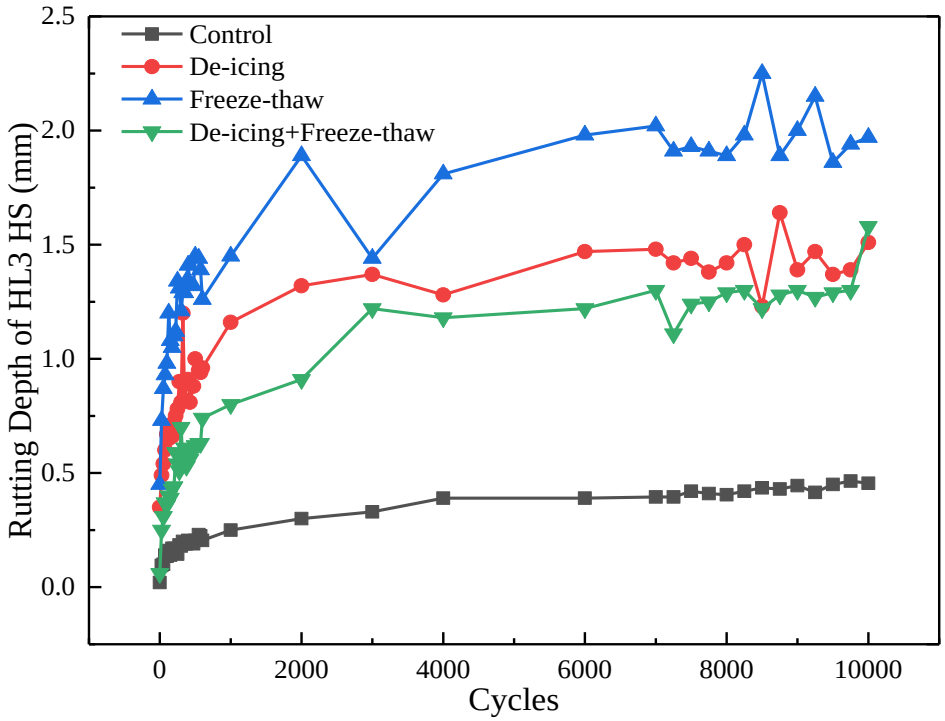

b. Rut Depth Curve of HL3 HS Mix

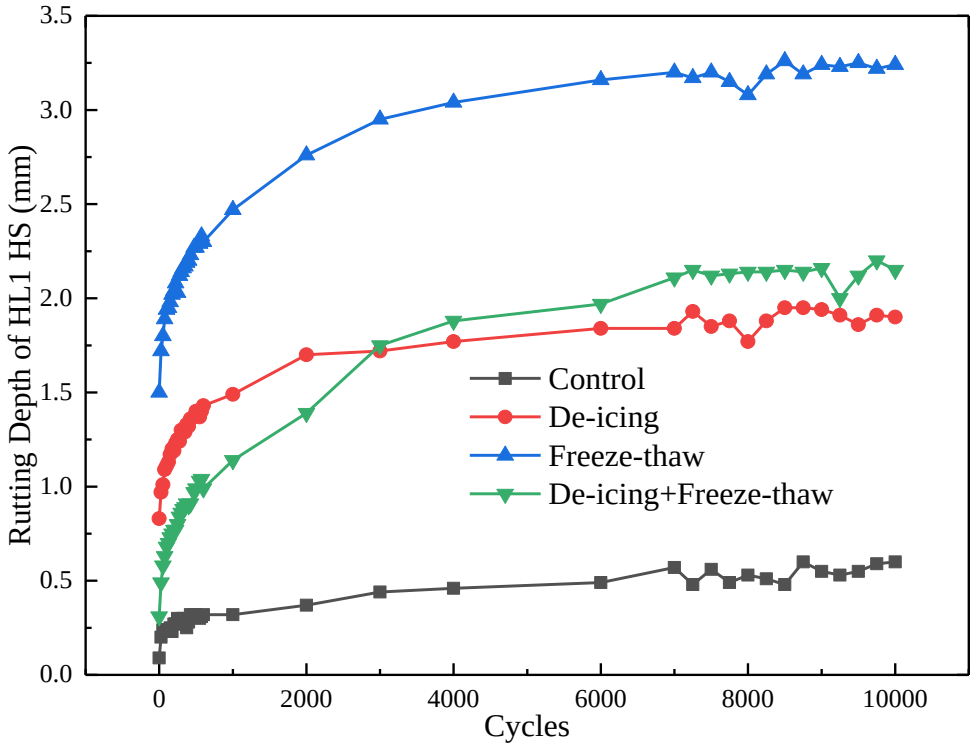

c. Rut Depth Curve of HL1 HS Mix

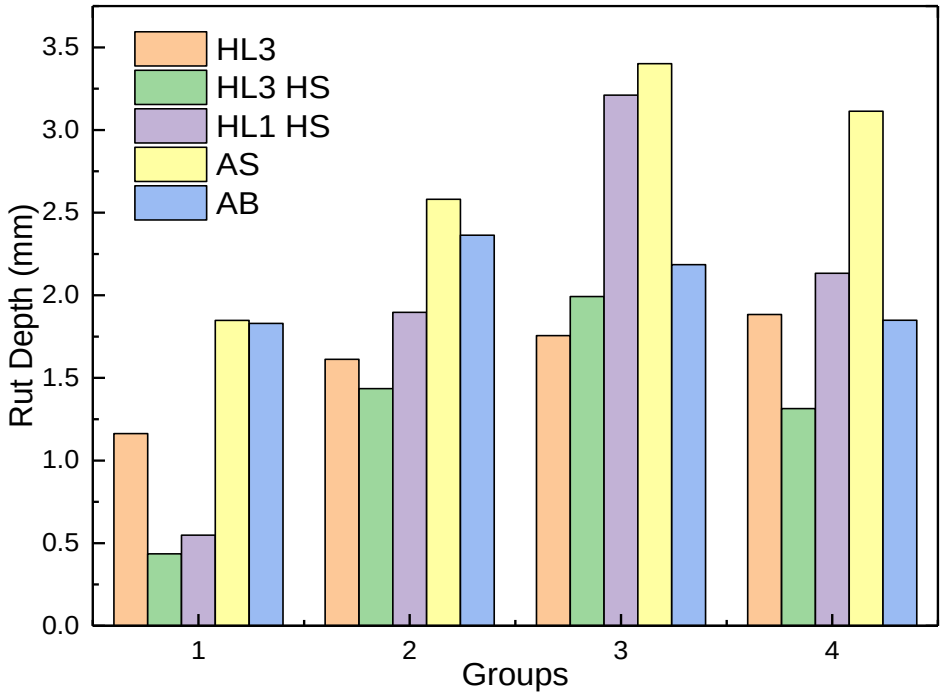

d. Rut Depth of all the Mixes

Figure 6-6 Effects of Different Treatments to Asphalt Mixes Rut Depth

6.3.2 Effects of Mix Types on Rutting Performance

Hamburg Wheel Rutting Test results show that different asphalt mixture type shows a various stiffness compromise when it subjecting to potassium acetate, freeze-thaw cycles treatment. Considering five different airport and roadway used asphalt mixes were tested in this study, the discussion of the rutting distress resistance of each asphalt mixture under various treatments is of great value.

As showed in Figure 6-7.a, no treatment was applied to this group, airport mixes show a less satisfactory performance for HWTT, while HL3 HS shows the best rut resistance after de-icer treatment and freeze-thaw conditioning. The permanent deformation resistance of different asphalt mixes compromised in various levels is shown in Figure 6-7.a – 6-7.d. The rut depth in Figure 6-8 was calculated as an average of recorded rut depth values corresponding with cycle numbers from 9,000 to 10,000. After treating with potassium acetate, the rut depth of HL3 and HL1HS seems to vary substantially. HL1 HS shows a worse rut performance than HL3 compared to the control group, after freeze-thaw conditioning. HL3 presents the most promising resistance to rutting compared with other mixes as showed in 6-7.c and 6-8.b. However, the combined effect of potassium acetate de-icer and freeze-thaw conditioning shows that HL3 HS and Airport surface mix remained the most and least satisfactory rutting performance, while Airport lower course, HL3 and HL1 HS exhibited a very close rutting resistance as showed in Figure 6-7.d, 6-8.a, and 6-8.b.

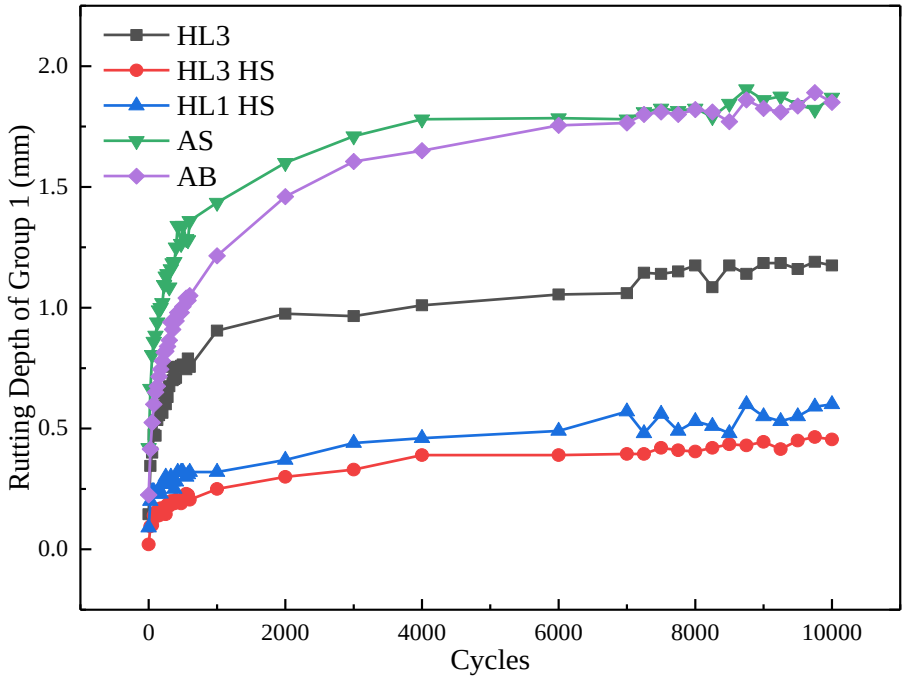

a. Rut Depth Curve of Control Group

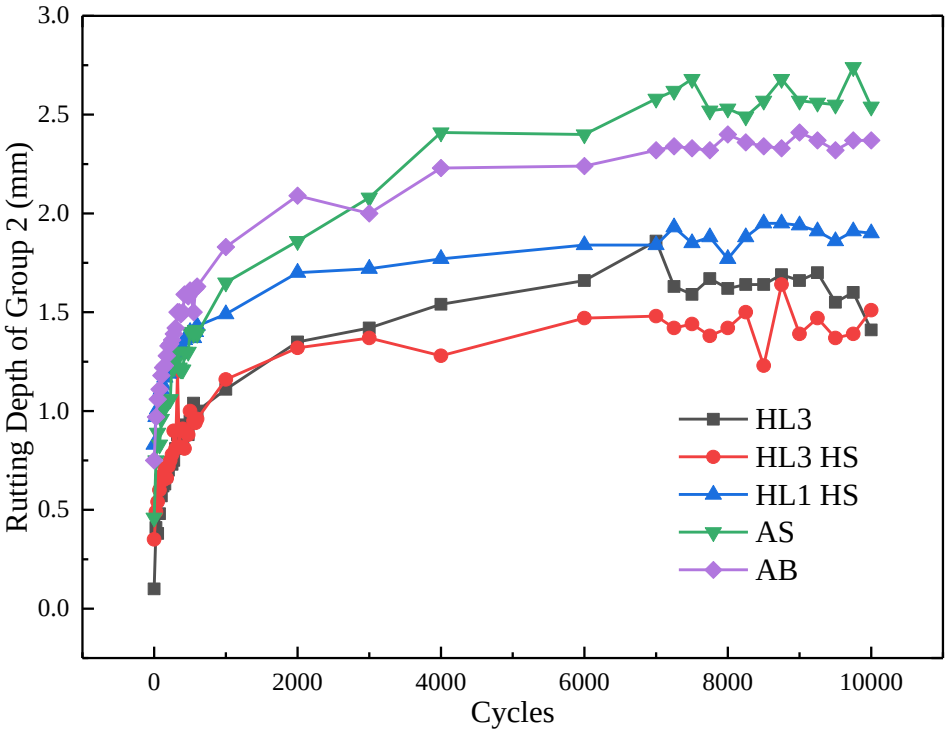

b. Rut Depth Curve of De-icing Group

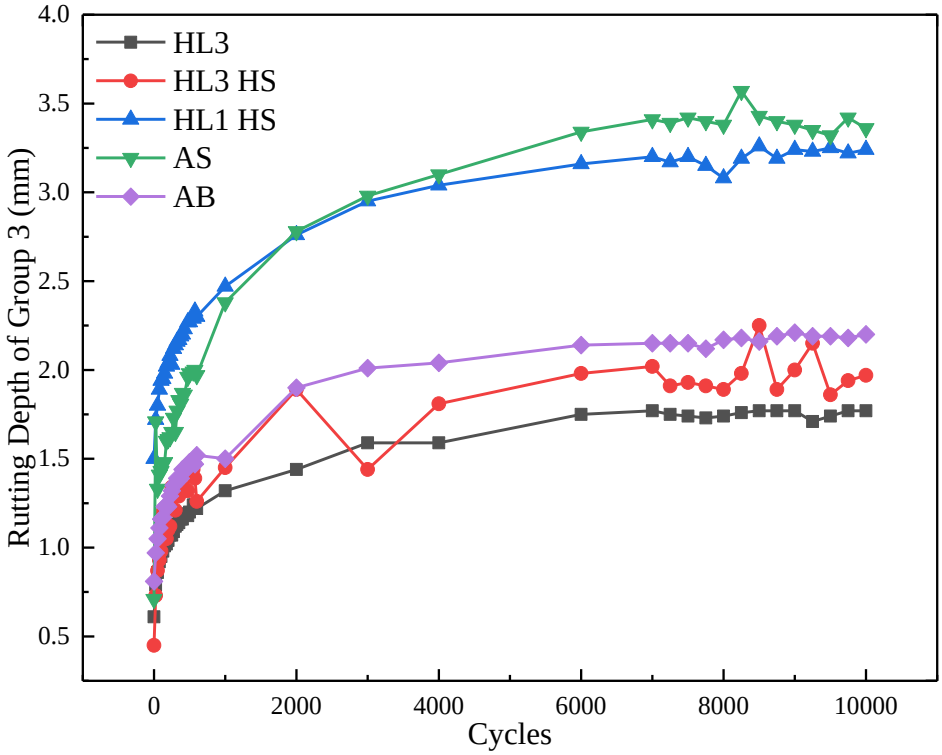

c. Rut Depth Curve of Freeze-thaw Group

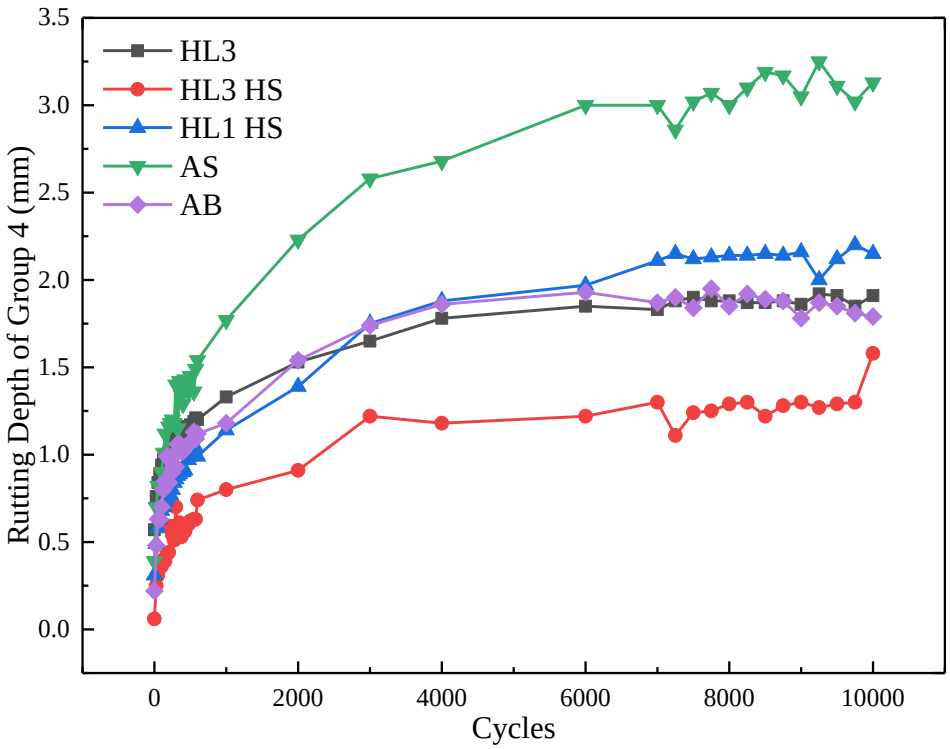

d. Rut Depth Curve of De-icing + Freeze-thaw

Figure 6-7 Effect of Different Mix Type on Rut Depth Curve

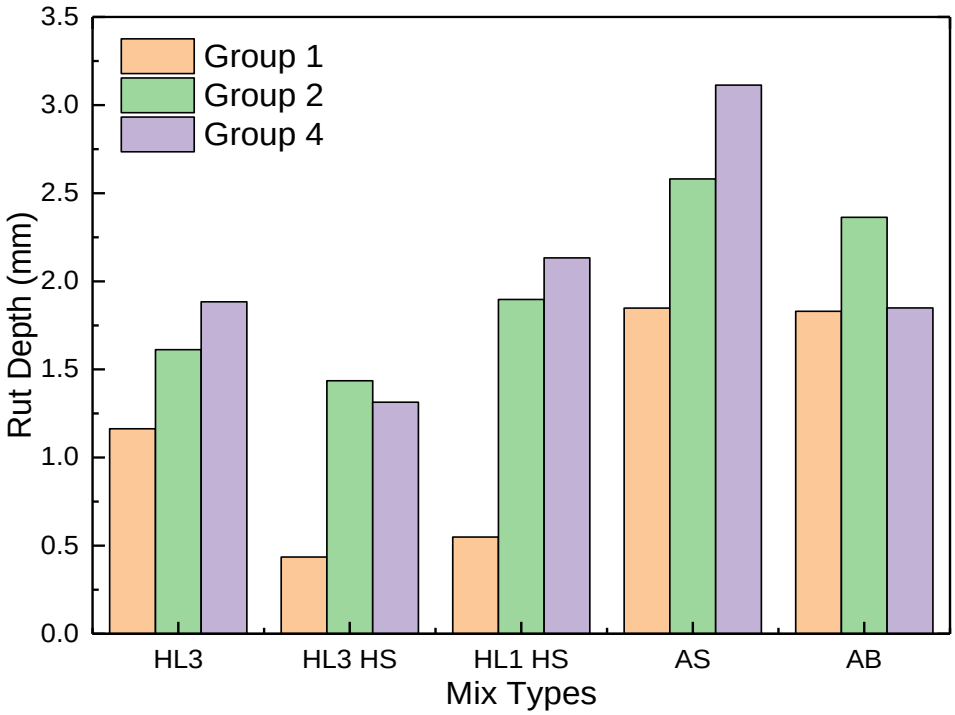

a. The Control, De-icing, and Combined Group

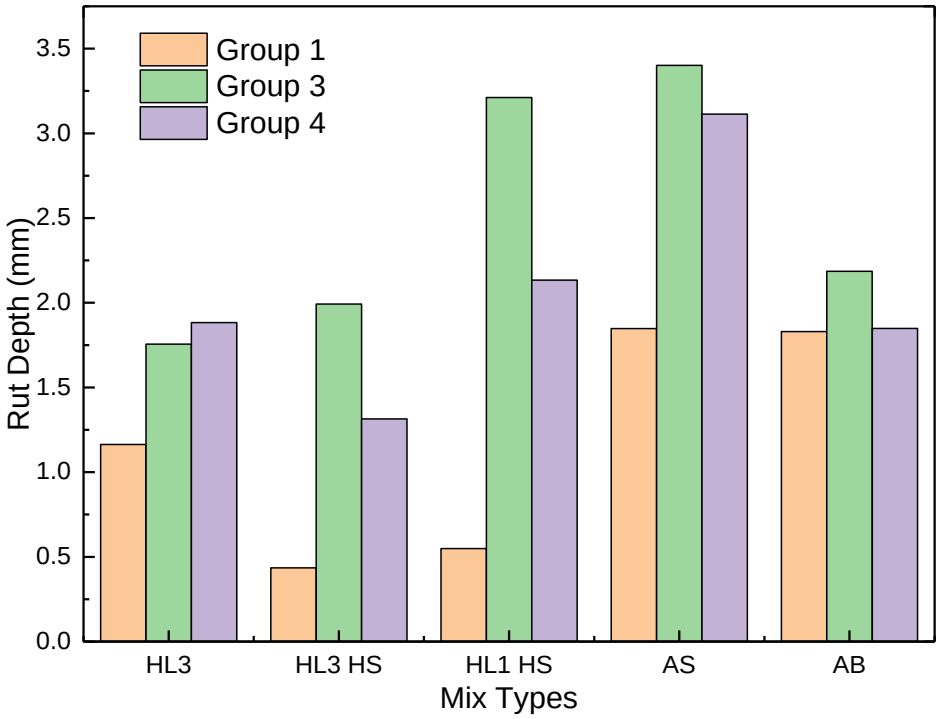

b. The Control, Freeze-thaw, and Combined Group

Figure 6-8 Effect of Different Mix Type on Rut Depth

6.3.3 Analysis of Variance

The important factors for asphalt mixture include asphalt binder performance grade, maximum aggregate size, coarse aggregates content, and asphalt binder content, etc. Each one of these factors plays a role in the asphalt mixture's performance. Previous analysis proved that different experimental treatments for specimens before the test can also affect the mechanical properties of asphalt pavement materials. The key mix design factors of all the five tested mixes and of which the Hamburg Wheel Tracking Test results under four types of treatment are listed in Table 6-5. The rut depth values listed in Table 6-5 are recorded rut depth corresponding with cycle numbers from 9,000 to 10,000 when it is reaching a stable level till the end of the test.

Table 6-5 Factors, Levels, and Results for Analysis of Variance

Factors (Levels)	A (2)	B (3)	C (4)	D (4)	Group1	Group2	Group3	Group4
Mix Type	Binder PG Type	Max Aggr Size	Coarse Aggr Cont	Asphalt Content	Rut Depth			
Unit	-	mm	%	%	mm	mm	mm	mm
AS	70-28	13.2	47	5.2	1.86	2.57	3.38	3.05
					1.88	2.56	3.35	3.25
					1.84	2.55	3.32	3.11
					1.82	2.74	3.42	3.02
					1.87	2.54	3.36	3.13
AB	64-28	19	52	5.2	1.83	2.41	2.21	1.78
					1.81	2.37	2.19	1.87
					1.84	2.32	2.19	1.85
					1.89	2.37	2.18	1.81
					1.85	2.37	2.2	1.79
HL3	64-28	9.5	40	5.1	1.19	1.66	1.77	1.86
					1.19	1.7	1.71	1.92
					1.16	1.55	1.74	1.91
					1.19	1.6	1.77	1.85
					1.18	1.41	1.77	1.91
HL3 HS	70-28	13.2	50	5	0.45	2.92	2	1.3
					0.42	2.92	2.15	1.27
					0.45	2.91	1.86	1.29
					0.47	2.94	1.94	1.3
					0.46	2.91	1.97	1.58
HL1 HS	64-28	9.5	40	5.5	0.55	1.94	3.24	2.16
					0.53	1.91	3.23	2
					0.55	1.86	3.25	2.12
					0.59	1.91	3.22	2.2
					0.6	1.9	3.24	2.15

To investigate if different factors of asphalt mixture have a significant effect on the rutting performance, statistical tool --- one-way analysis of variance (ANOVA) was employed in each treatment group for asphalt binder PG, maximum aggregate size, coarse aggregate content, and asphalt binder content. Before ANOVA, each factor must pass the homogeneity test of variance first. As shown in Table 6, Factor A (asphalt binder PG) passed the homogeneity test of variance for Group 2 and Group 3, of which the significance level is greater than 0.05. Factor B and C (Maximum Aggregate Size and Coarse Aggregate Content) failed to pass the homogeneity test of variance for all the groups and are not qualified for ANOVA analysis. Factor D (Asphalt Content) passed Group 1. ANOVA table of Factor A and D are listed in Table 6-7 and Table 6-8.

Table 6-6 Test of Homogeneity of Variances

Factor	Group	Levene Statistic	Degree of Freedom 1	Degree of Freedom 2	Sig.
A	1	7.829	1	23	0.010
	2	3.640	1	23	0.069
	3	2.046	1	23	0.166
	4	464.430	1	23	0.000
B	1	2144.299	2	22	0.000
	2	10.572	2	22	0.001
	3	407.924	2	22	0.000
	4	335.911	2	22	0.000
C	1	559.579	3	21	0.000
	2	11.528	3	21	0.000
	3	868.460	3	21	0.000
	4	3.290	3	21	0.041
D	1	2.286	3	21	0.108
	2	7.051	3	21	0.002
	3	503.481	3	21	0.000
	4	202.923	3	21	0.000
Treatment	--	0.364	3	16	0.780

As stated above, factors that pass the homogeneity test of variance can be analyzed in a one-way ANOVA table. F values of Factor A to Group 2 and Group 3 are 46.712 and

1.025, respectively. According to the F distribution table (Montgomery, 2001), $F_{0.05}(1, 23)$ is equal to 4.28, which is greater than 1.025 and smaller than 46.712. The P-values listed in Table 7 also shows that asphalt binder PG has a statistical effect on rut depth of asphalt mixtures with de-icing treatment, whereas the freeze-thaw conditioning to the asphalt specimen has no such effect. As for asphalt content in Table 8, F value is far greater than $F_{0.05}(3, 21) = 3.07$ and P-value is 0.000, which indicates that asphalt content in the mixture has a significant effect on rutting performance when specimens were not treated.

It is of interest that if different treatment methods have a significant effect on rutting resistance. One-way ANOVA was also conducted for treatment methods, which has four levels. The homogeneity test of variance in Table 6-6 shows that it is suitable for ANOVA analysis. In Table 9, F value 3.478 is greater than $F_{0.05}(3, 16) = 3.24$, and significance level 0.041 is smaller than 0.05, which implies that all four different treatments have a significant effect on rutting resistance of asphalt mixture applied both to airports and roadways.

Table 6-7 One-way ANOVA for Asphalt Binder PG

Group	Source	Sum of Squares	Degree of Freedom	Mean Square	F	Sig.
1	Between Groups	0.012	1	0.012	0.032	0.860
	Within Groups	9.046	23	0.393		
	Total	9.058	24			
2	Between Groups	3.878	1	3.878	46.712	0.000
	Within Groups	1.910	23	0.083		
	Total	5.788	24			
3	Between Groups	0.474	1	0.474	1.025	0.322
	Within Groups	10.635	23	0.462		
	Total	11.109	24			
4	Between Groups	0.486	1	0.486	1.369	0.254
	Within Groups	8.169	23	0.355		
	Total	8.655	24			

Table 6-8 One-way ANOVA for Asphalt Content

Group	Source	Sum of Squares	Degree of Freedom	Mean Square	F	Sig.
1	Between Groups	9.046	3	3.015	5448.449	0.000
	Within Groups	0.012	21	0.001		
	Total	9.058	24			
2	Between Groups	5.576	3	1.859	183.903	0.000
	Within Groups	0.212	21	0.010		
	Total	5.788	24			
3	Between Groups	7.620	3	2.540	15.290	0.000
	Within Groups	3.489	21	0.166		
	Total	11.109	24			
4	Between Groups	4.439	3	1.450	7.070	0.002
	Within Groups	4.306	21	0.205		
	Total	8.655	24			

Table 6-9 One-way ANOVA for Treatment Method

Factor	Source	Sum of Squares	Degree of Freedom	Mean Square	F	Sig.
Treatment Method	Between Groups	4.689	3	1.563	3.478	0.041
	Within Groups	7.191	16	0.449		
	Total	11.880	19			

6.4 Summary

Based on experimental observations and statistical analysis, the effects of different treatments before HWTT and various key mix design parameters of asphalt mixture used for airports and roadways were studied and discussed. A summary and some conclusions can be drawn as follows:

1. 50% Potassium acetate liquid seems to have the softening effect on asphalt mixture's

overall stiffness for both airport and roadway mixes. Freeze-thaw conditioning can deteriorate the rutting resistance for both mixes in different degrees.

2. De-icing treatment and freeze-thaw cycles have the potential to induce stripping. The unsettled rut depth at the end of the HWTT test shows that especially de-icing treated asphalt specimens are more likely to have stripping distress.

3. The combination effect of de-icing agent and freeze-thaw conditioning might have the effect of mitigating the rutting resistance compromise caused by the two treatments separately. The experimental results show that the rut depth of treatment group 4 is slightly smaller than Group 2 and Group 3.

4. Analysis of variance indicates that asphalt binder PG type and asphalt content have a statistical effect on rutting performance under the control group, de-icing treated group, and freeze-thaw conditioned group. ANOVA also shows treatment methods have a significant effect on rut depth of asphalt mixture applied both on airports and roadways.

Chapter 7
EVALUATING SHEAR RESISTANCE OF CANADIAN ASPHALT MIXTURES APPLIED ON ROAD AND AIRPORT PAVEMENT UNDER FREEZE-THAW CYCLE AND DE-ICING AGENT

7.1 Materials

The roadways and airport pavement asphalt mixtures that were tested in this chapter are the same as in Chapter 6. The asphalt content, gradation, and Job Mix Formula (JMB) information of HL3, HL3 HS, and HL1 HS as well as Air Surface and Air Base mix can be found in Chapter 4 and Chapter 6.

7.2 Uniaxial Shear Test

7.2.1 Introduction

Uniaxial Shear Test (UST) is a newly developed testing protocol that can be used to evaluate the shear properties of asphalt mixture. It was proved that the results of the Uniaxial Shear Test are highly correlated with that of the Superpave Shear Test (SST)(Zak et al., 2017a)(Zak et al., 2019).

UST testing apparatus consists of three main parts: cylindrical testing frame, shear rings, and steel loading insert (Figure7-1a). During the test, the asphalt specimen was cored and placed into the test frame. In the original test developed by Josef Zak, the load is applied through a knee joint on the top center of the steel insert with 1,850 N (Zak et al., 2017b). The vertical displacement of the steel insert was measured by three Linear Variable Differential Transformers with 120 degrees between each other. The apparatus was applied on the Universal Testing Machine (UTM). Two types of testing modes adopted in the original design are the repeated shear test and shear frequency sweep test, both tests are small-amplitude oscillation tests.

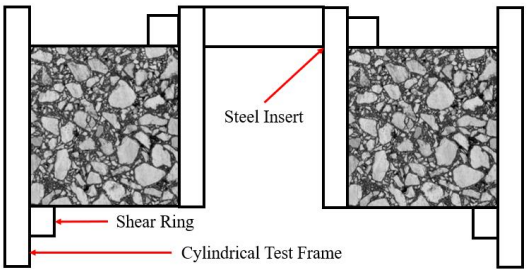

a. Testing Frame

b. Specimen

c. Original Design (Zak, 2017b)

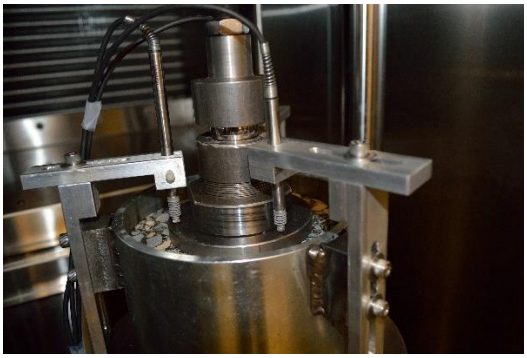

d. Original LVDTs (Zak, 2017b)

c. Loading Frame

d. Displacement Transducer

Figure 7-1 Uniaxial Shear Tester

Some simplifications were made to the testing setup in this study. First, the Marshall Load Frame was used for testing instead of UTM. The difference between the Marshall Load Frame and UTM or Material Testing System (MTS) is that the Marshall Load

Frame has a static loading rate (2 inches per minute) and therefore it is incapable of controlling the loading pattern. As a result, the simplified Uniaxial Shear Test is no longer non-destructive as in the original test. The shear zone was torn and deformed during the loading process. Second, the way the Marshall Load Frame works is that the loading head is fixed and the platen at the bottom which holds the cylinder and specimen are moving up. Instead of using three LVDTs, only one displacement transducer was applied on the edge of the cylinder (Figure 7-1d). In the original test, LVDTs are placed on the edge of the top of the steel insert as the loading head oscillates and the specimen and cylinder are fixed on the platen. Third, in the original Uniaxial Shear Test, both the repeated shear test and shear frequency sweep test are conducted in an environmental chamber that can accurately control the testing temperature. In the simplified shear test, the loading process is usually less than 15 seconds and the specimen placement only takes about 10 to 15 seconds. Therefore, the heat loss for the asphalt specimen is negligible and an oven was used for specimen conditioning and temperature control.

7.2.2 Specimen Preparation

All the specimens were compacted into 150 mm diameter and 50 mm height using a Superpave Gyratory Compactor. In the original UST test, the sample was compacted into 135 mm in height and cut into two 50 mm heigh specimens for a smoother loading surface (Zak et al., 2019). The mass of the loose mixture was back-calculated based on MRD, BRD, and volumetric properties to ensure that each specimen has air voids between 7 ± 0.5 percent. Afterward, the specimens were cored with a 48 mm coring bit.

a. Coring Apparatus at CPATT

b. Coring Apparatus at PSI

Figure 7-2 Coring Apparatus for UST

7.2.3 Treatments

Three types of treatment were applied to all 8 different asphalt mixes. Temperature treatment, de-icer treatment, and freeze-thaw cycle treatment. Accordingly, six groups of 8 mixed specimen replicates were fabricated at the pavement laboratory of the Centre for Pavement and Transportation Technology (CPATT). Each group has three tests, namely each mix under the corresponding treatment has three replicated tests. Group 1 was tested under room temperature at the PSI technology laboratory in Guelph, Ontario, which is 18.9 °C. Notably, Group 1 has only two tests. The first test was tested at a low temperature of minus 18 °C and failed as the shear strength reached the Marshall loader's limit. Group 2 was conditioned at 25 °C for two hours before testing. Group 3 was conditioned at 50 °C for one hour before the test. Specimens in Group 4 were soaked in airport pavement de-icing agent (potassium acetate, see chapter 6) for 40 hours before testing. Sixteen hours of freezing at -18 °C and 24 hours of thawing at 60 °C were applied to the specimens in Group 5. For Group 6, 16 hours of freezing with

the existence of de-icing agent and 24 hours of thawing were applied before the shear test.

The difference in de-icer treatment from that of Chapter 6 is that the de-icer treatment in this chapter did not apply the vacuuming process as the testing center was not fully equipped by the time that the test was conducted. Instead, test one was soaked in potassium acetate liquid for one hour before the test, while test two and test three were soaked overnight. The purpose of the vacuuming process is to make sure that the treated specimens are all saturated with de-icer.

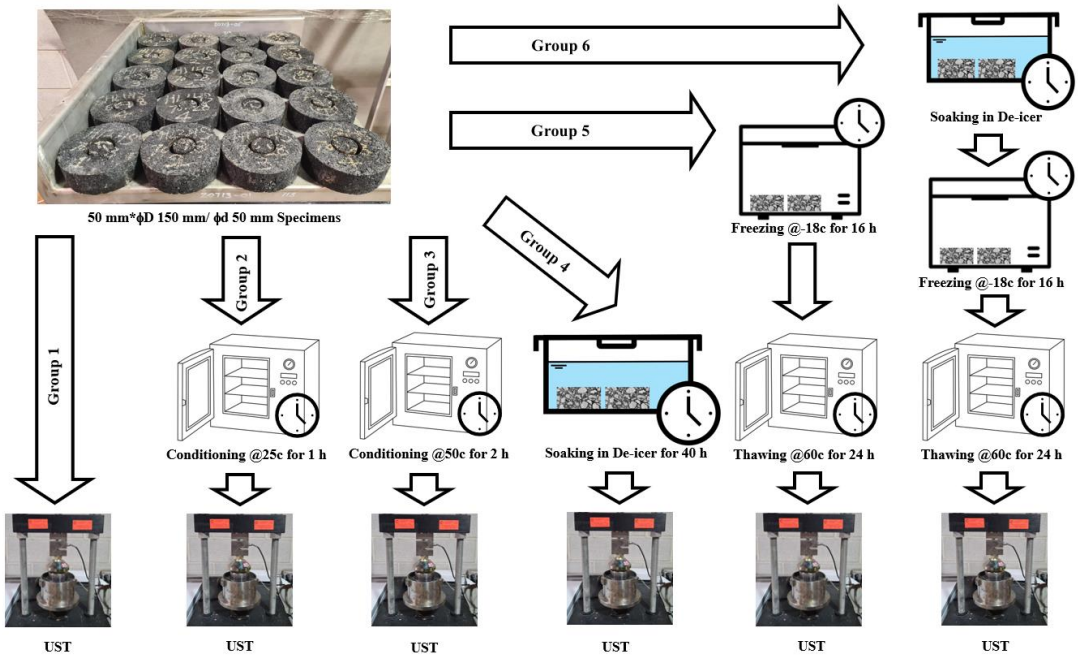

Figure 7-3 Specimen Treatments Procedures Before UST test

7.3 Results and Discussion

During the simplified Uniaxial Shear Test, the peak value of the loading force and displacement were recorded. The shear resistance is calculated from the following formula:

$$\tau_s = \frac{F}{A_s} \qquad \textbf{Equation 7-1}$$

$$A_s = 2\pi * r * h \qquad \textbf{Equation 7-2}$$

$$h = 50 - d \qquad \textbf{Equation 7-3}$$

Where:

F: Peak value of the shear force applied on the specimen, kN.

A_s: Area of the shear zone, mm^2.

τ_s: Shear Resistance, GPa.

r: Radius of the hollow, r = 25 mm.

h: Height of the shear zone, mm.

d: Displacement at the peak force, mm.

Test Group 6 was not completed as the loading force exceeded the loading limit of the Marshall loader and caused a testing halt; therefore, the results of Group 6 were eliminated from this study.

7.3.1 Influence of Mix Type on Loading Force at Different Temperatures

The loading force and displacement were recorded every one second, the loading force distribution of all the mixes at two different temperatures are shown in Figure 7-4.

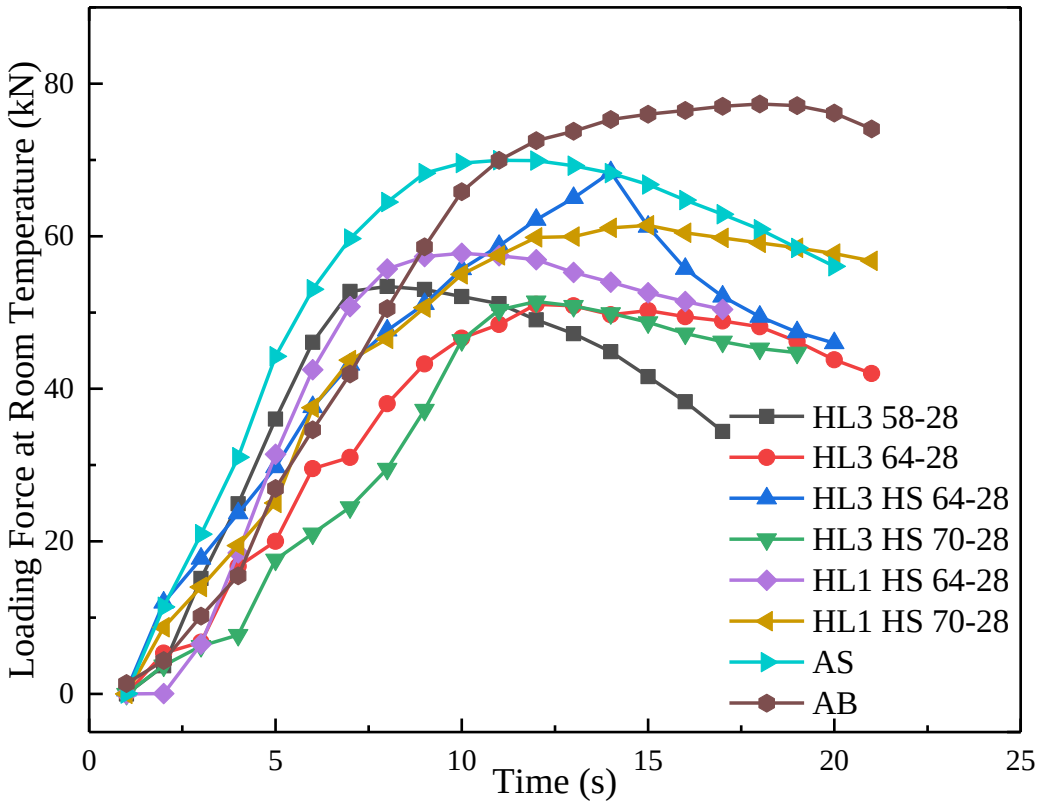

a. Test 2

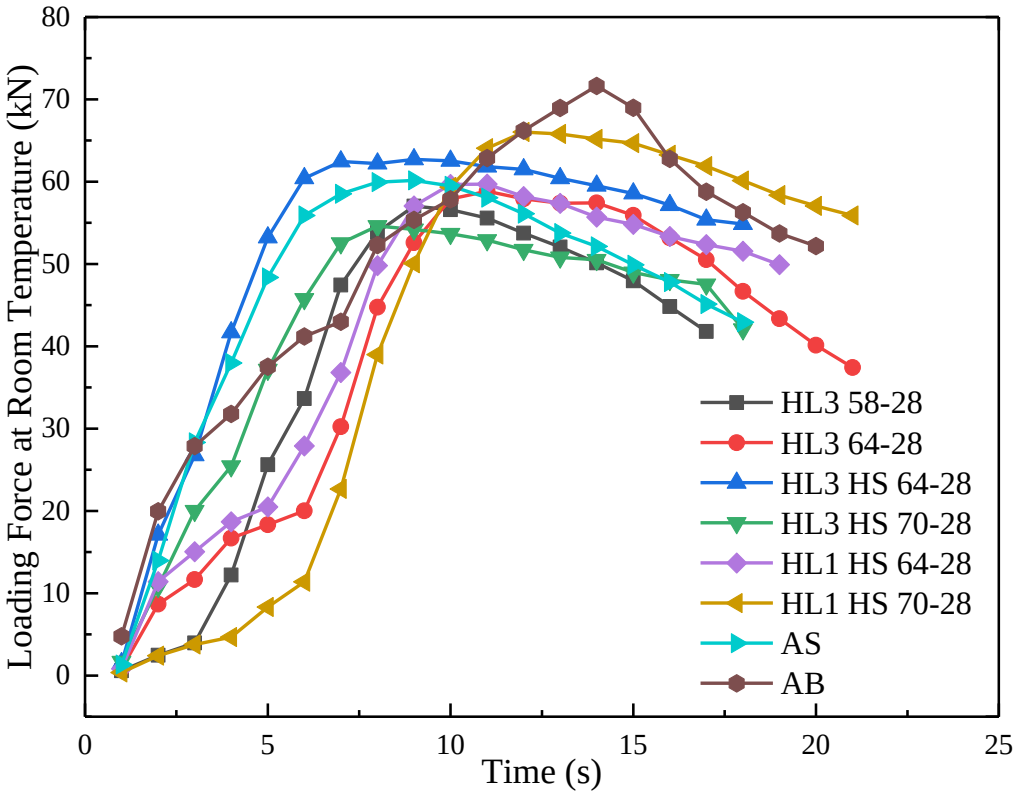

b. Test 3

Figure 7-4 Loading Force of Different Mixes at Room Temperature (18.9°C)

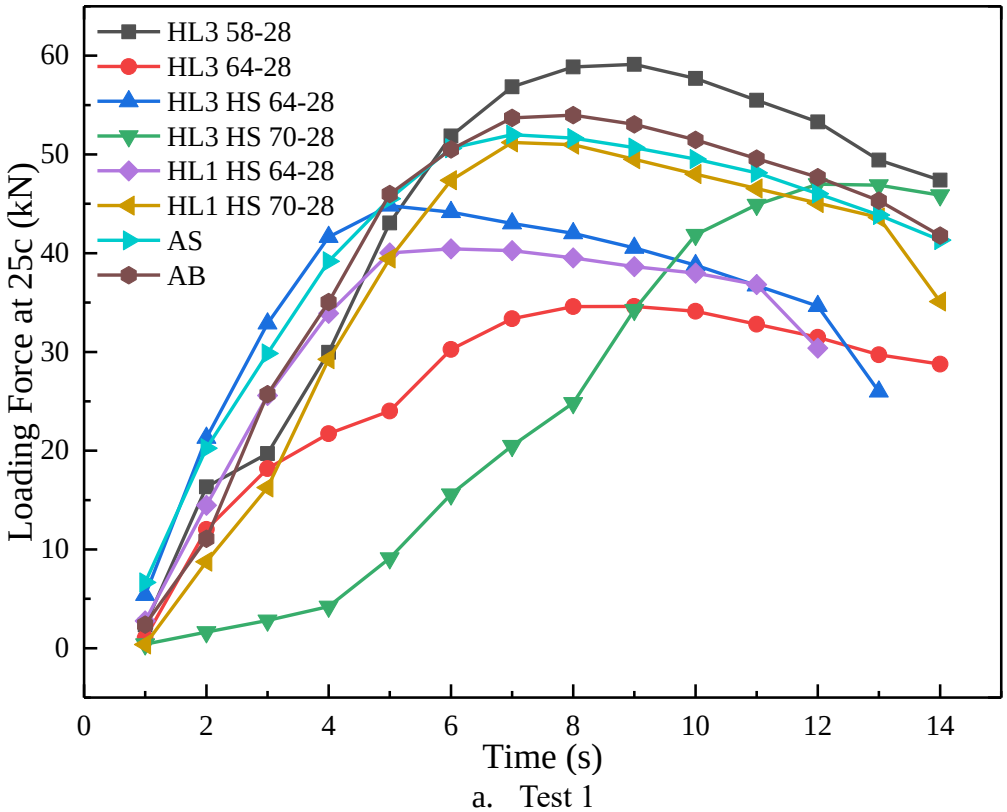

a. Test 1

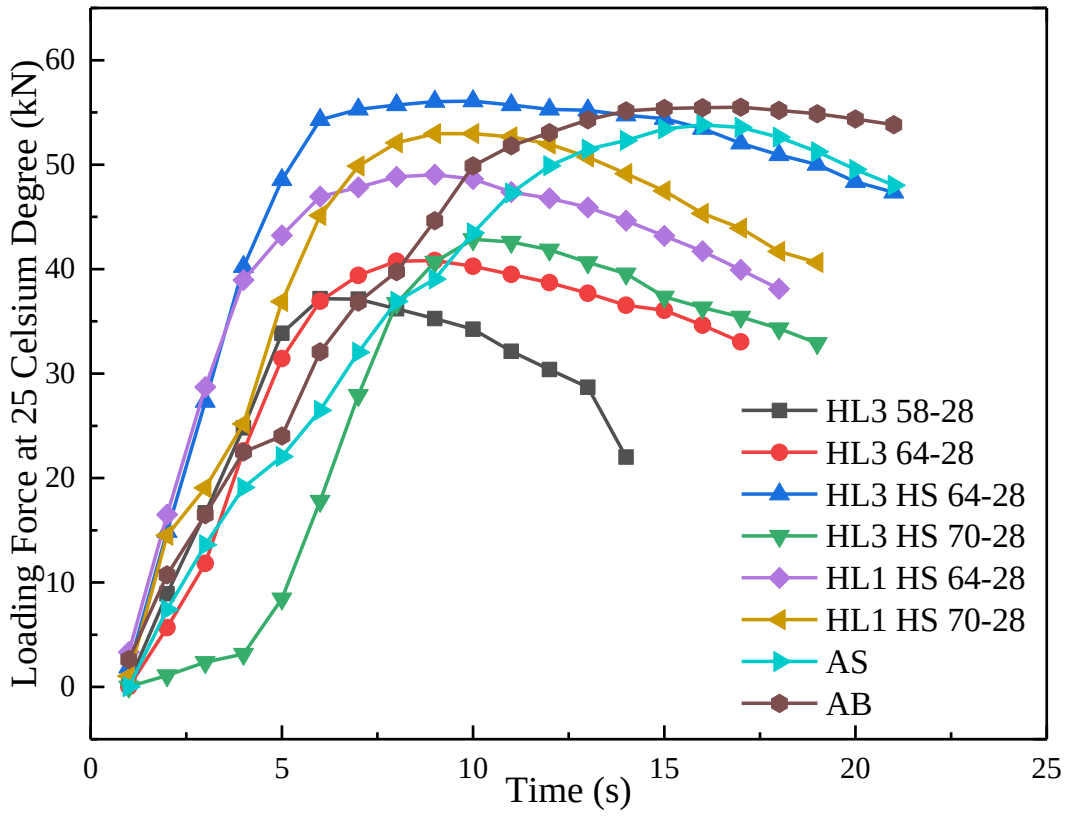

b. Test 2

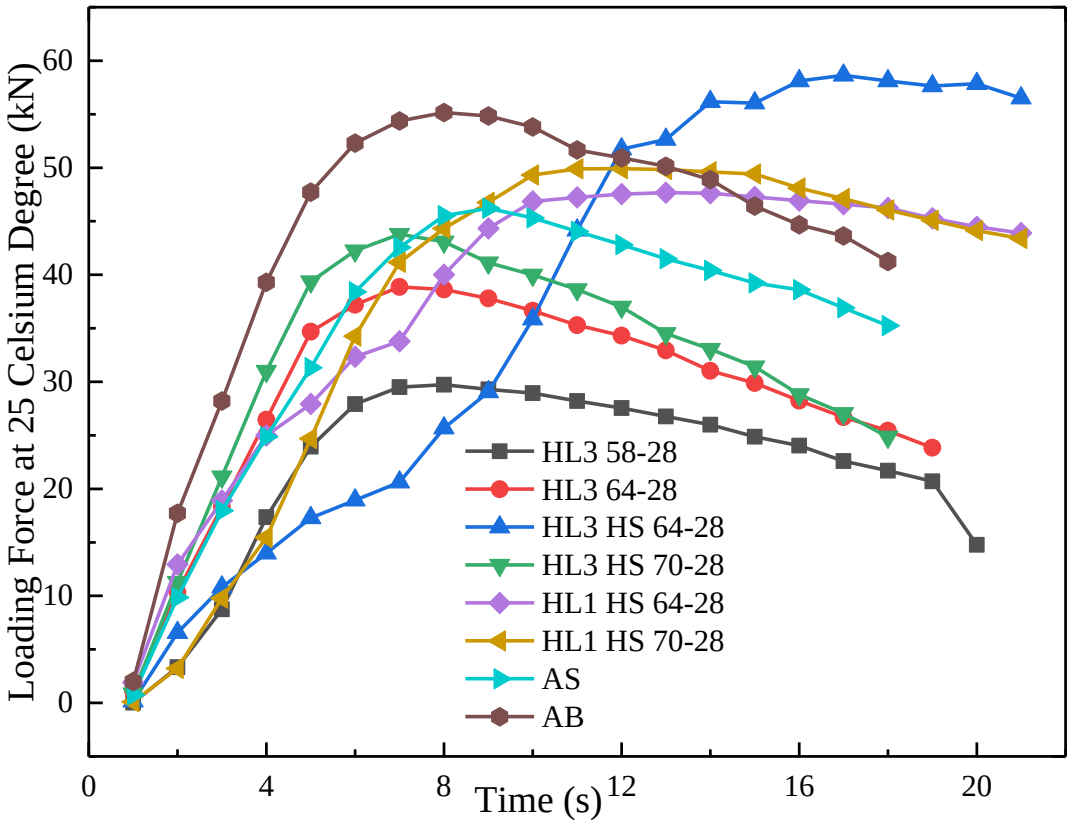

c. Test 3

Figure 7-5 Loading Force of Different Mixes at 25°C

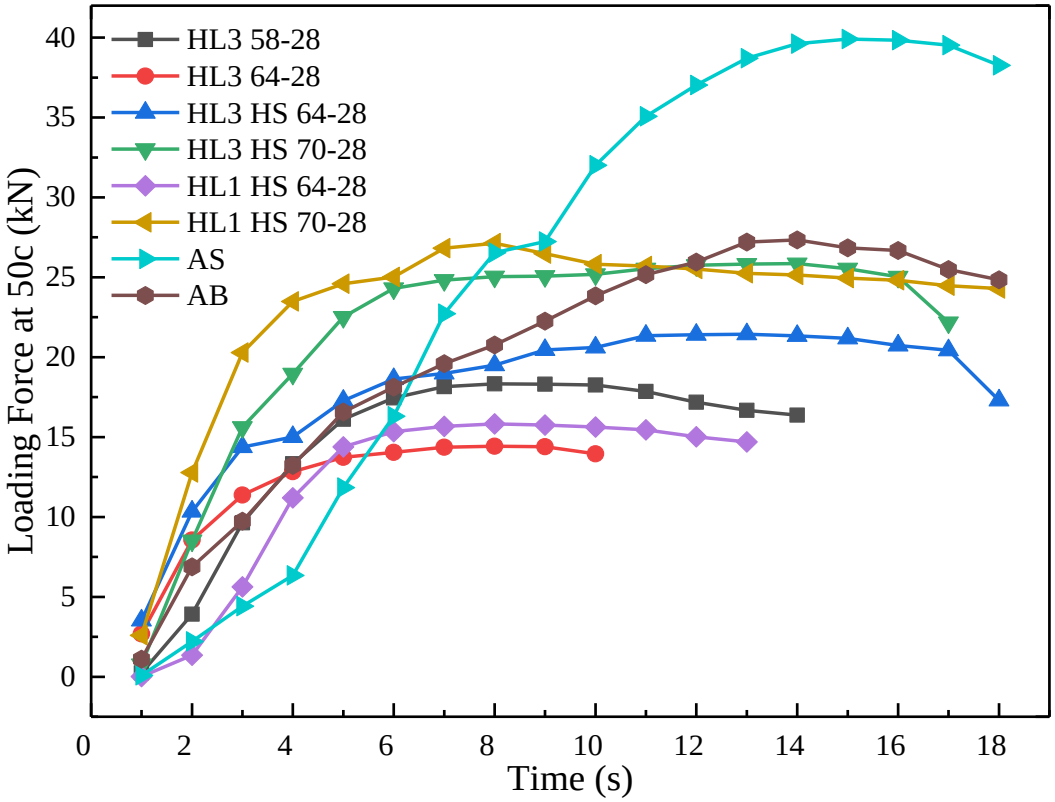

a. Test 1

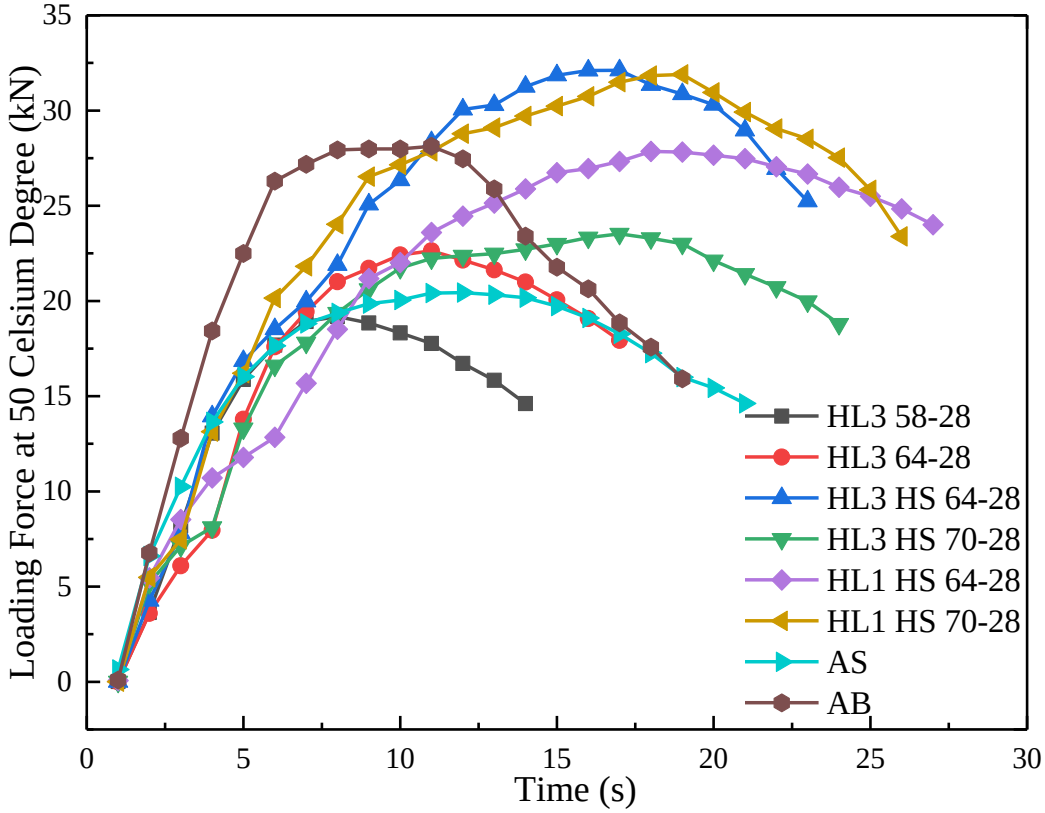

b. Test 2

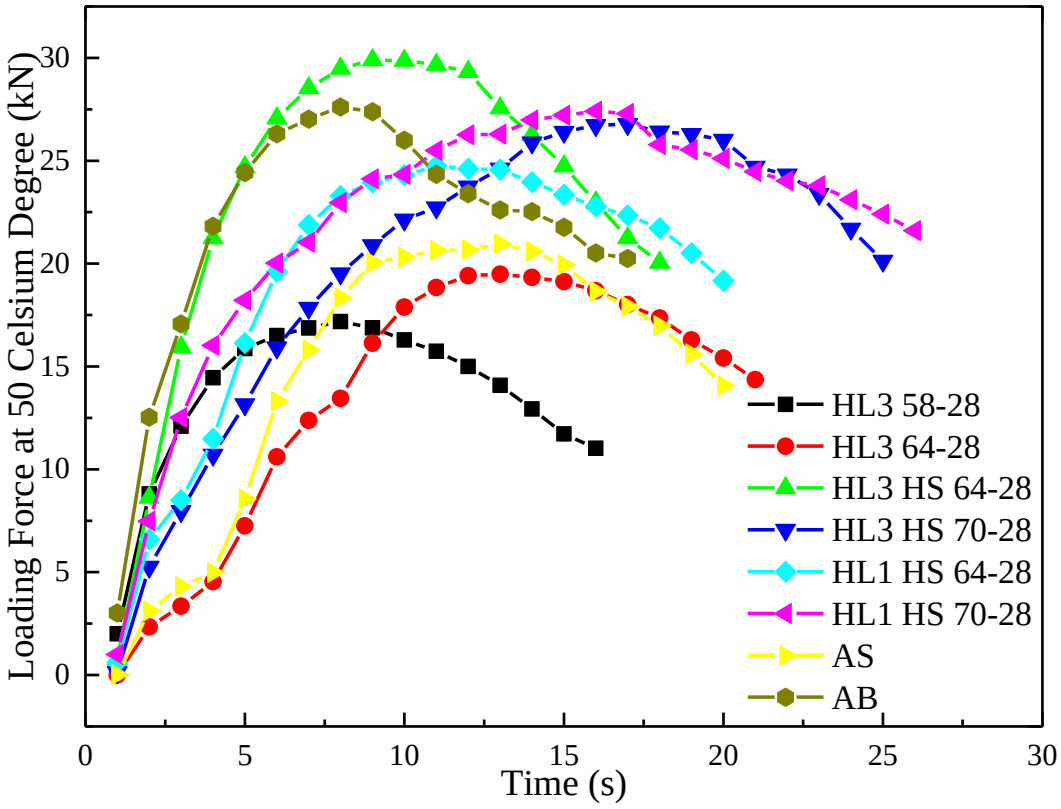

c. Test 3

Figure 7-6 Loading Force of Different Mixes at 50°C

Figure 7-4 shows that the airport binder course mix presents the best shear strength at 18.9 °C, it reached the shear peak value at about 15 seconds while most of the other mixes showed at about 7-8 seconds. Figure 7.5 Test 2 and Test 3 show that HL3 HS 64-28 has the highest shear strength at 25 °C while Test 1 shows that HL3 58-28 is the highest. Similarly, Figure 7.6 Test 2 and Test 3 display that HL3 HS 68-28 has the highest shear strength value at 50 °C while Test 1 shows the airport surface course has the highest level.

7.3.2 Influence of Mix Type on Loading Force after De-icer and Freeze-thaw

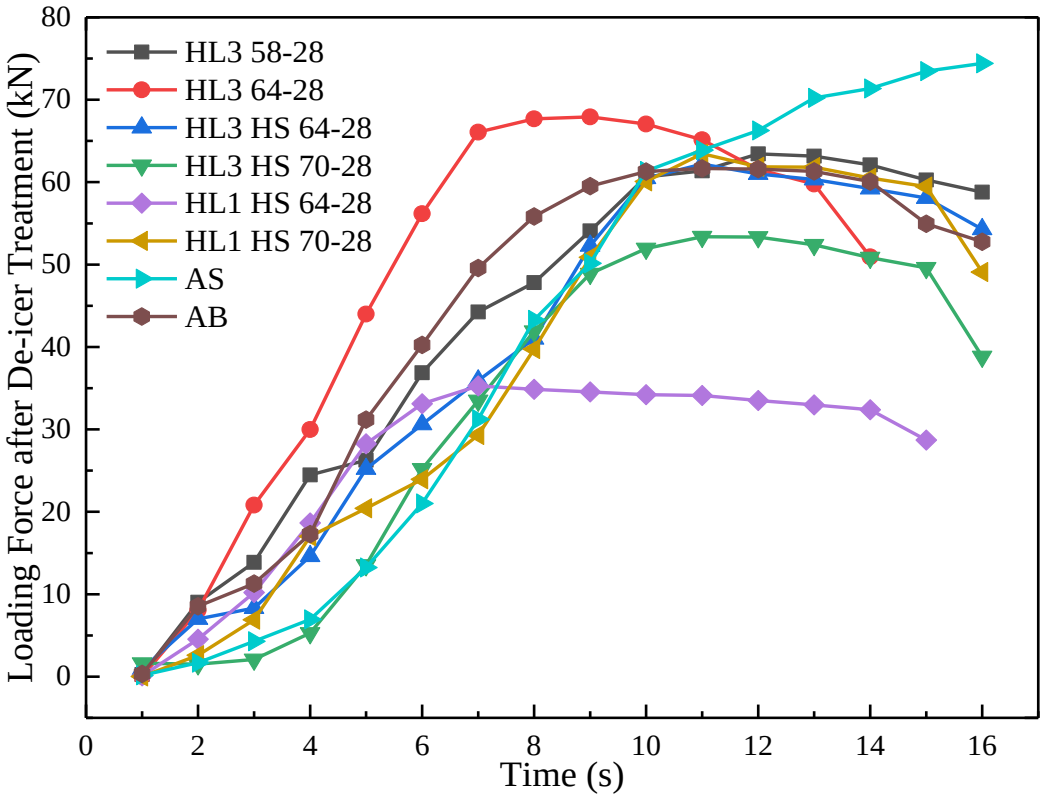

a. Test 1

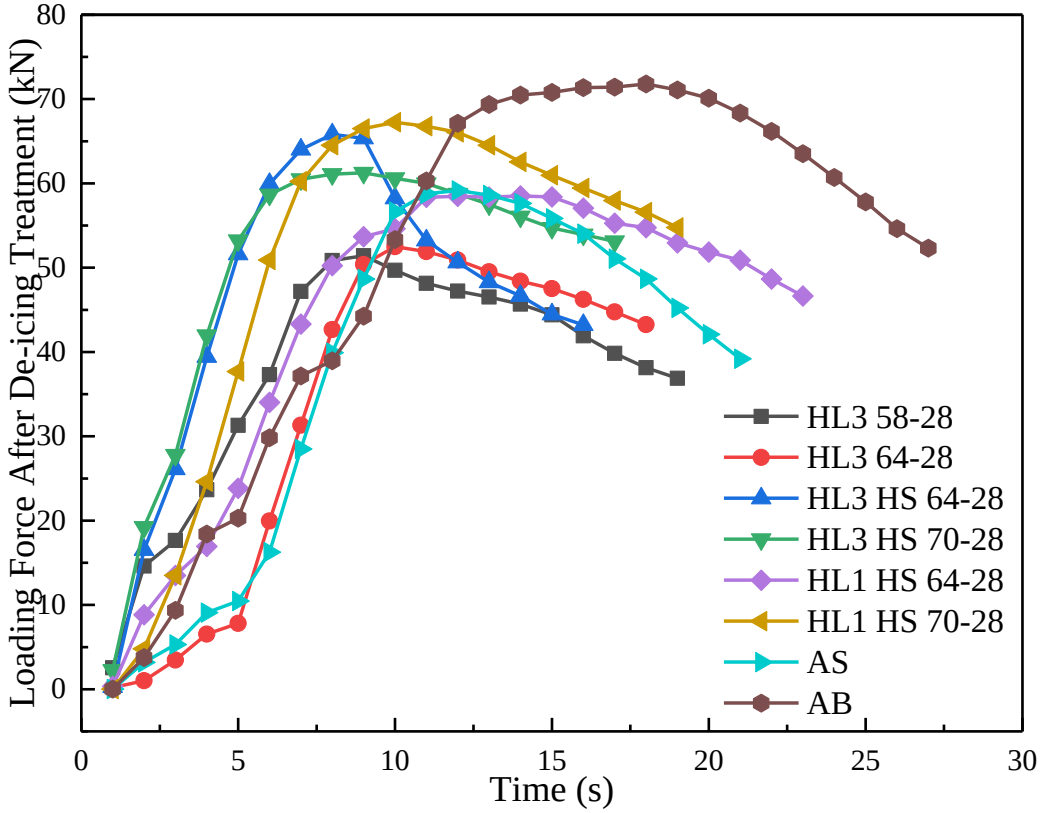

b. Test 2

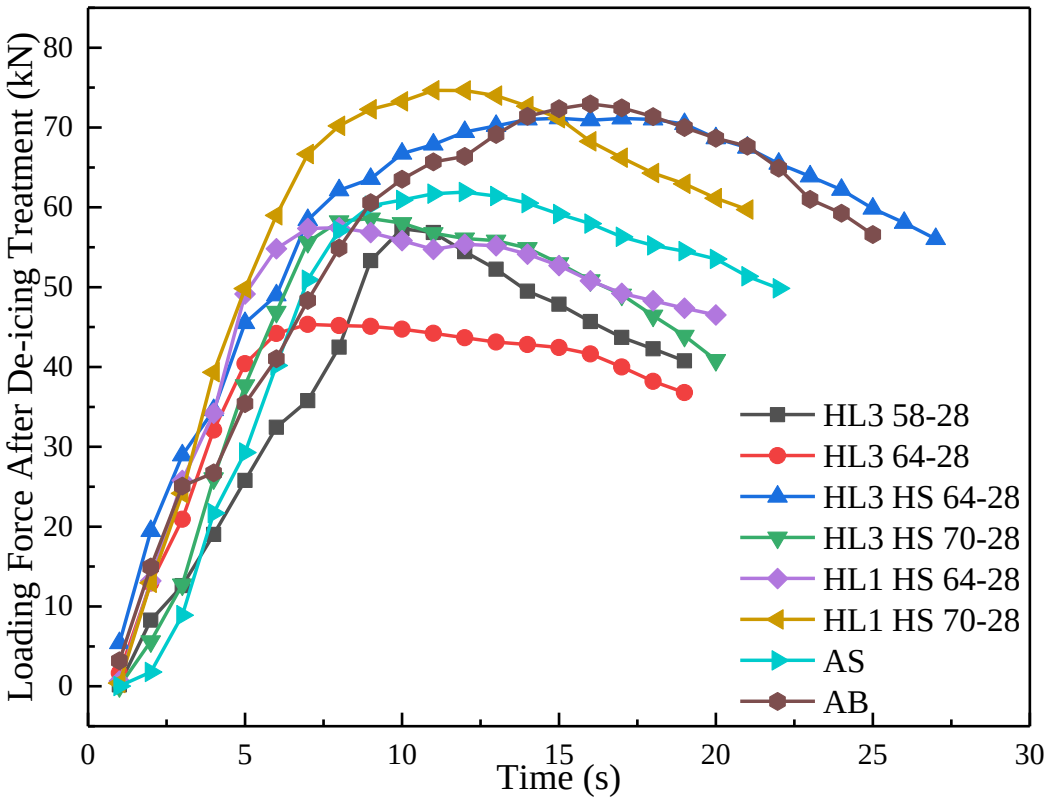

c. Test 3

Figure 7-7 Loading Force of Different Mixes After De-icer Treatment

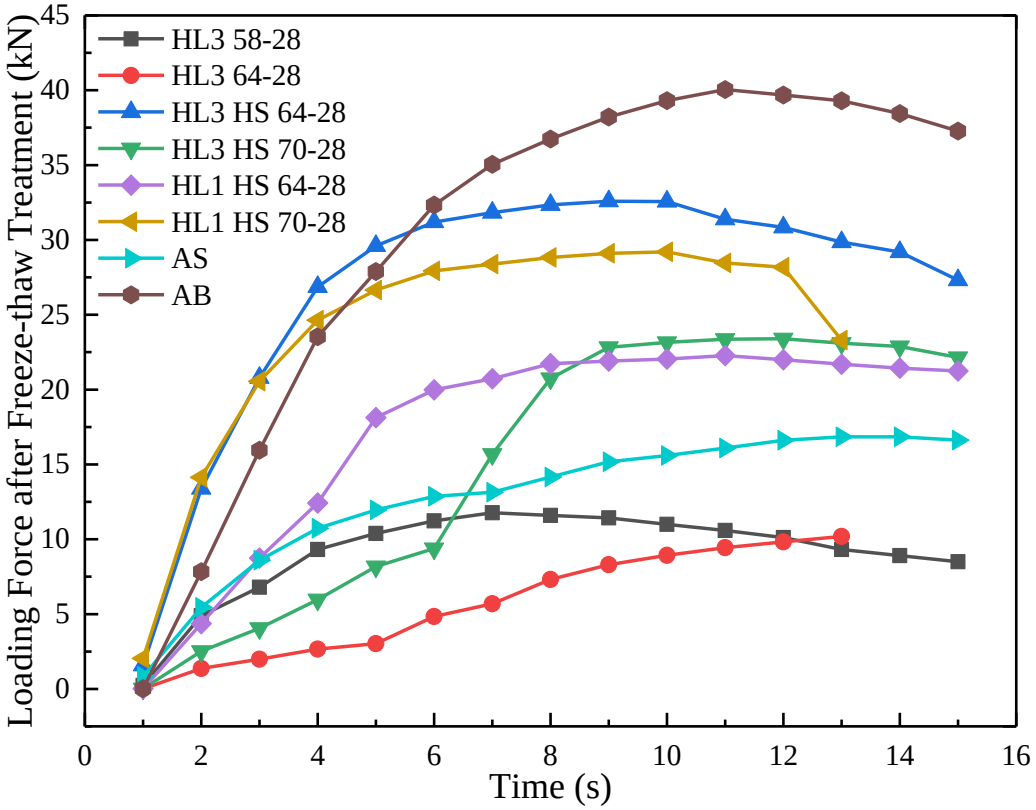

a. Test 1

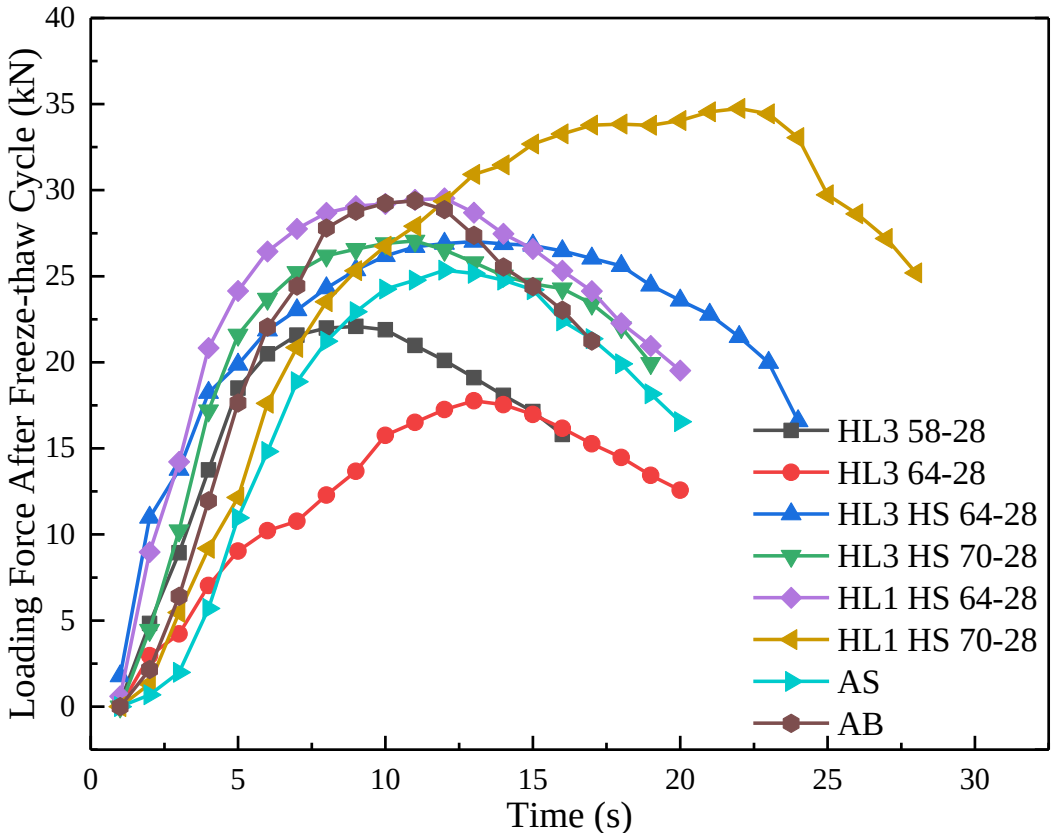

b. Test 2

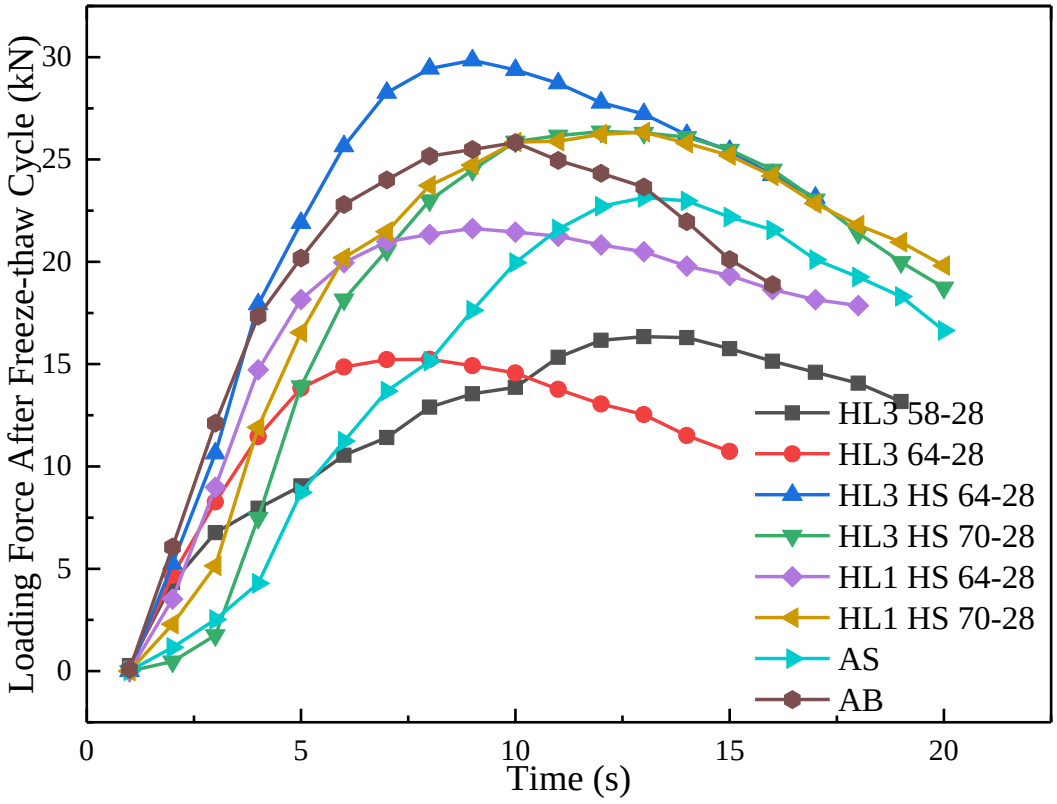

c. Test 3

Figure 7-8 Loading Force of Different Mixes After Freeze-thaw Cycle

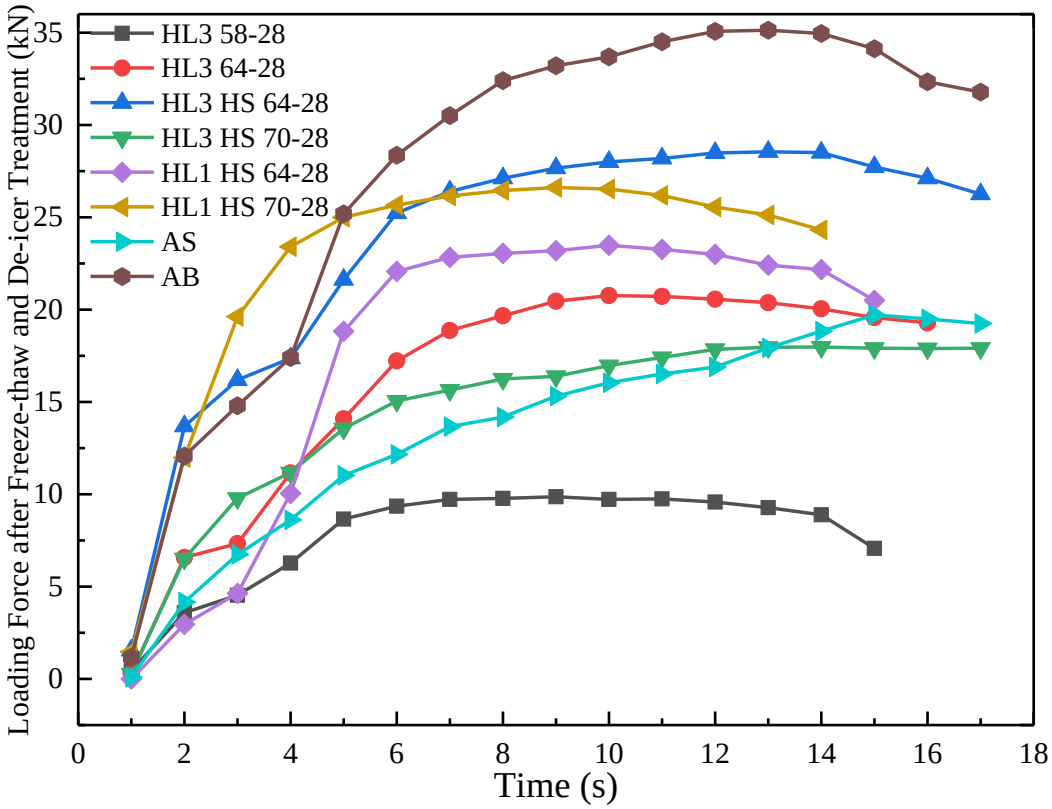

a. Test 1

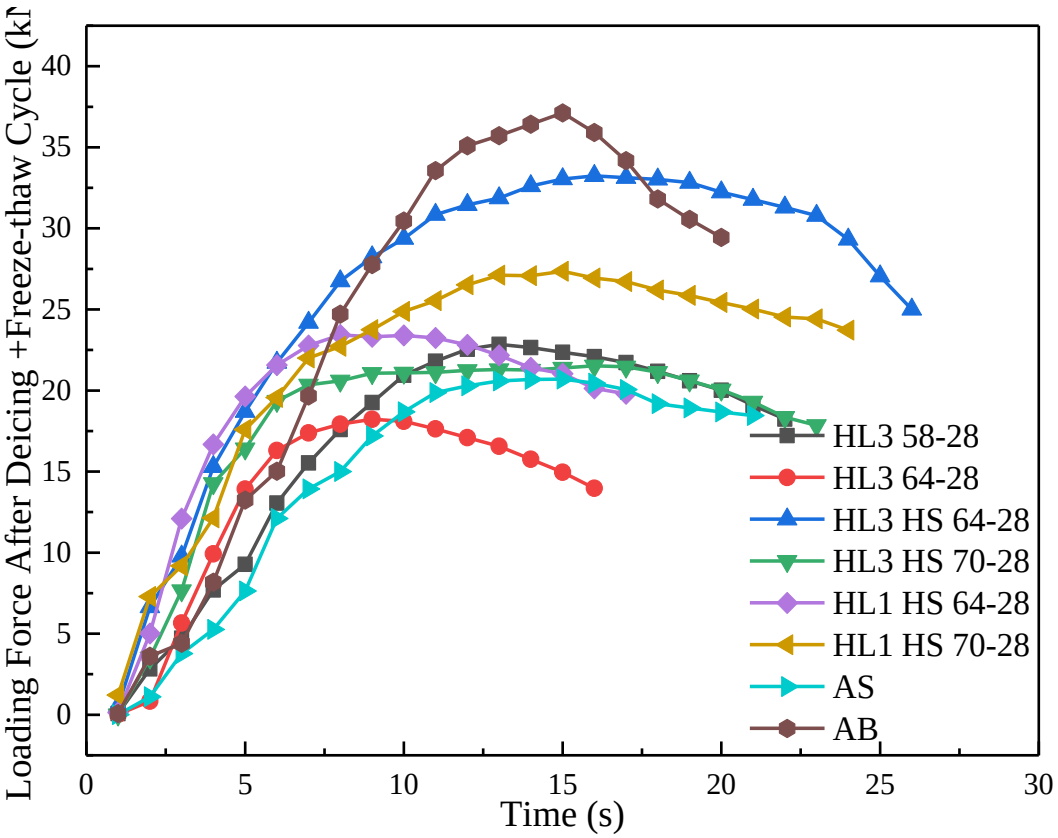

b. Test 2

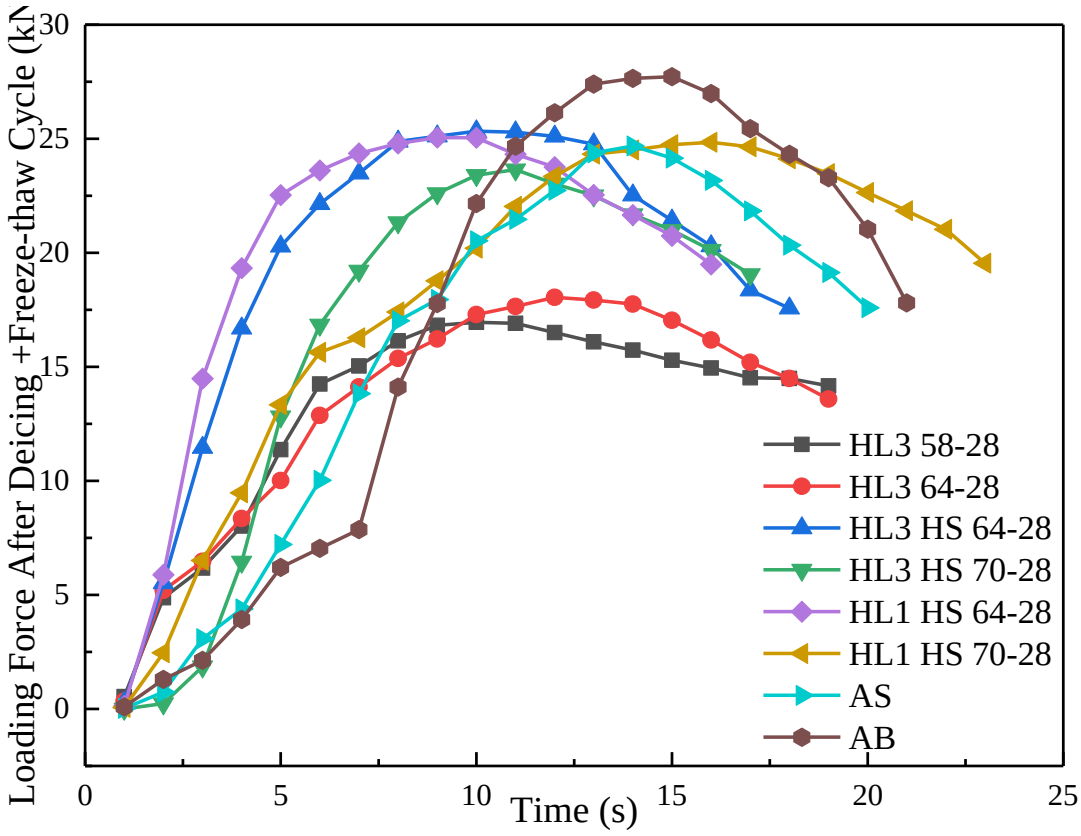

c. Test 3

Figure 7-9 Influence of Mix Type on Loading Force after De-icer and Freeze-thaw

Figure 7-7 presents the loading force of different mixes after de-icing treatment. Test 2 and Test 3 exhibit similar results in terms of the highest and the lowest shear strength, with airport binder course mix and HL1 HS 70-80 the highest, and HL3 58-28 and HL3 64-28 the lowest. However, Test 1 presents the airport surface course the best and HL1 HS 64-28 as the poorest. Figure 7-8 exhibits the shear strength after one freeze-thaw cycle. The results of three tests show inconsistency in terms of the highest shear strength after the treatment, with the airport binder course, HL1 HS 70-28, and HL3 HS 64-28 showed the highest shear loading force level in Test 1, Test 2, and Test 3, respectively. The HL3 64-28 displayed the poorest shear strength level in all three tests. Figure 7-9 shows that after de-icing and freeze-thaw treatment, the airport binder course has the best shear loading force in all three tests, and HL3 58-28 and HL3 64-28 have the lowest shear loading force.

7.3.3 Influence of Treatment on Loading Force of Road Mixes

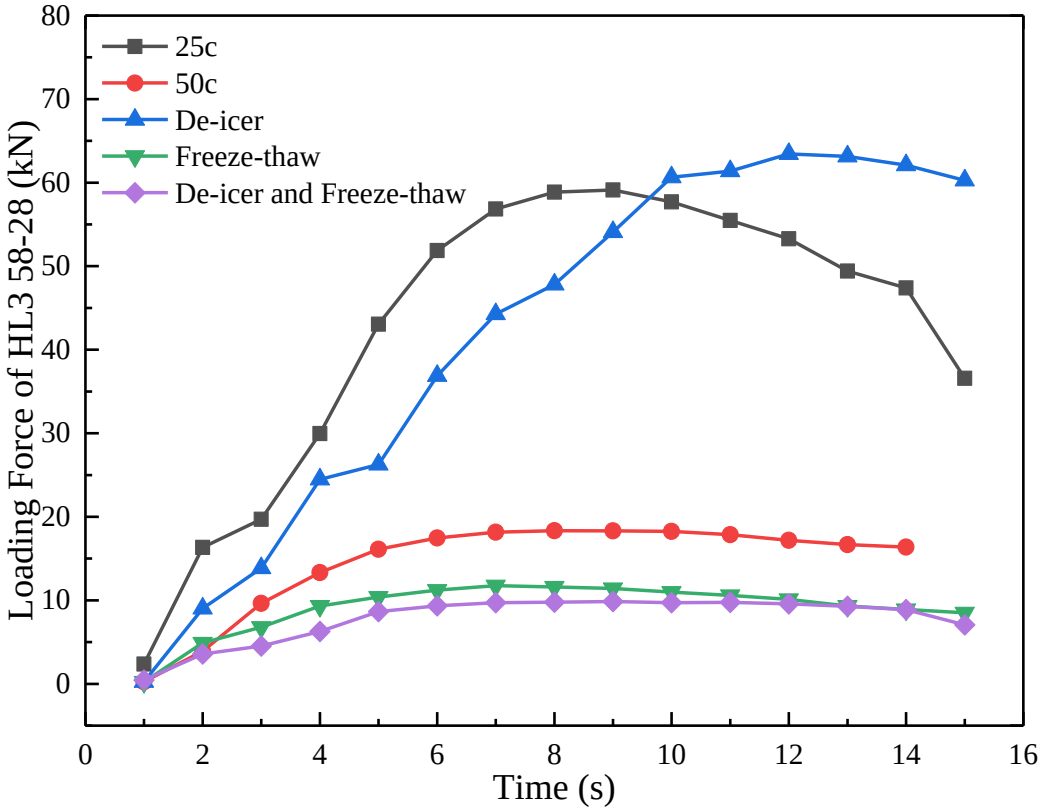

a. Test 1

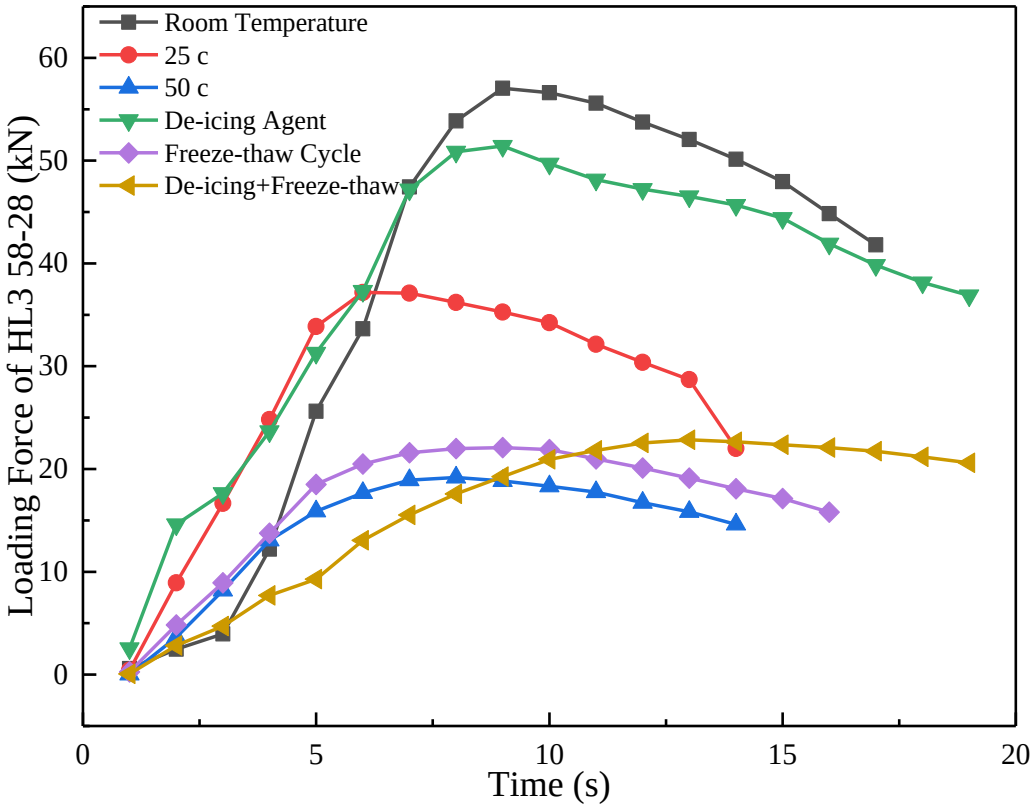

b. Test 2

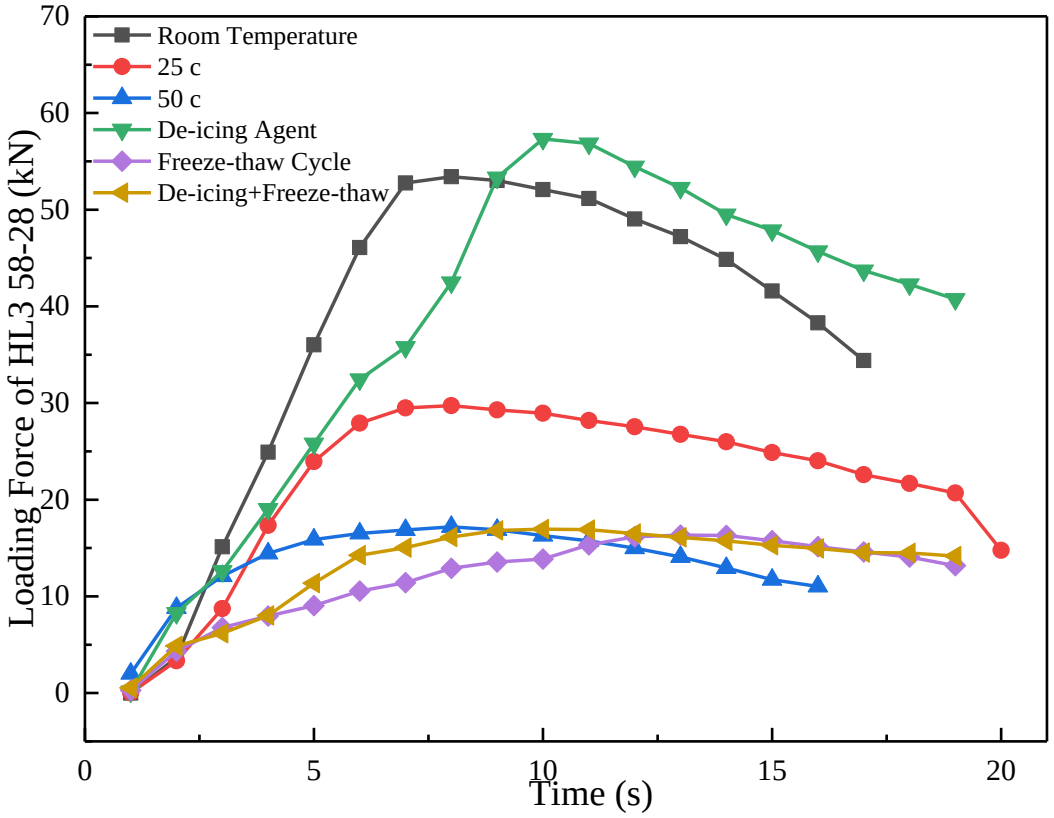

c. Test 3

Figure 7-10 Loading Force of HL 3 58-28

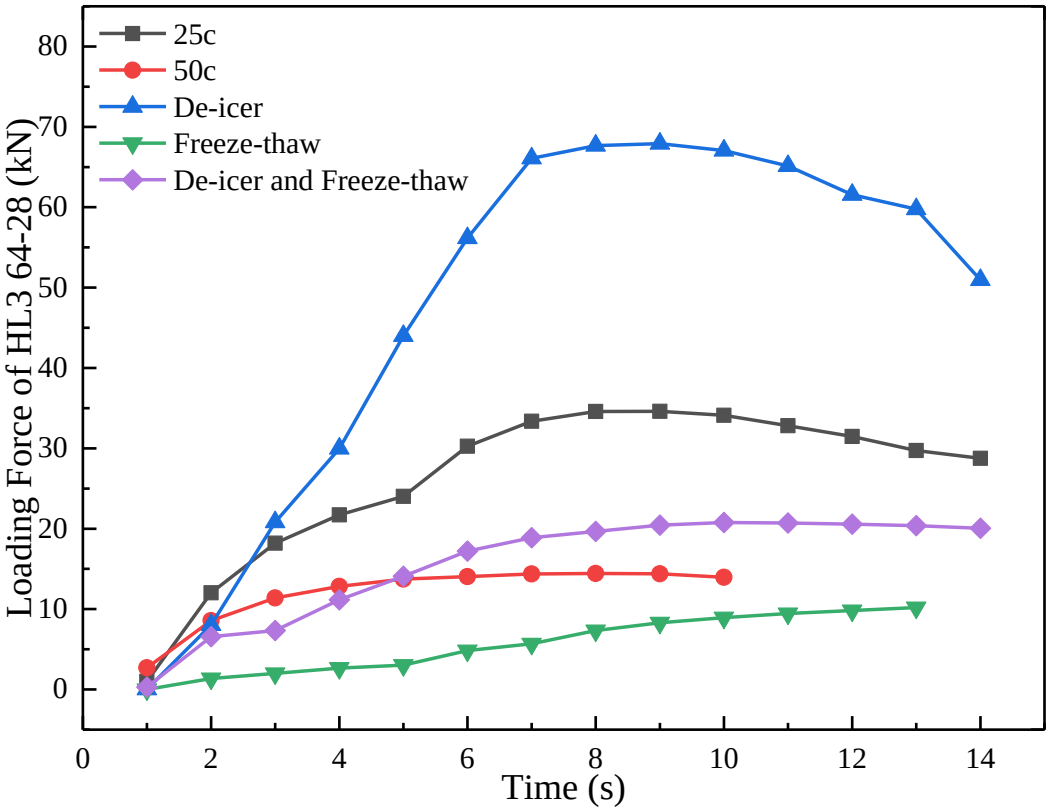

a. Test 1

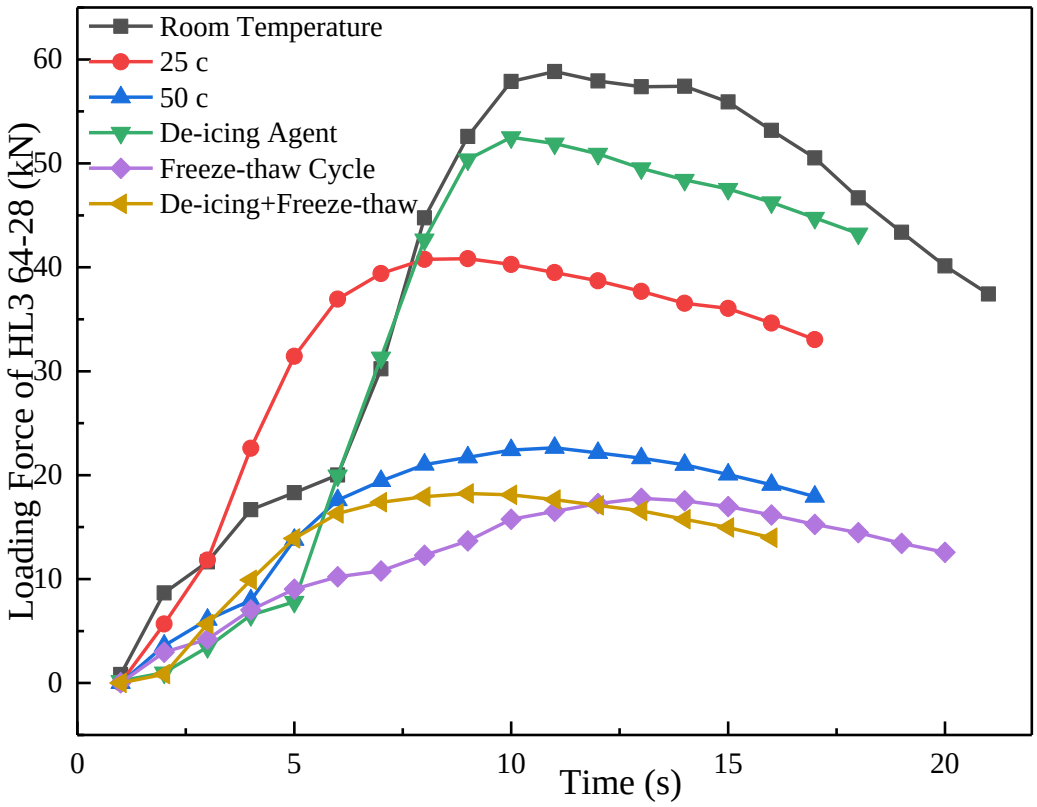

b. Test 2

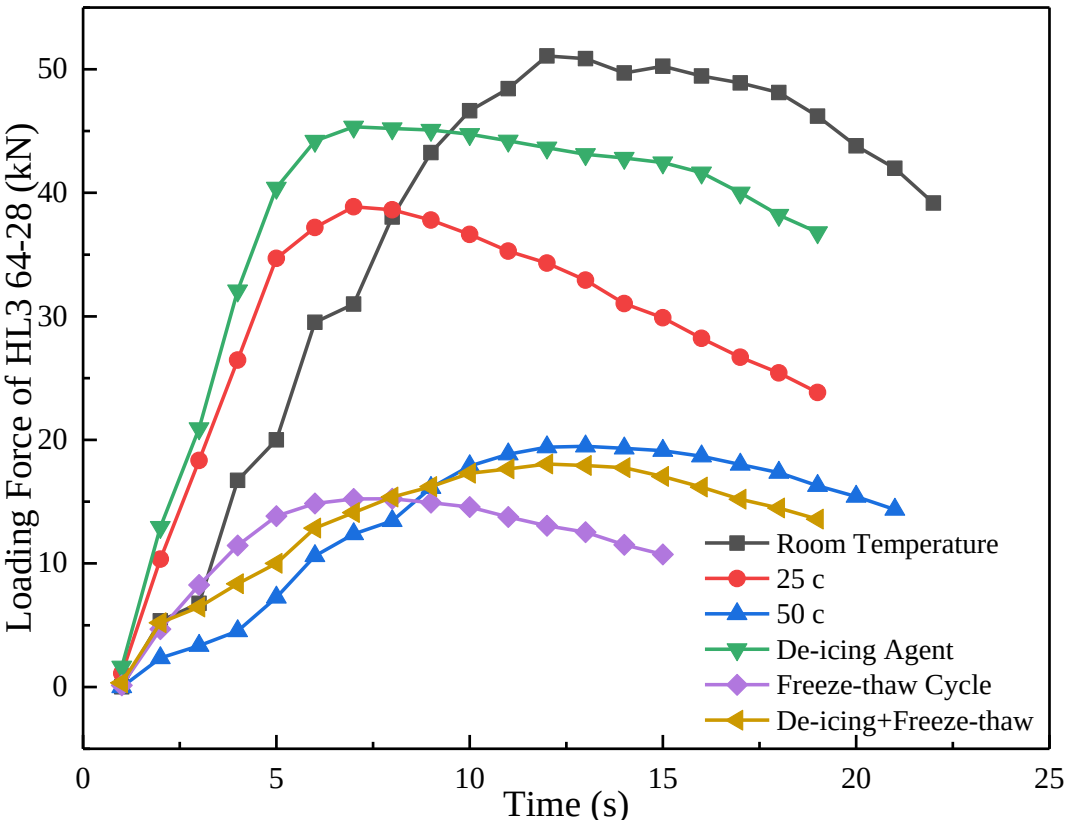

c. Test 3

Figure 7-11 Loading Force of HL3 64-28

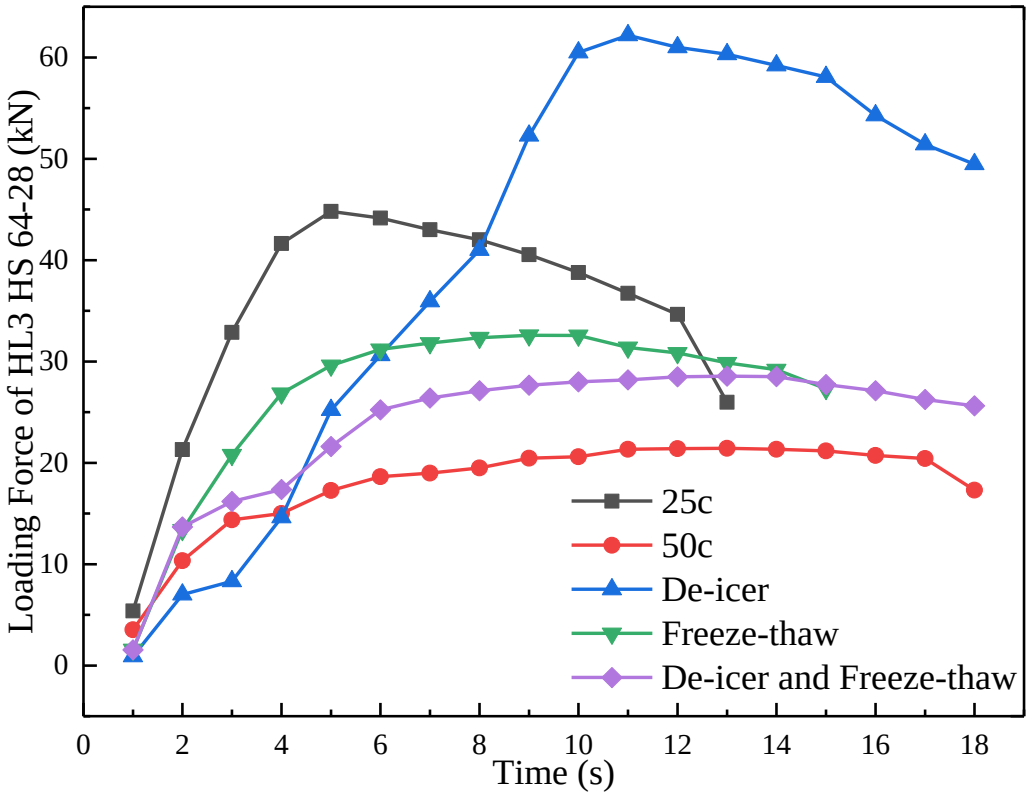

a. Test 1

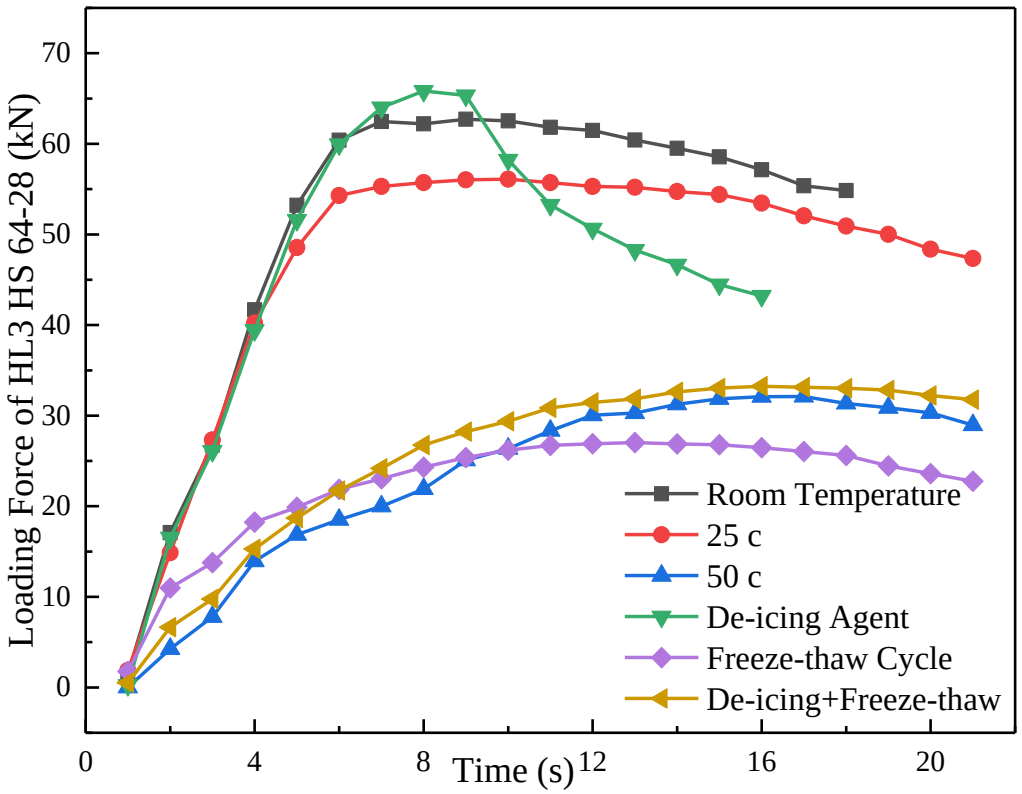

a. Test 2

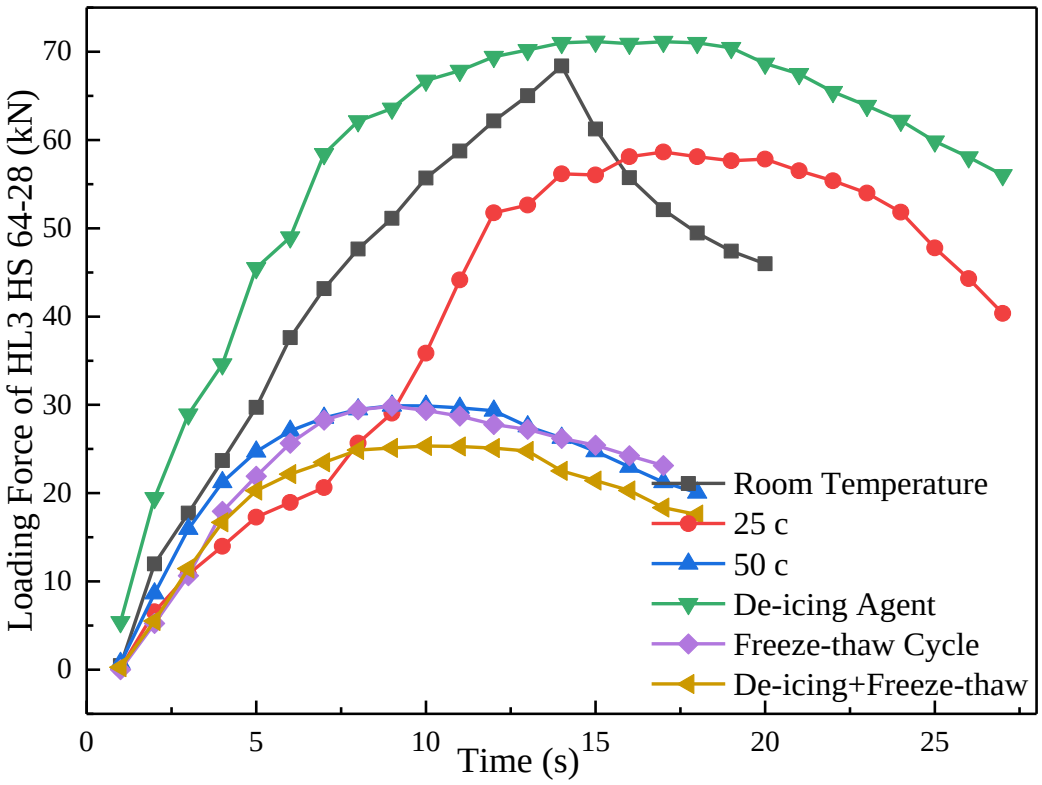

b. Test 3

Figure 7-12 Loading Force of HL3 HS 64-28

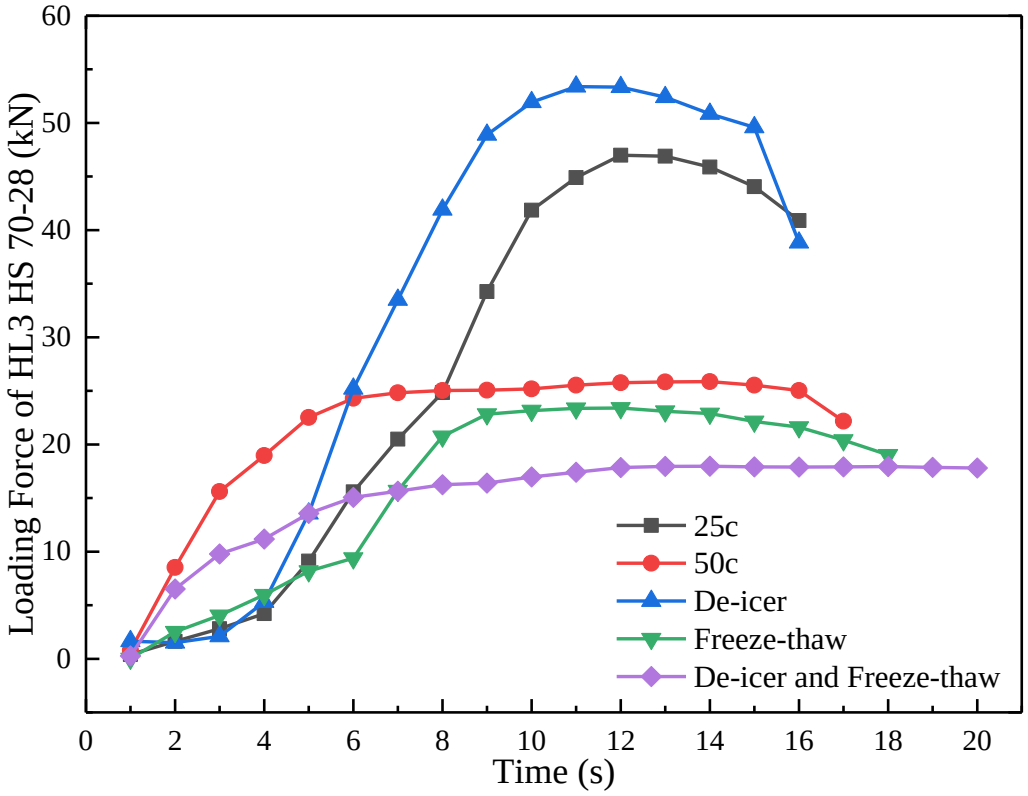

a. Test 1

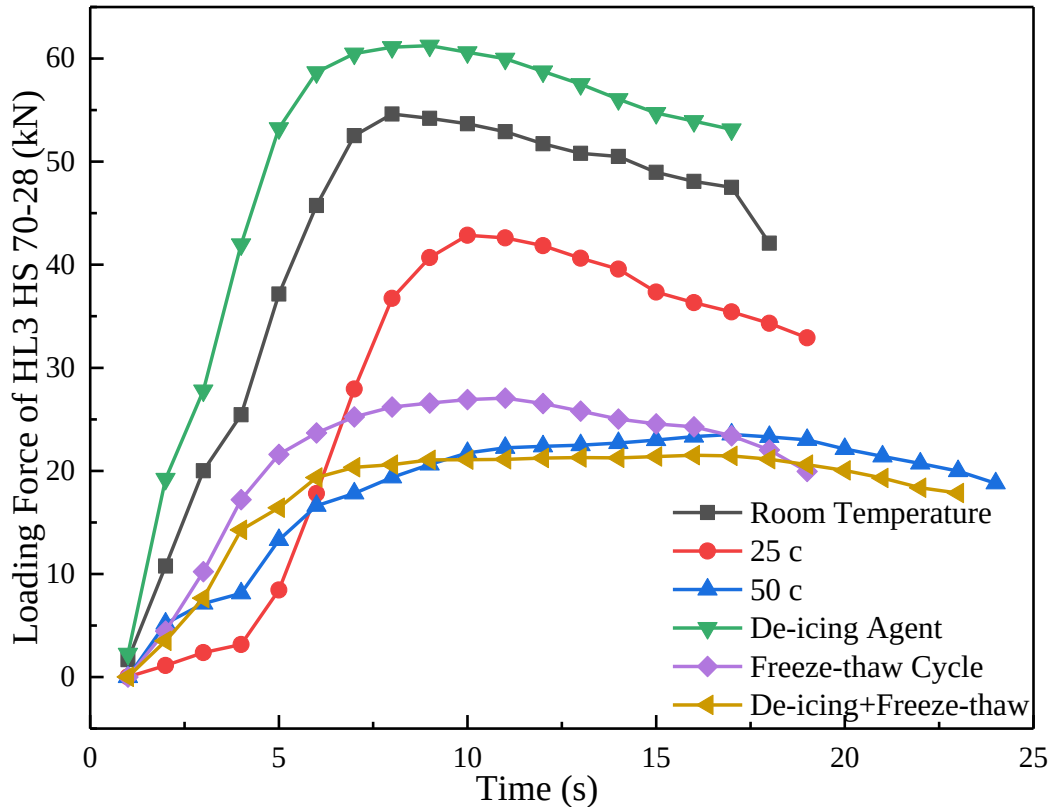

b. Test 2

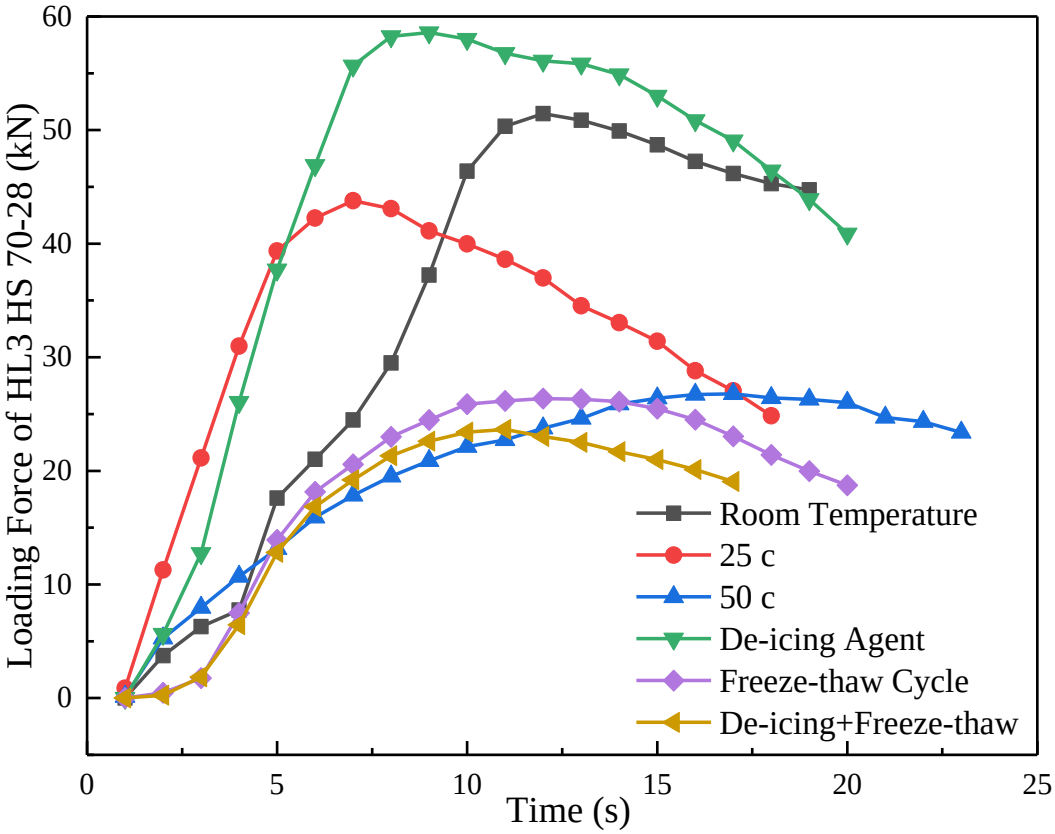

c. Test 3

Figure 7-13 Loading Force of HL3 HS 70-28

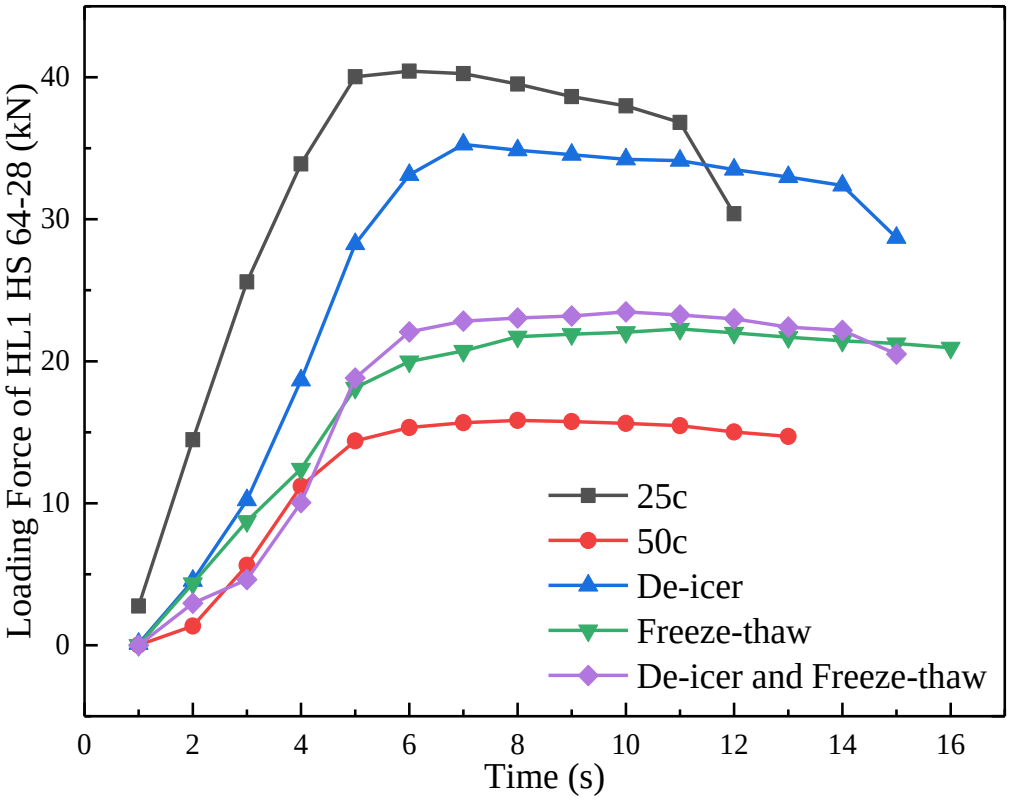

a. Test 1

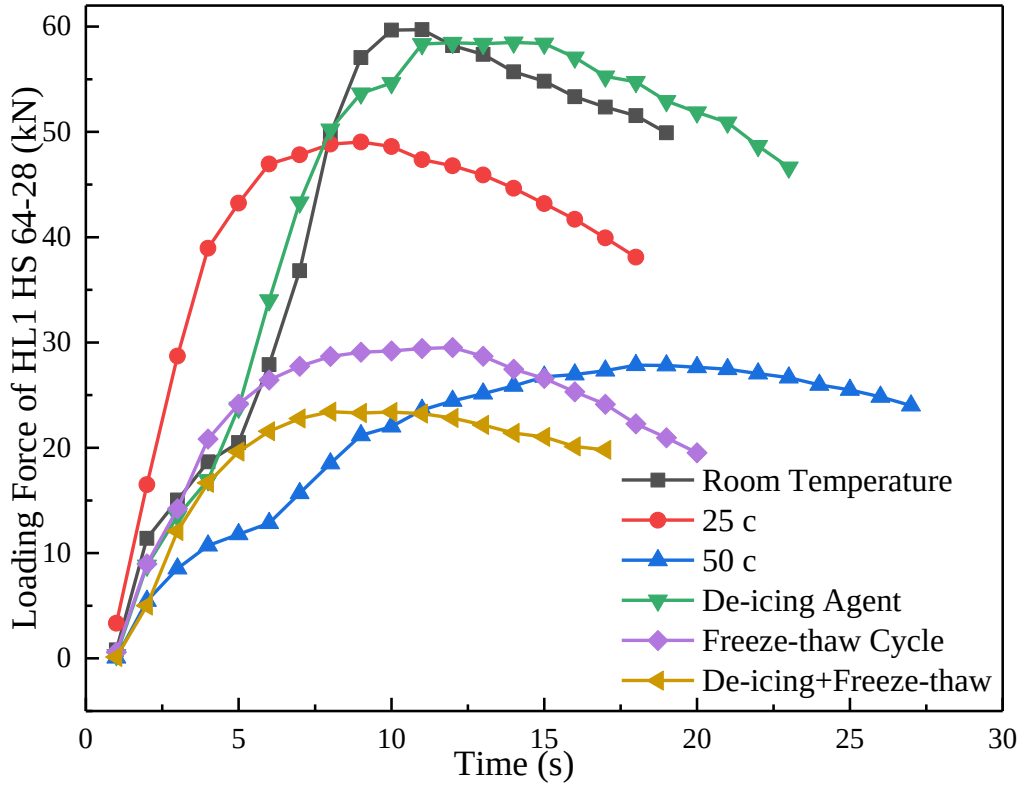

b. Test 2

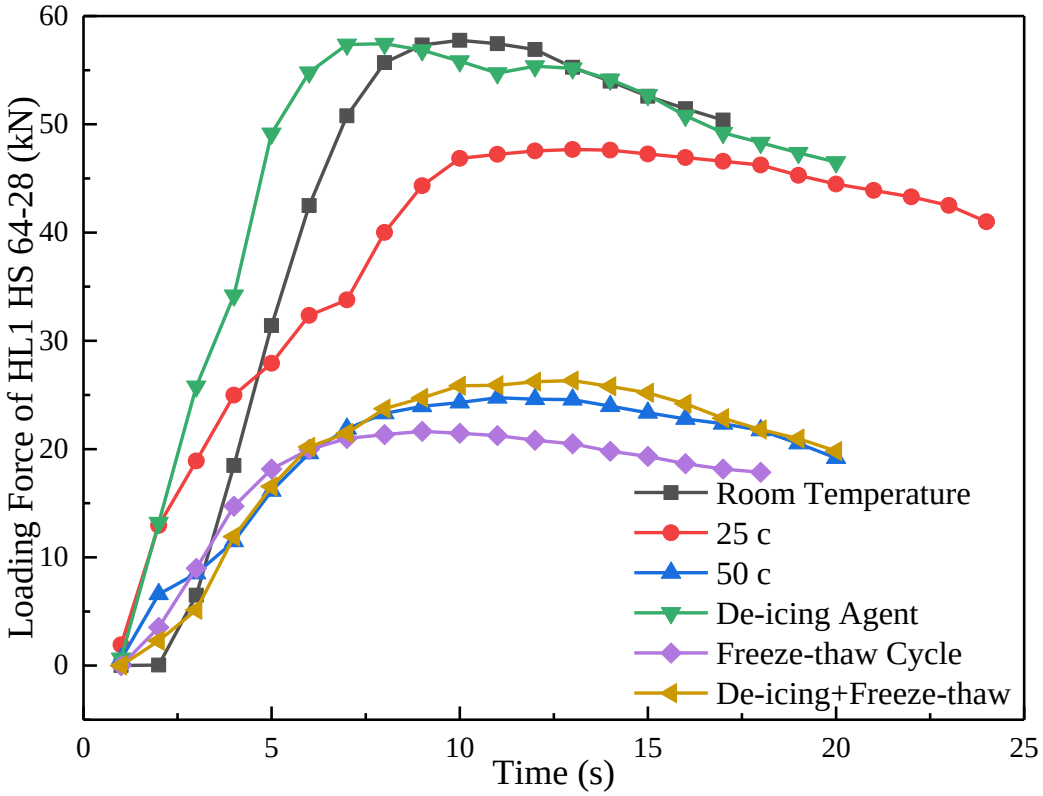

c. Test 3

Figure 7-14 Loading Force of HL1 HS 64-28

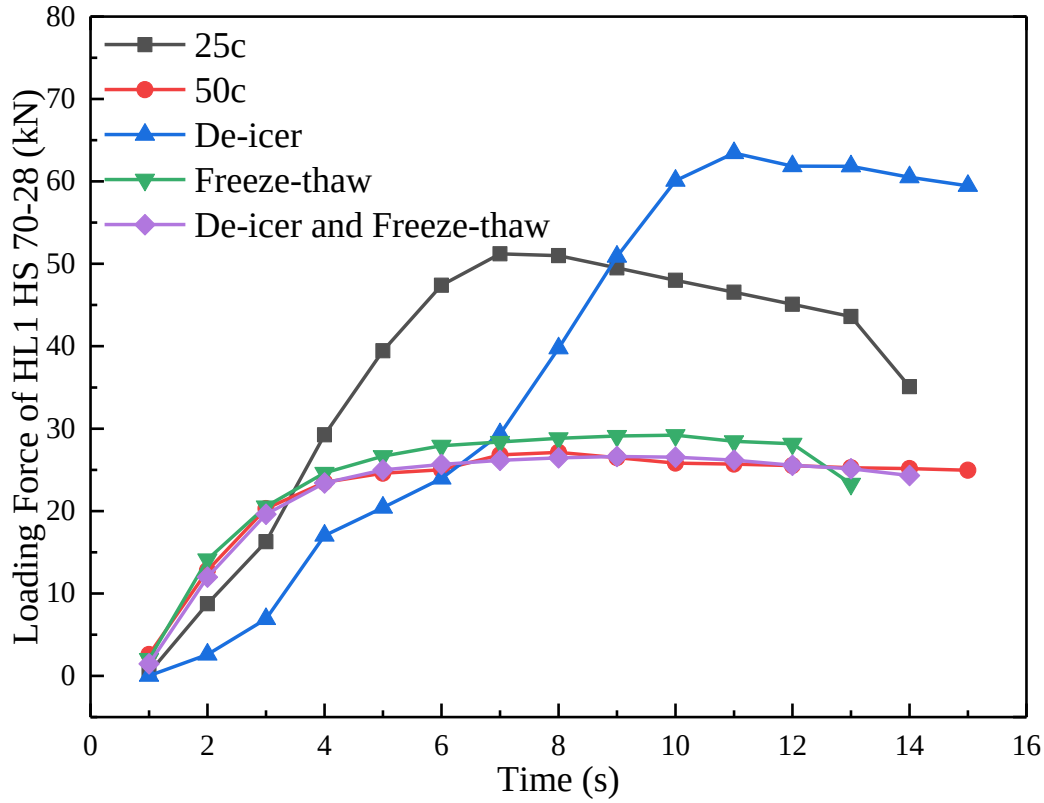

a. Test 1

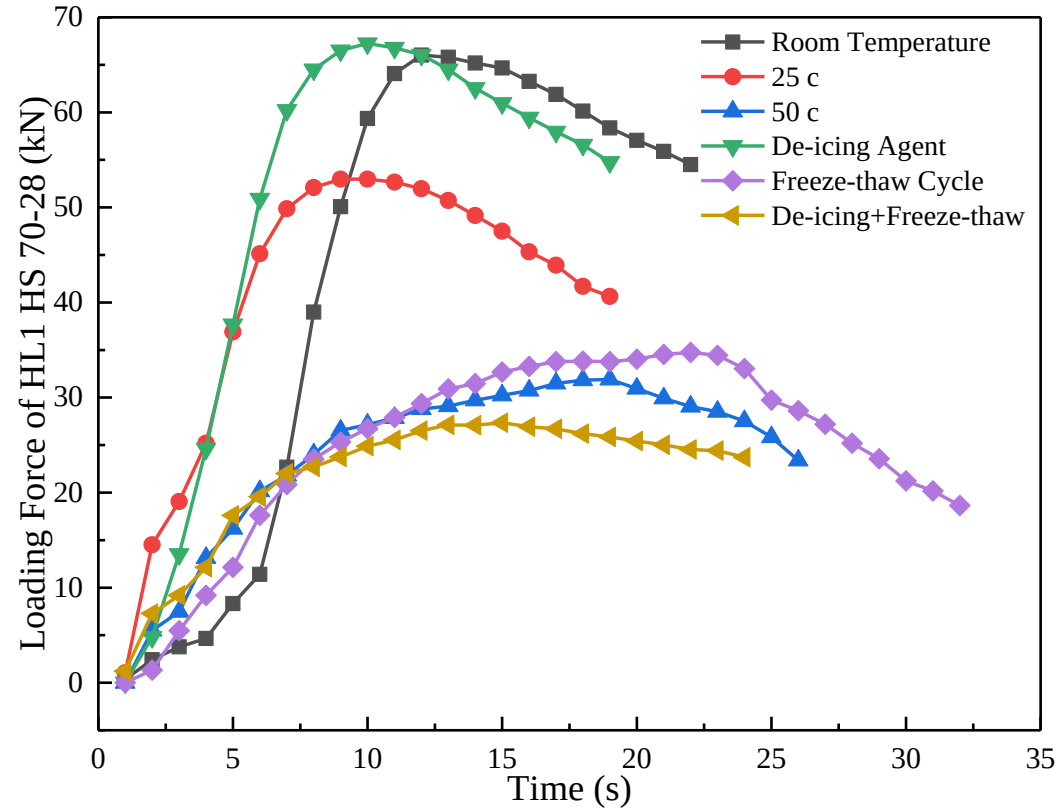

b. Test 2

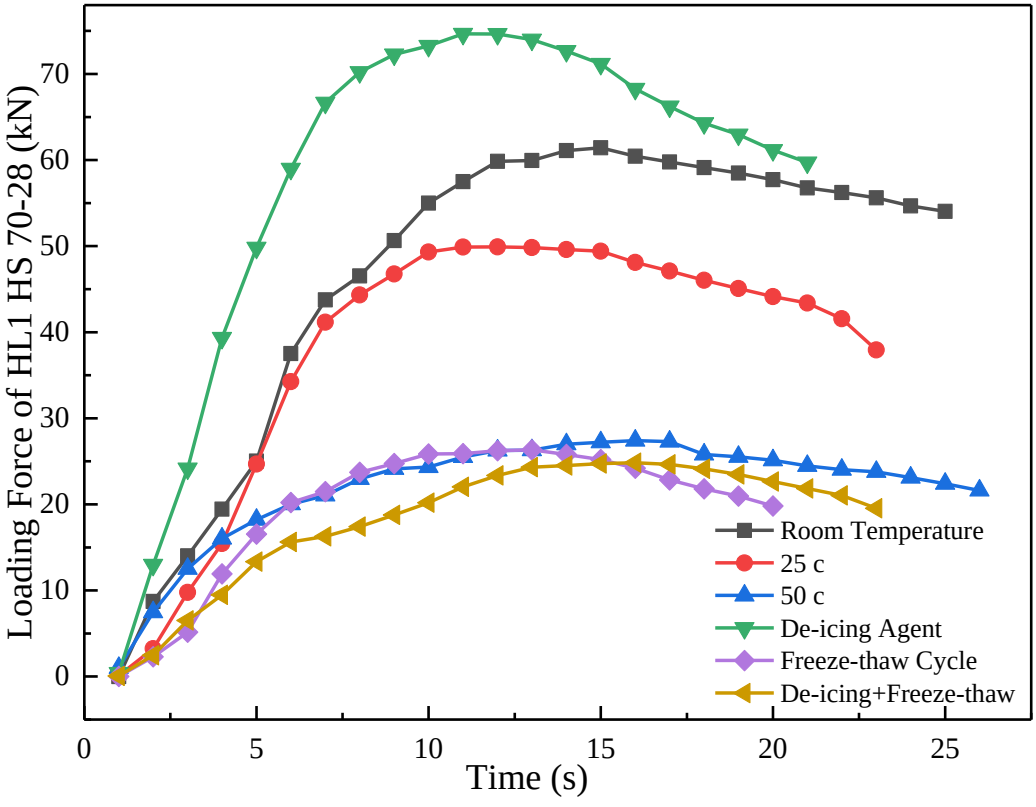

c. Test 3

Figure 7-15 Loading Force of HL1 HS 70-28

Figure 7-10 exhibits the loading force of HL3 58-28 after various treatments. It shows that high temperature 50 °C and the freeze-thaw cycle can significantly reduce the shear resistance. The specimens under room temperature and de-icing treatment show the highest shear resistance.

Figure 7-11 shows the results of HL3 64-28. The specimens at room temperature display the best shear resistance, and those after the freeze-thaw cycle show the poorest. However, inconsistency was found in HL3 HS 64-28. As shown in Figure 7-12, the highest shear loading force appeared on specimens after de-icing treatment in Test 2 and Test 3, and the lowest shear resistance showed at high temperature, freeze-thaw cycle, and de-icing plus freeze-thaw treatment, respectively.

Figure 7-13 presents that the highest shear resistance of HL3 HS 70-28 appeared on specimens after de-icing treatment, and the lowest loading force occurred after de-icing plus freeze-thaw treatment for all three tests.

For HL1 HS 64-28 in Figure 7-14, the best shear resistance shows after room temperature and de-icing treatment, while the poorest performance occurs at high temperature, de-icing plus freeze-thaw, and freeze-thaw cycle in Test 1, Test 2, and Test 3, respectively.

In Figure 7-15, the highest shear resistance occurred at specimens after de-icing treatment and the lowest appeared at de-icing plus freeze-thaw treatment.

Figure 7-11 to Figure 7-15 indicate that shear resistance of roadway asphalt mixtures reduces with the increase of temperature, and the freeze-thaw cycle has the most severe impact on reducing the shear strength among different mixes.

The existence of de-icing agent at room temperature maintains the shear resistance of the asphalt mixture. However, when combined with the freeze-thaw cycle, it shows some inconsistency in terms of shear resistance. Therefore, it may not protect the freeze-thaw as expected.

7.3.4 Influence of Treatment on Loading Force of Airport Mixes

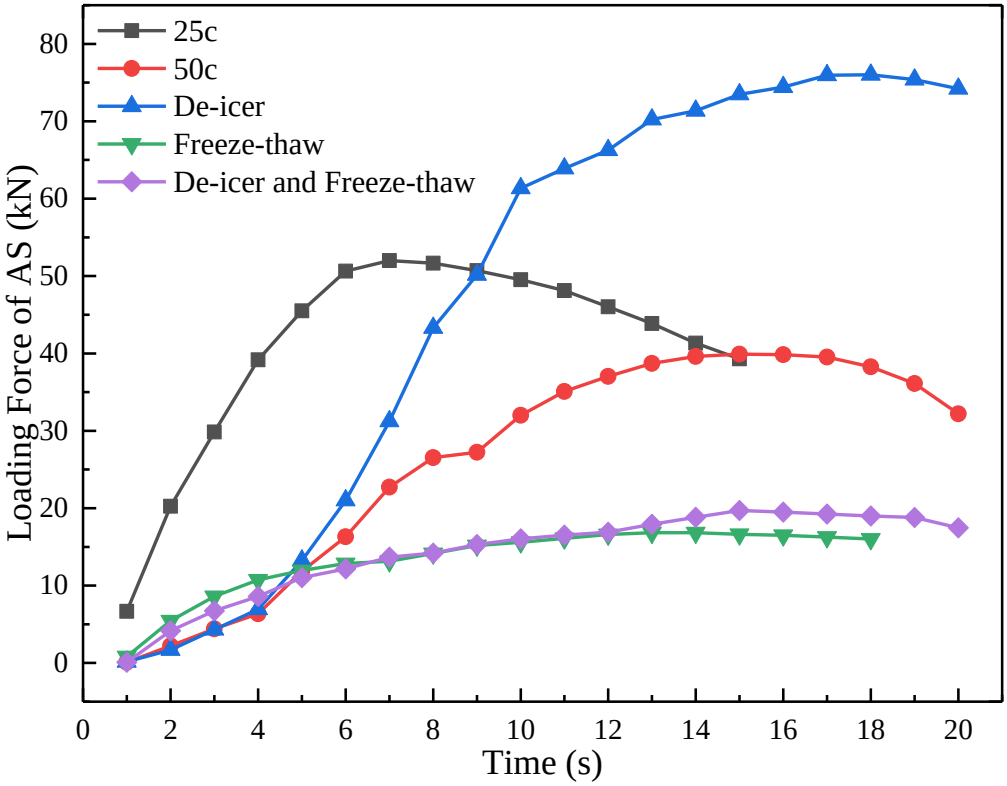

a. Test 1

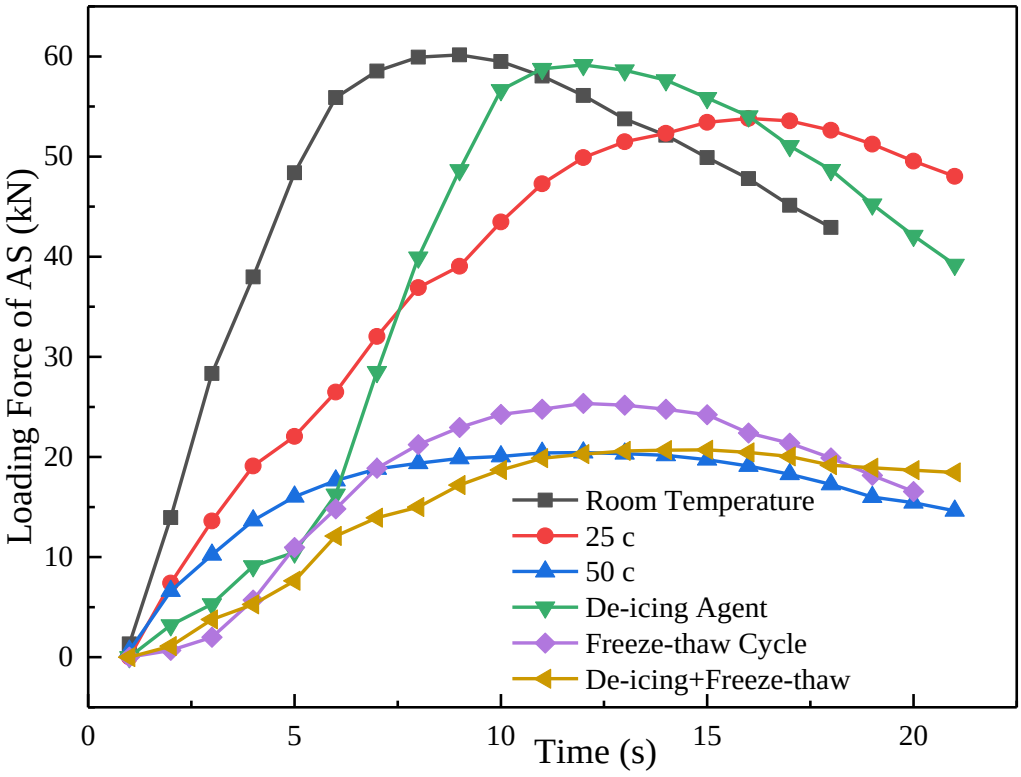

b. Test 2

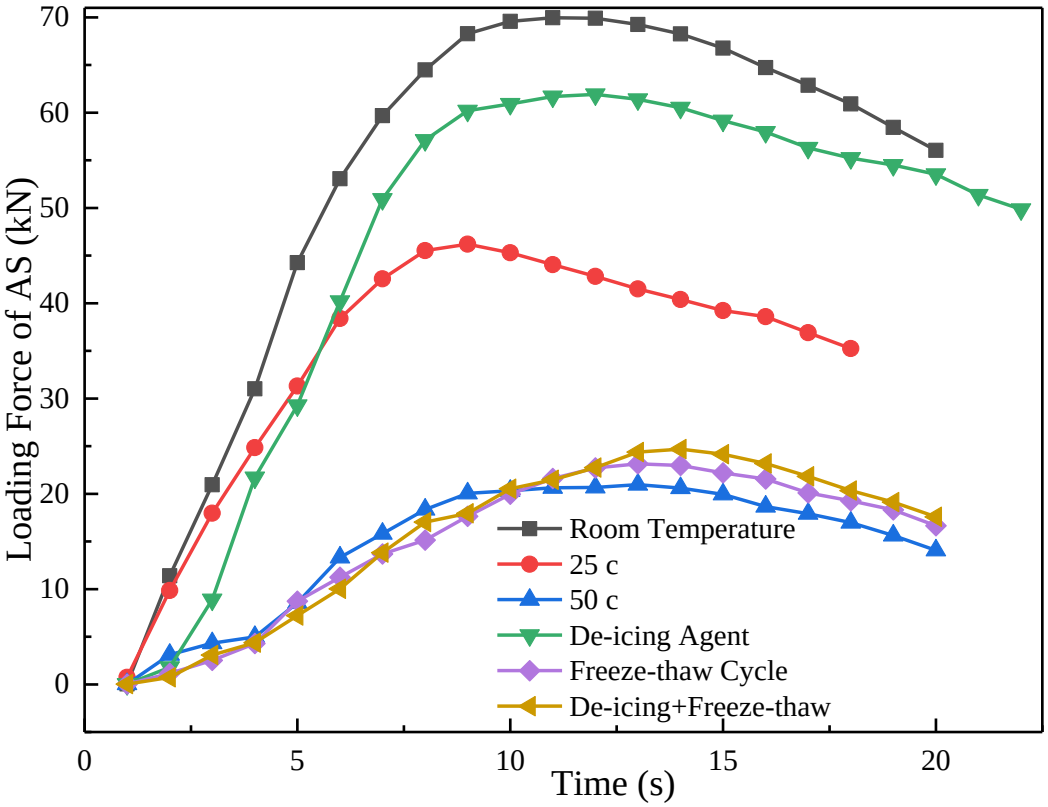

c. Test 3

Figure 7-16 Airport Surface Course

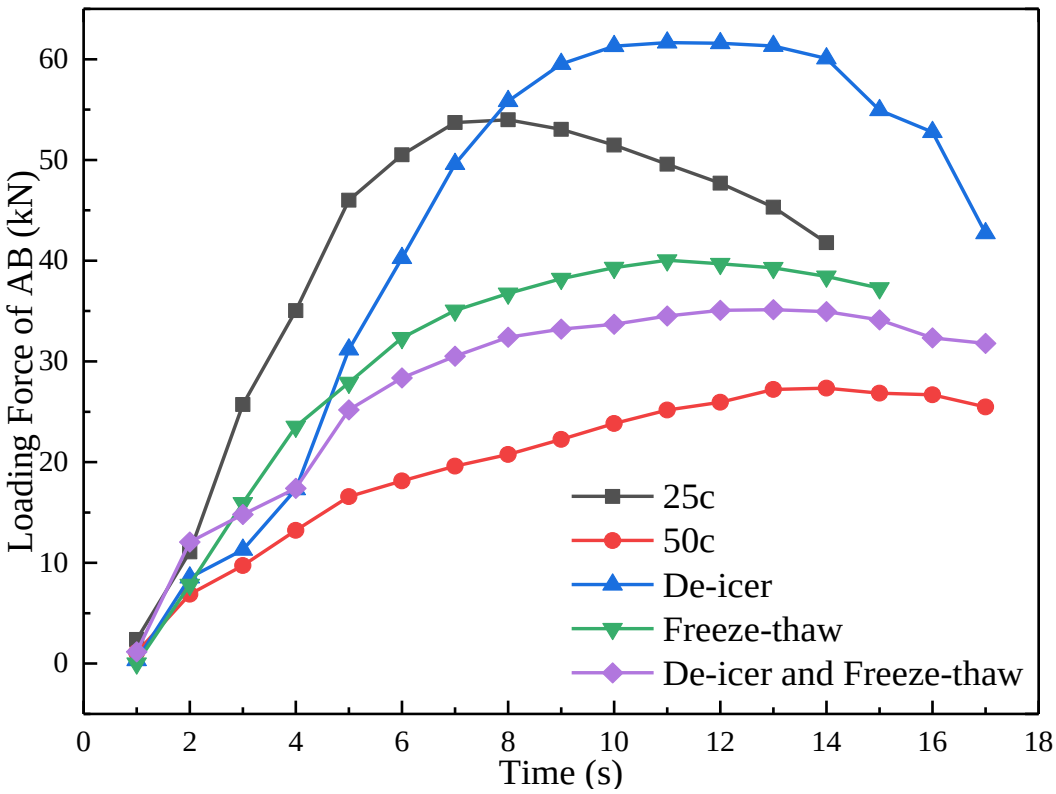

a. Test 1

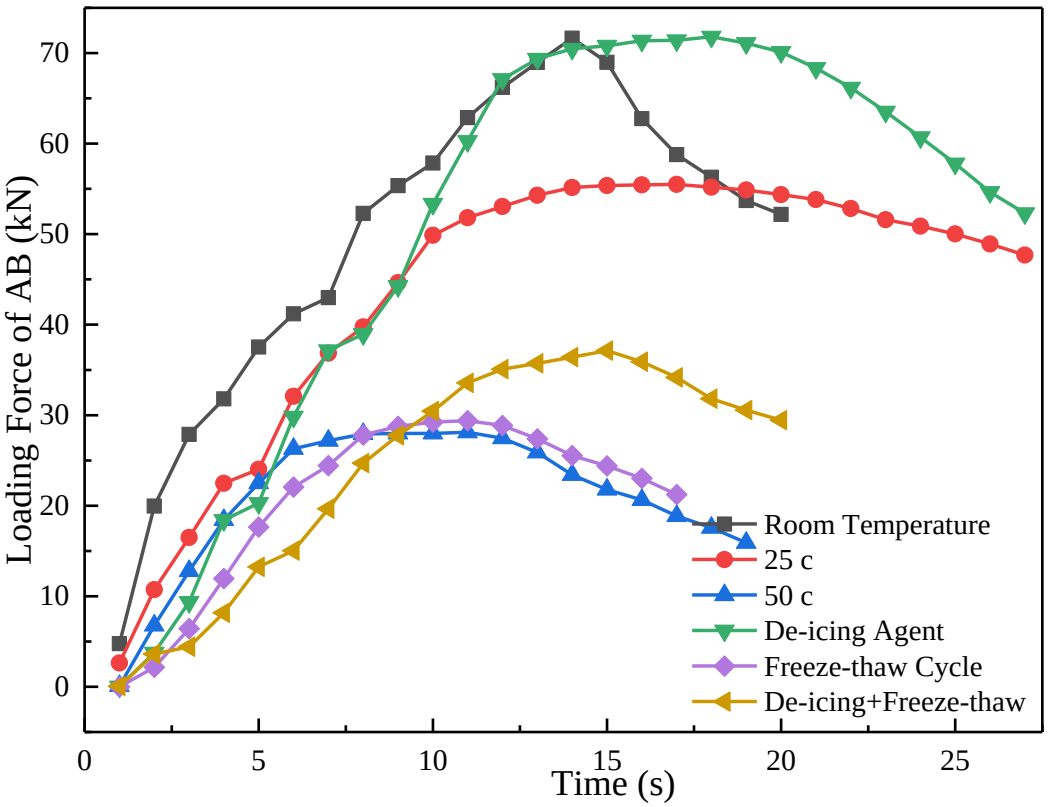

b. Test 2

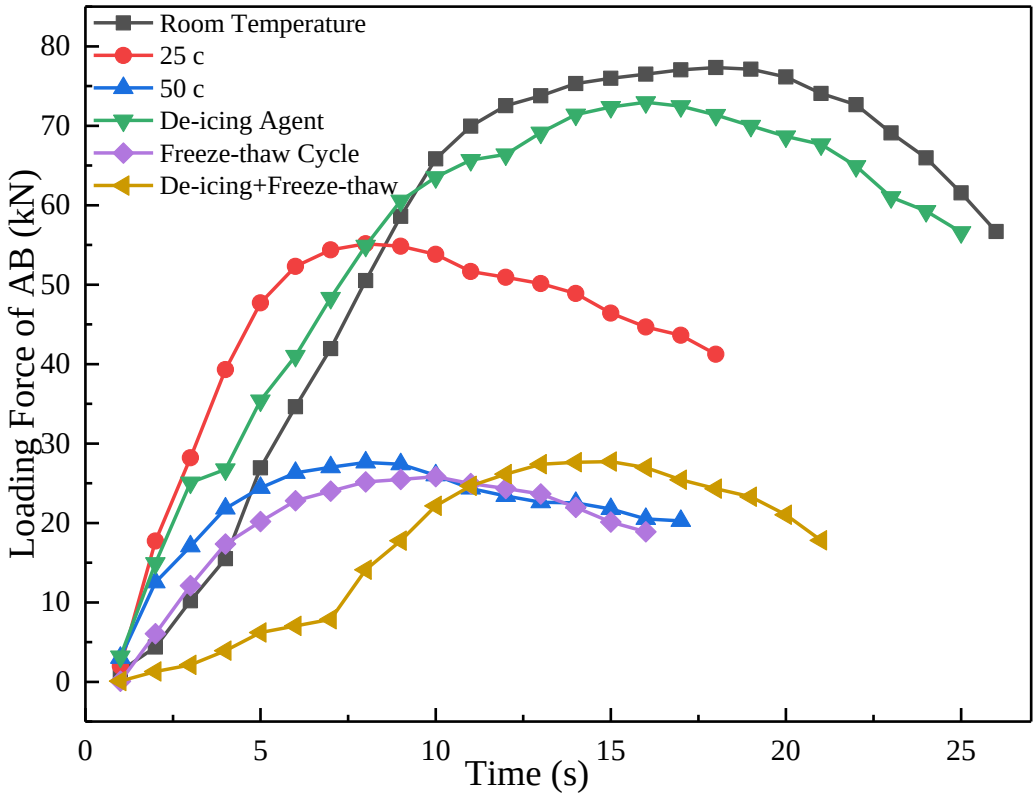

c. Test 3

Figure 7-17 Airport Binder Course

For airport surface course and binder course mixes as shown in Figure 7-16 and Figure 7-17, a similar trend can be seen for both mixes. Specimens after de-icing treatment or room temperature show the highest shear loading force while freeze-thaw, de-icing plus freeze-thaw appears to reduce the shear resistance.

7.3.5 Influence of Mix Type and Treatment on Shear Resistance

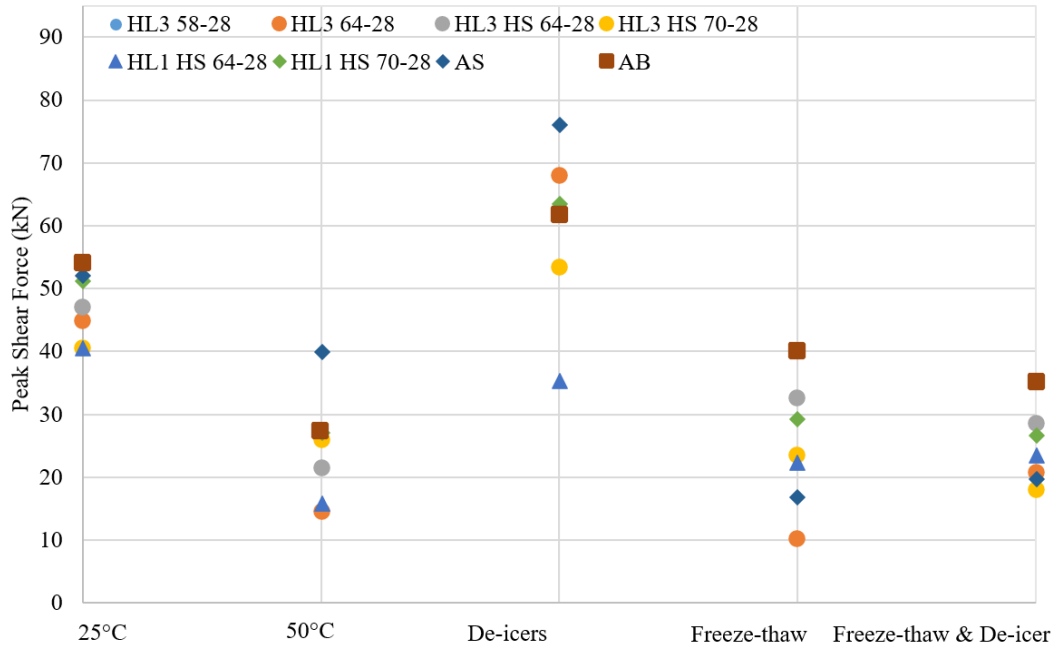

a. Test 1

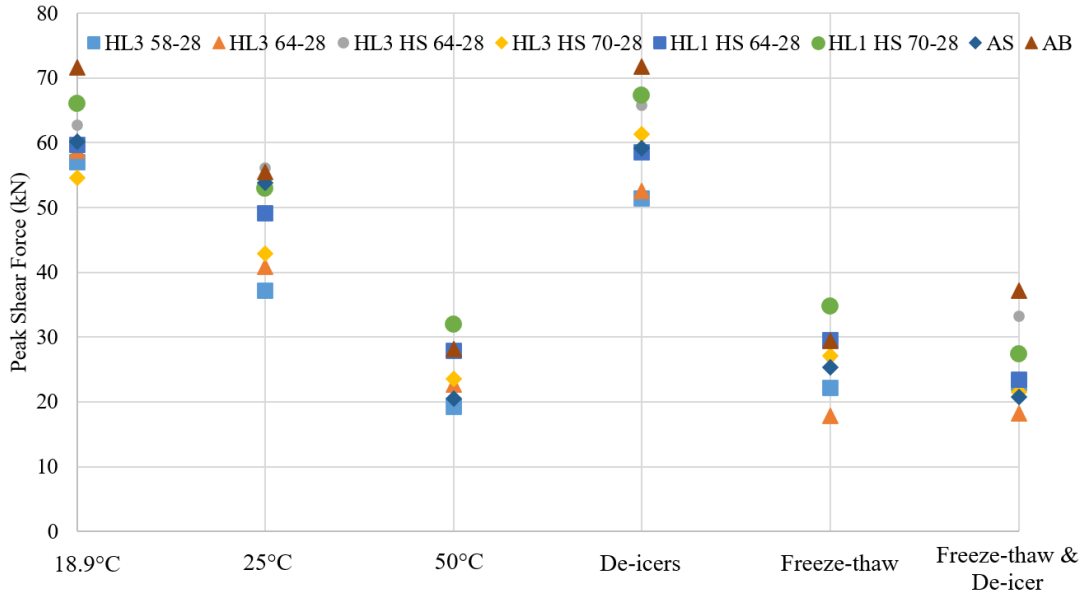

b. Test 2

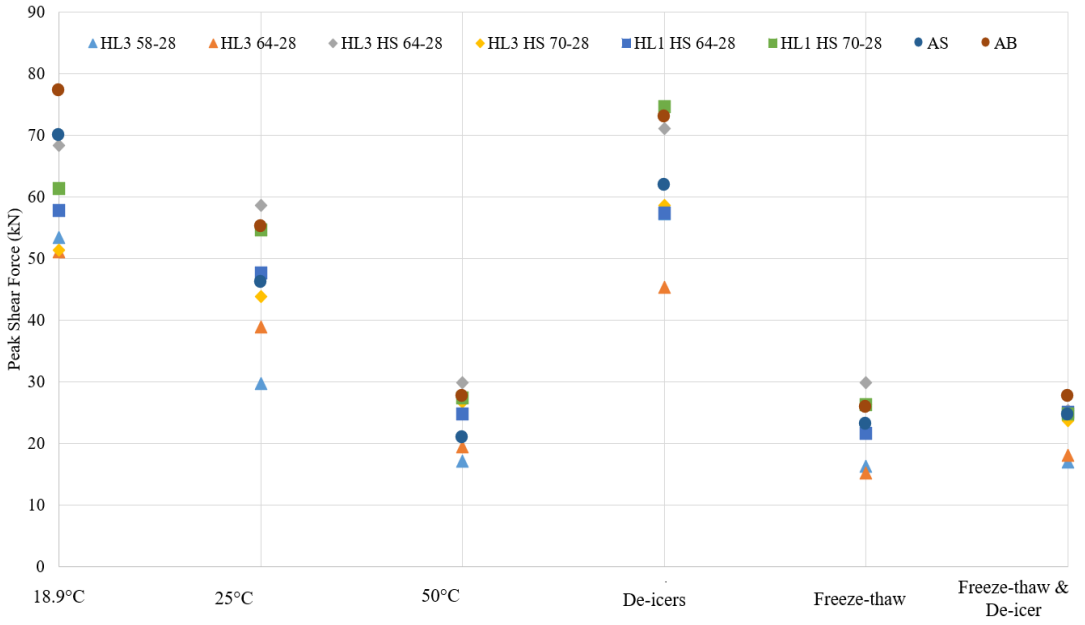

c. Test 3

Figure 7-18 Peak Shear Force

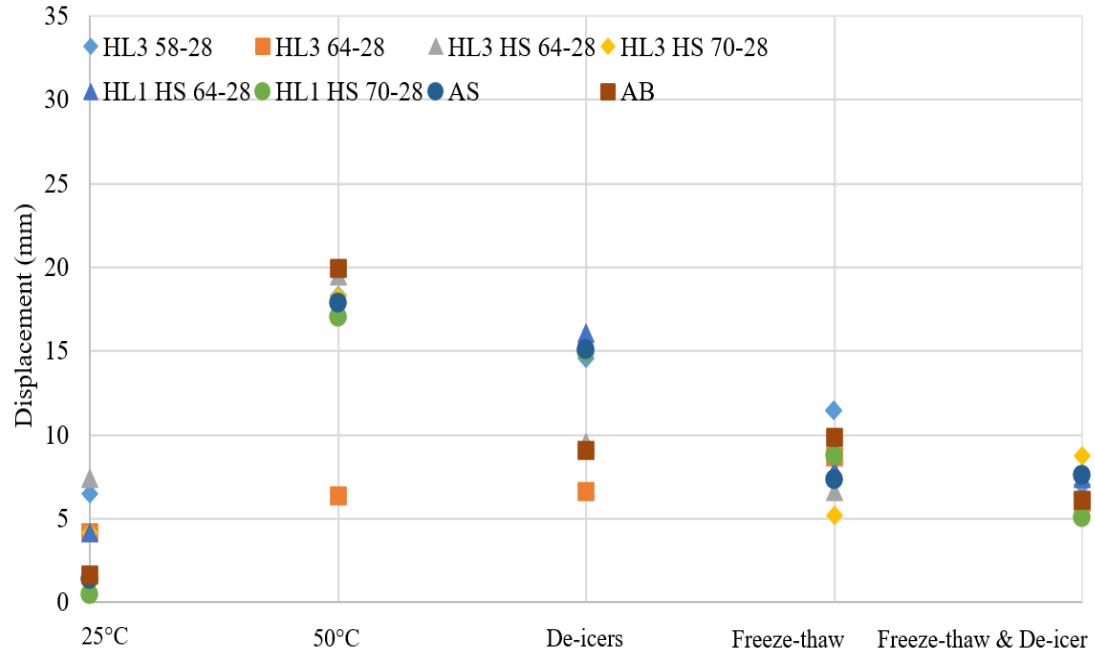

a. Test 1

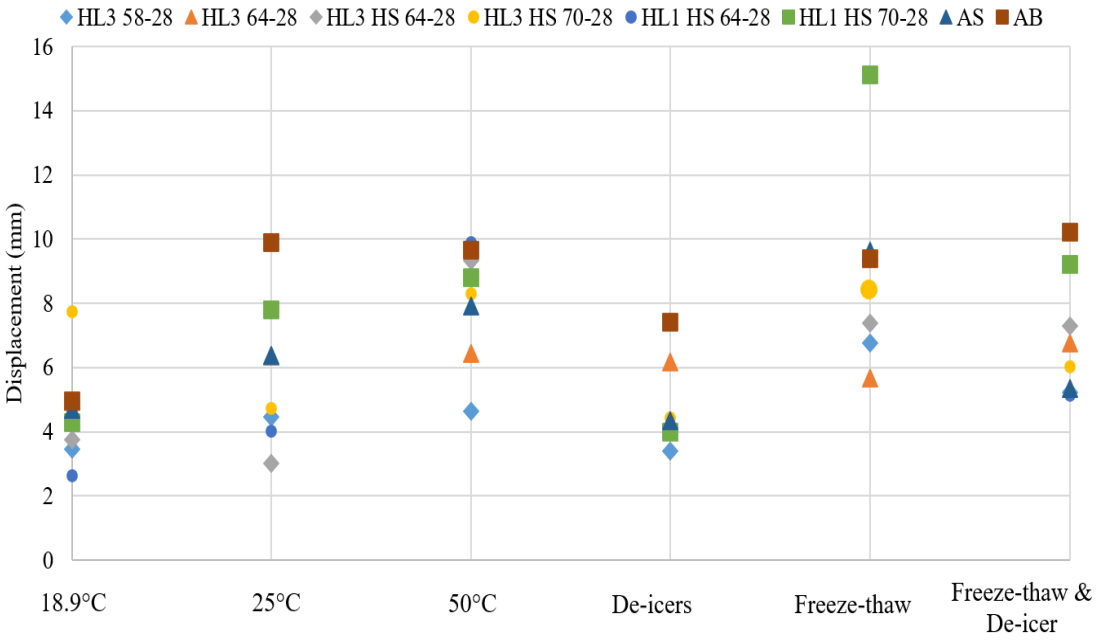

b. Test 2

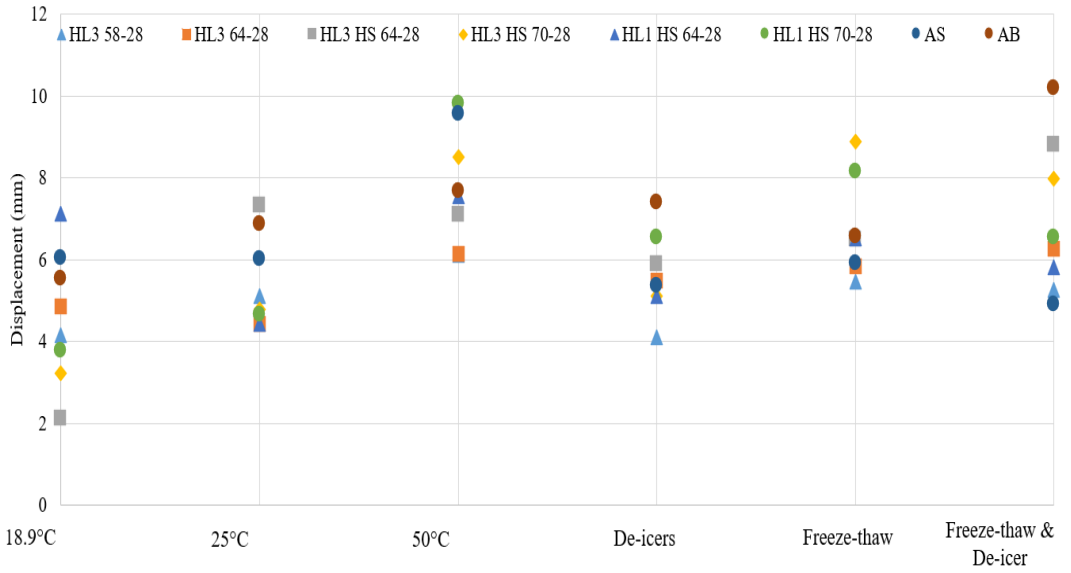

c. Test 3

Figure 7-19 Displacement

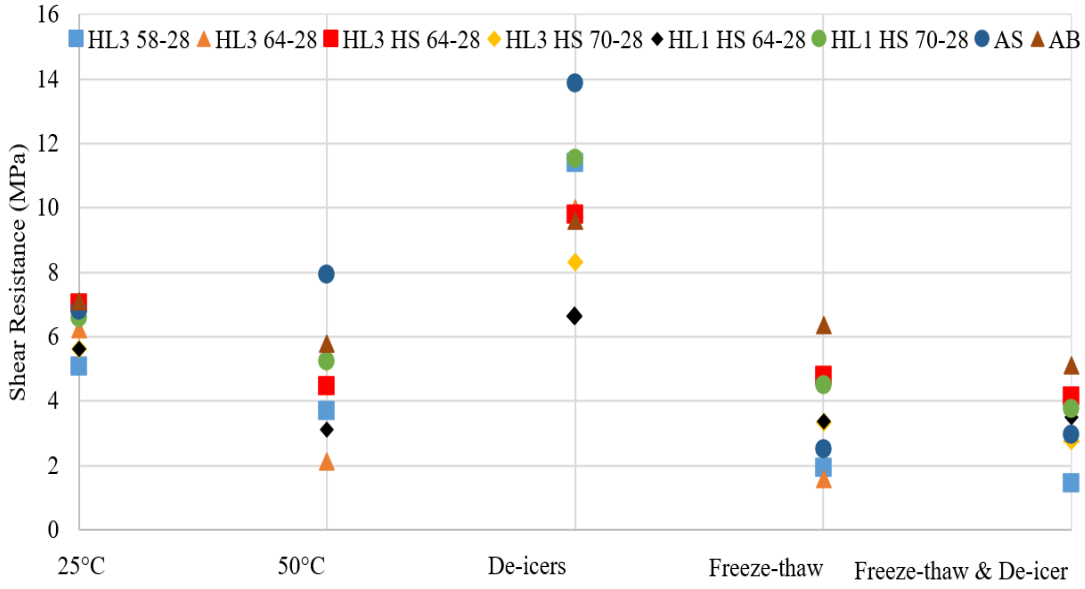

a. Test 1

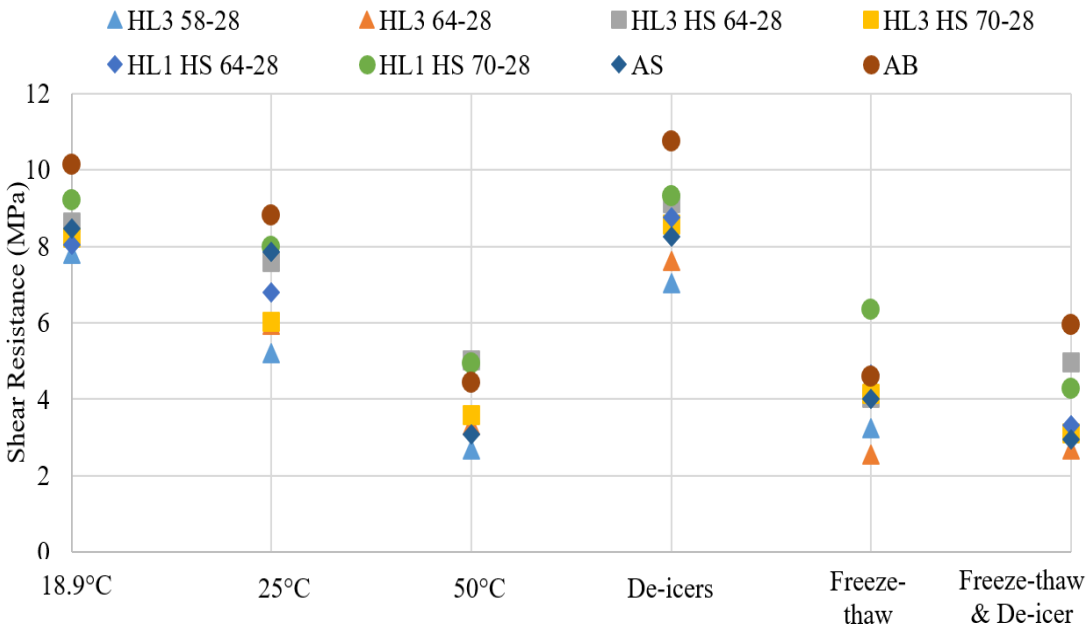

b. Test 2

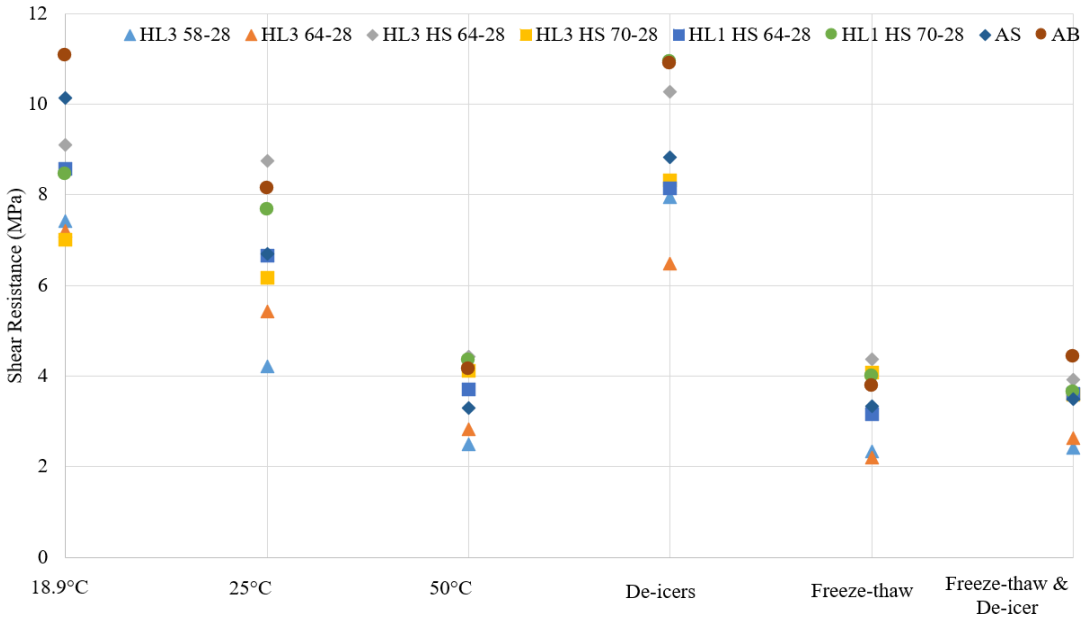

c. Test 3

Figure 7-20 Shear Resistance of Asphalt Mixture after Various Treatments

Figures 7-18 to 7-20 show that the peak shear force, displacement, and shear resistance of all mixes decrease with the increase of temperature. The peak shear force and shear resistance perform the best after room temperature or de-icer treatment. The shear resistance reduced with the increase of the temperature. Freeze-thaw can significantly damage the shear resistance as well, however, with the existence of a de-icing agent, this impact can be reduced.

7.4 Statistical Analysis: Single-Factor ANOVA

7.4.1 Effect of Mix Type on Loading Shear Force

The peak loading force of each mix at six different treatments was analyzed with single factor ANOVA (shown in Table 7-1) to investigate the effect of mixes type on maximum shear loading force. The single factor ANOVA test null hypothesis is that the means of observations grouped by mix type are the same, namely the mixes type does not affect the maximum loading force means. The alpha level is 0.05.

Table 7-1 Single Factor ANOVA of Effect of Mixes Type on Shear Loading Force

	Source	*SS*	*df*	*MS*	*F*	*P-value*	*F crit*
Room Temp.	Between Groups	727.66	7.00	103.95	6.18	1.0E-02	3.50
	Within Groups	134.52	8.00	16.81			
	Total	862.17	15.00				
	Source	*SS*	*df*	*MS*	*F*	*P-value*	*F crit*
25 c	Between Groups	1155.99	7.00	165.14	12.60	1.9E-05	2.66
	Within Groups	209.72	16.00	13.11			
	Total	1365.71	23.00				
	Source	*SS*	*df*	*MS*	*F*	*P-value*	*F crit*
50 c	Between Groups	363.88	7.00	51.98	1.87	1.4E-01	2.66
	Within Groups	444.13	16.00	27.76			
	Total	808.00	23.00				
	Source	*SS*	*df*	*MS*	*F*	*P-value*	*F crit*
De-icing	Between Groups	1007.77	7.00	143.97	2.17	9.4E-02	2.66
	Within Groups	1061.14	16.00	66.32			
	Total	2068.91	23.00				
	Source	*SS*	*df*	*MS*	*F*	*P-value*	*F crit*
Freeze-thaw	Between Groups	848.82	7.00	121.26	5.88	1.6E-03	2.66
	Within Groups	329.74	16.00	20.61			
	Total	1178.56	23.00				
	Source	*SS*	*df*	*MS*	*F*	*P-value*	*F crit*
De-icing and Freeze-thaw	Between Groups	635.22	7.00	90.75	7.07	6.1E-04	2.66
	Within Groups	205.25	16.00	12.83			
	Total	840.47	23.00				

As shown in Table 7-1, the p-values of observations under room temperature, 50 °C, and de-icing treatment are greater than 0.05. Therefore, the hypothesis is accepted, and the mix type does not have a significant effect on maximum shear loading force under the aforementioned treatment. However, the p-values of observations under 25 °C, freeze-thaw, and de-icing plus freeze-thaw treatment are far smaller than 0.05. Thus the hypothesis is rejected and the mix type has a significant effect on maximum shear loading force under these treatments.

7.4.2 Effect of treatment on Loading Shear Force

One single factor ANOVA was conducted to investigate the effect of treatment on the peak shear loading force. The null hypothesis is that means of observations grouped by

treatment type are the same, namely, the treatments don't affect the maximum shear loading force of the asphalt mixture. The alpha level is 0.05.

Table 7-2 Single Factor ANOVA on Effect of Treatment on Shear Loading Force

	Source	*SS*	*df*	*MS*	*F*	*P-value*	*F crit*
HL3 58-28	Between Groups	5005.54	5.00	1001.11	44.51	6.24E-07	3.20
	Within Groups	247.43	11.00	22.49			
	Total	5252.97	16.00				
	Source	*SS*	*df*	*MS*	*F*	*P-value*	*F crit*
HL3 64-28	Between Groups	4890.85	5.00	978.17	28.08	6.54E-06	3.20
	Within Groups	383.22	11.00	34.84			
	Total	5274.07	16.00				
	Source	*SS*	*df*	*MS*	*F*	*P-value*	*F crit*
HL3 HS 64-28	Between Groups	4787.29	5.00	957.46	43.41	7.09E-07	3.20
	Within Groups	242.60	11.00	22.05			
	Total	5029.89	16.00				
	Source	*SS*	*df*	*MS*	*F*	*P-value*	*F crit*
HL3 HS 70-28	Between Groups	3446.09	5.00	689.22	104.28	6.94E-09	3.20
	Within Groups	72.71	11.00	6.61			
	Total	3518.79	16.00				
	Source	*SS*	*df*	*MS*	*F*	*P-value*	*F crit*
HL1 HS 64-28	Between Groups	3289.61	5.00	657.92	14.28	1.70E-04	3.20
	Within Groups	506.80	11.00	46.07			
	Total	3796.41	16.00				
	Source	*SS*	*df*	*MS*	*F*	*P-value*	*F crit*
HL1 HS 70-28	Between Groups	5028.20	5.00	1005.64	81.43	2.60E-08	3.20
	Within Groups	135.84	11.00	12.35			
	Total	5164.04	16.00				
	Source	*SS*	*df*	*MS*	*F*	*P-value*	*F crit*
AS	Between Groups	6069.64	5.00	1213.93	24.63	1.26E-05	3.20
	Within Groups	542.23	11.00	49.29			
	Total	6611.87	16.00				
	Source	*SS*	*df*	*MS*	*F*	*P-value*	*F crit*
AB	Between Groups	5500.28	5.00	1100.06	47.70	4.35E-07	3.20
	Within Groups	253.66	11.00	23.06			
	Total	5753.94	16.00				

As shown in Table 7-2, the p-values of all mixes are much smaller than 0.05. Therefore, the null hypothesis was rejected, and these treatments have a significant effect on maximum loading shear force.

7.4.3 Effect of Mix Type on Shear Resistance

The single factor ANOVA (Table 7-3) test the null hypothesis is that the means of shear resistance grouped by mix type are the same, namely the mix type does not affect the shear resistance means. The alpha level is 0.05.

Table 7-3 Single Factor ANOVA on Effect of Mixes Type on Shear Resistance

	Source	*SS*	*df*	*MS*	*F*	*P-value*	*F crit*
Room Temp	Between Groups	14.706	7.000	2.101	4.397	0.027	3.500
	Within Groups	3.822	8.000	0.478			
	Total	18.529	15.000				
	Source	*SS*	*df*	*MS*	*F*	*P-value*	*F crit*
25c	Between Groups	25.55	7.00	3.65	8.57	0.00	2.66
	Within Groups	6.82	16.00	0.43			
	Total	32.36	23.00				
	Source	*SS*	*df*	*MS*	*F*	*P-value*	*F crit*
50c	Between Groups	15.19	7.00	2.17	1.67	0.19	2.66
	Within Groups	20.76	16.00	1.30			
	Total	35.95	23.00				
	Source	*SS*	*df*	*MS*	*F*	*P-value*	*F crit*
De-icing	Between Groups	26.77	7.00	3.82	1.43	0.26	2.66
	Within Groups	42.75	16.00	2.67			
	Total	69.52	23.00				
	Source	*SS*	*df*	*MS*	*F*	*P-value*	*F crit*
Freeze -thaw	Between Groups	23.01	7.00	3.29	4.81	0.00	2.66
	Within Groups	10.93	16.00	0.68			
	Total	33.95	23.00				
	Source	*SS*	*df*	*MS*	*F*	*P-value*	*F crit*
De-icing Freeze -thaw	Between Groups	16.93	7.00	2.42	9.20	0.00	2.66
	Within Groups	4.21	16.00	0.26			
	Total	21.13	23.00				

As shown in Table 7-3, for treatment 50 °C and de-icing, the p-values are greater than the alpha level. Therefore, the null hypothesis was accepted. Under these two treatments, the mix type does not affect the shear resistance of these asphalt mixtures. For the other treatment, the p-values are smaller than 0.05. Thus, the null hypothesis was rejected, and the mix type has a significant effect on shear resistance.

7.4.4 Effect of Treatment on Shear Resistance

The single factor ANOVA (Table 7-4) test null hypothesis is that the means of shear resistance grouped by treatments are the same, namely, the treatments do not affect the shear resistance means. The alpha level is 0.05.

Table 7-4 Single Factor ANOVA on Effect of Treatment on Shear Resistance

	Source	*SS*	*df*	*MS*	*F*	*P-value*	*F crit*
HL3 58-28	Between Groups	89.04	5.00	17.81	4.02	0.02	3.11
	Within Groups	53.21	12.00	4.43			
	Total	142.26	17.00				
	Source	*SS*	*df*	*MS*	*F*	*P-value*	*F crit*
HL3 64-28	Between Groups	79.62	5.00	15.92	3.93	0.02	3.11
	Within Groups	48.68	12.00	4.06			
	Total	128.30	17.00				
	Source	*SS*	*df*	*MS*	*F*	*P-value*	*F crit*
HL3 HS 64-28	Between Groups	72.56	5.00	14.51	3.12	0.05	3.11
	Within Groups	55.76	12.00	4.65			
	Total	128.33	17.00				
	Source	*SS*	*df*	*MS*	*F*	*P-value*	*F crit*
HL3 HS 70-28	Between Groups	52.60	5.00	10.52	3.03	0.05	3.11
	Within Groups	41.68	12.00	3.47			
	Total	94.29	17.00				
	Source	*SS*	*df*	*MS*	*F*	*P-value*	*F crit*
HL1 HS 64-28	Between Groups	46.84	5.00	9.37	2.18	0.12	3.11
	Within Groups	51.54	12.00	4.29			
	Total	98.38	17.00				
	Source	*SS*	*df*	*MS*	*F*	*P-value*	*F crit*
HL1 HS 70-28	Between Groups	88.71	5.00	17.74	3.57	0.03	3.11
	Within Groups	59.59	12.00	4.97			
	Total	148.31	17.00				
	Source	*SS*	*df*	*MS*	*F*	*P-value*	*F crit*
AS	Between Groups	110.22	5.00	22.04	2.79	0.07	3.11
	Within Groups	94.98	12.00	7.91			
	Total	205.20	17.00				
	Source	*SS*	*df*	*MS*	*F*	*P-value*	*F crit*
AB	Between Groups	74.55	5.00	14.91	2.13	0.13	3.11
	Within Groups	83.95	12.00	7.00			
	Total	158.50	17.00				

As shown in Table 7-4, for mix HL1 HS 64-28, airport surface course, and airport binder course, the p-values are greater than 0.05. Thus, the null hypothesis was accepted, and treatments do not affect the shear resistance of these three mixes. For all other mixes, the p-values are smaller than 0.05. Thus, the null hypothesis was rejected, and these treatments have a significant effect on shear resistance.

7.5 Statistical Analysis: Two-Factor ANOVA

7.5.1 Peak Shear Loading Force

Table 7-5 Two-factor ANOVA Summary of Peak Shear Loading Force

ANOVA: Two-Factor With Replication							
SUMMARY	Room Temp	25 c	50 c	De-icing	Freeze-thaw	De-icing+Freeze-thaw	Total
HL3 58-28							
Count	3	3	3	3	3	3	18
Sum	110.45	101.52	54.70	172.18	50.20	49.66	538.71
Average	36.82	33.84	18.23	57.39	16.73	16.55	29.93
Variance	1019.93	14.33	1.00	36.08	26.75	42.28	364.79
HL3 64-28							
Count	3	3	3	3	3	3	18
Sum	109.91	124.50	56.56	165.76	43.20	57.04	556.96
Average	36.64	41.50	18.85	55.25	14.40	19.01	30.94
Variance	1021.72	9.17	17.14	133.08	14.88	2.31	369.87
HL3 HS 64-28							
Count	3	3	3	3	3	3	18
Sum	131.11	161.72	83.44	199.17	89.45	87.13	752.01
Average	43.70	53.91	27.81	66.39	29.82	29.04	41.78
Variance	1440.49	37.56	31.73	20.35	7.76	15.83	404.59
HL3 HS 70-28							
Count	3	3	3	3	3	3	18
Sum	106.07	127.07	76.17	173.23	76.83	63.14	622.50
Average	35.36	42.36	25.39	57.74	25.61	21.05	34.58
Variance	940.00	2.99	2.81	16.05	3.77	8.22	281.48
HL1 HS 64-28							
Count	3	3	3	3	3	3	18
Sum	117.47	137.15	68.43	151.22	73.43	71.95	619.66
Average	39.16	45.72	22.81	50.41	24.48	23.98	34.43
Variance	1150.92	21.41	38.97	172.03	19.19	0.85	297.13
HL1 HS 70-28							
Count	3	3	3	3	3	3	18
Sum	127.45	158.85	86.43	205.37	90.29	78.80	747.18
Average	42.48	52.95	28.81	68.46	30.10	26.27	41.51
Variance	1358.91	2.97	7.14	32.56	18.31	1.66	411.09
AS							
Count	3	3	3	3	3	3	18
Sum	130.10	152.02	81.32	197.08	65.34	65.10	690.95
Average	43.37	50.67	27.11	65.69	21.78	21.70	38.39
Variance	1434.60	15.80	123.10	81.76	19.48	6.94	480.71
AB							
Count	3	3	3	3	3	3	18
Sum	148.96	164.64	83.07	206.42	95.26	99.98	798.34
Average	49.65	54.88	27.69	68.81	31.75	33.33	44.35
Variance	1857.21	0.63	0.16	38.67	54.73	24.55	460.99
Total							
Count	24	24	24	24	24	24	
Sum	981.52	1127.47	590.11	1470.43	583.99	572.79	
Average	40.90	46.98	24.59	61.27	24.33	23.87	
Variance	910.12	59.38	35.13	89.95	51.24	36.54	

The three null hypotheses for two-factor ANOVA of Peak Shear Loading Force are as follows:

1. The means of observations grouped by mix type are the same.
2. The means of observations grouped by treatments are the same.
3. The mix type and treatment do not have an interaction effect on Peak Shear Loading force. The alpha level is 0.05.

The summary and Two-factor ANOVA for Peak Shear Loading Force are presented in Table 7-5 and Table 7-6.

Table 7-6 Two-factor ANOVA of Peak Shear Loading Force

Source	*SS*	*df*	*MS*	*F*	*P-value*	*F crit*
Mix Types	3569.79	7.00	509.97	2.16	0.04	2.11
Treatments	28576.28	5.00	5715.26	24.17	0.00	2.31
Interaction	927.00	35.00	26.49	0.11	1.00	1.55
Within	22697.54	96.00	236.43			
Total	55770.61	143.00				

As shown in Table 7-6, the p-value for mix type and treatment are both smaller than 0.05, thus the null hypotheses one and two were rejected. Namely, these mix types and treatment both have a significant effect on the peak shear loading force. However, the p-value of interaction is greater than 0.05, thus the null hypothesis is accepted and there is no interaction between the mix type and treatment for maximum shear loading force.

7.5.2 Shear Resistance

The three null hypotheses for two-factor ANOVA of Shear resistance are as follows:

1. The means of observations grouped by mix type are the same;
2. The means of observations grouped by treatment are the same;
3. The mix type and treatment do not have an interaction effect on the shear resistance of asphalt mixtures. The alpha level is 0.05.

The summary and Two-factor ANOVA for peak shear loading force are presented in Table 7-7 and Table 7-8.

Table 7-7 Two-factor ANOVA Summary of Shear Resistance

ANOVA: Two-Factor with Replication							
SUMMARY	18.9c	25c	50c	De-icer	Freeze-thaw	Freeze-thaw and De-icer	Total
HL3 58-28							
Count	3.00	3.00	3.00	3.00	3.00	3.00	18.00
Sum	15.22	14.48	8.87	26.38	7.53	7.12	79.59
Average	5.07	4.83	2.96	8.79	2.51	2.37	4.42
Variance	19.34	0.28	0.41	5.32	0.45	0.80	8.37
HL3 64-28							
Count	3	3	3	3	3	3	18
Sum	15.51	17.61	8.24	24.08	6.32	8.31	80.08
Average	5.17	5.87	2.75	8.03	2.11	2.77	4.45
Variance	20.36	0.16	0.37	3.17	0.25	0.04	7.55
HL3 HS 64-28							
Count	3	3	3	3	3	3	18
Sum	17.72	23.37	13.94	29.19	13.18	13.01	110.41
Average	5.91	7.79	4.65	9.73	4.39	4.34	6.13
Variance	26.23	0.77	0.11	0.33	0.14	0.30	7.55
HL3 HS 70-28							
Count	3	3	3	3	3	3	18
Sum	15.23	17.80	12.88	25.18	11.55	9.47	92.13
Average	5.08	5.93	4.29	8.39	3.85	3.16	5.12
Variance	19.71	0.08	0.66	0.02	0.21	0.16	5.55
HL1 HS 64-28							
Count	3	3	3	3	3	3	18
Sum	16.60	19.07	11.24	23.51	11.17	10.44	92.03
Average	5.53	6.36	3.75	7.84	3.72	3.48	5.11
Variance	23.04	0.42	0.44	1.21	0.64	0.02	5.79
HL1 HS 70-28							
Count	3	3	3	3	3	3	18
Sum	17.65	22.25	14.51	31.77	14.85	11.68	112.70
Average	5.88	7.42	4.84	10.59	4.95	3.89	6.26
Variance	26.11	0.54	0.21	1.32	1.51	0.11	8.72
AS							
Count	3	3	3	3	3	3	18
Sum	18.59	21.35	14.31	30.93	9.85	9.40	104.42
Average	6.20	7.12	4.77	10.31	3.28	3.13	5.80
Variance	29.50	0.41	7.43	9.50	0.55	0.09	12.07
AB							
Count	3	3	3	3	3	3	18
Sum	21.20	24.06	14.38	31.23	14.74	15.47	121.08
Average	7.07	8.02	4.79	10.41	4.91	5.16	6.73
Variance	37.68	0.74	0.76	0.51	1.72	0.57	9.32
Total							
Count	24	24	24	24	24	24	
Sum	137.73	159.98	98.36	222.27	89.20	84.90	
Average	5.74	6.67	4.10	9.26	3.72	3.54	
Variance	17.99	1.41	1.56	3.02	1.48	0.92	

Table 7-8 Two-factor ANOVA of Peak Shear Resistance

Source	*SS*	*df*	*MS*	*F*	*P-value*	*F crit*
Mix Types	92.54	7.00	13.22	2.59	0.02	2.11
Treatments	589.44	5.00	117.89	23.13	0.00	2.31
Interaction	24.71	35.00	0.71	0.14	1.00	1.55
Within	489.39	96.00	5.10			
Total	1196.08	143.00				

As shown in Table 7-8, the p-values of mix type and treatment are both smaller than 0.05. Therefore, null hypotheses one and two were rejected, and mix type and treatment both have a significant effect on the shear resistance of asphalt mixtures. However, the p-value of interaction is greater than 0.05, thus the null hypothesis is accepted. Namely the mix type and treatment do not have interaction on shear resistance performance.

7.6 Summary

Based on the Simplified UST experimental results of six types of road mixes and two types of airport mixes under six treatments, the following conclusions are drawn:

1. Simplified UST is capable of evaluating the shear resistance of asphalt mixture.
2. Base on the single factor ANOVA test, mix type has a significant effect on peak shear loading force at 25 °C, freeze-thaw, and de-icing plus freeze-thaw treatment. While mix type has a significant effect on shear resistance at room temperature, 25 °C, freeze-thaw, and de-icing plus freeze-thaw treatment.
3. The single factor ANOVA test also indicates that treatment type affects shear resistance of the asphalt mixture applied to both on-road and airport pavement. Treatments have a significant effect on peak shear loading force for all types of mixes. While for shear resistance, treatments significantly affect all the mixes except HL1 HS 64-28, airport surface course, and airport binder course mix.
4. Based on two-factor statistical analysis, the mix types and treatments both have a significant effect on maximum shear loading force and shear resistance performance. However, there is no interaction effect between these two factors.

5. The de-icing agent itself does not significantly affect the shear performance of the asphalt mixture. However, the existence of de-icer, the impact from freeze-thaw on the reduction of shear resistance of asphalt mixture can be reduced.

Chapter 8
ANALYSIS OF MECHANICAL RESPONSE OF CANADIAN AIRSIDE PAVEMENT UNDER VARIOUS GROUND MANEUVERINGS THROUGH FINITE ELEMENT METHOD

8.1 Stress Tensor and Pavement Distress

Understanding the mechanisms of horizontal impact of aircraft gears to the pavement materials is key to address shear-related failures from the perspective of material and layer thickness design. Shear force results from the interface between aircraft gear tires and asphalt surface layer when aircraft takeoff or land. It is of great significance to understand the mechanical response between aircraft tires and pavement. A general forces diagram between aircraft tires and pavement is shown in Figure 8-1 (Hisao, 1970a).

If both vertical and horizontal directions are in force balance status, summing all the vertical and horizontal forces will give, respectively.

Vertical: $F_l + N = G$ **Equation 8-1**

Horizontal: $f_A + f_B + f_F = F_T$ **Equation 8-2**

$f_F = \mu * N$ **Equation 8-3**

Where:

G: Overall Gravity

N: Gravity Support Force

F_l: Aerodynamic lift

f_A: Air Resistance Force

f_B: Brake Force

f_F: Friction Force

F_T: Traction Force (Thrust Force)

μ : Friction Coefficient

F_H: Horizontal Force (equal to Friction Force)

During the aircraft takeoff process, the whole aircraft is in an acceleration condition. The gravity support force N is decreasing, while the aerodynamic lift F_l is increasing

until it is greater than the gravity force G. During this process, the friction force f_F reduces with decreasing N. However, it should be noted that before the aircraft moves, the gravity support force is extremely large due to passenger loading (or goods and full fuel loading). Therefore, at the aircraft start-up process, the friction force is very large. During the aircraft landing process, aerodynamic lift force and jet traction force both decrease to contribute to lower the aircraft speed. The whole aircraft is in the deceleration process. The gravity support force N increases tremendously once the main gear touches the pavement surface. The friction force increase accordingly. The pavement horizontal force increases as well to oppose the friction force. During aircraft movement, the gravity supportive force is equal to the overall gravity of the aircraft body due to negligible aerodynamic lift. In the meantime, the friction force of the tire is very large, and the horizontal force of the asphalt pavement is extremely large accordingly. This results in asphalt pavement shear distress in areas connecting runway and taxiways because these areas experience the aircraft moving slowly or performing turning operations.

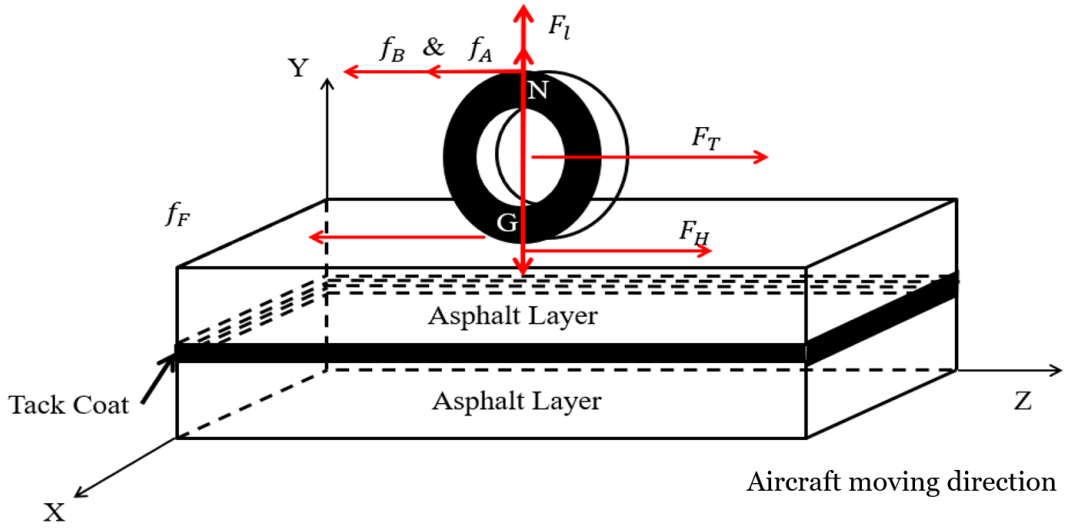

Figure 8-1 Aircraft Tire & Asphalt Pavement Mechanical Interaction (Hisao, 1970)

Taking a small stress unit cube from the asphalt surface layer to understand each stress contributes to the corresponding deformation, shear stress in different planes, and various directions are shown in Figure 8-2.

Located in three different planes, all the six shear stresses appear in pairs. They are quantitatively equal but in opposite directions. For example, τ_{yx} (S_{21}) indicates that shear stress is within XZ-plane and in the direction of the X-axis; τ_{xy} (S_{12}) means the shear stress is at YZ-plane and in the direction of the Y-axis, τ_{yx} (S_{21}) and τ_{xy} (S_{12}) are quantitively equal and always appear in pairs, respectively.

Assuming that the aircraft moving along with Z-axis as shown in Figure 8-2, shear stress τ_{xy} (S_{12}) and τ_{yx} (S_{21}) tend to strain the material into rutting (Figure 3a) and transverse slippage distress (Figure 3b). Shear stress τ_{xz} (S_{13}) and τ_{zx} (S_{31}) have the potential to strain the material into transverse deformation (Figure 3c) and longitudinal deformation (Figure 3d). Shear stress τ_{yz} (S_{23}) and τ_{zy} (S_{32}) will strain the material into delamination (Figure 3e) and longitudinal wave (Figure 3f), respectively. Since the asphalt layer horizontal deformation and asphalt layers interface delamination are the most frequent distresses observed in airports, it is very important to understand τ_{xz} (S_{13}) and τ_{zy} (S_{32}) as they are the main cause for the aforementioned distresses. Moreover, as one of the most common distress forms, rutting needs to be paid more attention as well. Shear stress τ_{xy} (S_{12}) is directly related to rutting and is therefore investigated.

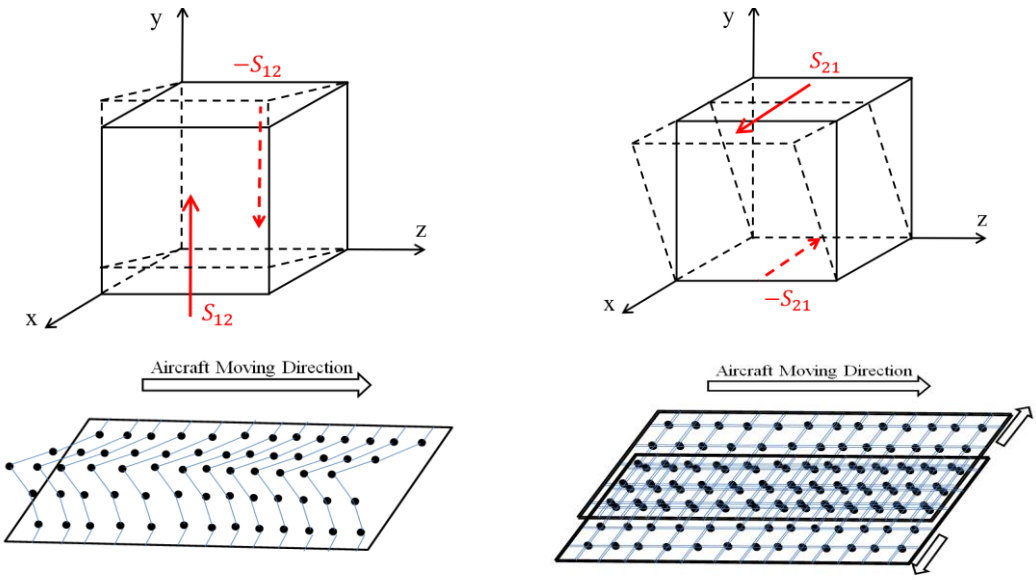

a. S_{12} & Rutting

b. S_{21} & Transverse Slippage

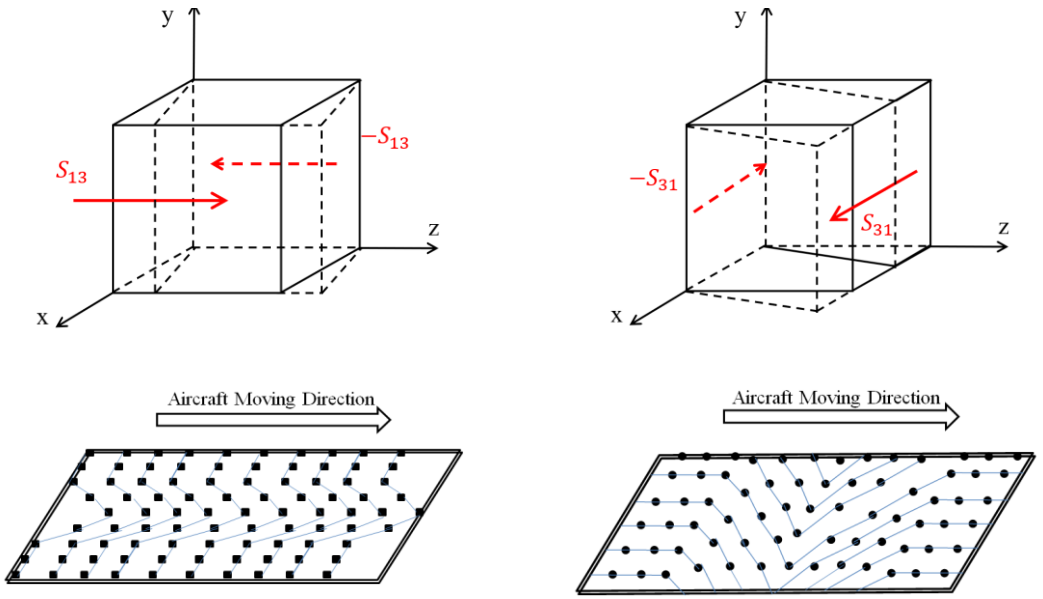

c. S_{13} & Horizontal Deformation

d. S_{31} & Longitudinal Deformation

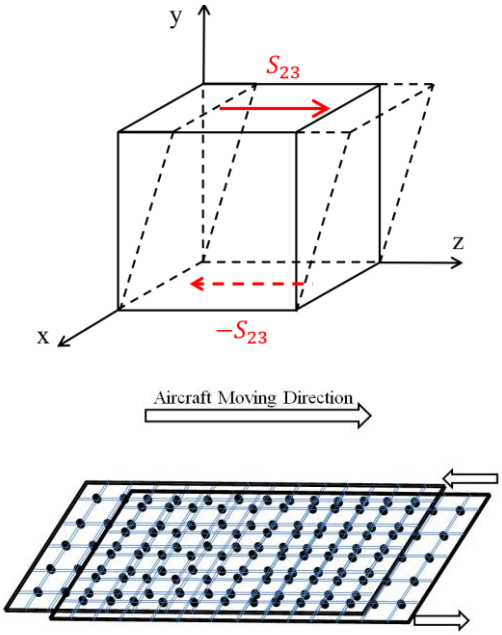

e. S_{23} & Slippage (Delamination)

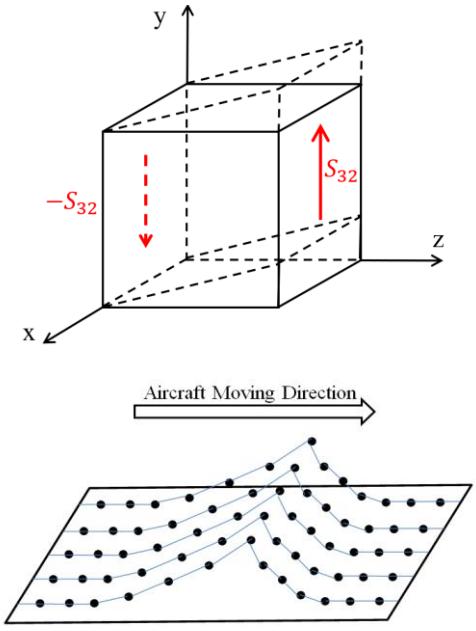

f. S_{32} & Longitudinal Wave (upheaval)

Figure 8-2 Shear Stress in Different Planes and Corresponding Deformation

Note:

1. τ_{xy} and S_{12} means the same shear stress, the former is more frequently used in mechanics while the latter is used in ABAQUS software.

2. The coordination system shown in the figure is not a standard one. A standard coordination system should follow the right-hand rule, in the case of this figure, all the x-axis should point into the paper.

8.2 Modeling Parameters

8.2.1 Material Property

The ratio of stress and elastic strain is defined as modulus. For pure linear elastic material, this ratio is a constant and named Young's modulus.

$$E = \frac{\sigma}{\varepsilon} \qquad \textbf{Equation 8-4}$$

A material with a higher Young's modulus means at given stress, the strain is smaller than other materials and means the material is "stiffer". A good example of pure linear elastic material is a spring. Applying a force, the spring shows displacement, while removing the force, the spring goes back to its original shape. The relationship between stress and time, and strain and time are shown in Figure 8-3a.

For viscous material, viscosity is defined as the resistance of a fluid to flow and expressed as the ratio of shear stress $\frac{F}{A}$ and velocity gradient $\frac{\Delta v}{\Delta z}$ (Figure 8-3b). Therefore, viscosity is a time-dependent property. An ideal viscous example is a dashpot. Apply stress at a dashpot, and the strain gradually increases with time. After removing the load, the strain does not return to zero (Figure 8-3c).

$$\eta = \frac{F/A}{\Delta v/\Delta y} = \frac{\sigma}{\varepsilon} \qquad \textbf{Equation 8-5}$$

$$\eta = \frac{F/A}{\frac{dv}{dy}} = \frac{\sigma}{\frac{1}{dy}(\frac{du_x}{dt})} = \frac{\sigma}{\frac{1}{dt}(\frac{du_x}{dy})} = \frac{\sigma}{\frac{1}{dt}(d\gamma)} = \frac{\sigma}{\dot{\gamma}} \qquad \textbf{Equation 8-6}$$

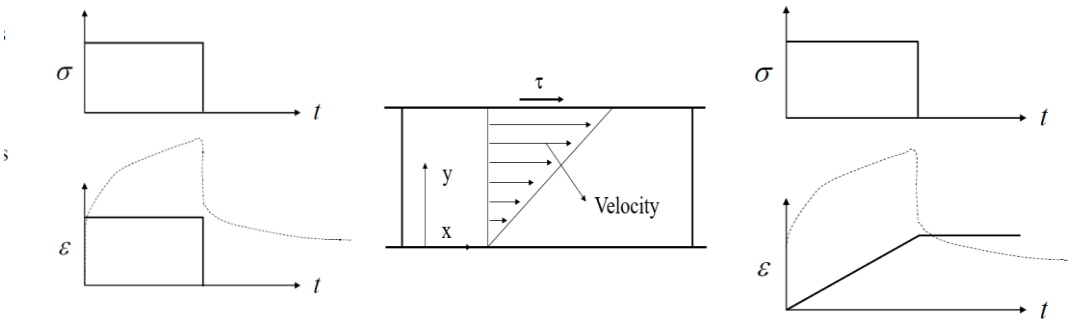

a. Elastic material b. Viscosity c. Viscous Material

Figure 8-3 Pure Elastic and Linear Viscous Materials

The viscoelastic material has both elasticity and viscosity. When giving stress, there will be instantaneous elastic strain along with a time-dependent viscous strain. Elastic strain will recover while the viscous strain will remain once the applied load has been removed. Typical models describing viscoelastic materials include Maxwell Model, Kelvin Model, and Burgers Model. The Maxwell Model is a series of spring and linear dashpots (Figure 8-4a). The Kelvin Model is a spring and linear dashpot in parallel (Figure 8-4b). The Burgers model is a combination of the Maxwell and Kelvin Models (Figure 8-4c).

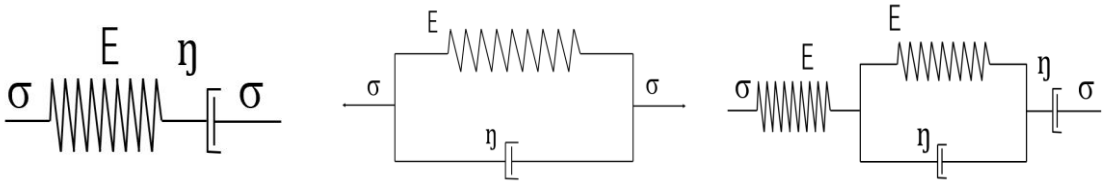

a. Maxwell Model b. Kelvin Model c. Burgers Model

Figure 8-4 Typical Viscoelastic Models

In this study, asphalt materials are considered linear viscoelastic materials. Creep compliance and relaxation modulus can be converted from each other if both of them are modeled with a power law in analytical form (S.W.Park & Y.R.Kim, 1999). Prony series, which has one Maxwell model and several Kelvin Models, has been widely used for representation for linear viscoelastic materials (J. Kim et al., 2008). The parameters for the Prony series used in this study are shown in Table 8-1.

Table 8-1 Prony Series Parameter for Asphalt Materials (Wang et al., 2013)

Prony Series	G_i	K_i	τ_i
1	0.127	0.127	1.69E-02
2	0.3768	0.3768	8.57E-02
3	0.239	0.239	6.08E-01
4	0.1814	0.1814	3.85E+00
5	0.0587	0.0587	1.11E+02
6	0.0063	0.0063	1.37E+04

At the Toronto Pearson Airport, taxiways are constructed with multiple layers as roadway pavement are. The materials that were used in each layer from the top to bottom are surface course Hot Mix Asphalt Concrete (HMAC), lower course HMAC, Portland Cement Concrete (PCC), Cement Stabilized Base (CSB), subbase, and soil subgrade. The thickness, physical properties, and mechanical parameters of the aforementioned materials of each layer are referenced from previous studies and are listed in Table 8-2 (Xu, 2014)(Roston et al., 1976).

Table 8-2 Thickness, Physical and Mechanical Properties of Paved Material

Material	Thickness	Density	Young's modulus	Poisson's ratio
Unit	mm	Kg/m3	Pa	-
Surface course HMAC	60	2400	7.00E+09	0.3
Lower course HMAC	65	2400	7.00E+09	0.3
Portland Cement Concrete (PCC)	380	2200	2.00E+10	0.2
Cement Stabilized Base (CSB)	200	2070	1.70E+11	0.3
Subbase	150	1500	4.00E+08	0.35
Subgrade	4145	1500	7.00E+07	0.33

8.2.2 Geometric Design

The 3D pavement model was built through ABAQUS standard mode. The geometric design of the model was derived from a Toronto Pearson International Airport taxiway (Figure 8-5a). Materials and layer combinations of the model are shown in Figure 8-6b. The model only simulated the central part of the taxiway. Shoulders on each side were not included for computational cost and accuracy.

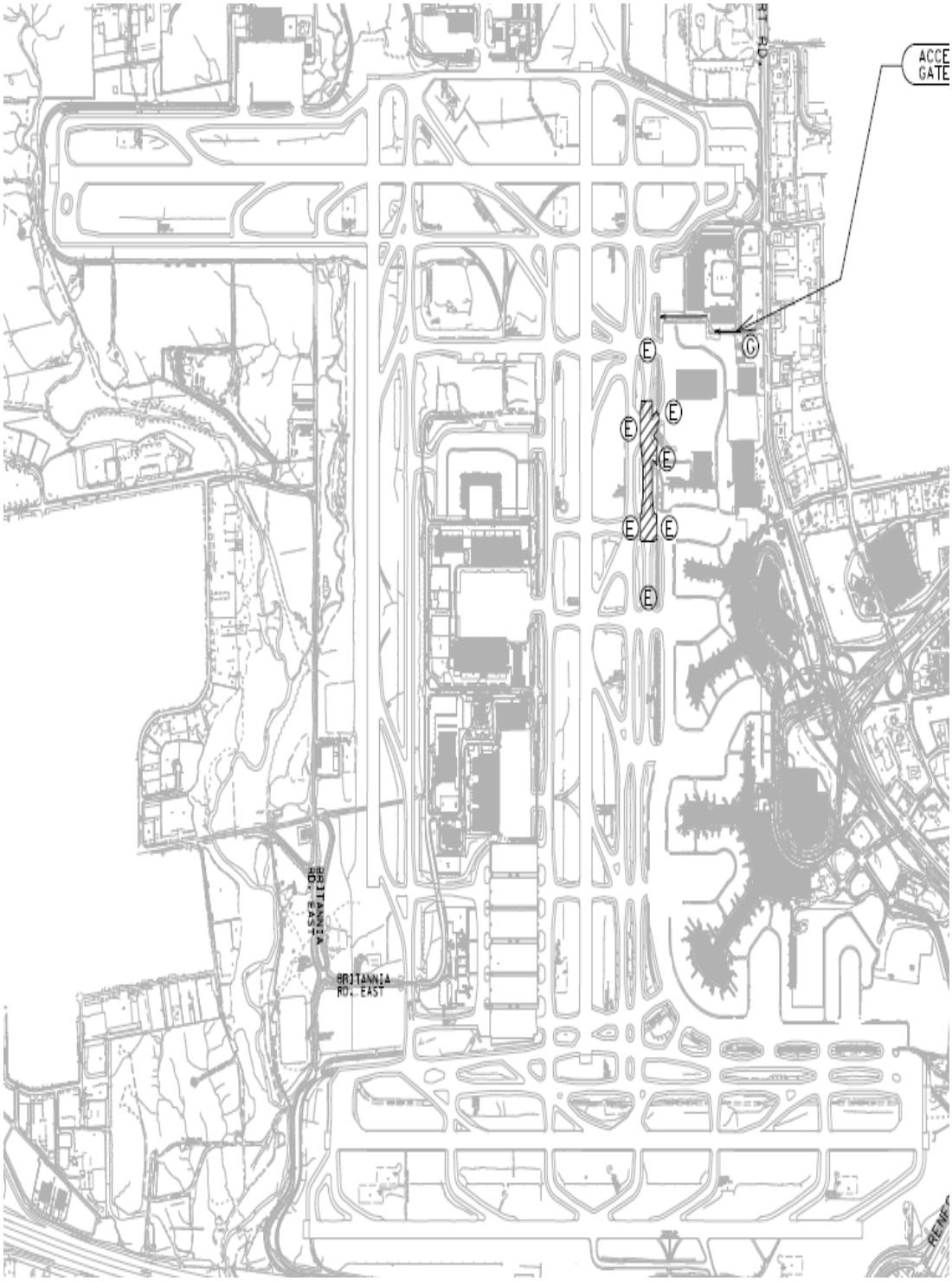

a. Site plan drawing for Toronto Pearson International Airport (Greater Toronto Airport Authority, 2018)

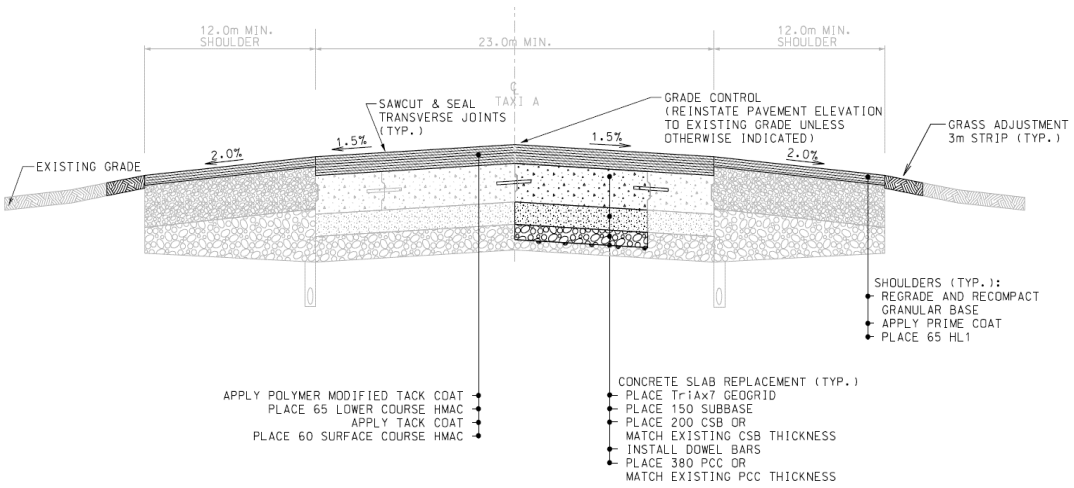

b. Taxiway A intersection (Greater Toronto Airport Authority, 2018)

Figure 8-5 Site Plan and Taxiway Intersection Drawing of Toronto Airport

8.2.3 Loads and Boundary Conditions

The model is 50 m long, 23 m wide, 5 m in depth. An ideal contact condition was assumed between each layer. The load applied on pavement surfaces used Boeing 777 series aircraft (Boeing Commercial Airplanes, 1998). The dimensions of aircraft tires, the distance between main gears, nose gear, and main gears are following the Michelin Aircraft Tire data (Michelin Aircraft Tyre, 2017), as shown in Figure 8-6. The aircraft tire and pavement contact area were simulated as rectangular based on actual dimensions of aircraft tires. The vertical load considered in the model was based on various ground maneuverings such as taxi, takeoff, landing, and zero fuel operation as shown in Table 8-3. The friction force between pavement and tires was considered as horizontal pressure applied on the contact area in the direction of an aircraft moving as shown in Figure 8-6.

Table 8-3 Maximum Design Weight of Boeing 777-300ER Under Various Ground Maneuverings (Boeing Commercial Airplanes, 2015)

Characteristics	Taxi	Takeoff	Landing	Zero Fuel	Operating Empty
Mass (Kg)	352442.00	351535.00	251290.00	237683.00	167829.00
10 % Nose Gear (N)	345393.16	344504.30	246264.20	232929.34	164472.42
Nose Gear Pressure (Pa)	271963.12	271263.23	193908.82	183408.93	129505.84
Nose Gear Surface Traction (Pa)	135981.56	135631.61	96954.41	91704.47	64752.92
90 % Main Gear (N)	3108538.44	3100538.70	2216377.80	2096364.06	1480251.78
Main Gear Pressure (Pa)	27815889.35	813789.69	581726.46	550226.79	388517.53
Main Gear Surface Traction (Pa)	407944.68	406894.84	290863.23	275113.39	194258.76

The boundary conditions of this model include two parts, the bottom and the sides (the front, back, left, and right side of the computational model) as shown in Figure 8-7. The bottom was set to ENCASTRE (U1=U2=U3=UR1=UR2=UR3=0), which restricts all the translational and rotational motions. Based on the pavement deformation mechanism, all the sides were set to YASYMM (U1=U3=UR2=0), which restricts the translational motion in the direction of the X-axis, Z-axis, and the rotational motion around the Y-axis.

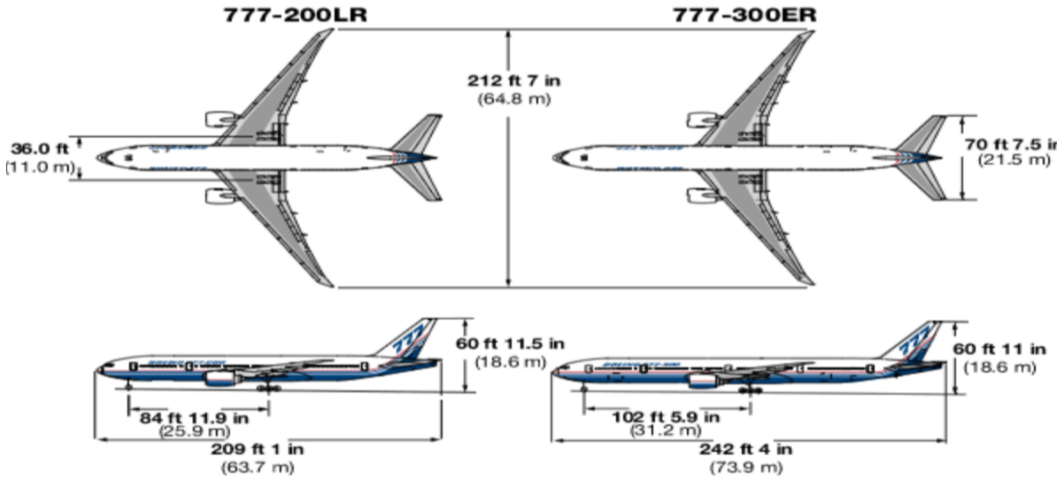

Figure 8-6 Boeing 777 Series Aircraft Dimensions (Modern Airliners, 2020)

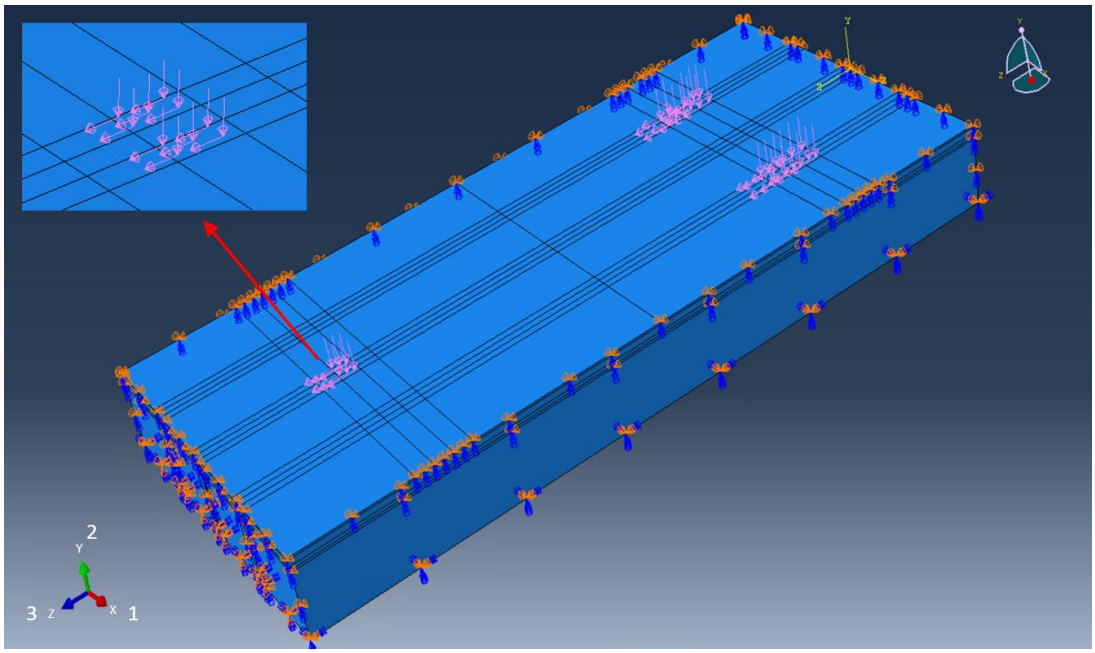

Figure 8-7 Load and Boundary Conditions

8.2.4 Mech Techniques

Giving the whole model is structurally established and each edge in three coordination axes are perpendicular to each other, the whole model was meshed using structural control, the density of the general seed is 0.5 m, and densified mesh seeds with 0.1 m were applied at the location where aircraft gear tire contact with pavement surface as indicated in Figure 8-8. Linear hexahedra element of type C3D8R was assigned to the model. The total number of elements is 175,392. The total number of nodes is 193,596.

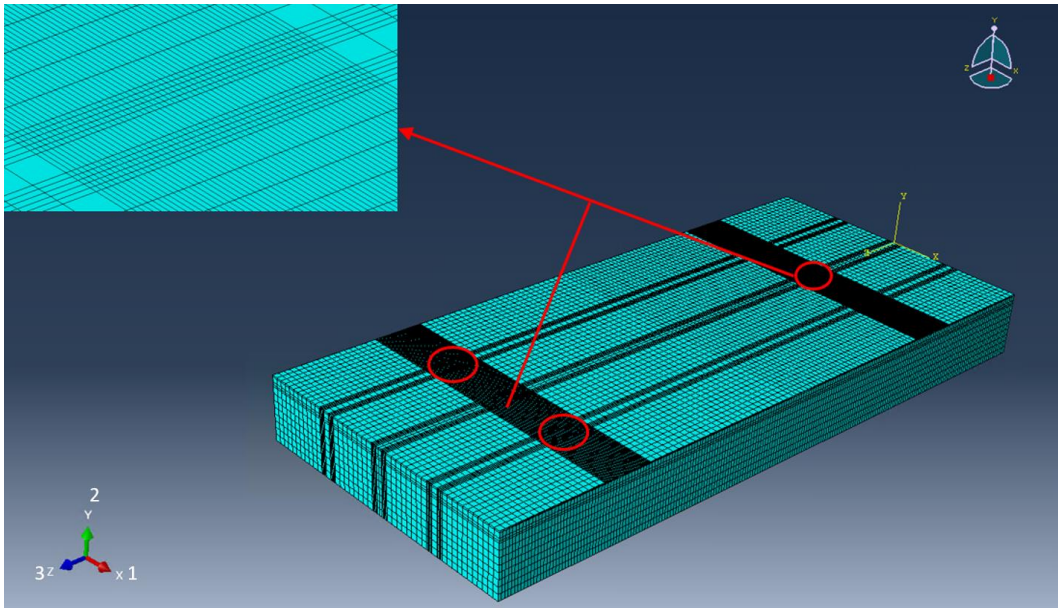

Figure 8-8 Mesh Technique of FEM Model

8.3 Results and Discussion Part 1: Aircraft Taxiing

Four ground maneuverings of Boeing 777-300ER including taxiing, takeoff, landing, and zero fuel operation were considered in the finite element modeling. The stress and displacement in each layer under different conditions were analyzed.

8.3.1 Critical Stress Distribution

Normal stresses cause tension or compression, while shear stresses cause element rotation. Taking taxiing as an example, Von Mises Stress, maximum principal stress, normal stress S_{22}, as well as three shear stress S_{12}, S_{23}, and S_{13} are presented in Figure 8-9.

The figure shows that maximum Von Mises stress appears at main gears and near edges in the Cement Stabilized Base layer with a quantity of 3.29 MPa (Figure 8-9a), Maximum Principal stress occurred right at the center of the main gear in the base layer with a quantity of 2.99 MPa (Figure 8-9b). For shear stress S_{12} and S_{21}, the maximum shear stress occurs at the left and right sides of the main gear loads in the Portland cement concrete layer (Figure 8-9c). The maximum shear stress is 0.36 MPa. S_{12} and S_{21} dominate rutting and transverse delamination, respectively. Maximum shear stress

S_{13} and S_{31} appear at the edge of the Cement Stabilized Base layer, with a quantity of 1.4 MPa (Figure 8-9d). S_{13} and S_{31} control transverse deformation and longitudinal deformation, respectively. Maximum shear stress S_{23} and S_{32} also occurred at the edges in the cement stabilized base layer (Figure 8-9e), S_{23} and S_{32} dominate longitudinal delamination and rippling damage, respectively.

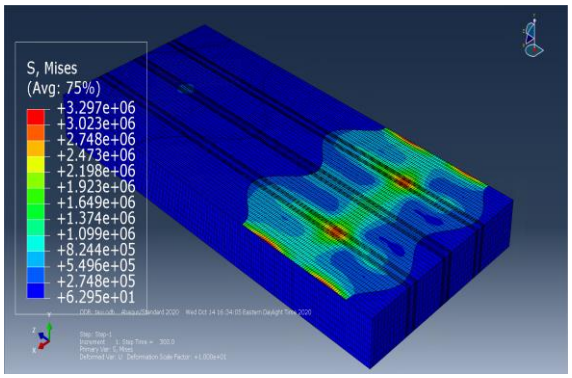

a. Von Mises Stress

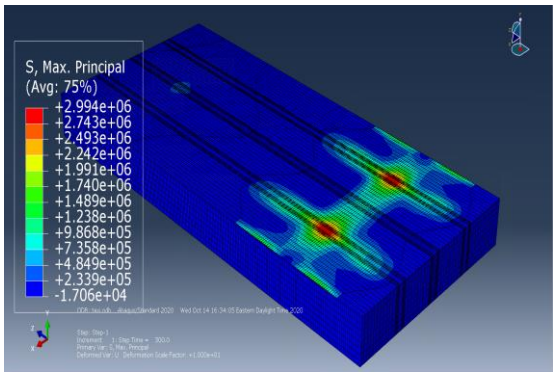

b. Max. Principal Stress

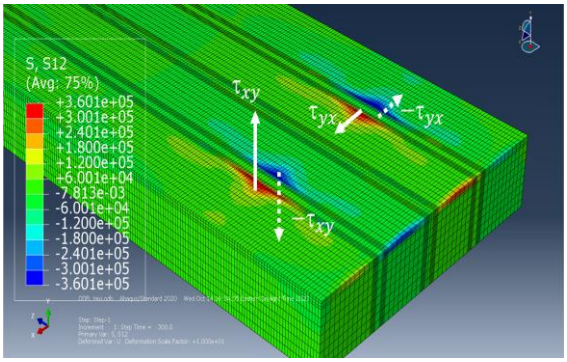

c. Shear Stress τ_{xy} & τ_{yx}

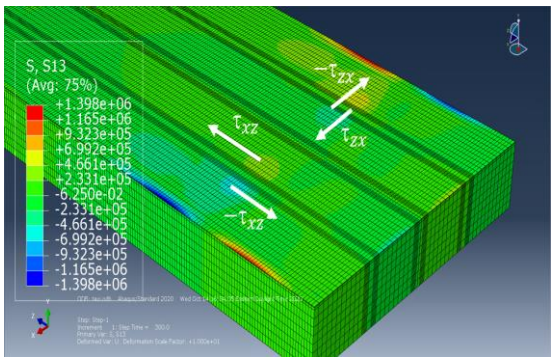

d. Shear Stress τ_{xz} & τ_{zx}

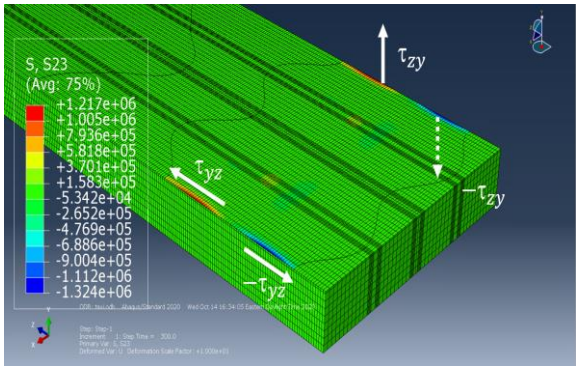

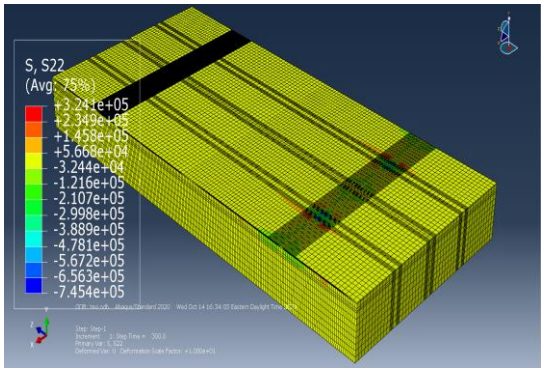

e. Shear Stress τ_{yz} & τ_{zy} f. Normal Stress σ_y

Figure 8-9 Normal Stress and Shear Stress Contour of Boeing 777 Taxiing

8.3.2 Von Mises Stress Distribution

Figure 8-10 displays the von mises stress distribution at different layers in the whole model. It can be observed that the von Mises stress is distributed uniformly within the asphalt surface layer and cement concrete layer (Figure 8-10a and 10b). The main gear has a more significant impact on stress distributions than the nose gear. The main gear loading shows a more obvious impact on stress distributions at a lower position of the pavement such as subbase. The lower the pavement depth, the more nonuniform the Von Mises stress displays.

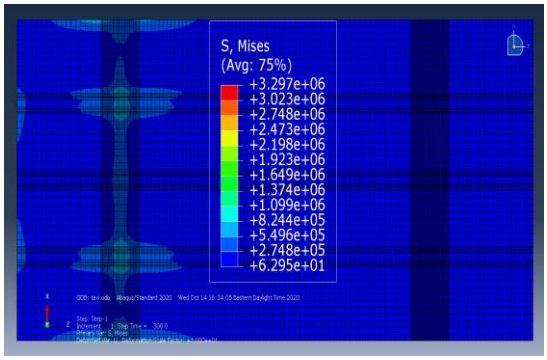

a. Top of Asphalt Layer (0 m)

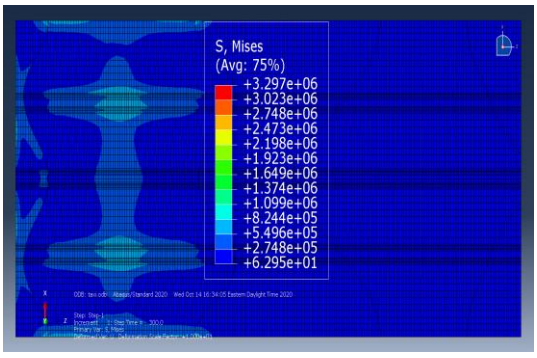

b. Top of PCC Layer (0.125 m)

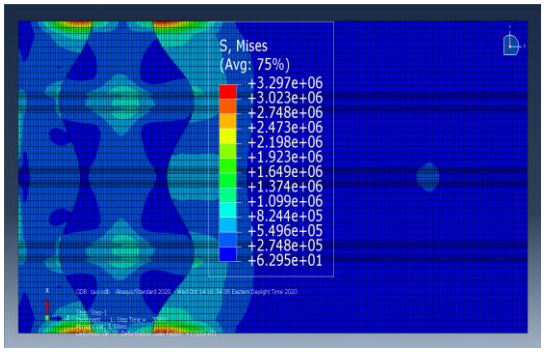

c. Top of SCB Layer (0.505 m)

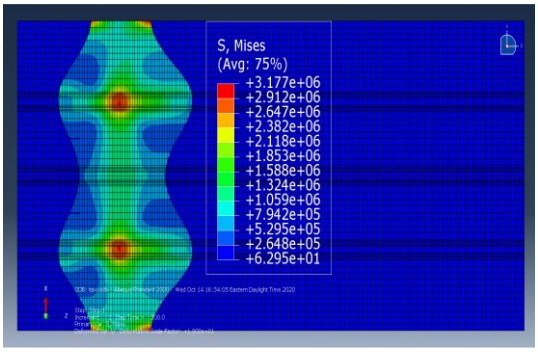

d. Top of Subbase Layer (0.705 m)

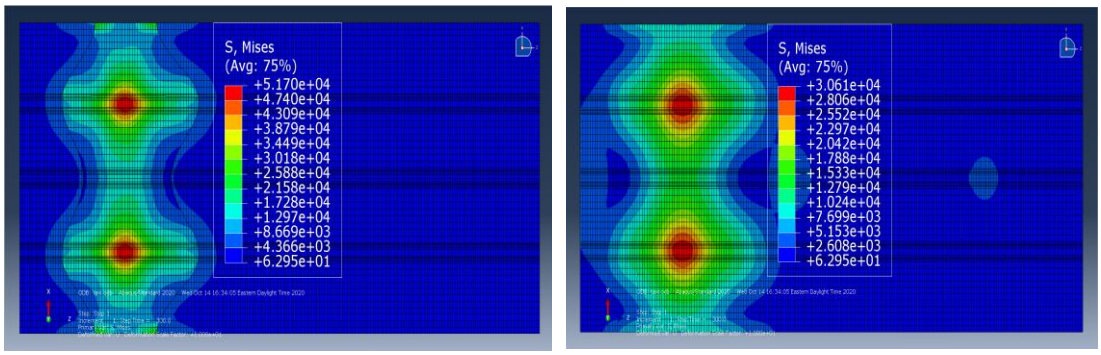

e. Top of Subgrade (0.855 m) f. Subgrade (1.0 m)

Figure 8-10 Von Mises Stress Distribution in Different Depth of Pavement

The Von Mises stress distribution underneath the main gear and nose gear along with the transverse direction and depth are shown in Figure 8-11 through Figure 8-13. The peak level of Von Mises stress appears at the cement stabilized base layer for main gear and nose gear loads. The maximum Von Mises stress under the main gear loads is 3 MPa while the maximum Von Mises stress for the nose gear is only 0.43 MPa. It can be observed from both charts that asphalt materials do not support most of the load from the gear. Instead, it serves the role of transferring the loads to a lower pavement position. The Portland cement concrete and cement stabilized base layer take the most vertical load. It can be seen from Figure 8-13 that Von Mises stress drastically changes within the 1 m depth underneath the nose gear and the main gear. The stress level under the main gear is approximately 5 times greater than that of the nose gear. The figure further demonstrates that the critical Von Mises stress appears at the cement stabilized base layer.

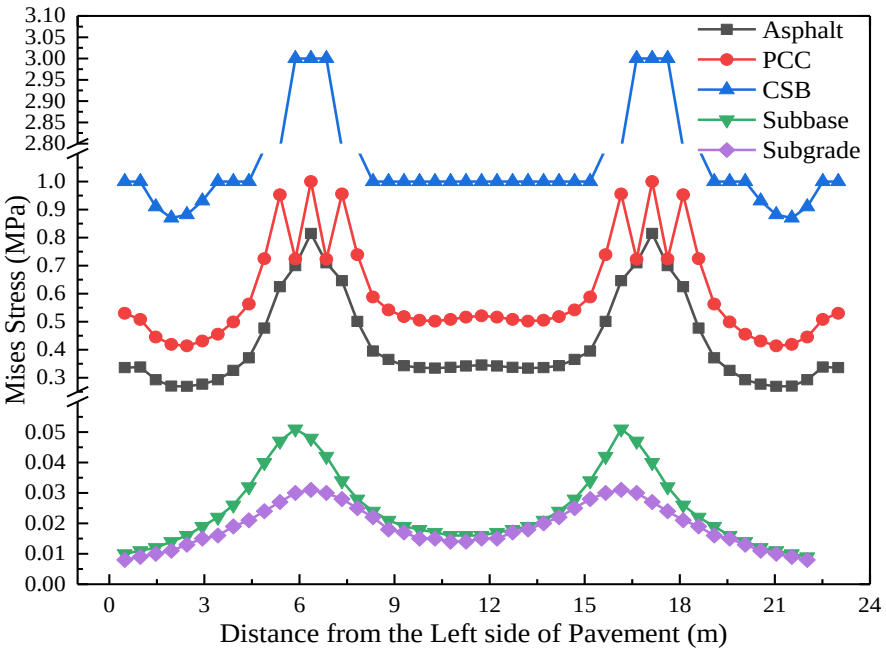

Figure 8-11 Von Mises Stress Distribution Under the Main Gear

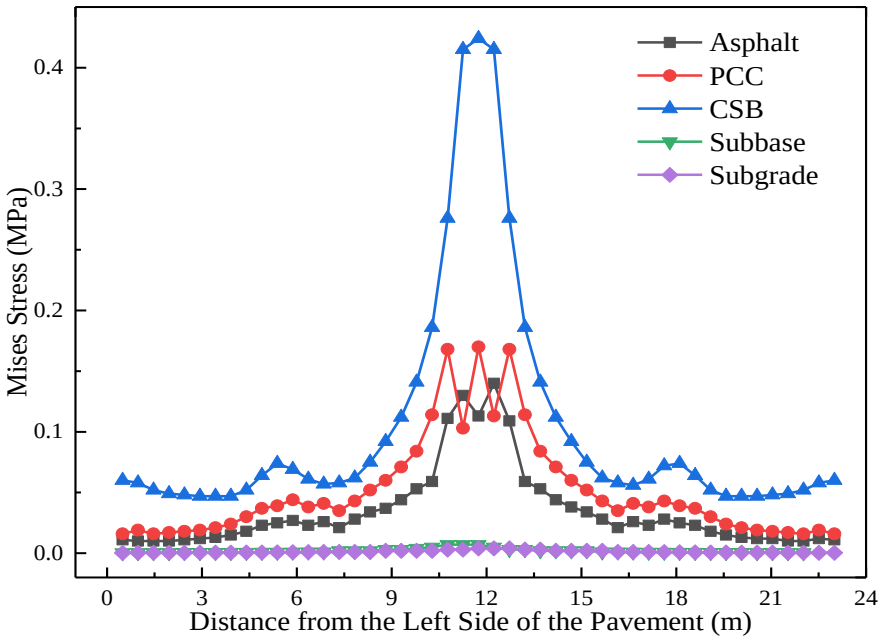

Figure 8-12 Von Mises Stress Distribution Under the Nose Gear

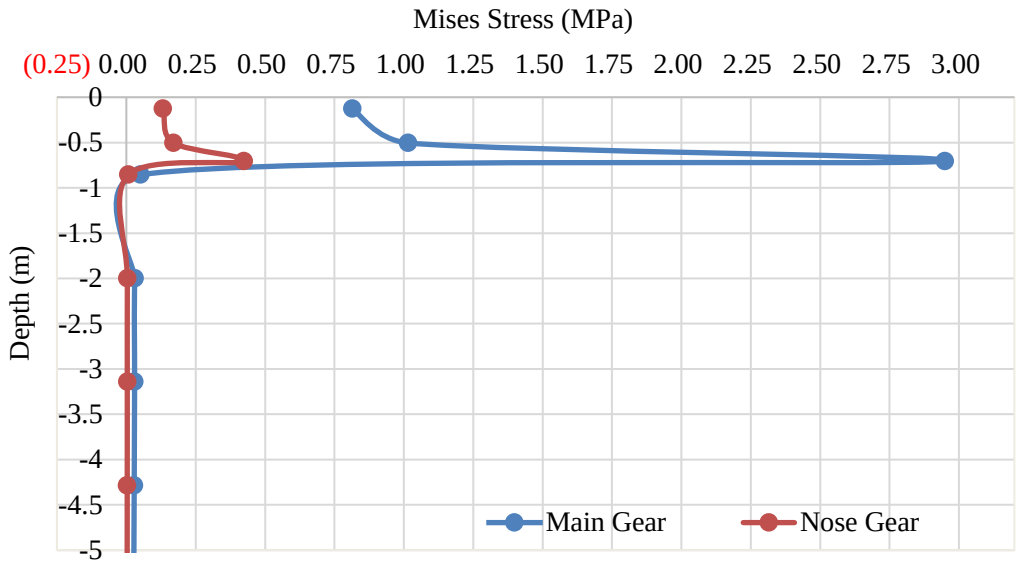

Figure 8-13 Distribution of Von Mises Stress Along with Pavement Depth

8.3.3 Shear Stress Distribution

The distribution of shear stress S12, S13, and S23 along with the depth are shown in Figure 8-14 to Figure 8-16. As presented in Figure 8-14, shear stress S12, which dominates the rutting and transverse slippage failure, distributes symmetrically beneath main gear loads. The maximum shear stress also appears at the cement stabilized base layer. The maximum shear stress underneath the main gear is approximately 5 times that of the nose gear. The shear stress on the asphalt surface layer is 100 kPa, which indicates the potential of rutting. Transverse slippage increases with increasing pavement depth from the asphalt surface layer until the cement stabilized base layer.

Figure 8-15 shows the distribution of shear stress S13, which controls the longitudinal and transverse deformation distress. Unlike the shear stress S12, shear stress S13 underneath the main gear does not exhibit symmetrical behavior. The maximum shear stress level on the main gear left is 1.5 times greater than that of the main gear right. This means the pavement surface under the main gear left side is more likely to develop longitudinal and transverse deformation. The shear stress S13 underneath the nose gear shows a negative value within the 0.5 m depth range, which becomes positive beneath the 0.5 m depth range. This indicates that above and below 0.5 m, the deformation direction may be subject to change.

The distribution of shear stress S23 along the depth is displayed in Figure 8-16. S23 predominates the longitudinal delamination and rippling (upheaval damage). Unlike shear stress S12 and S13, shear stress S23 does not distribute differently beneath the main gear. The figure shows that the main gear and nose gear have a significantly different impact on the distribution of S23 along with the pavement depth. The shear stress level on the asphalt surface layer underneath the main gear is almost 17 times greater than that under the nose gear, which indicates that the asphalt surface layer under the main gear is very likely to develop layer delamination or upheaval damage compared with nose gear loads. Particularly, the peak value for shear stress S23 is at the depth of 0.5 m.

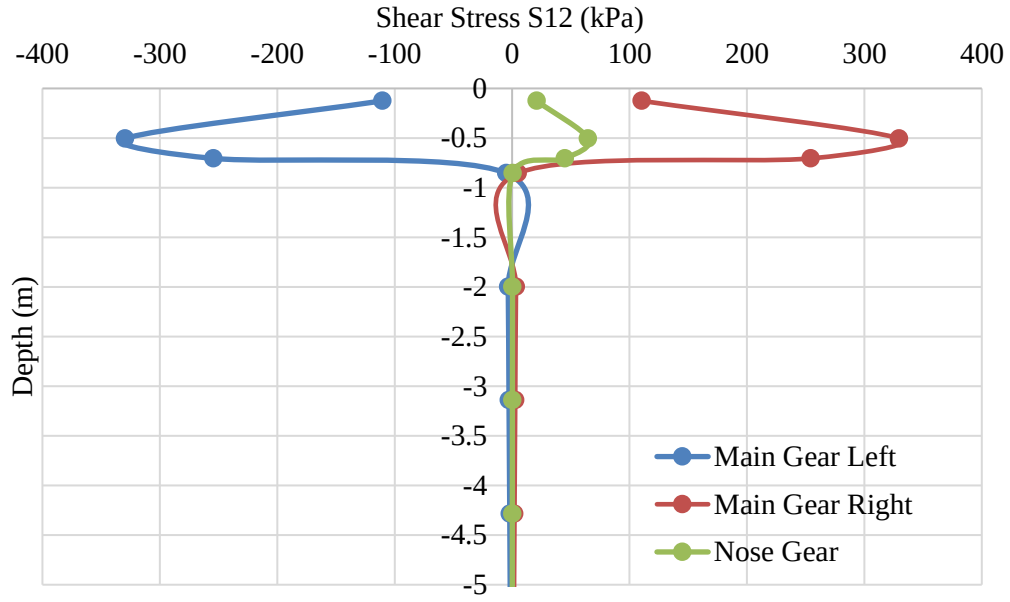

Figure 8-14 Distribution of Shear Stress S12 Stress Along with Pavement Depth

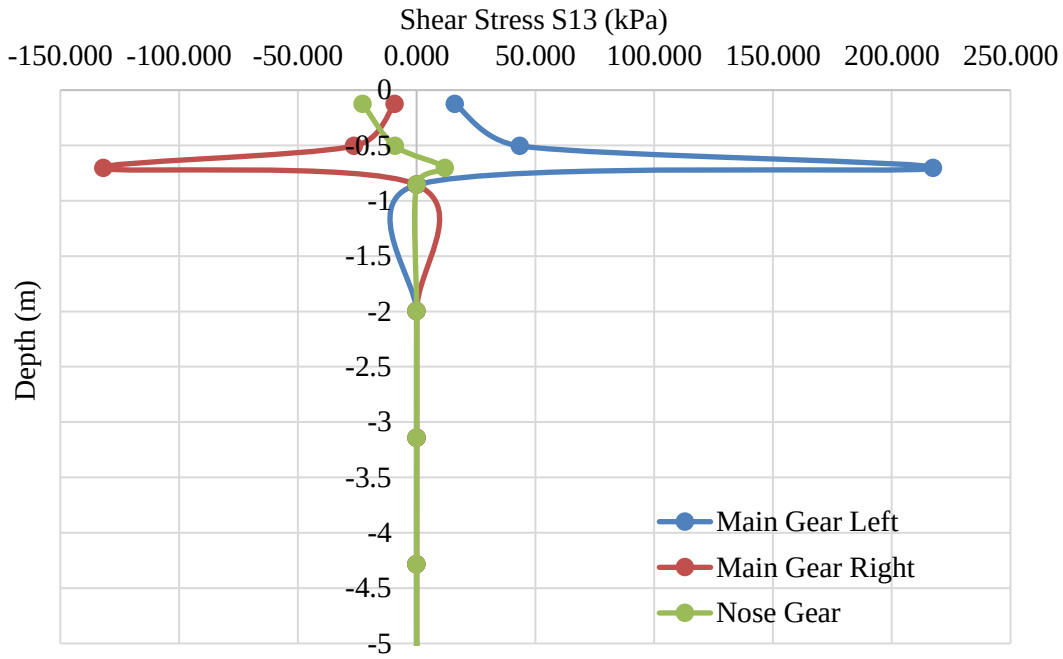

Figure 8-15 Distribution of Shear Stress S13 Stress Along with Pavement Depth

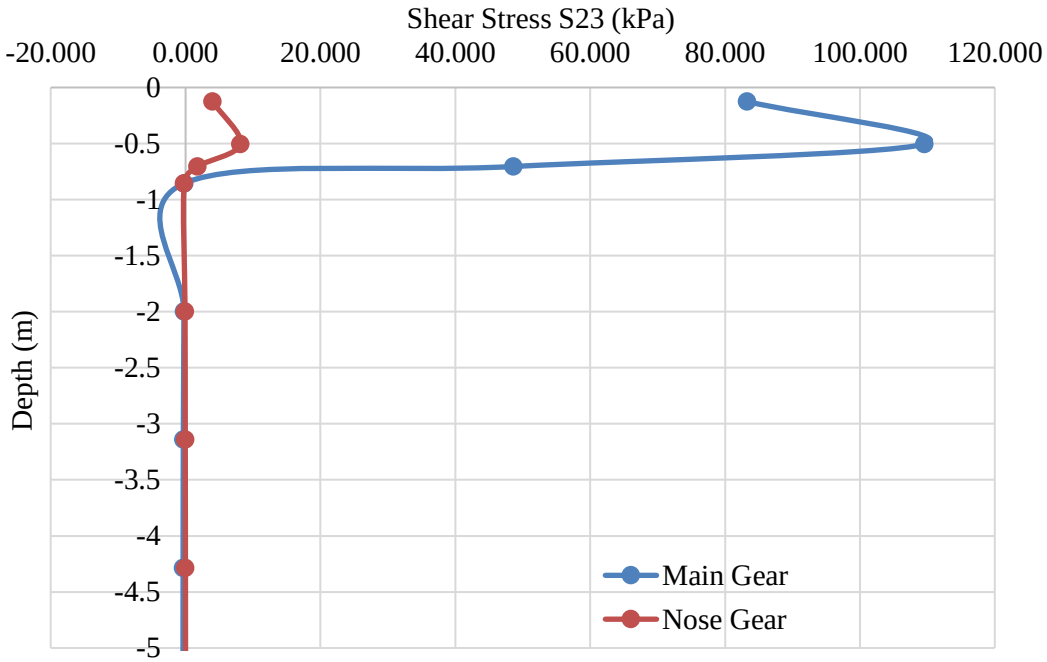

Figure 8-16 Distribution of Mises and Shear Stress Underneath Gear Loads

8.3.4 Displacement Analysis

The displacement magnitude contours, U1, U2, and U3 are shown in Figure 8-17. It can be seen that the displacement magnitude and displacement along the y-axis are similar

to each other, which indicates that overall displacement is mainly induced by displacement U2.

From Figure 8-2, it can be concluded that normal stress σ_x, shear stress τ_{yx} and τ_{zx} induce U1; normal stress σ_y, shear stress τ_{xy} and τ_{zy} induce U2; normal stress σ_z, shear stress τ_{xz} and τ_{yz} induce U3. Therefore U1 reflects transverse deformation and transverse delamination, U2 reflects rutting and rippling damage, and U3 reflects longitudinal deformation and longitudinal delamination.

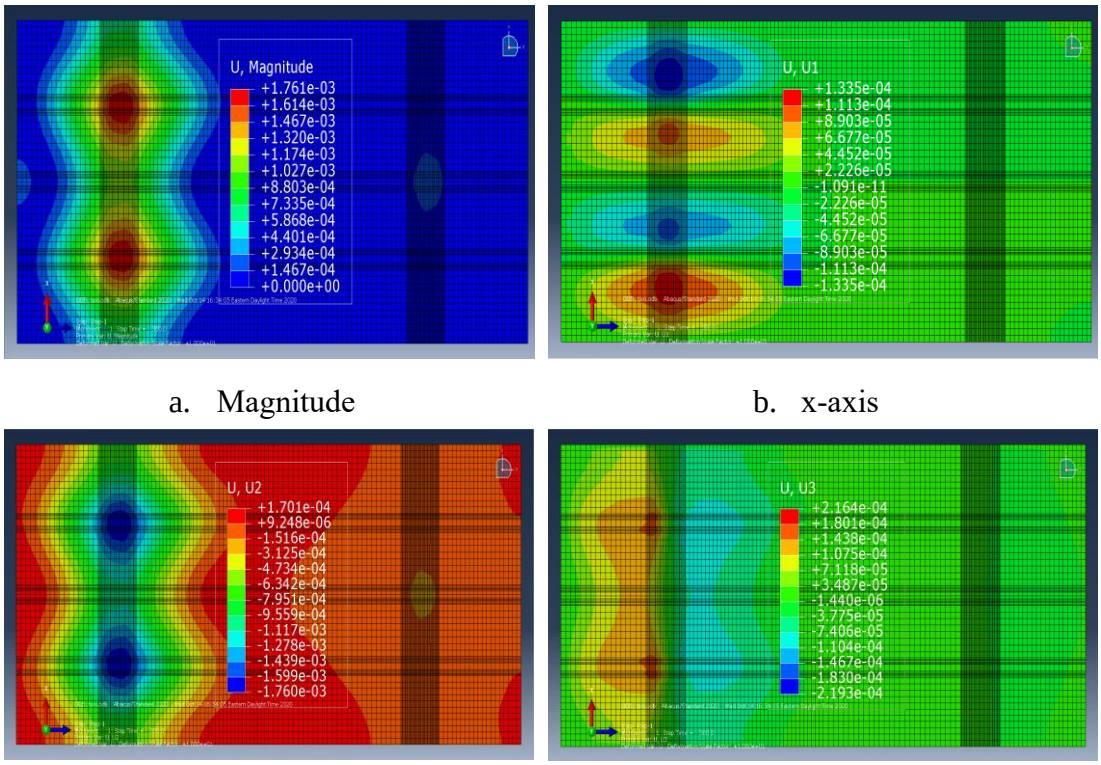

a. Magnitude b. x-axis

c. y-axis d. z-axis

Figure 8-17 Displacement Distribution at Asphalt Surface Layer

The displacement magnitude distribution, U1, U2, and U3 along with transverse distance and depth are shown in Figure 8-18 through Figure 8-21. From the displacement magnitude curve with transverse distance and depth in Figure 8-18, it can be seen that the effect of the main gear on displacement magnitude is much more significant than that of the nose gear. The maximum displacement magnitude for the main gear is 2 mm while it is only 0.2 mm for the nose gear. The displacement magnitude drastically decreases below the depth of 1.5 m for both main gear and nose

gear. For the displacement under the main gear, it reaches 1 mm at a depth range of 2 m to 3 m, and it decreases linearly with the further increase in pavement depth.

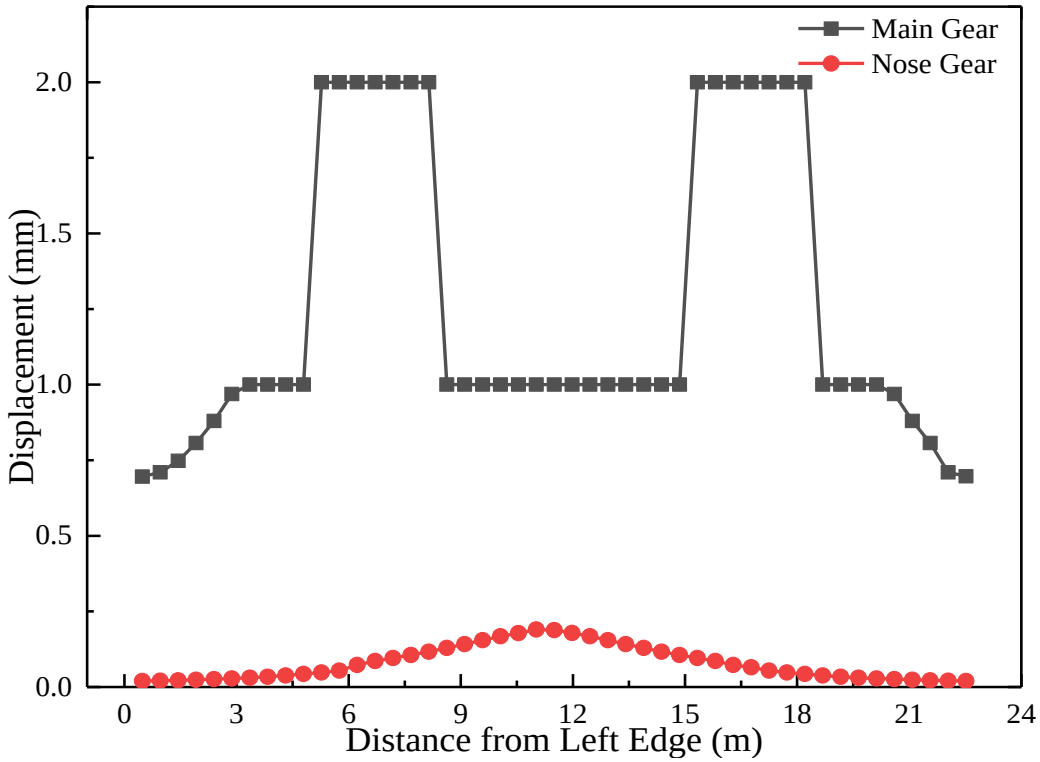

a. Displacement with Distance from the Left Edge

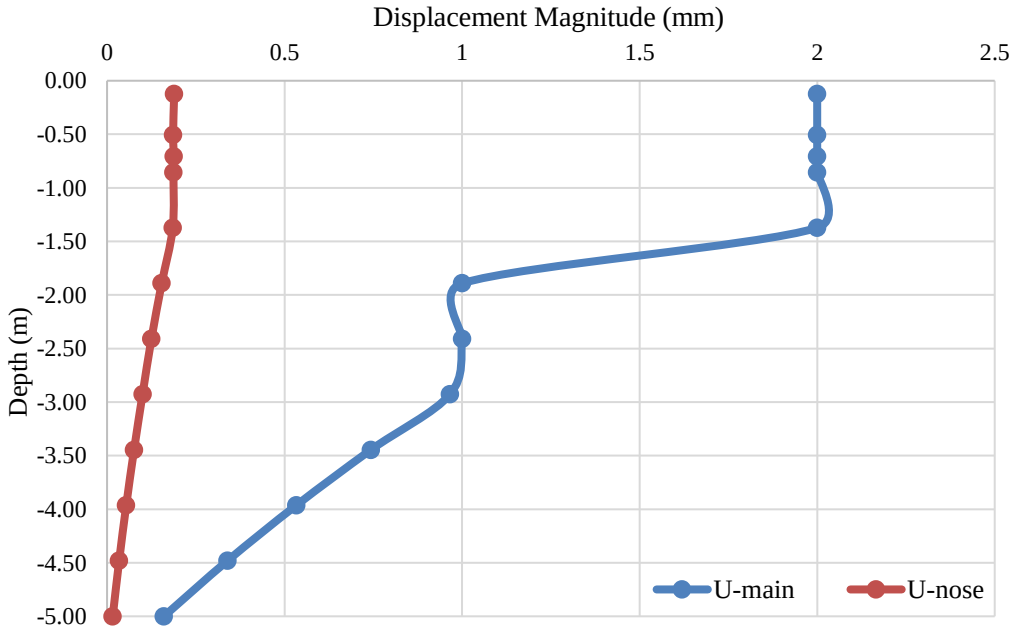

b. Displacement with Depth

Figure 8-18 Distribution of Displacement Magnitude Under Nose Gear and Main Gear Loads

Figure 8-18 indicates that the distribution of displacement U1 under the main gear is significantly different from that of the nose gear. Figure 8-18a shows that at the left and right side of each main gear, the potential for displacement U1 is in the opposite direction, which implies that at each main gear, the pavement material tends to transversely deform or delaminate in different directions. Figure 8-18b indicates that for the main gear, the displacement U1 decreases with increasing pavement depth in a different pattern. The top of the asphalt surface layer on the left side of the main gear shows a greater displacement U1 than that on the right side of the main gear. With the increase of pavement depth, the pavement under the left side of the main gear drastically decreases until the depth reaches 2.25 m. The pavement under the right side of the main gear, displacement U1 changes randomly but with a smaller magnitude than the left side.

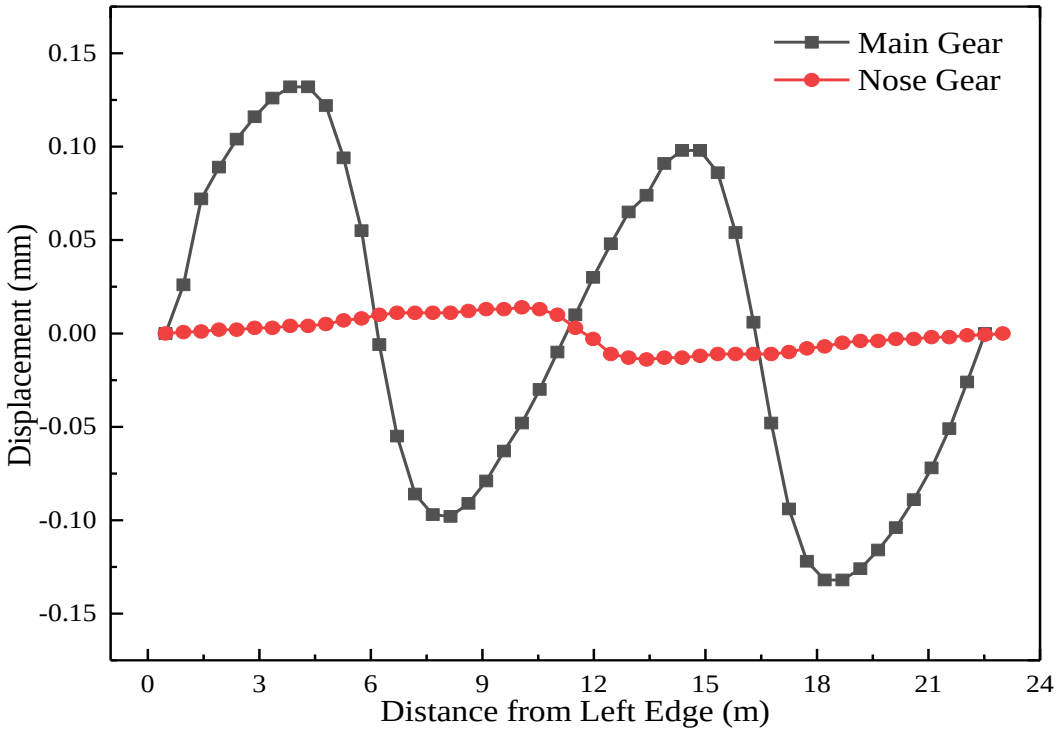

a. Displacement with Distance from the Left Edge

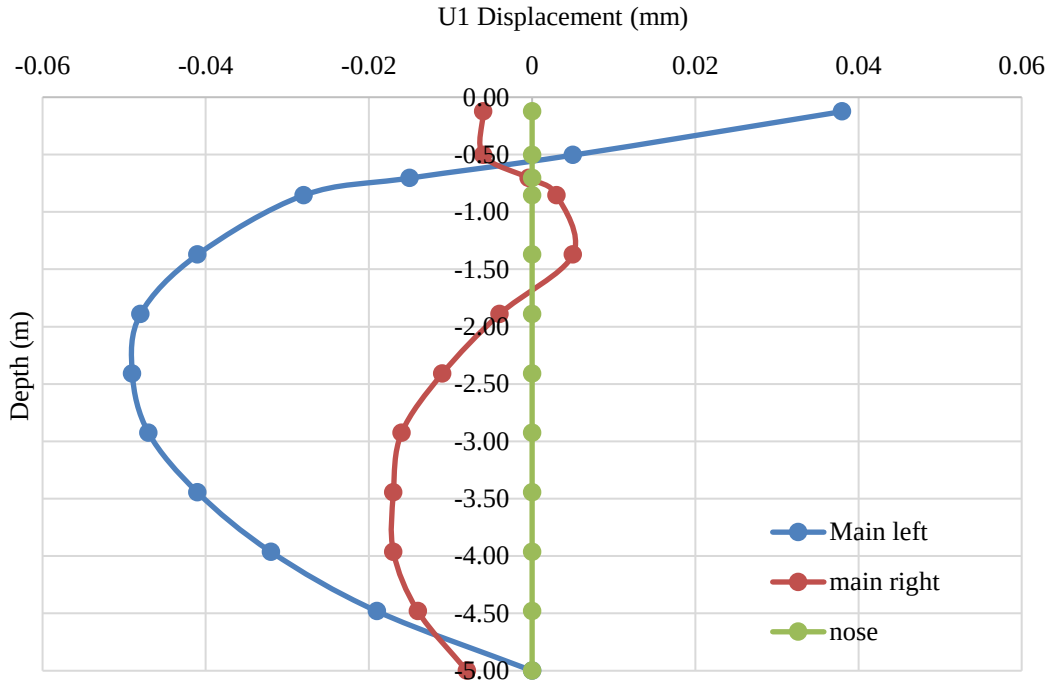

b. Displacement with Depth

Figure 8-19 Distribution of Displacement U1 Under Nose Gear and Main Gear Loads

The distribution of displacement U2 as a function of the transverse direction and pavement depth is displayed in Figure 8-19, which exhibits a similar distribution to the overall displacement, this demonstrates that the overall displacement magnitude is mainly induced by displacement U2, namely the deformation in y-axis dominates the whole displacement of the pavement system. Compared to main gear loads, the nose gear has much less impact on pavement displacement.

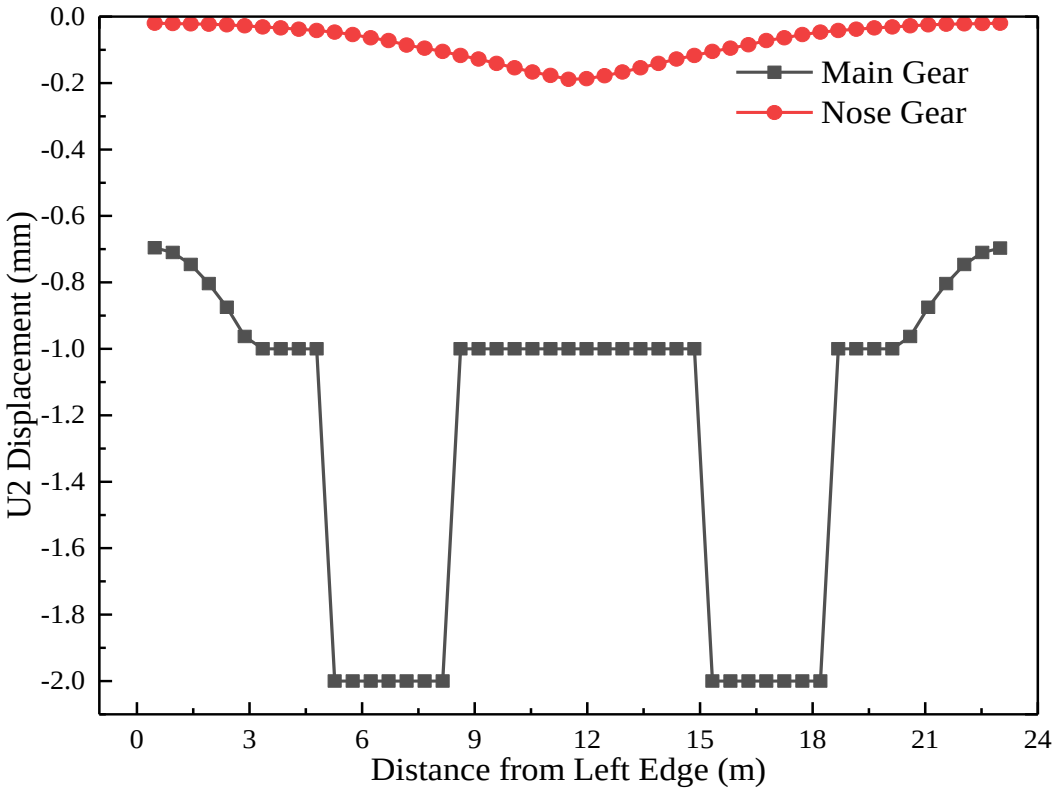

a. Displacement with Distance from the Left Edge

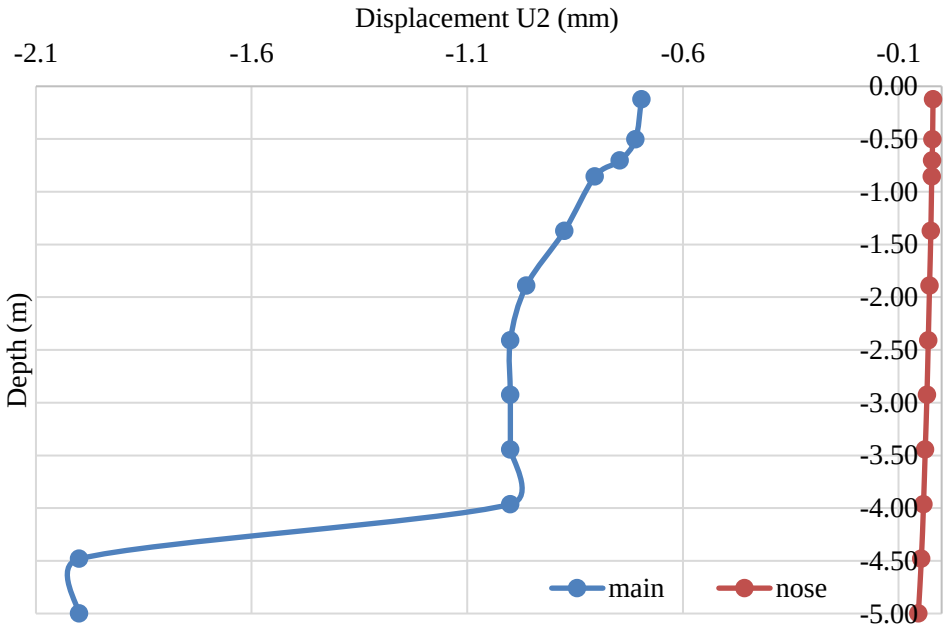

b. Displacement with Depth

Figure 8-20 Distribution of Displacement U2 Under Nose Gear and Main Gear Loads

The distribution of displacement U3, displacement along with z-axis, are presented in Figure 8-20. As can be seen, the main gear has a significant impact on displacement U3. The displacement reaches a peak level at the center of the main gear loads. The maximum displacement U3 on top of the asphalt surface layer for the main gear is 0.062 mm and drops to 0 when the depth reaches 1.5 m. The displacement of the asphalt surface layer for the nose gear, however, is 0.015 mm.

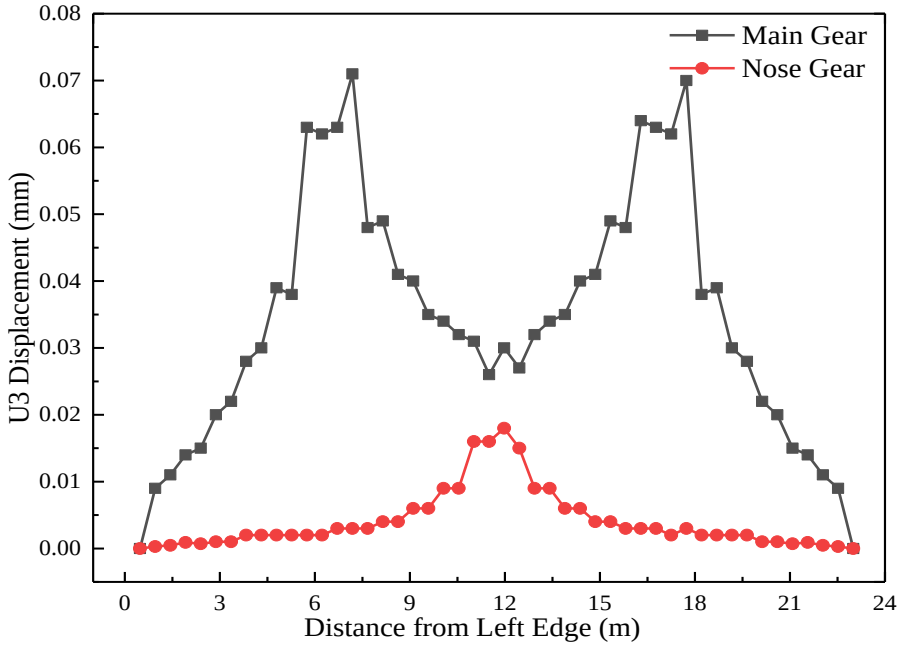

a. Displacement with Distance from the Left Edge

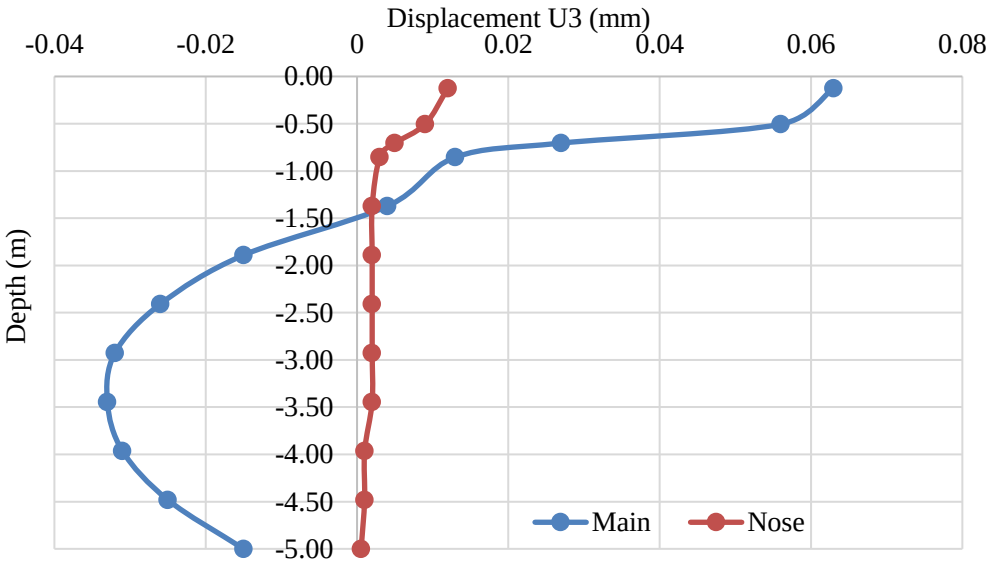

b. Displacement with Depth

Figure 8-21 Distribution of Displacement U3 Under Nose Gear and Main Gear Loads

8.4 Results and Discussion Part 2: Different Ground Maneuverings

8.4.1 Von Mises Stress Analysis

Five types of aircraft ground maneuverings including taxi, takeoff, landing, zero fuel, and operating empty are simulated through the same FE model. The distribution of Von Mises stress under the main gear and nose gears loads along with the distance from the left edge are shown in Figure 8-22 and Figure 8-23.

Figure 8-22 shows that among all the aircraft ground maneuverings, takeoff has the most significant impact on Von Mises Stress distribution. The difference of Von Mises stress under the two sets of main gears and space in between is 0.6 MPa while the empty operating has the least impact. The difference between the main gear loads and space in between is 0.2 MPa. Figure 8-23 indicates that nose gear has only a mild influence on the Von Mises stress distribution but a similar trend. The takeoff has the most and the empty operating has the least impact on Von Mises distribution on the asphalt surface layer.

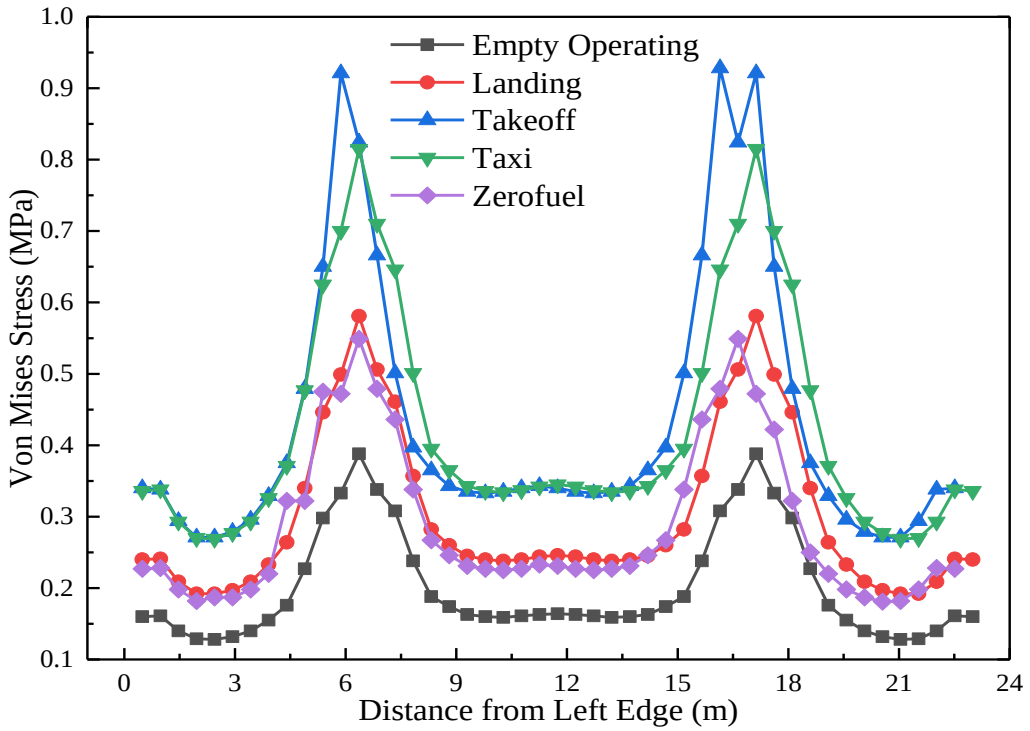

Figure 8-22 Von Mises Stress Distributing Underneath Main Gear Loads with Distance from Left Edge

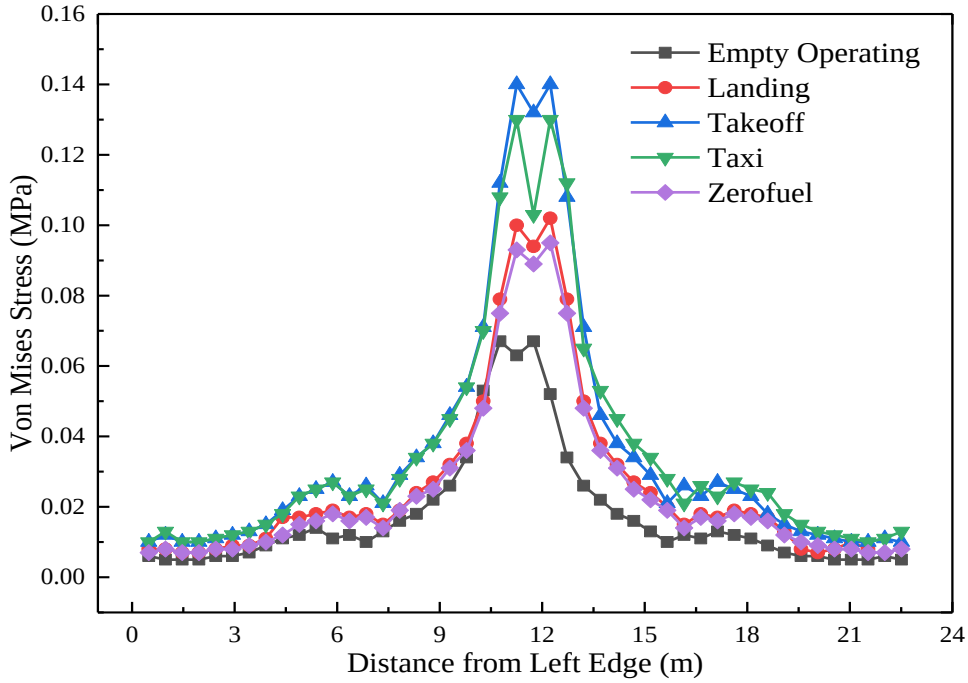

Figure 8-23 Von Mises Stress Distributing Underneath Nose Gear Loads with Distance from Left Edge

The Von Mises stress distribution along with pavement depth under the main gear and nose gear loads are displayed in Figure 8-24 and Figure 8-25. It appears that Von Mises stress reaches peak value at approximately 0.7 m depth, right where the cement stabilized base layer is located at. Among all the ground maneuverings, taxiing induces the maximum Von Mises stress. The impact caused by gear loads seems only to affect the depth within a range of 1 m. Different ground maneuverings have no impact on Von Mises stress distribution at a pavement depth lower than 1 m.

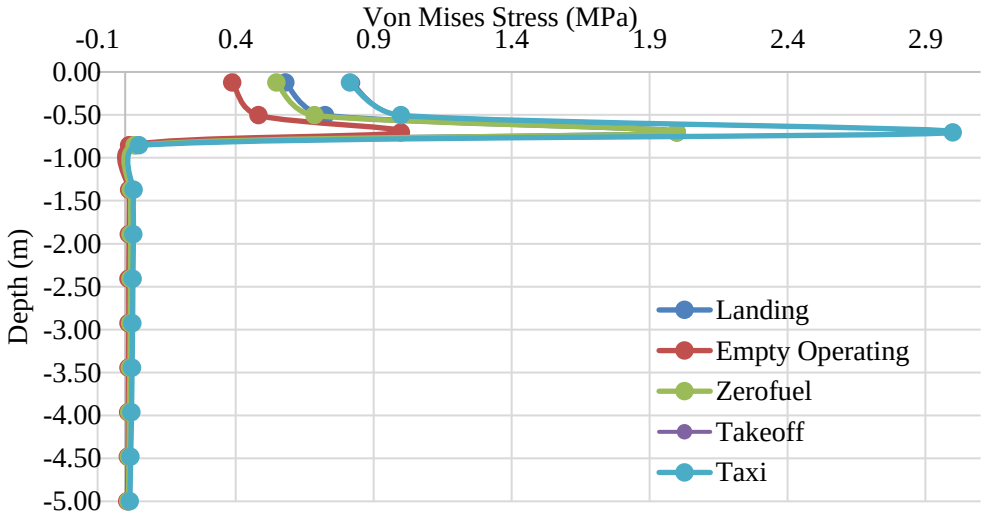

Figure 8-24 Von Mises Stress Distributing Underneath Main Gear Loads with Pavement Depth

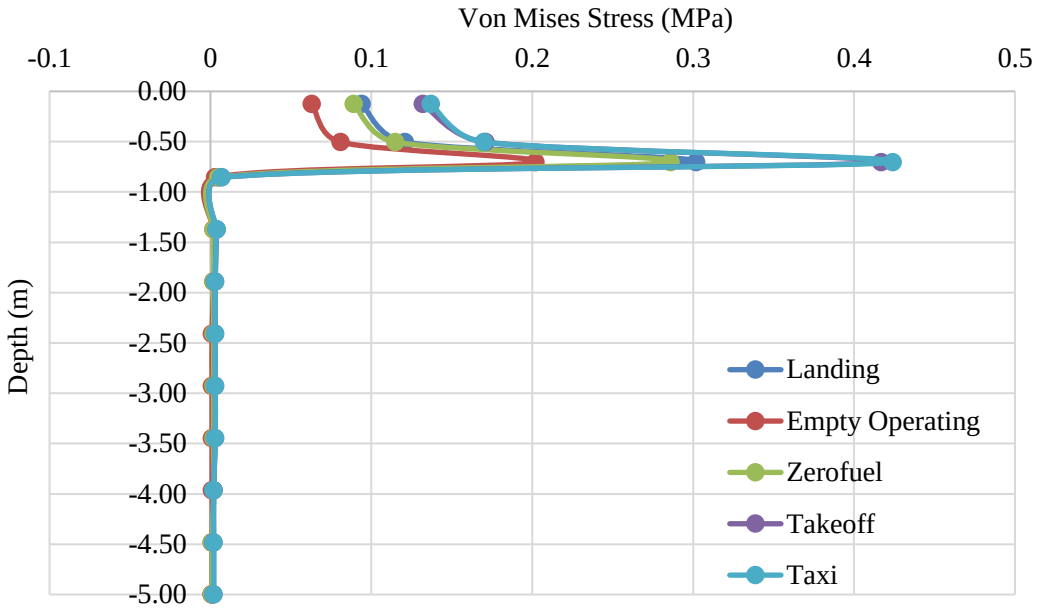

Figure 8-25 Von Mises Stress Distributing Underneath Nose Gear Loads with Pavement Depth

8.4.2 Shear Stresses Distribution under Main Gear Loads

As aforementioned, main gear loads have a much more significant impact on pavement stress distribution compared to nose gear loads. Therefore, for shear stresses only the impact of main gear loads was taken into consideration. The shear stress S12 distribution on the asphalt surface layer as a function of the distance from the left edge and pavement depth is shown in Figure 8-26 and Figure 8-27. It seems that different ground maneuverings have the almost same amount of impact on shear stress distribution on the asphalt surface with taxiing having slightly more impact than other maneuverings. The distribution along the pavement depth is significantly affected by various ground maneuverings with taxiing the most and empty operating the least. Shear stress S12 is symmetrically distributed on the left and right side of the main gear loads as shown in Figure 8-28.

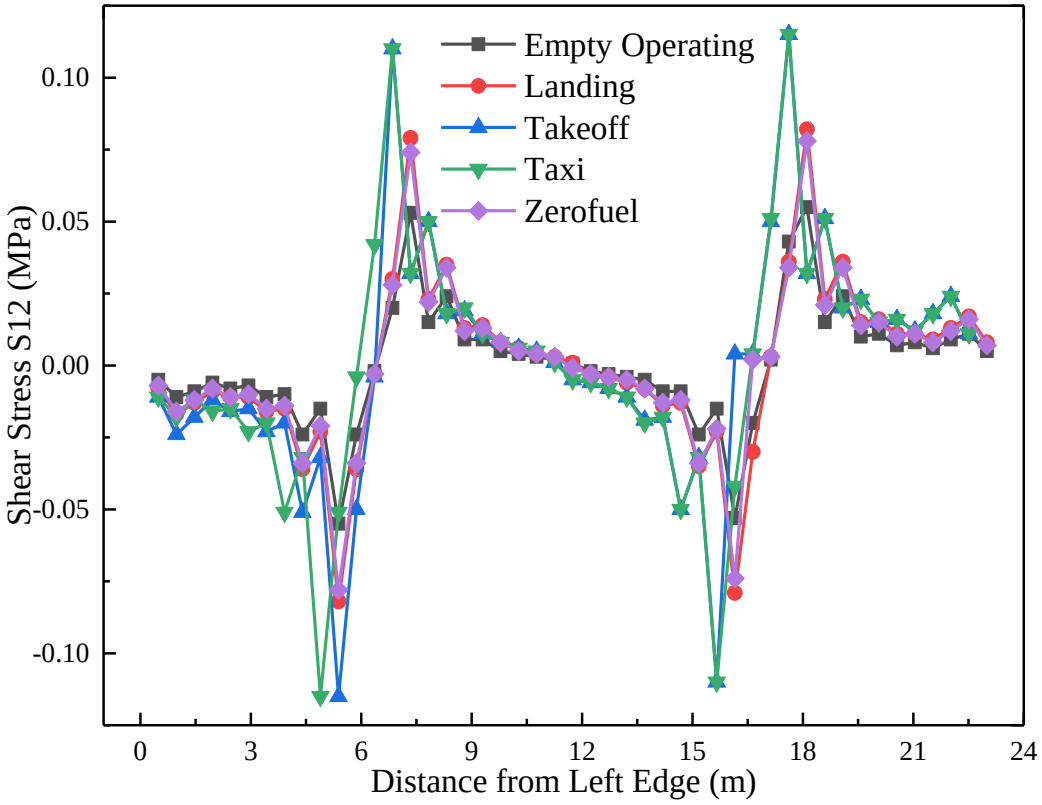

Figure 8-26 Distribution of Shear Stress S12 Along with Distance from the Left Edge

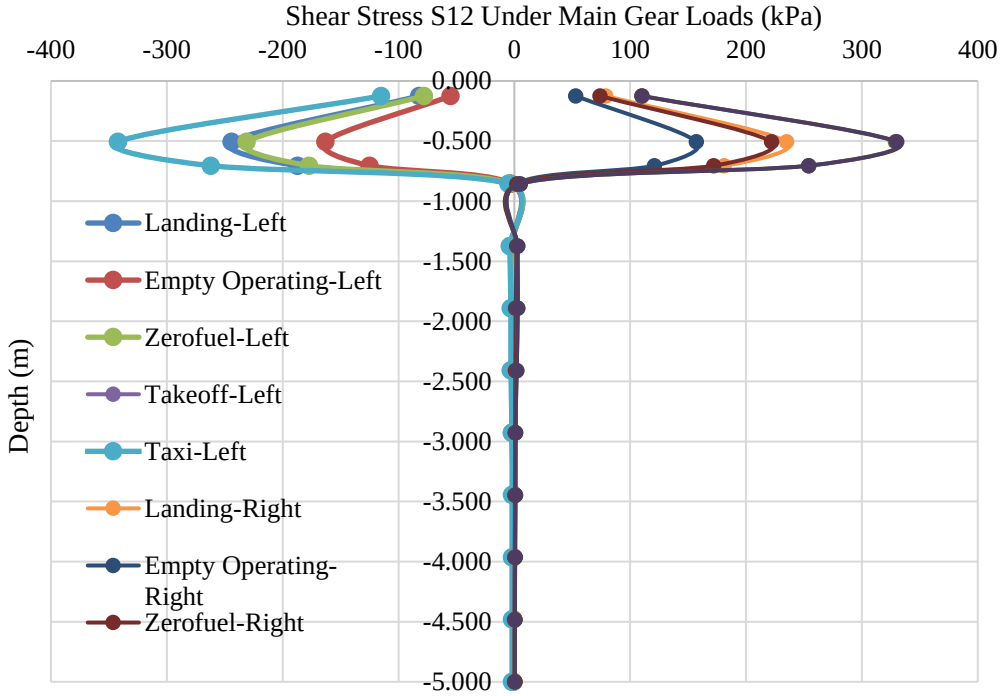

Figure 8-27 Distribution of Shear Stress S12 Along with Pavement Depth

Figure 8-28 and Figure 8-29 presents the distribution of shear stress S13 on the asphalt surface as a function of distance to the left edge and pavement depth under the main gear loads. Takeoff has the most impact on the shear stress S13 distribution and zero fuel operation the least. The S13 dominates the damage of transverse and longitudinal deformation, which means aircraft takeoff maneuvering is more likely to cause asphalt surface horizontal deformation. Zero fuel operation has the least potential to cause this type of pavement failure.

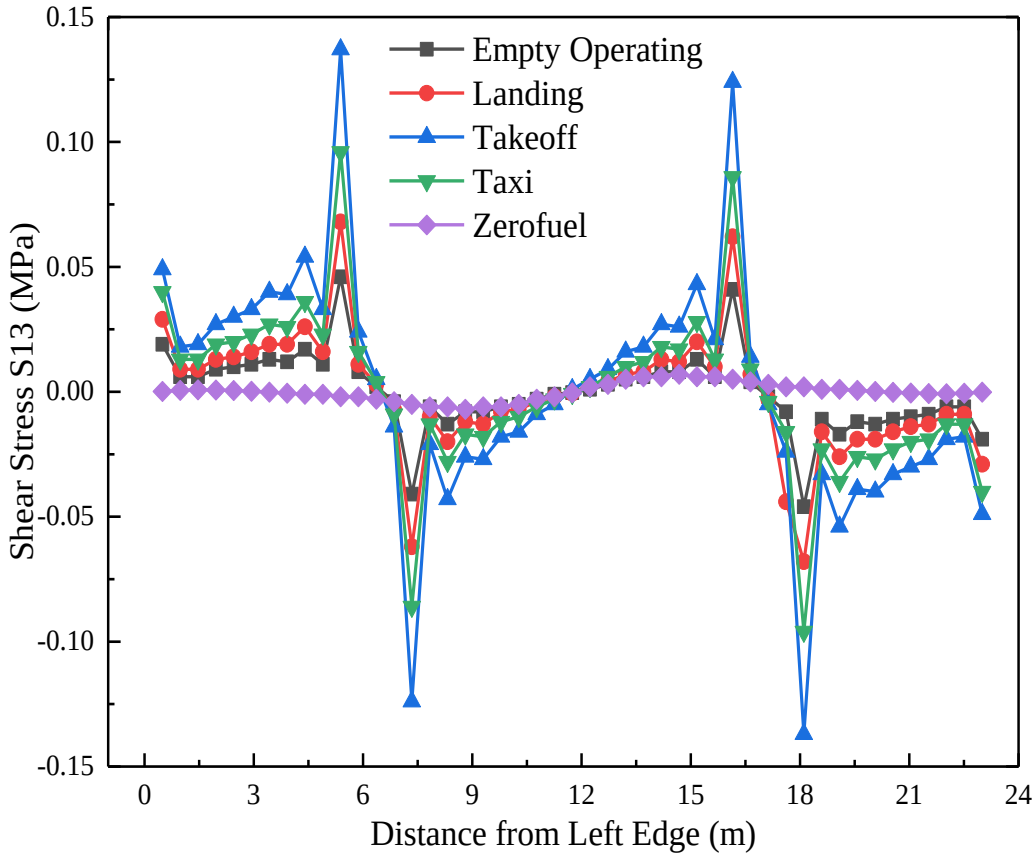

Figure 8-28 Distribution of Shear Stress S13 Along with Distance from the Left Edge

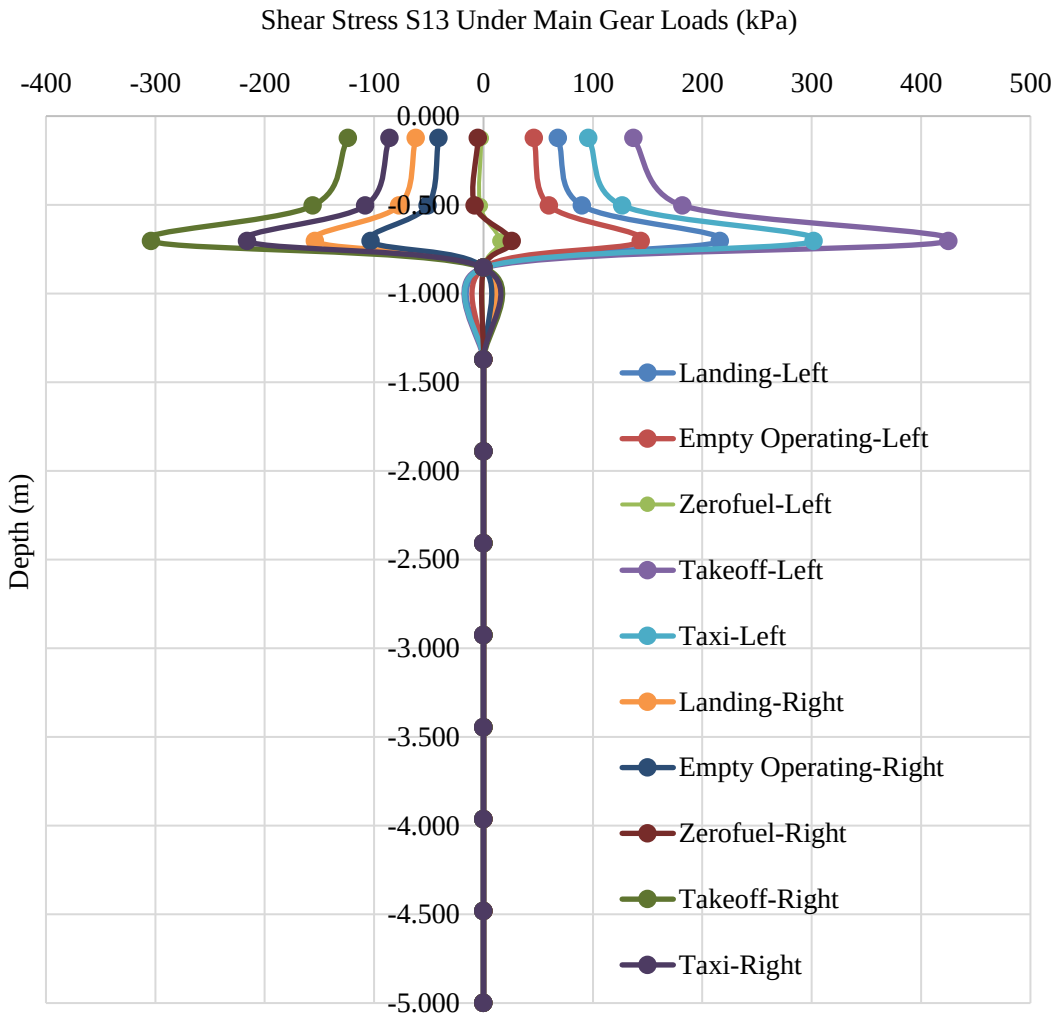

Figure 8-29 Distribution of Shear Stress S13 Along with Pavement Depth

The distribution of shear stress S23 on the asphalt surface layer along with the distance from the left edge and pavement depth are presented in Figure 8-30 and Figure 8-31. For shear stress S23, takeoff operation generates the highest level of stress while empty operating the lowest. S23 dominates the longitudinal delamination and rippling distress. Therefore, takeoff is more likely to result in asphalt layers delamination longitudinally or upheaval waves on the asphalt surface.

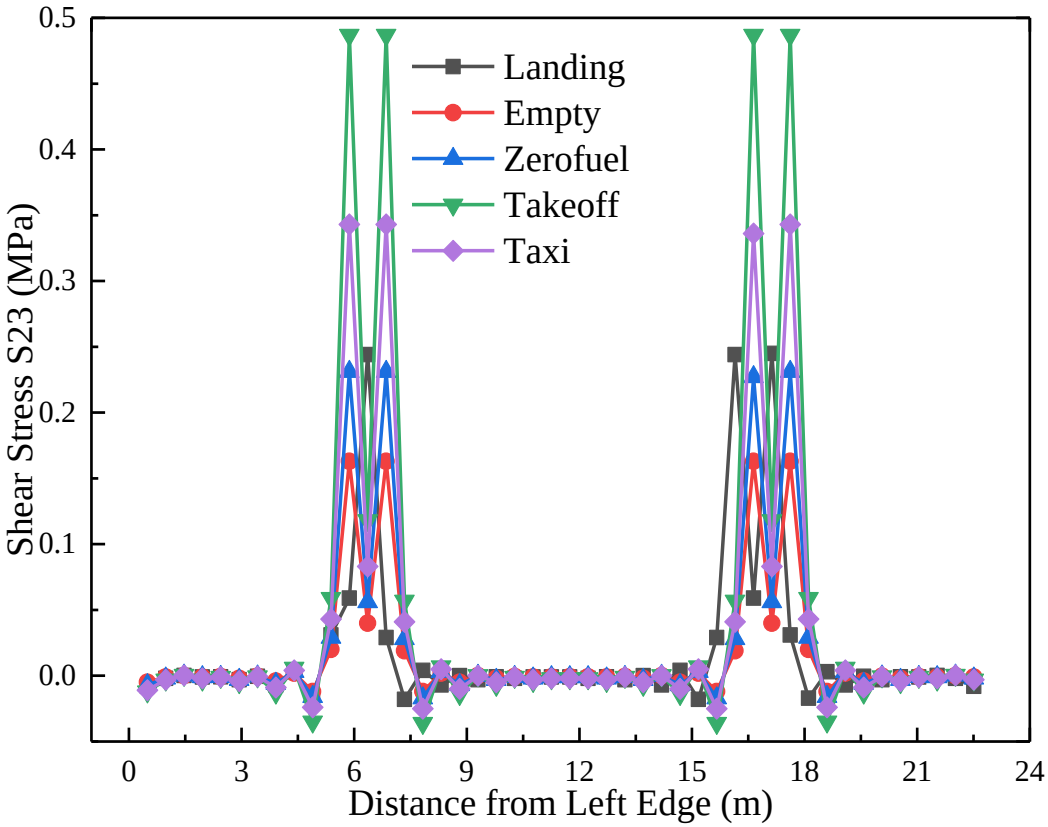

Figure 8-30 Distribution of Shear Stress S23 Along with Distance from the Left Edge

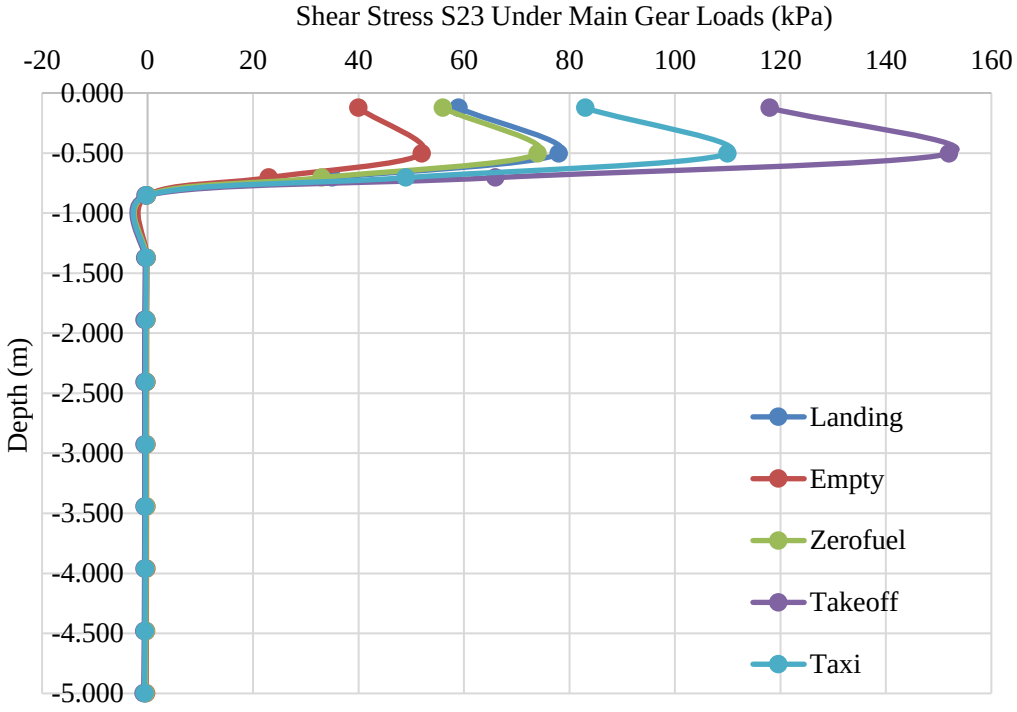

Figure 8-31 Distribution of Shear Stress S23 Along with Pavement Depth

8.4.3 Displacement Analysis under Main Gear Loads

Figure 8-32 and Figure 8-33 presents the distribution of displacement U1 under the main gear loads as a function of the distance from the left edge of the asphalt surface layer and the pavement depth. Displacement U1 represents the displacement of the pavement structure in the x-axis direction. As mentioned before, U1 displacement was generated by normal stress S11 (σ_x), shear stress S21 (τ_{yx}) and shear stress S31 (τ_{zx}). Hence the displacement U1 is the result of tension or compression (transverse deformation) and shear strain along with the x-axis (transverse delamination).

Figure 8-32 reveals that among various aircraft ground maneuverings, takeoff and zero fuel operation cause the greatest displacement in the x-direction, while the landing causes the least displacement U1. Moreover, Figure 8-32 also shows that the main gear loads will cause the material on the two sides to move in a direction against each other. In Figure 8-33, the displacement U1 underneath the main gear loads is displayed for various ground maneuverings. It shows that the displacement on the left and right sides of each main gear load is in opposite directions but similar in quantity. Displacement on the left side of each main gear set is greater than on the right. The quantity of displacement U1 varies with the depth of pavement and it reaches zero at a depth of -0.5 m. For the material underneath the left side of each main gear, the maximum displacement U1 is at subgrade while for the material underneath the right side of the main gear, the peak displacement U1 is located at the subbase layer.

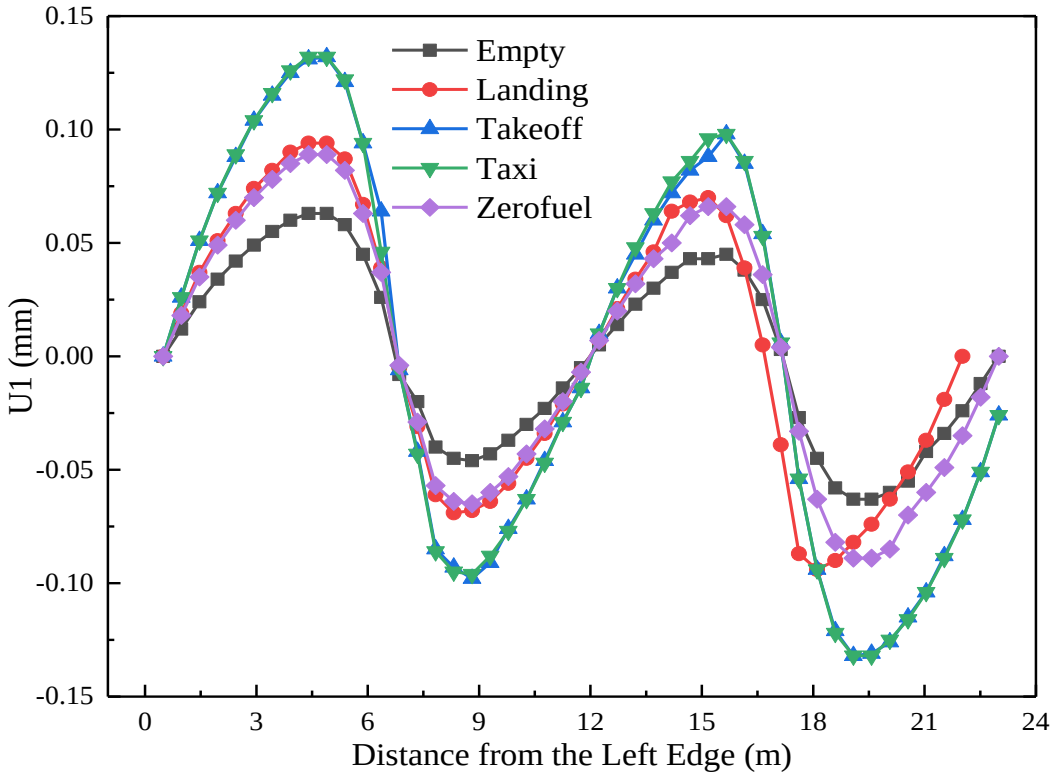

Figure 8-32 Asphalt Surface Displacement U1 with Distance from the Left Edge

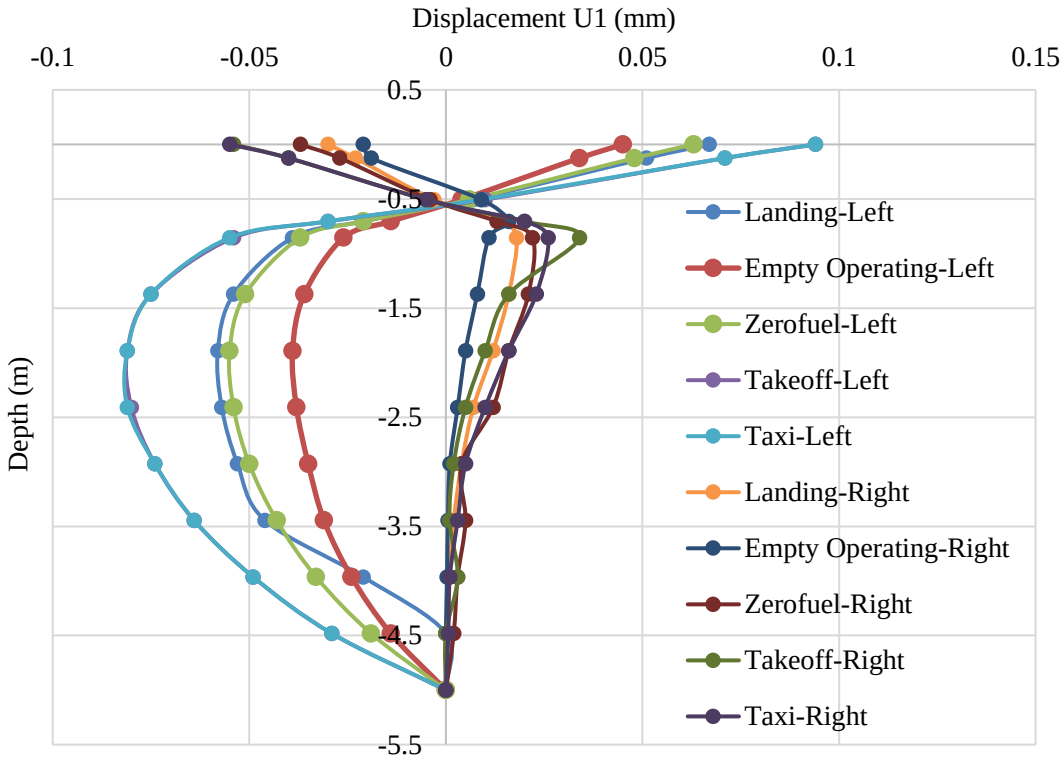

Figure 8-33 Distribution of Displacement U1 Along with Pavement Depth

Figure 8-34 and Figure 8-35 exhibit the displacement U2 under the main gear loads as a function of the distance from the left edge on the asphalt surface layer and the pavement depth. U2 is the displacement in the y-direction. It is mainly induced by normal stress S22 (σ_y), shear stress S12 (τ_{xy}) and shear stress S32 (τ_{zy}). Displacement U2 is therefore the reflection of rutting and rippling (vertical relocation of materials). From Figure 8-35 it can be concluded that taxiing and takeoff generate the greatest vertical movement of asphalt materials underneath the main gear loads. Landing and zero fuel operation have a similar impact on displacement U2 while operating empty have the minimum impact.

Figure 8-35 indicates that at a pavement depth range of 0.7 m at the subbase layer, the displacement U2 induced by main gears is unchanged under each different ground maneuverings. The displacement U2 follows a nearly linear decrease trend as the pavement depth reaches -2.5 and lower.

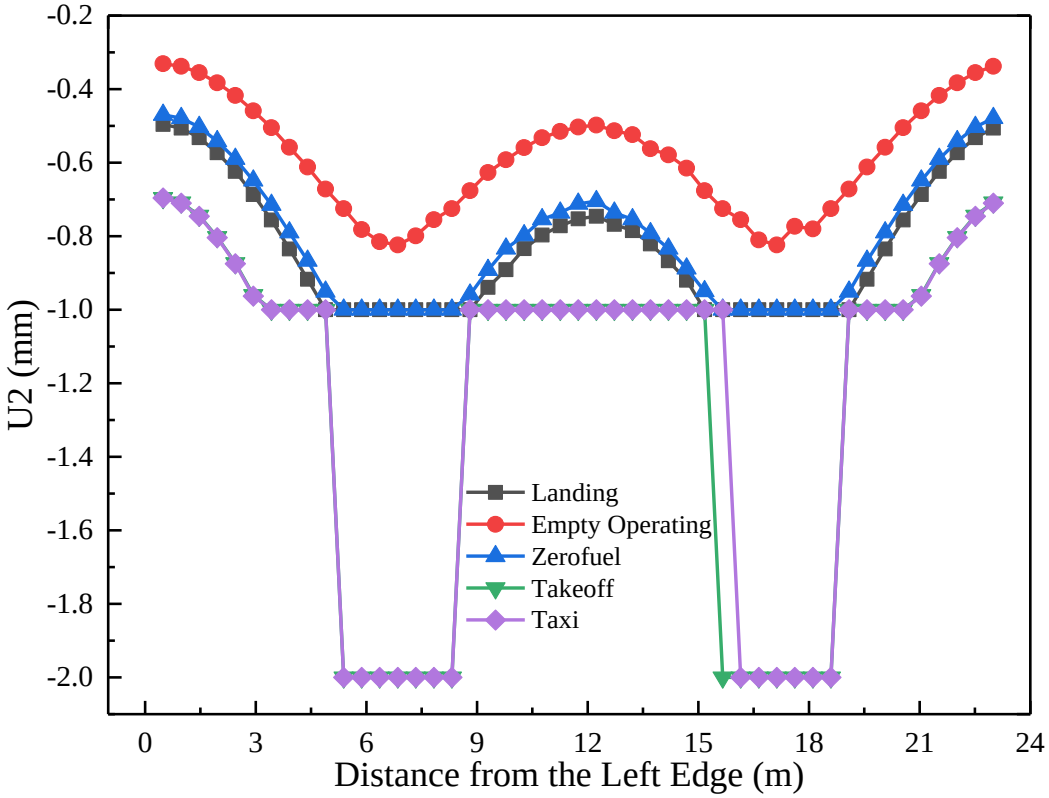

Figure 8-34 Asphalt Surface Displacement U2 with Distance from the Left Edge

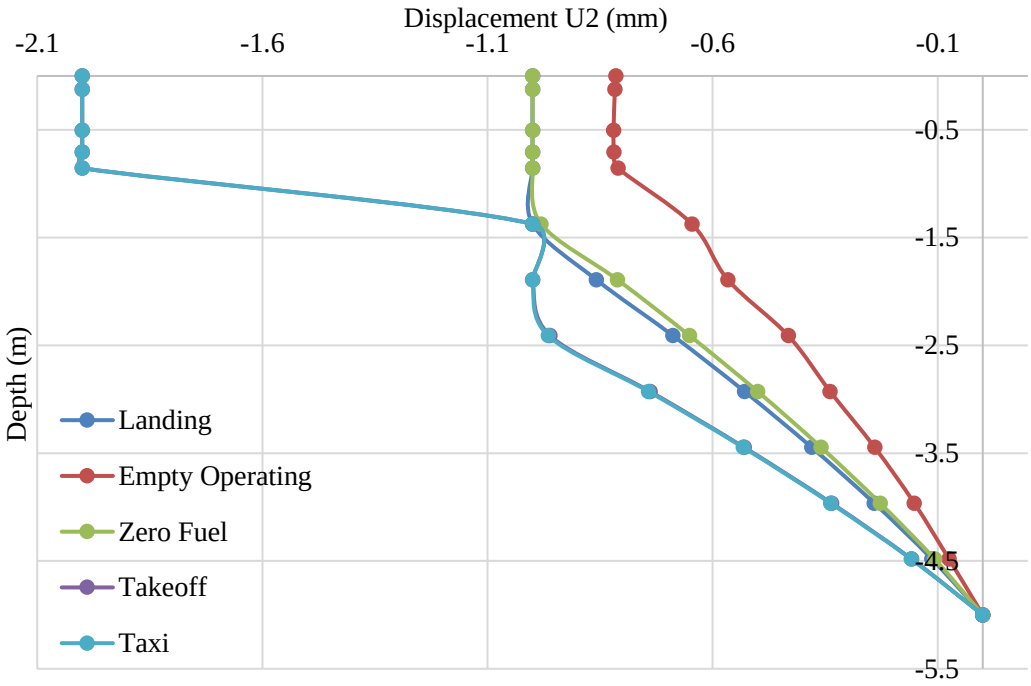

Figure 8-35 Distribution of Displacement U2 Along with Pavement Depth

The distribution of displacement U3 under the main gear loads is presented in Figure 8-36 and Figure 8-37. U3 is dependent on normal stress S33 (σ_z), shear stress S13 (τ_{xz}) and shear stress S23 (τ_{yz}), and is an indication of combined movement of longitudinal delamination and longitudinal deformation. Figure 8-36 shows that different aircraft ground maneuverings generate nearly the same amount of displacement U3 on the asphalt surface layer, with takeoff producing a slightly higher displacement as can be seen in Figure 8-38. Operating empty causes the least U3 displacement.

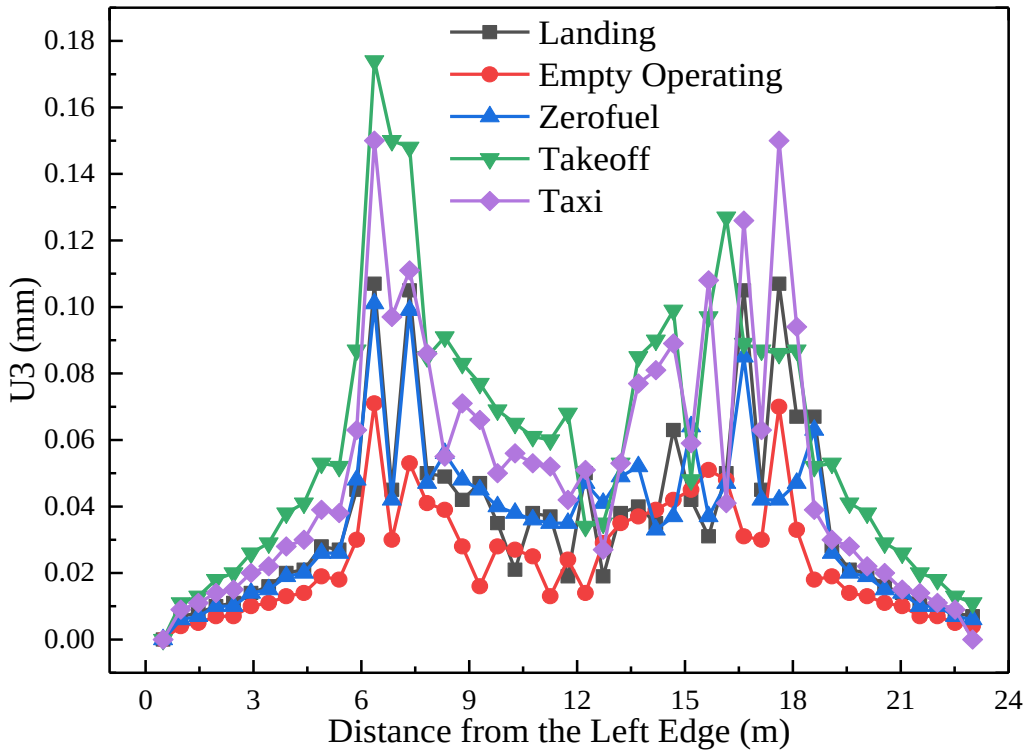

Figure 8-36 Asphalt Surface Displacement U3 with Distance from the Left Edge

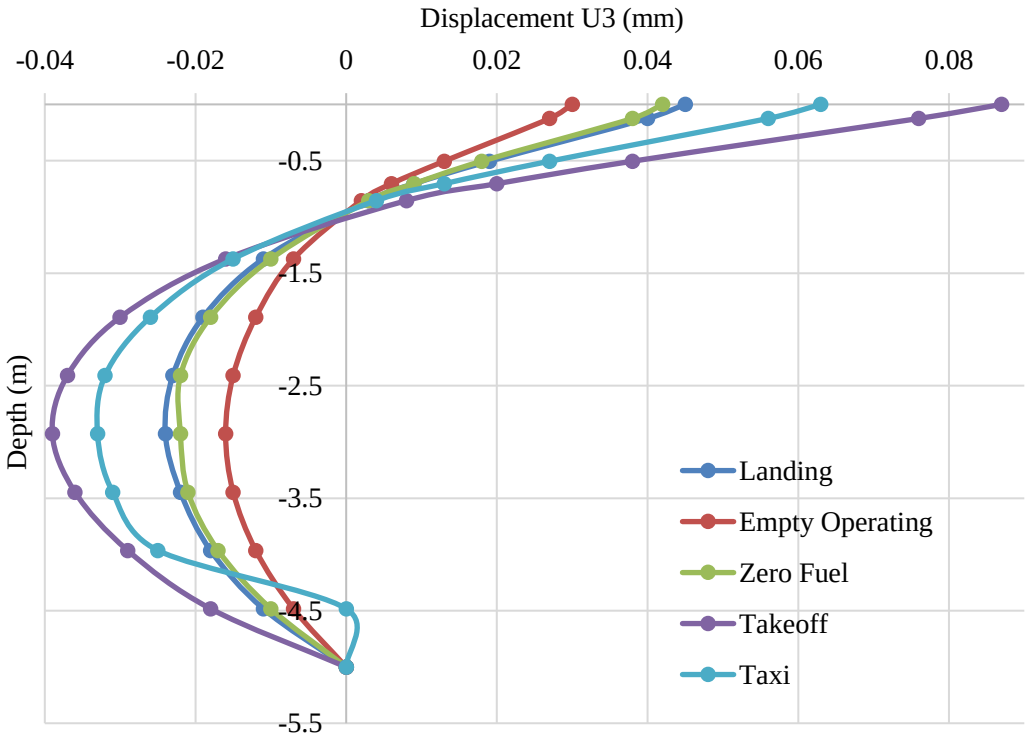

Figure 8-37 Distribution of Displacement U3 Along with Pavement Depth

Figures 8-38 and Figure 8-39 show the displacement magnitude distribution over the distance from the left edge on the asphalt surface layer and pavement depth.

Displacement magnitude is a displacement resultant considering all the directions. The displacement magnitude distribution is similar to displacement U2, which demonstrates that most displacement is generated by the vertical movement of materials. Figure 8-38 shows that taxiing and takeoff produce the same amount of displacement magnitude. The displacement caused by zero fuel operation and landing is close, and empty operating has minimum impact. Figure 8-39 indicates that the displacement magnitude generated by main gear loads is constant from the asphalt surface to the subbase layer. For taxiing and takeoff, the displacement magnitude stays the same between 1.5 m to 2.5 m. However, the other three ground maneuverings show a nearly linear decrease beneath 1.5 m.

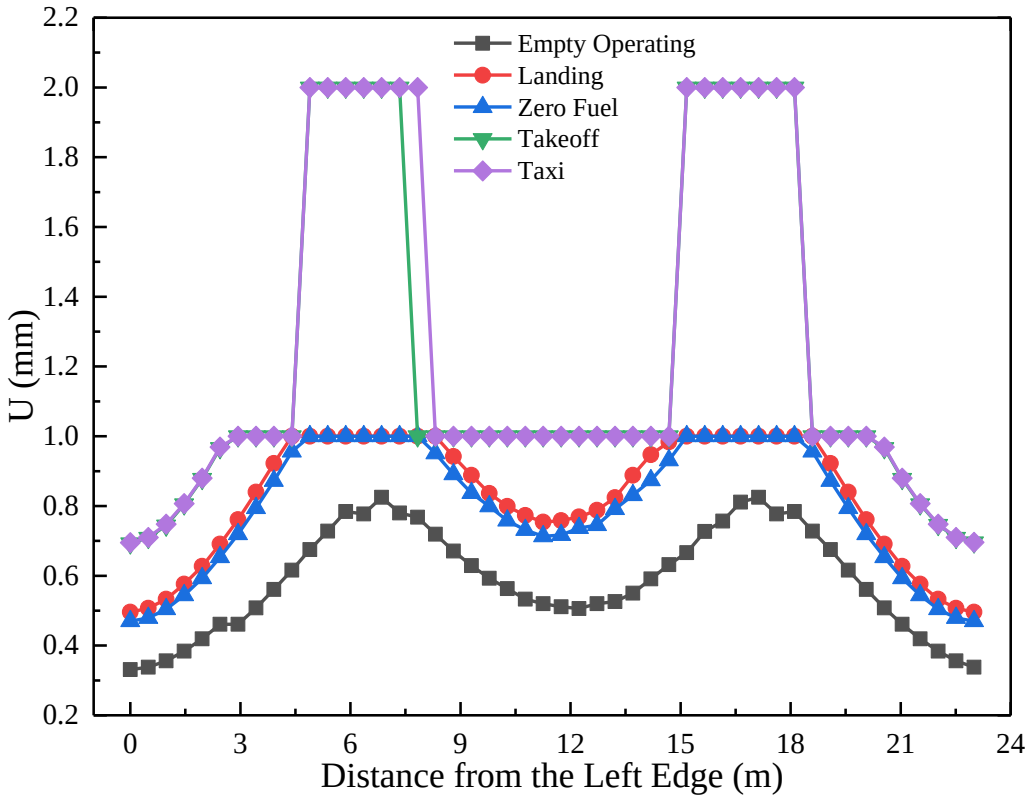

Figure 8-38 Asphalt Surface Displacement Magnitude with Distance from the Left Edge

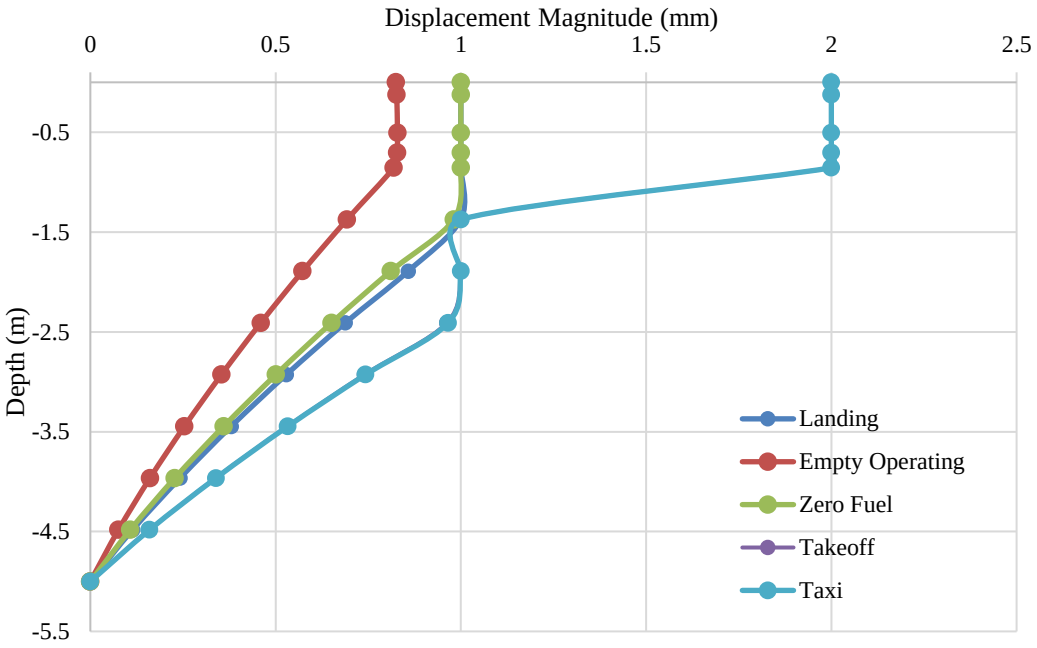

Figure 8-39 Distribution of Displacement Magnitude Along with Pavement Depth

8.5 Summary

A three-dimensional finite element model was established using ABAQUS standard mode based on the geometric design of taxiways at the Toronto Pearson International Airport. The asphalt surface layer and lower layer were considered as linear viscoelastic materials using the Prony series model. The Cauchy stress tensor was implemented to explain the relationship between different stress components and various asphalt pavement failures. Five types of common aircraft ground maneuverings including taxiing, takeoff, landing, zero fuel, and empty operating were considered and analyzed in this study. Von Mises Stress and various shear stress distributions as a function of the distance from the left edge on the asphalt surface layer and pavement depth under the main gear and nose gear loads were presented. Different pavement distress potential has been discussed under each type of ground maneuvering. Major conclusions can be drawn as follows:

1. Critical Von Mises Stresses of pavement under the main gear and nose gear loads both occur at the cement stabilized base layer for aircraft taxi operation. The maximum

Von Mises Stress generated by main gear loads is 6 times greater than that generated by nose gear loads. **Conclusions 2 to 5 are based on taxi operation analysis.**

2. Shear stress S12 (τ_{xy}), which is quantitatively equal to shear stress S21 (τ_{yx}), distributes on the left and right side of each main gear loading with the same quantity but opposite directions. Shear stress S12 generates the movement of the material in the x-direction and dominates the transverse delamination or transverse slippage distress. S21 generates materials movement in the y-direction and dominates rutting. S12 reaches a peak level at the depth of 0.5 m below the asphalt surface layer. Shear stress S12 generated by main gear loads is 5 times greater than that generated by the nose gear on the asphalt surface.

3. Shear stress S13 (τ_{xz}) generates the displacement in the z-direction and dominates the transverse deformation. S31 (τ_{zx}) causes material movement and leads to longitudinal deformation. Similarly, shear stress S13 (τ_{xz}) and S31 (τ_{zx}) are equal in quantity but represent shear stresses in different planes. For shear stress S13 (τ_{xz}) and S31 (τ_{zx}), the material underneath the left side of each main gear generates a greater stress level than that from the right side of the main gear. Shear stress S13 generated by main gear loads is equal to that by the nose gear but in the opposite direction.

4. Shear stress S23 (τ_{yz}) creates the movement of the material in the z-direction and dominates the longitudinal delamination. S32 (τ_{zy}) produces the displacement on the y-axis and dominates the pavement rippling damage. Correspondingly, shear stress S23 (τ_{yz}) and S32 (τ_{zy}) are quantitatively equal but represent two pairs of stresses in the XZ-plane and XY-plane, respectively. S23 (τ_{yz}) and S32 (τ_{zy}) distribute symmetrically on the left and right side of each main gear loading center along with the pavement depth. Shear stress S23 generated by main gear loads is almost 16 times greater than that by nose gear loads on the asphalt surface layer.

5. Displacement U1, U2, and U3 represent the movement on the x-axis, y-axis, and z-axis, respectively. U1 displacement results from the normal stress S11, shear stress S21, and shear stress S31. Hence U1 is an indication of transverse delamination and

longitudinal deformation. The displacement U1 of the materials on the left and right side of each main gear load is different in terms of quantity and direction. U1 displacement is usually small in quantity (less than 0.05 mm). U2 results from the normal stress S22, shear stress S12, and shear stress S32. Displacement U2 is therefore the combined effect of rutting and rippling distress. Compared to displacement U1, main gear loads can generate much more significant displacement in the y-direction than nose gear. Displacement U3 is induced by normal stress S33, shear stress S13, and shear stress S23. U3 results from the transverse deformation and longitudinal delamination. Similar to U1, displacement U3 is significantly smaller than U2. The quantity is usually less than 0.07 mm.

6. A similar analysis was conducted for the other aircraft ground maneuverings: taxiing, takeoff, landing, zero fuel, and operating empty. It was found that takeoff generates the greatest level of Von Mises stress on the asphalt surface layer while operating empty the least underneath the main gear and nose gear loads. For shear stress S12, taxiing creates the greatest level while operating empty the lowest. For shear stresses S13 and S23, takeoff generates the highest stress level while empty operating generates the lowest.

7. The displacement analysis of various aircraft ground maneuverings underneath the main gear loads showed that takeoff and taxi operation generate the most significant displacement for all three displacements U1, U2, and U3, and operating empty has the least impact on the displacement.

Chapter 9
CONCLUSIONS AND RECOMMENDATIONS

9.1 Research Conclusions

The main conclusions of this research can be concluded as follows:

- Asphalt binder PG level has a significant impact on the permanent deformation of HL3 and HL3 HS. Higher PG can provide asphalt mixtures with stronger rutting resistance of those two mixes. However, the impact of a higher PG level on HL1 HS is negligible.
- Mix gradation affects permanent deformation resistance. The rate of aggregate passing the 4.75 mm sieve plays an important role in rutting resistance: a higher passing rate can result in a better rutting performance. However, HL3 HS and HL1HS with PG 70-28 do not follow this trend.
- Rutting growth rates of all six mixes show similar trends: a short increase within the first 200 cycles, then a drop until 500-600 cycles, then another increase to a peak at 1000-2000 cycles, and another decrease until the end of the test.
- Machine learning technology (MLT) was used to segmentize the particles and voids, among various supervised learning methods, Fast-Random-Forest (FastRF) is adapted in this study. Through the binary process, the particles, asphalt binder, and voids were obtained.
- Four morphological indexes were introduced in analyzing the 2D shapes of particles: aspect ratio, roundness, solidity, and circularity. Among the four indexes, only roundness has a skewness value less than ± 0.5 and therefore is considered symmetrically distributed. The skewness of circularity and solidity are less than 1 and are treated as moderately skewed. The Aspect Ratio is highly skewed as its skewness is greater than 1.
- From the particle-processed images, the majority of particles' perimeter and the area are less than 10 mm and 10 mm^2, respectively. The number of particles drastically decreases when the perimeter is greater than 10 mm and the area is greater than 10 mm^2.

All six samples follow the same pattern. Sample 5 shows a higher roundness and solidity level. The processed images from lab-produced and plant-produced mix have a similar distribution according to the major axis of particles. The aggregate gradation distribution shows the opposite trend to the major axis particles distribution. This demonstrates that the distribution of image-processed particles based on the major axis can not reflect the gradation curve.

- The voids distribution of processed images shows consistency in perimeter and area for all six mixes. More than 60 percent of the voids have less than 1 mm^2 in the area for all the processed images. However, the distribution of the voids of all the mixes shows a similar pattern in perimeter from 0 to 10 mm. The number of voids decreases with the increase in the area and perimeter ranges.
- The relationship between rutting depth and morphological indexes is not satisfied. Possible explanations include whether the rut test can represent the actual stiffness of the corresponding asphalt mixture, the binary process might misrecognize the small particles and voids, the analysis ignored the effect of asphalt binder impacts and the combined impact of volumetric parameters and binder types.
- 50% potassium acetate liquid seems to have the softening effect on asphalt mixture's overall stiffness for both airport and roadway mixes. Freeze-thaw conditioning can deteriorate the rutting resistance for both mixes in different degrees.
- De-icing treatment and freeze-thaw cycles have the potential to induce stripping. The unsettled rut depth at the end of the HWTT test shows that especially de-icing treated asphalt specimens are more likely to have stripping distress.
- The combination effect of de-icing agent and freeze-thaw conditioning might have the effect of mitigating the rutting resistance compromise caused by the two treatments separately. The experimental results show that the rut depth of treatment Group 4 is slightly smaller than Group 2 and Group 3.
- Analysis of variance indicates that asphalt binder PG type and asphalt content have a statistical effect on rutting performance under the control group, de-icing treated

group, and freeze-thaw conditioned group. ANOVA also shows treatment methods have a significant effect on rut depth of asphalt mixture applied both on airports and roadways.

- Mix type can significantly affect the shear performance of asphalt mixture applied on both road and airport pavement. Before freeze-thaw treatment, the airport surface course mix shows the highest shear resistance among all other mixes, while the airport lower course mix displays the best shear performance after free-thaw treatment.
- Various treatments can also influence the shear resistance of the asphalt mixture. High-temperature exposure can reduce the shear resistance of all types of asphalt mixture. While with the treatment de-icer at 19°C, all the mixture shows the highest shear resistance among other treatments. However, this can be attributed to the comparatively low room temperature or the existence of a de-icer. Further experiments are recommended to investigate each effect of individual variables on the shear resistance performance of asphalt mixture.
- Critical Von Mises Stresses of pavement under the main gear and nose gear loads both occur at cement stabilized base layer for aircraft taxi operation. The maximum Von Mises stress generated by main gear loads is 6 times greater than that generated by nose gear loads.
- Shear stress S12 (τ_{xy}), which is quantitatively equal to shear stress S21 (τ_{yx}), distributes on the left and right side of each main gear loading center along with the pavement depth with the same quantity but opposite directions. Shear stress S12 generates the movement of the material in the direction of the x-axis and dominates the transverse delamination or transverse slippage distress. S21 generates the movement of the material on the y-axis and dominates rutting. S12 reaches a peak level at the depth of 0.5 m below the asphalt surface layer. Shear stress S12 generated by main gear loads is 5 times greater than that generated by the nose gear.
- Shear stress S13 (τ_{xz}) generates the displacement on the z-axis and dominates the transverse deformation. S31 (τ_{zx}) causes material movement on the x-axis and leads to

longitudinal deformation. Similarly, shear stress S13 (τ_{xz}) and S31 (τ_{zx}) are equal in quantity but represent shear stresses in different planes. For shear stress S13 (τ_{xz}) and S31 (τ_{zx}), the material underneath the left side of each main gear load generates a greater stress level than that from the right side of the main gear. Shear stress S13 generated by main gear loads is equal to that by the nose gear but in the opposite direction.

- Shear stress S23 (τ_{yz}) creates material movement on the z-axis and dominates the longitudinal delamination. S32 (τ_{zy}) produces displacement on the y-axis and dominates the pavement rippling damage. Correspondingly, shear stress S23 (τ_{yz}) and S32 (τ_{zy}) are quantitatively equal but represent two pairs of stresses in the XZ-plane and XY-plane, respectively. S23 (τ_{yz}) and S32 (τ) distribute symmetrically on the left and right side of each main gear loading center along with the pavement depth. Shear stress S23 generated by main gear loads is almost 16 times greater than that by the nose gear loads on the asphalt surface layer.
- Displacement U1, U2, and U3 represent the movement of the x-axis, y-axis, and z-axis. U1 displacement results from the normal stress S11, shear stress S21, and shear stress S31. Hence U1 is an indicator of transverse delamination and longitudinal deformation. The displacement U1 of the materials on the left and right side of each main gear load is different in terms of quantity and direction. U1 displacement is usually small in quantity (less than 0.05 mm). U2 results from the normal stress S22, shear stress S12, and shear stress S32. Displacement U2 is therefore the combined effect of rutting and rippling distress. Compared to displacement U1, main gear loads can generate much more significant displacement in the y-axis than nose gear. Displacement U3 results from the normal stress S33, shear stress S13, and shear stress S23. U3 is a measure of transverse deformation and longitudinal delamination. Similar to U1, displacement U3 is significantly smaller than U2. The quantity is usually less than 0.07 mm.

- A similar analysis was conducted for various aircraft ground maneuverings such as taxiing, takeoff, landing, zero fuel, and operating empty. It was found that takeoff generates the greatest level of Von Mises stress on the asphalt surface layer while operating empty the least for both underneath the main gear and nose gear loads. For shear stress S12, taxiing creates the greatest level while operating empty the lowest. However, for shear stresses S13 and S23 takeoff generates the highest stress level while operating empty generates the lowest.
- The displacement analysis of various aircraft ground maneuverings underneath the main gear loads showed that takeoff and taxi operation generate the most significant displacement for all three displacements U1, U2, and U3, and operating empty has the least impact on the displacement.

9.2 Research Contributions

The major contributions of rutting resistance evaluation of Ontario roadway mix by using Hamburg Wheel Rutting Test and CT scanning are: Hot laid 3 and Hot laid 3 High Stability are sensitive to asphalt binder, but Hot laid 1 high stability is not. The passing rate of 4.75 mm sieve size seems to affect the rutting performance. The significance of using CT scanning is to correlate morphological indices with mechanical test results. Ideally in the future, asphalt mixture's performance can be characterized or evaluated by simply scanning the specimen and analyze the image data from the computer instead of conducting a destructive test. However, the correlation in this study cannot serve this purpose yet, the possible explanation of not satisfactory correlation result can be the accuracy of digital image processing and the quality of the scanned images, a large number of small particles and voids could be misidentified into each other.

Through various treatments applied on roadway and airport pavement mix, rutting resistance and shear resistance laboratory test was conducted through HWTT and simplified UST. It was found that potassium acetate has a minor effect on shear resistance, but it can induce stripping distress. Mix type and treatment both have a significant effect on rutting and shear resistance, but no interaction was found between

these two factors. Freeze-thaw and 50 °C have the greatest impact on shear resistance. Freeze-thaw treatment can also cause stripping damage. However, the de-icing agent can mitigate the impact of freeze-thaw to the shear and rutting resistance of the asphalt mixture. A simple high binder PG or coarser mix gradation cannot secure a good shear resistance, these factors work together.

Through airport pavement 3D modeling, it shows the critical von mises stress and different shear stresses under the main gear and nose gear are both occurred at the cement stabilized base layer when the aircraft is performing taxiing, the stress under main gear is 6 times greater than that of the nose gear. The impact of aircraft load does not transfer deeper than 1 meter underneath the pavement surface. For the five different aircraft ground maneuvers, taxiing is most likely to cause rutting distress, while takeoff is more likely to cause horizontal deformation and layer slippage distress.

9.3 Recommendations for Future Research

- For all the lab-produced loose mixes (HL3 64-28, HL3 HS 70-28, and HL1 HS 70-28), it is very difficult to obtain a 63 mm height of cylindrical specimen from the Superpave Gyratory compactor at a required air voids level of 7 ± 0.5 percent. The author tried to minimize all the causes of aggregate segregation during the preparation of specimens. Increasing gyrations can help some specimens to reach 63 mm, but over compaction may cause crushing of coarse aggregates and affect overall gradation. Some specimens ended up with 64 mm height for the compaction workability and testing specimen size requirements.
- All the HWTT results did not present an obvious stripping stage at a testing temperature of 60 °C and 10,000 loading cycles. The author suggests that the overall loading cycles of HWTT should be extended. For example, the French Laboratory Rutting Tester (FLRT) is capable of 30,000 cycles for asphalt mixture to display rutting failure.
- Single LVDT rutting data collector on each load wheel is not enough to provide accurate rutting information. The false-negative rut depth appearing at the very

beginning of some tests and extremely unstable depth records at the end of every test support this finding. Aggregate relocation and shear flow under test conditions might be possible explanations for this finding.

- A more accurate method is needed for identifying small particles and voids of which area is smaller than 5 mm^2. A major concern for the unsatisfactory relationship between morphological indexes and rutting depth is that those small particles and voids are misidentified. Asphalt mastic should also be considered in the extracting process in future studies.
- Only top view images were analyzed in this study due to the large workload in terms of the data process. The front view and right view should also be analyzed in a more efficient way to possibly find more in-depth information regarding using 2-dimensional images representing three-dimensional realistic objects as well as bridging road performance with morphological properties.
- Dynamic Modulus and flow number tests are highly recommended for future research for permanent deformation verification. HWTT itself might not be sufficient for high-temperature performance evaluation.
- Solid de-icing chemicals such as urea are suggested to be considered in future studies as solid chemicals are still major de-icing agents for many airports due to their low cost and easy accessibility. The chemical reaction between asphalt binder and the de-icing agent is suggested to be investigated using advanced research devices such as the scanning electron microscope (SEM).
- There are limited methods of verifying finite element model calculation results for shear stress and displacement analysis. Lab experiments are suggested to compare with modeling results.

REFERENCES

AASHTO. (2013a). *AASHTO T269: Percent Air Voids in Compacted Dense and Open Asphalt Mixtures*. 1–4.

AASHTO. (2013b). *Bulk Specific Gravity (Gmb) of Compacted Hot Mix Asphalt ((HMA) Using Saturated Surface- Dry Specimens*.

AASHTO. (2013c). *Mixture Conditioning of Hot Mix Asphalt(HMA)* (Vol. 02, Issue 2010).

AASHTO. (2013d). *Resistance of Compacted Hot Mix Asphalt (HMA) to Moisture-Induced Damage* (Vol. 07, Issue 2011).

AASHTO. (2013e). *Theoretical Maximum Specific Gravity of Hot Mix Asphalt (HMA)*.

AASHTO. (2016). *Standard Method of Test for Hamburg Wheel Track Testing of Compacted Hot Mix Asphalt* (Vol. 16).

Abdul, N., Airey, G. D., & Rosli, M. (2014). Characterization of microstructural damage in asphalt mixtures using image analysis. *CONSTRUCTION & BUILDING MATERIALS*, *54*, 27–38. https://doi.org/10.1016/j.conbuildmat.2013.12.047

Akash Purochem Pvt. Ltd. (2020). *Potassium Acetate ACS*. https://www.vinipul.net/potassium-acetate-acs-5009210.html

Al-bayati, H. K. A. (2019). *Evaluation of Various Treatment Methods for Enhancing the Properties of Recycled Concrete Aggregate for Hot Mix Asphalt*.

Alpaydin, E. (2009). *Introduction to Machine Learning Second Edition* (T. M. Press (ed.)).

Arganda-Carreras I, Kaynig V, R. C. (2017). Trainable Weka Segmentation: a machine learning tool for microscopy pixel classification. *Bioinformatics*, 1–14.

Aschenbrener, Tim. (1995). Evaluation of Hamburg Wheel-Tracking Device to Predict

Moisture Damage in Hot-Mix Asphalt. *Transportation Research Record*, 193–201.

Aschenbrener, Timothy, & Currier, G. (1993). *Influence of Testing Variables on The Results From the Hamburg Wheel-Tracking Device*.

ASTM. (2017). *Standard Test Method for Percent Air Voids in Compacted Asphalt Mixtures*. 1–3. https://doi.org/10.1520/D3203

ASTM. (2019a). *Bulk Relative Density of Hot Mix Asphalt*.

ASTM. (2019b). *Theoretical Maximum Relative Density: Vol. i*. https://doi.org/10.1520/D2041

Badeli, S. (2018). *Evaluation of the Damage of an Asphalt Mix under Repeated Freeze-Thaw Cycles*.

Boeing Commercial Airplanes. (1998). *Airport Planning 777*. *July*.

Boeing Commercial Airplanes. (2015). 777-200LR/300ER -Freighter Airplane Characteristics for Airport Planning. *The Economic Journal*, *80*(318), 307. https://doi.org/10.2307/2230120

Buncher, M. (2020). What percentage of our roads are asphalt? *The Magzine of the Asphalt Institute*, 8–12.

Buonsanti, M., & Leonardi, G. (2012). A Finite element model to evaluate airport flexible pavements response under impact. *Applied Mechanics and Materials*, *138–139*(April), 257–262. https://doi.org/10.4028/www.scientific.net/AMM.138-139.257

C.F. Mora, A.K.H. Kwan1, and H. C. C. (1998). Particle Shape Analysis of Coarse Aggregate Using Digital Image Processing. *Cement and Concrete Research*, *28*(6), 921–932.

Chaturabong, P., & Bahia, H. U. (2017). Mechanisms of asphalt mixture rutting in the dry Hamburg Wheel Tracking test and the potential to be an alternative test in measuring rutting resistance. *Construction and Building Materials*, *146*, 175–182. https://doi.org/10.1016/j.conbuildmat.2017.04.080

Coleri, E. (2013). *Investigation of asphalt concrete rutting mechanisms by X-ray*

computed tomography imaging and micromechanical finite element modeling. *January 2015*. https://doi.org/10.1617/s11527-012-9951-x

Coleri, E., Harvey, J. T., Yang, K., & Boone, J. M. (2012). Development of a micromechanical finite element model from computed tomography images for shear modulus simulation of asphalt mixtures. *Construction and Building Materials*, *30*, 783–793. https://doi.org/10.1016/j.conbuildmat.2011.12.071

Collier, M. (2011). Road Pricing in North America & Other Jurisdictions. *Transport Futures / Healthy Transport Consulting*.

Cui, P., Xiao, Y., Yan, B., Li, M., & Wu, S. (2018). Morphological characteristics of aggregates and their influence on the performance of asphalt mixture. *Construction and Building Materials*, *186*, 303–312. https://doi.org/10.1016/j.conbuildmat.2018.07.124

Dai, Q. (2011). Two- and three-dimensional micromechanical viscoelastic finite element modeling of stone-based materials with X-ray computed tomography images. *Construction and Building Materials*, *25*(2), 1102–1114. https://doi.org/10.1016/j.conbuildmat.2010.06.066

Dongré, R., Angelo, J. D., & Copeland, A. (n.d.). *Refinement of Flow Number as Determined by Asphalt Mixture Performance Tester Use in Routine Quality Control – Quality Assurance Practice*. 127–136. https://doi.org/10.3141/2127-15

Edwards, Y., Rollen, J., Lange, G., Aurstad, J., Nilsen, T., & Civil, S. (1999). *Durability Problems on Nordic Airfields-the Influence of De-icing Agents on Asphalt Concrete Pavements*.

Engineerign Forum. (2020). *Corrugation And Shoving In Flexible Pavements: Causes and Remedies*.

European Asphalt Pavement Association. (2018). *Heavy Duty Surfaces-the Argument for SMA*.

Advisory Circular, Area 1 (2016). https://doi.org/AFS-800 AC 91-97

Fay, L., Volkening, K., & Gallaway, C. (2008). *Performance and Impacts of Current*

Deicing and Anti-icing Products : User Perspective versus Experimental Data. 1–23.

Feng, D., Yi, J., Wang, D., & Chen, L. (2010). Impact of salt and freeze-thaw cycles on the performance of asphalt mixtures in coastal frozen regions of China. *Cold Regions Science and Technology*, *62*(1), 34–41. https://doi.org/10.1016/j.coldregions.2010.02.002

Gong, Y., Bi, H., Liang, C., & Wang, S. (2018). *Microstructure Analysis of Modified Asphalt Mixtures under Freeze-Thaw Cycles Based on CT Scanning Technology*. https://doi.org/10.3390/app8112191

Greater Toronto Airport Authority. (2018). *Rehabilitate Taxi A (AF to AT)*.

Harmoney Deicing Product. (2020). *Liquid Potassium Acetate*. https://www.harmoneydeicing.com/runway-deicers

Hassan, N. A., Airey, G. D., Khan, R., & Collop, A. C. (2012). *Nondestructive Characterisation of the Effect of Asphalt Mixture Compaction on Aggregate Orientation and Segregation Using X-ray Computed Tomography*. *5*(2), 84–92.

Hassan, Y., Razaqpur, G., & Bekheet, W. (2002). *Effects of Runway Deicers on Pavement Materials and Mixes : Comparison with Road Salt Effects of Runway Deicers on Pavement Materials and Mixes : Comparison with Road Salt*. *4*(July). https://doi.org/10.1061/(ASCE)0733-947X(2002)128

Hernandez, J. A., Gamez, A., Shakiba, M., & Al-Qadi, I. L. (2015). *Numerical Prediction of Three-Dimensional Tire-Pavement Contact Stresses*. *April 2015*.

Hisao, T. (1970a). *Tire-Pavement Friction Coefficients*.

Hisao, T. (1970b). *Tire-Pavement Friction Coefficients*.

Ho, T. K. (2002). *A Data Complexity Analysis of Comparative Advantages of Decision Forest Constructors*. 102–112.

Hu, C., Youtcheff, J., Wang, D., Zhang, X., Kutay, E., & Hu, R. (2020). *Characterization of Asphalt Mixture Homogeneity Based on X-ray Computed Tomography*. *40*(7), 1082–1088. https://doi.org/10.1520/JTE20120159

Hu, X., Faruk, A. N. M., Zhang, J., Souliman, M. I., & Walubita, L. F. (2017). Effects of tire inclination (turning traffic) and dynamic loading on the pavement stress-strain responses using 3-D finite element modeling. *International Journal of Pavement Research and Technology*, *10*(4), 304–314. https://doi.org/10.1016/j.ijprt.2017.04.005

Huang, C. W., Abu Al-Rub, R. K., Masad, E. A., & Little, D. N. (2011). Three-Dimensional Simulations of Asphalt Pavement Permanent Deformation Using a Nonlinear Viscoelastic and Viscoplastic Model. *Journal of Materials in Civil Engineering*, *23*(1), 56–68. https://doi.org/10.1061/(ASCE)MT.1943-5533.0000022

Ivanović, M., & Radovanović, M. (2014). *Modern machine learning techniques and their applications*.

Izzo, R., & Tahmoressi, M. (n.d.). *Use of the Hamburg Wheel-Tracking Device for Evaluating Moisture Susceptibility of Hot-Mix Asphalt*. *99*.

James, G., Witten, D., Hastie, T., & Tibshirani, R. (2013). *An Introduction to Statistical Learning*.

Johnston, A. G. (Art), Lakkavalli, V., & Sharma, V. (2017). *Meeting the Unique Challenges of Pavements Engineering in the Urban Context, City of Calgary*.

Julio-betancourt, G. A. (2009). *Effect of De-icer and Anti-Icer Chemicals on the Durability, Microstructure, and Properties of Cement-Based Materials*. University of Waterloo.

Kanitpong, K., & Bahia, H. (2005). *Relating Adhesion and Cohesion of Asphalts to the Effect of Moisture on Laboratory Performance*. 33–43.

Kassem, E., Masad, E., Lytton, R., Chowdhury, A., Kassem, E., Masad, E., & Lytton, R. (2011). *Influence of Air Voids on Mechanical Properties of Asphalt Mixtures Influence of Air Voids on Mechanical Properties of Asphalt Mixtures*. *0629*. https://doi.org/10.3166/RMPD.12.493-524

Khan, R., & Collop, A. (2010). *The Use of X-Ray Computed Tomography to*

Characterize Microdamage in Road Materials and Pavement Design The Use of X-Ray Computed Tomography to Characterize Microdamage in Asphalt. *January*. https://doi.org/10.1080/14680629.2010.9690328

Khanal, S., Olidis, C., & Hein, D. K. (2016). Modeling pavement response to superheavy load movement. *2016 Transportation Association of Canada's Conference and Exhibition, TAC 2016*, 1–19.

Kim, J., Sholar, G. A., & Kim, S. (2008). Determination of accurate creep compliance and relaxation modulus at a single temperature for viscoelastic solids. *Journal of Materials in Civil Engineering*, *20*(2), 147–156. https://doi.org/10.1061/(ASCE)0899-1561(2008)20:2(147)

Kim, M., & Tutumluer, E. (2011). *Validation of a Three-Dimensional Finite Element Model using Airfield Pavement Multiple Wheel Load Responses Validation of a Three-Dimensional Finite Element Model using Airfield Pavement Multiple Wheel Load Responses*. *0629*. https://doi.org/10.3166/RMPD.11.387-408

Leahy, R., Yang, S. S., Vargas, A., & Schmalzer, P. (2014). *Effects of Deicing/Anti-Icing Chemicals (DIAICs) on Rubberized Asphalt Pavements* (Issue September).

Leonardi, G. (2016). *Finite element analysis for airfield asphalt pavements rutting prediction*. *July 2015*. https://doi.org/10.1515/bpasts-2015-0045

Liu, P., Wang, D., & Oeser, M. (2015). Application of semi-analytical finite element method coupled with an infinite element for analysis of asphalt pavement structural response. *Journal of Traffic and Transportation Engineering (English Edition)*, *2*(1), 48–58. https://doi.org/10.1016/j.jtte.2015.01.005

Liu, P., Xing, Q., Dong, Y., Wang, D., Oeser, M., & Yuan, S. (2017). Application of Finite Layer Method in Pavement Structural Analysis. *Applied Sciences*, *7*(6), 611. https://doi.org/10.3390/app7060611

Liu, T., Zhang, X., Li, Z., & Chen, Z. (2014). Research on the homogeneity of asphalt pavement quality using X-ray computed tomography (CT) and fractal theory. *Construction and Building Materials*, *68*, 587–598.

https://doi.org/10.1016/j.conbuildmat.2014.06.046

Lu, Q., & Harvey, J. T. (2006). *Evaluation of Hamburg Wheel-Tracking Device Test with Laboratory and Field Performance Data*. 25–44.

Lv, Q., Huang, W., Bahia, H. U., Ph, D., Asce, M., Tang, N., & Zhu, T. (2018). *Three-Stage Damage Evolution of Asphalt Mixture in the Wet Hamburg Wheel Tracking Device Test Using X-Ray Computed Tomography*. *30*(7), 1–9. https://doi.org/10.1061/(ASCE)MT.1943-5533.0002355

M. Wensel, Shalaby, M. Thiessen, V. M. (2002). *Investigation of Asphalt Pavement Rutting at Two Canadian Airfields*. 1–9.

M.H.Farha, & Y.Hassan. (2002). *Effects of New Deicing Alternatives on Airfield Asphalt Concrete Pavements*. 1–12.

Masad, E., Jandhyala, V. K., Dasgupta, N., Somadevan, N., & Shashidhar, N. (2002). *Characterization of Air Void Distribution in Asphalt Mixes using X-ray Computed Tomography*. *14*(April), 122–129.

Michelin Aircraft Tyre. (2017). *Aircraft Tire Engineering Data*.

Mills, B. N., Tighe, S. L., Ph, D., Andrey, J., Ph, D., Smith, J. T., & Huen, K. (2009). *Climate Change Implications for Flexible Pavement Design and Performance in Southern Canada*. *135*(October), 773–782.

Ministry of Transportation of Ontario. (2011). *Method of Test for Modified Hamburg Wheel Track Testing of Compacted Hot Mix Asphalt* (Issue 26).

Modern Airliners. (2020). *Boeing 777-200 and Boeing 777-300 Specs*.

Montgomery, D. C. (2001). *Design and Analysis of Experiments*.

MTO. (1996). *Method of Test for Determination of Air Voids in Compacted Dense Bituminous Pavement Mixtures*. *16*, 265.

MTO. (1999). *Method of Test For Bulk Relative Density of Compacted Bituminous Mixtures*. *18*, 6–8.

MTO. (2012). *Method of Test for Theoretical Maximum Relative Density of Bituminous Paving Mixtures*. *27*.

Olson, E. (2011). Particle Shape Factors and Their Use in Image Analysis. *The Journal of GXP*, *15*(1).

Ontario Asphalt Pavement Council. (2017). *OAPC Asphalt Fact Sheet*.

Material Specification for Hot Mix Asphalt, 1 (2008) (testimony of Ontario Provincial Standard Specification).

Osmari, P. H., Costa, R. rio F. da, Araga˜o, F. T. S., Braz, D., Barroso, R. C. R., Nogueira, L. P., & Ng, A. K. Y. (2020). Determination of Volumetric Characteristics of FAM Mixtures using X-Ray Micro-Computed Tomography and Their Effects on the Rheological Behavior of the Material. *Transportation Research Record*. https://doi.org/10.1177/0361198120914607

Pan, T., He, X., & Shi, X. (2008). *Laboratory Investigation of Acetate-Based Deicing/Anti-Icing Agents Deteriorating Airfield Asphalt Concrete*.

Pan, T., Tutumluer, E., & Carpenter, S. H. (2005). Effect of coarse aggregate morphology on the resilient modulus of hot-mix asphalt. *Transportation Research Record*, *1929*, 1–9. https://doi.org/10.3141/1929-01

Rizvi, R., Tighe, S. L., & Uzarowski, L. (2015). Research to Identify Advanced Asphalt Technology to Address Shear Distresses on Airside Facilities. *Transportation Association of Canada*.

Roston, J. P., Roberts, F. L., & Baron, W. (1976). Density Standards for Field Compaction of Granular Bases and Subbases. In *Natl Coop Highw Res Program Rep* (Issue 172).

S.W.Park, & Y.R.Kim. (1999). *Interconversion Between Relaxation Modulus and Creep Compliance for Viscoelastic Solids*. *February*, 76–82.

Safiuddin, M., Tighe, S. L., & Uzarowski, L. (2014a). Evaluation of stiffness to predict rutting resistance of hot-mix asphalt: a Canadian case study. *The Baltic Journal of Road and Bridge Engineering*, *9*(4), 283–296. https://doi.org/10.3846/bjrbe.2014.35

Safiuddin, M., Tighe, S. L., & Uzarowski, L. (2014b). Evaluation of stiffness to predict

rutting resistance of hot-mix asphalt: A Canadian case study. *Baltic Journal of Road and Bridge Engineering*, *9*(4), 283–296. https://doi.org/10.3846/bjrbe.2014.35

Santagata, E., Baglieri, O., & Riviera, P. P. (2013). Effect of anti-icing chemicals on stripping of asphalt concrete mixtures for airport runway wearing courses. *Sustainable and Efficient Pavements*, 1229–1239.

Schram, S., Williams, R. C., & Buss, A. (2014). *Reporting Results from the Hamburg Wheel Tracking Device*. *2446*, 89–98. https://doi.org/10.3141/2446-10

Schweigert, N. (2016). *Characterization of Runway Deicers*.

ScienceLab.com. (2013). *Material Safety Data Sheet of Potassium Acetate*. https://sciencelab.com/

Shafabakhsh, G., Kashi, E., & Tahani, M. (2018). Analysis of runway pavement response under aircraft moving load by FEM. *Journal of Engineering, Design, and Technology*, *16*(2), 233–243. https://doi.org/10.1108/JEDT-09-2017-0093

Shaheen, M. (2015). *Evaluation of X-Ray Computed Tomography and Finite Element Models for Fatigue Experimental Hot Mix Asphalt Characterization*. University of Waterloo.

Shaheen, M., Al-Mayah, A., & Tighe, S. (2013). Evaluating the Potential for Hot Mix Asphalt Rutting Performance Using Laboratory and Digital Imaging Technique. *Transportation Association of Canada*.

Shashidhar, N. (1999). *X-Ray Tomography of Asphalt Concrete*. *99*, 186–192.

Shi, X. (2008). *Impact of Airport Pavement De-icing Products on Aircraft and Airfield Infrastructure*.

Shi, X., Akin, M., Pan, T., Fay, L., Liu, Y., & Yang, Z. (2009). *Deicer Impacts on Pavement Materials : Introduction and Recent Developments*. 16–27.

Shi, X., Fay, L., Gallaway, C., Volkening, K., Peterson, M., Pan, T., Creighton, A., & Lawlor, C. (2009). *EVALUATION OF ALTERNATE ANTI-ICING AND DEICING COMPOUNDS USING SODIUM CHLORIDE AND MAGNESIUM CHLORIDE*

AS BASELINE DEICERS – PHASE I (Issue February).

Sultan, S. A., & Guo, Z. (2017). Evaluating the performance of sustainable perpetual pavements using recycled asphalt pavement in China. *International Journal of Transportation Science and Technology*, *5*(3), 200–209. https://doi.org/10.1016/j.ijtst.2017.01.001

Sumsion, E. S., Guthrie, W. S., & Ph, D. (2013). *PHYSICAL AND CHEMICAL EFFECTS OF DEICERS ON CONCRETE PAVEMENT : LITERATURE REVIEW* (Issue July).

Runway Ice Control Chemicals, 3 (2013).

Airport Winter Maintenance and Planning, 1 (2018).

Uzarowski, L. (2006). *THE DEVELOPMENT OF ASPHALT MIX CREEP PARAMETERS AND FINITE ELEMENT MODELING OF ASPHALT RUTTING*.

Uzarowski, L., Paradis, M., & Paul Lum. (2004). Accelerated Performance Testing of Canadian Asphalt Mixes Using Three Different Wheel Rut Testers. *2004 Annual Conference of the Transportation Association of Canada*, *February*.

Vacin, O., Ponniah, J., & Tighe, S. (2005). Quantifying the shear strength at the asphalt interface. *AISIM Symposium, Waterloo*.

Walubita, L. F., Faruk, A. N. M., Zhang, J., Hu, X., & Ick, S. (2016). The Hamburg rutting test – Effects of HMA sample sitting time and test temperature variation. *Construction and Building Materials*, *108*, 22–28. https://doi.org/10.1016/j.conbuildmat.2016.01.031

Wang, Hainian, Bu, Y., Wang, Y., Yang, X., & You, Z. (2016). The effect of morphological characteristic of coarse aggregates measured with fractal dimension on asphalt mixture's high-temperature performance. *Advances in Materials Science and Engineering*, *2016*(February). https://doi.org/10.1155/2016/6264317

Wang, Hainian, Huang, Z., Li, L., You, Z., & Chen, Y. (2014). Three-dimensional modeling and simulation of asphalt concrete mixtures based on X-ray CT

microstructure images. *Journal of Traffic and Transportation Engineering*, *1*(1), 55–61. https://doi.org/10.1016/S2095-7564(15)30089-1

Wang, Hainian, Liu, Y., Bu, Y., Zhou, Y., & Li, X. (2015). Study on the Influential Factors in and the Optimization of Asphalt Mixture Scanning with X-ray CT Technology. *Journal of Highway and Transportation Research and Development*, *9*(3), 34–40.

Wang, Hainian, Wang, C., Bu, Y., You, Z., Yang, X., & Oeser, M. (2020). Correlate aggregate angularity characteristics to the skid resistance of asphalt pavement based on image analysis technology. *Construction and Building Materials*, *242*, 118150. https://doi.org/10.1016/j.conbuildmat.2020.118150

Wang, Hao, Al-Qadi, I. L., Portas, S., & Coni, M. (2013). Three-dimensional finite element modeling of instrumented airport runway pavement responses. *Transportation Research Record*, *2367*, 76–83. https://doi.org/10.3141/2367-08

Wang, L. B., Frost, J. D., & Shashidhar, N. (2001). Microstructure Study of WesTrack Mixes from X-Ray Tomography Images. *Transportation Research Record*, *01*, 85–94.

Wheeler, D. J. (2004). *Advanced Topics in Statistical Process Control*.

White, G. (2016). Shear stresses in an asphalt surface under various aircraft braking conditions. *International Journal of Pavement Research and Technology*, *9*(2), 89–101. https://doi.org/10.1016/j.ijprt.2016.02.002

White, G. (2018). State of the art : Asphalt for airport pavement surfacing. *International Journal of Pavement Research and Technology*, *11*(1), 77–98. https://doi.org/10.1016/j.ijprt.2017.07.008

White, G., Tighe, S., Emery, S., & Yeaman, J. (2016). Developing a framework for the diagnosis of shear distress in asphalt surfaces. *International Journal of Pavement Engineering*, *8436*(August), 1–13. https://doi.org/10.1080/10298436.2016.1141413

Williams, C., & Prowell, B. (1997). Comparison of Laboratory Wheel-Tracking Test

Results with WesTrack Performance. *Transportation Research Record*, *99*, 121–128.

Wollny, I., Behnke, R., Villaret, K., & Kaliske, M. (2016). Numerical modeling of tyre–pavement interaction phenomena: coupled structural investigations. *Road Materials and Pavement Design*, *17*(3), 563–578. https://doi.org/10.1080/14680629.2015.1094399

Wright, M. (2013). *A Study of the Effects of Adding Ice Retardant Additives to Pavement Surface*. *April*.

Wu, J., Wang, L., Hou, Y., Xiong, H., Lu, Y., & Zhang, L. (2018). A digital image analysis of gravel aggregate using CT scanning technique. *International Journal of Pavement Research and Technology*, *11*(2), 160–167. https://doi.org/10.1016/j.ijprt.2017.08.002

Wu, W., Li, Z., Zhang, X., & Li, M. (2018). Evaluating RLWT Rutting Test of Asphalt Mixtures Based on Industrial Computerized Tomography. *Advances in Materials Science and Engineering*, *2018*.

Xie, N., Shi, X., & Zhang, Y. (2015). *Comparing the Direct Costs and Infrastructure Implications of Anti-Icing Strategies* (Issue 531).

Xing, C., Xu, H., Tan, Y., Liu, X., Zhou, C., & Scarpas, T. (2018). Gradation Measurement of Asphalt Mixture by X-Ray CT Images and Digital Image Processing Methods Gradation measurement of asphalt mixture by X-Ray CT images and digital image processing methods. *Measurement*, *132*(November), 377–386. https://doi.org/10.1016/j.measurement.2018.09.066

Xu, L. (2014). *Typical values of Young's elastic modulus and Poisson's ratio for pavement materials*. www.academia.adu

Yin, F., Arambula, E., Lytton, R., Martin, A. E., & Cucalon, L. G. (2014). Novel Method for Moisture Susceptibility and Rutting Evaluation Using Hamburg Wheel Tracking Test. *Transportation Research Record*. https://doi.org/10.3141/2446-01

Ying, H., Elseifi, M. A., Asce, M., Mohammad, L. N., Asce, M., Hassan, M. M., & Asce,

M. (2014). *Heterogeneous Finite-Element Modeling of the Dynamic Complex Modulus Test of Asphalt Mixture Using X-ray Computed Tomography*. *26*(9), 1–7. https://doi.org/10.1061/(ASCE)MT.1943-5533.0000949

You, Z., Adhikari, Æ. S., & Kutay, Æ. M. E. (2009). *Dynamic modulus simulation of the asphalt concrete using the X-ray computed tomography images*. 617–630. https://doi.org/10.1617/s11527-008-9408-4

Yu, X., Wang, Y., Luo, Y., & Yin, L. (2013). *The Effects of Salt on Rheological Properties of Asphalt after Long-Term Aging*. *2013*.

Zak, J., Coleri, E., & Harvey, J. (2019). *Incremental Rutting Prediction with Asphalt Mixture Shear Properties* (Vol. 1). Springer International Publishing. https://doi.org/10.1007/978-3-319-95792-0_2

Zak, J., Monismith, C. L., Coleri, E., & Harvey, J. T. (2017a). Uniaxial Shear Tester–new test method to determine shear properties of asphalt mixtures. *Road Materials and Pavement Design*, *18*, 87–103. https://doi.org/10.1080/14680629.2016.1266747

Zak, J., Monismith, C. L., Coleri, E., & Harvey, J. T. (2017b). Uniaxial Shear Tester – new test method to determine shear properties of asphalt mixtures. *Road Materials and Pavement Design*, *18*(sup1), 87–103. https://doi.org/10.1080/14680629.2016.1266747

Zelelew, H. M., & Papagiannakis, A. T. (2011). *A volumetrics thresholding algorithm for processing asphalt concrete X-ray CT images*. *8436*. https://doi.org/10.1080/10298436.2011.561345

Zheng, M., Wu, S., Wang, C., Li, Y., Ma, Z., & Peng, L. (n.d.). *A Study on Evaluation and Application of Snowmelt Performance of Anti-Icing Asphalt Pavement*. https://doi.org/10.3390/app7060583